NASA/TM–20210011456

Marshall Space Flight Center Faculty Fellowship Program

N.F. Six, Program Director
Marshall Space Flight Center, Huntsville, Alabama

G. Karr, Compiler
The University of Alabama in Huntsville, Huntsville, Alabama

May 2021

NASA STI Program Report Series

The NASA STI Program collects, organizes, provides for archiving, and disseminates NASA's STI. The NASA STI program provides access to the NTRS Registered and its public interface, the NASA Technical Reports Server, thus providing one of the largest collections of aeronautical and space science STI in the world. Results are published in both non-NASA channels and by NASA in the NASA STI Report Series, which includes the following report types:

- TECHNICAL PUBLICATION. Reports of completed research or a major significant phase of research that present the results of NASA programs and include extensive data or theoretical analysis. Includes compilations of significant scientific and technical data and information deemed to be of continuing reference value. NASA's counterpart of peer-reviewed formal professional papers but has less stringent limitations on manuscript length and extent of graphic presentations.
- TECHNICAL MEMORANDUM. Scientific and technical findings that are preliminary or of specialized interest, e.g., quick release reports, working papers, and bibliographies that contain minimal annotation. Does not contain extensive analysis.
- CONTRACTOR REPORT. Scientific and technical findings by NASA-sponsored contractors and grantees.
- CONFERENCE PUBLICATION. Collected papers from scientific and technical conferences, symposia, seminars, or other meetings sponsored or cosponsored by NASA.
- SPECIAL PUBLICATION. Scientific, technical, or historical information from NASA programs, projects, and mission, often concerned with subjects having substantial public interest.
- TECHNICAL TRANSLATION. English-language translations of foreign scientific and technical material pertinent to NASA's mission.

Specialized services also include organizing and publishing research results, distributing specialized research announcements and feeds, providing information desk and personal search support, and enabling data exchange services.

For more information about the NASA STI program, see the following:

- Access the NASA STI program home page at http://www.sti.nasa.gov
- Help desk contact information:

https://www.sti.nasa.gov/sti-contact-form/ and select the "General" help request type.

NASA/TM–20210011456

Marshall Space Flight Center Faculty Fellowship Program

N.F. Six, Program Director
Marshall Space Flight Center, Huntsville, Alabama

G. Karr, Compiler
The University of Alabama in Huntsville, Huntsville, Alabama

National Aeronautics and
Space Administration

Marshall Space Flight Center • Huntsville, Alabama 35812

May 2021

Acknowledgments

All are grateful to those who, through their diligence, brought the 2020 NASA Marshall Space Flight Center Aerospace Fellowship program to completion. These professionals include Jody Singer, Larry Leopard, John Honeycutt, Steve Cash, Frank Six, Brooke Graham, Debora Nielson, Judy Drinnon, and Kevin McGhaw.

TRADEMARKS

Available from:

NASA STI Information Desk
Mail Stop 148
NASA Langley Research Center
Hampton, VA 23681–2199, USA
757–864–9658

This report is also available in electronic form at
<http://www.sti.nasa.gov>

EXECUTIVE SUMMARY

The 2020 Marshall Aerospace Fellowship Program involved 11 faculty in the laboratories and departments at Marshall Space Flight Center and one faculty researcher working from Colorado. These faculty engineers and scientists worked with NASA collaborators on NASA projects, bringing new perspectives and solutions to bear. This Technical Memorandum is a compilation of nine research reports of the 2020 Marshall Aerospace Fellowship program, along with the Program Announcement (Appendix A) and the Program Description (Appendix B). The research affected the following five areas:

(1) Materials
(2) Propulsion
(3) Spacecraft systems
(4) Vehicle systems
(5) Space science.

Additive manufacturing was the single materials investigation during the summer of 2020. Spacecraft systems tasks dominated the fellows' explorations: covering camera sensors for lunar surface mobility, a real-time system for navigation and mapping, flexible sensor modeling, and transmitter design for high data rate telemetry. One project concentrated on Human-System Interactions. Another fellow designed a model to predict heat leak into a cryogen tank, as in most vehicle systems. One of the scientists worked on a proposed space-based gravitational wave interferometer that will detect Galactic white dwarf binaries. Another space science fellow used a mature astrophysical code to synthesize galactic stellar populations. Our goal is to continue the Marshall Aerospace Program funded by Center project offices.

TABLE OF CONTENTS

Spacecraft-to-Ground Transmitter Design for High Data Rate Telemetry in Space Communications

Anthony Bessios [1], William Hopkins [2]
NASA MSFC, Huntsville, AL, 35812, USA

Category A missions with telemetry data rates of 10Mbps and SC type analog modulation are considered in this paper. A spacecraft transmitter for its telemetry task needs to produce a transmitted waveform with the strict spectral containment properties fitting the NTIA and SFCG masks. We mainly focus on GMSK modulation and OQPSK modulation with SRRC pulse shaping filter. Comparisons with MSK are also provided. We focus on designing key parameters such as the excess bandwidth used or rolloff factor α, and the time-bandwidth product. In the uncoded telemetry application a data rate of 10 Mb/s needs to be achieved through a 5 MHz bandwidth channel in the presence of a nonlinear power amplifier at the transmitter end. Detailed study of the amplifier effects on the system performance is provided. Predistortion is also introduced to process the amplifier's input and improve both the transmission spectral containment and the receiver's BER performance. This study includes a novel algorithm for initially calibrating the transmitter's PA optimum operating power point and its predistortion scheme.

I. Nomenclature

ACI = adjacent channel interference
AGC = automatic gain control
AM/AM = amplitude modulation to amplitude modulation conversion
AM/PM = amplitude modulation to phase modulation conversion
APD = analog predistortion
BER = bit-error-rate
BPSK = Binary Phase Shift Keying
BW = bandwidth
CMCP = constant magnitude constant phase
CMVP = constant magnitude varying phase
DPD = digital predistortion
ΔDOR = Delta-Differential One-Way Ranging
EVM = error-vector-magnitude
FR = frequency response
GMSK = Gaussian MSK
I = in-phase channel
IBO = input backoff point
IR = impulse response
ISI = intersymbol interference
LNA = low-noise amplifier

[1] NASA/MSFC AFP Faculty Fellow, Summer 2020.
[2] NASA/MSFC Team Lead, AST Tracking & Telemetry Systems.

LPF	=	Lowpass filter
MER	=	modulation error ratio
MF	=	matched filter
MLSE	=	maximum likelihood sequence estimator
MSK	=	Minimum Shift Keying
NLA	=	nonlinear power amplifier
NTIA	=	National Telecommunications and Information Administration
OBO	=	output backoff
OBW	=	occupied bandwidth
OQPSK	=	Offset Quadrature Phase Shift Keying
PA	=	power amplifier
PA	=	power amplifier
PAPR	=	peak-to-average power ratio
PD	=	predistortion
Q	=	quadrature-phase channel
QAM	=	Quadrature Amplitude Modulation
RFI	=	radio frequency interference
Rx	=	receive
SBS	=	symbol-by-symbol
SC	=	suppressed carrier
SFCG	=	Space Frequency Coordination Group
SIF	=	spectral improvement factor
SINR	=	signal-to-interference-and-noise ratio
SNR	=	signal-to-noise ratio
SNR_{phs-ns}	=	phase noise SNR
SPS	=	samples per symbol
SR	=	spectral regrowth
SRRC	=	squared root raised cosine
Tx	=	transmit
VMCP	=	varying magnitude constant phase
VMVP	=	varying magnitude varying phase

II. Introduction

This paper addresses the design problem of a telemetry transmitter for space communications. More specifically we are concerned with the downlink from the spacecraft transmitter towards the ground receivers. Operating in the S-band, we are dealing with regulatory restrictions, due to the spectral channel crowding. The data rate requirement is $R_b = 10\,Mbps$ and the available transmission bandwidth W is equal to *5 MHz*. Therefore, spectrally efficient modulation schemes need to be considered such as M-ary where M=4, QPSK, OQPSK, MSK, GMSK with spectral bit rates $\frac{R_b}{W} = \frac{1}{W \cdot T_b} = log_2 M = 2\,b/s/Hz$. The smaller the time bandwidth product $W \cdot T_b$ the more bandwidth efficient the modulation is[1].

Each of the two orthogonal substreams, I and Q, is demodulated independently and has the same detection efficiency, i.e. probability of bit error P_b for the same $\frac{E_b}{N_0}$ level, as the BPSK antipodal signal: $P_b = \frac{1}{2} erfc\left(\sqrt{\frac{E_b}{N_0}}\right)$. Therefore, quaternary PSK versions double the BPSK bandwidth efficiency without any power penalty. On the other hand, the 8-PSK shows a bandwidth efficiency gain of $1.5\times$ over QPSK, at the cost of a power loss of approximately 3.4 dB at the BER level of $P_b = 10^{-5}$.

The transmitted waveform needs to have several properties among which its spectral containment is of primary importance in order to reduce any out-of-band emissions. For both modulations QPSK and OQPSK the symbol period $T_s = 200\ ns$ for each of the two orthogonal substreams is double in duration of the bit period $T_b = 100\ ns$. However, in OQPSK there is a shift by a bit period T_b between the two substreams I and Q (staggering) preventing their simultaneous change and therefore halving the QPSK maximum phase shift of π down to $\frac{\pi}{2}$. That bit-shift between I and Q substreams prevents the simultaneous transitions through 0 by both substreams, which limits the size of the amplitude fluctuations and makes the OQPSK spectrally more efficient[2] than QPSK. Furthermore, pulse shaping lowpass filtering, such as an SRRC LPF, is being used to obtain an initial narrowing of the transmitted spectrum compared to the raw OQPSK modulated data using rectangular baseband pulse and presenting its first spectral null at T_s^{-1} yielding a double sideband bandwidth of 10 MHz. The smoothening effect obtained via lowpass filtering of the rectangular pulse reduces significantly the high frequency content but also causes variations of the signal amplitude which plays a role when nonlinear power amplifiers need to be driven by those types of signals. The pulse dispersion effect induced by the filter, causes ISI which can be optimally mitigated via the deployment of the corresponding MF at the receiver's end before detection takes place.

The MSK can be viewed as a special case of OQPSK where the rectangular baseband pulse is substituted by the half sine pulse. The smoother nature of this baseband pulse suppresses further the sidelobes and renders this modulation suitable when dealing with ACI. More specifically, the out-of-band behavior ($F \gg$), in terms of the normalized frequency $F_n = F \cdot T_s$, OQPSK sidelobes decay at a rate $\propto F_n^{-2}$, while the MSK sidelobes decay at a much higher rate[3,4] $\propto F_n^{-4}$. However, the MSK's wider main lobe (its 1st spectral null is located[2] at $0.75 \cdot R_b$) renders this modulation unsuitable for narrowband links. Further suppression of the sidelobes and spectral narrowing is achievable by GMSK whereby the rectangular pulse is now substituted by a Gaussian-shaped pulse which is even smoother than the MSK's sine pulse. The Gaussian filter used to shape the baseband pulse in GMSK, does not have all the ripples in its IR that an SRRC filter has, limiting this way the AM and PM effect on the modulated data.

Another important aspect of the modulated waveforms is that they need to go through amplitude limiting nonlinear power amplifiers characterized by certain AM/AM and AM/PM conversion functions. It was shown[5] that the NLA's constant amplitude operation causes crosstalk effect between the shapes of the two orthogonal I and Q waveforms (see Fig. 1). Finally, the NLA-induced ISI is expected to degrade the system's end-to-end BER performance, since the MF is not designed to compensate for that part of the system's ISI. For example, the matched SRRC receive filter is designed to mitigate the ISI introduced by its corresponding transmit SRRC filter. The insertion of an NLA degrades its performance since it changes the tx-filter induced ISI, which cannot be completely compensated by the receive SRRC filter anymore. Predistortion techniques have been used in the past with 64 and 256 QAM signals[6]. We will introduce and compare digital and analog techniques to precompensate and ameliorate the NLA's rotation effect and help contain better the spectrum with OQPSK and GMSK type modulations.

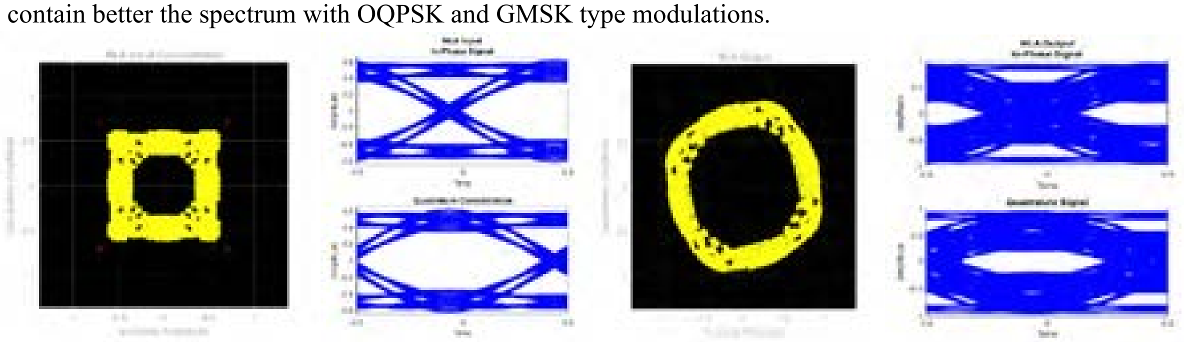

Figure 1. OQPSK-SRRC filtered signal constellations & eye-diagrams: (left) NLA input; (right) NLA output.

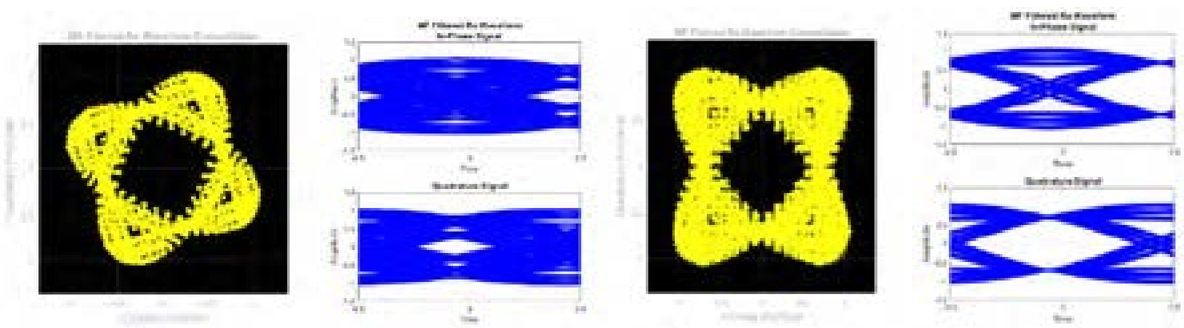

Figure 2. Pairs of constellations & eye-diagrams for the MF output: (left pair) w/o PD; (right pair) w/ PD.

III. OQPSK Transmitter System Block Architecture

The OQPSK modulated data are being filtered by an SRRC filter of various roll off factors to address the tradeoff between induced ISI and transmission bandwidth requirements. By substituting the rectangular baseband pulse with a half sine or a Gaussian we correspondingly address the MSK and GMSK systems. The modulated filtered signal is initially applied to a PD block which can be implemented either in the digital or analog domain. Finally, the PD block output is applied to the memoryless NLA to produce the final waveform for transmission. Our focus is on the transmitter end; however, we do address the receive side too, in order to be able to produce overall BER performance and compare all the alternate transmitter system architectures in terms of their corresponding detection efficiency. The receive end simply uses a MF, i.e., the corresponding SRRC filter, or alternately a quasi-MF such as a Butterworth filter and an SBS detector. Finally, for the GMSK case, a Viterbi MLSE detector is being used.

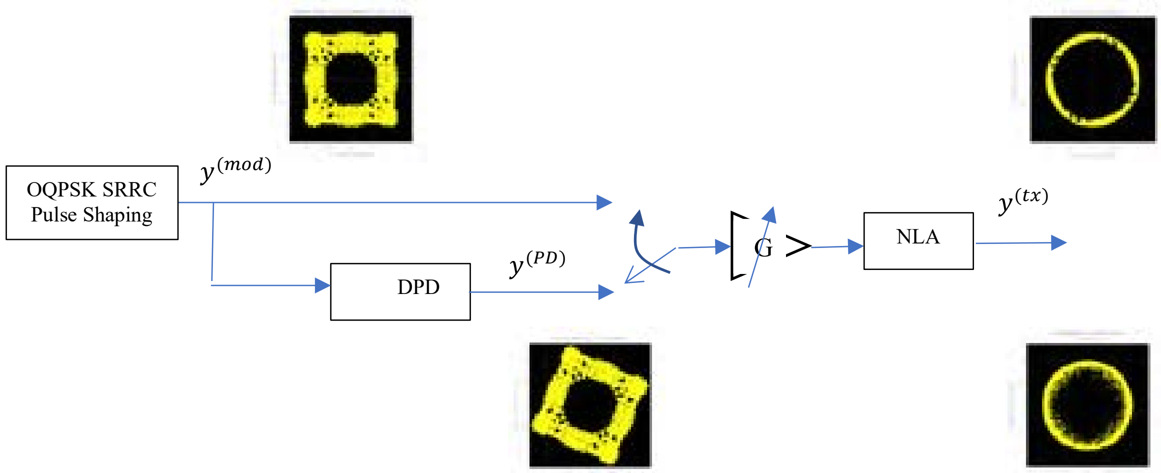

Figure 3. The OQPSK tx-er block diagram with digital PD, adjustable gain *G*, and NLA.

A. The Memoryless Nonlinear Power Amplifier Model

For the NLA we adopted the Saleh NLA PA model[7,8]described by the following conversion equations:

$$\text{AM/AM:} \quad \left|y^{(NLA)}\right| = A^{(NLA)}(V) = \frac{a_a V}{1+\beta_a V^2}, \qquad \text{AM/PM:} \quad \langle y^{(NLA)} = \Phi^{(NLA)}(V) = \frac{a_\varphi V^2}{1+\beta_\varphi V^2} \quad (1)$$

where $V = \begin{cases} G \cdot y^{(PD)}, & \text{if PD on} \\ G \cdot y^{(mod)}, & \text{if PD off} \end{cases}$, $a_a = 2.1587$, β_a=1.1517, a_φ=4.0033, β_φ=9.104.

In the linear region and for very small values of V ≪ , the following approximations can be derived:

$$A^{(NLA)}(V) \cong a_a V, \qquad \Phi^{(NLA)}(V) \cong a_\varphi V^2 \cong 0 \quad (1a)$$

In this case AM/AM and AM/PM conversion functions are independent of β_a, and β_φ. From Eq. (1a), we can calculate the linear gain of this amplifier:

$$G_{NLA} = \left(\frac{|y^{(NLA)}|}{V}\right)^2 \cong {a_a}^2 = 4.66 \tag{1b}$$

While in saturation and for relatively large values of V ≫ :

$$A^{(NLA)}(V) < \frac{a_a}{\beta_a V}, \qquad \Phi^{(NLA)}(V) < \frac{a_\varphi}{\beta_\varphi} = 0.4397\, rad = 25.2^o \tag{1c}$$

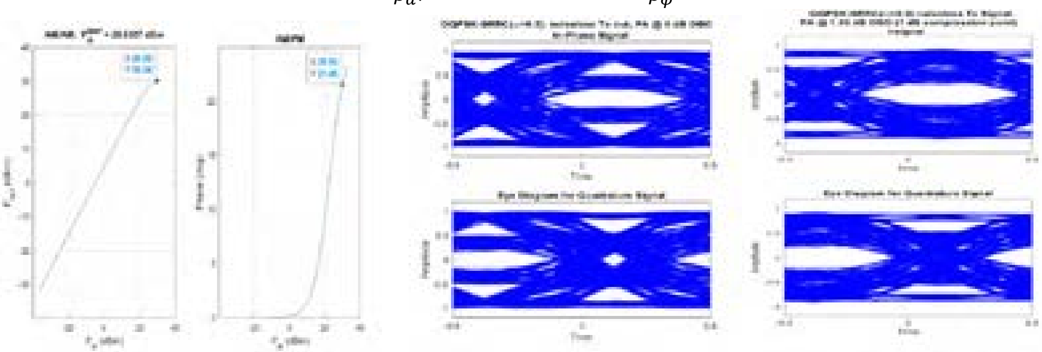

Figure 4. (left) The NLA model; The NLA output eye diagram: (middle) with severe ISI when the PA is operated at 0 dB OBO; (right) with reduced ISI when the PA is operated at 1 dB compression point.

B. Digital Predistortion (DPD)

We concentrate in manipulating the signal's magnitude so that the signal waveforms obtain optimum propagation properties through the transmitter's system components such as the NLA. Various DPD forms are proposed below. For example, the constant magnitude DPDs use the fact that in an X-QPSK modulation system the information is in the phase and therefore the magnitude information can be ignored. Below are listed various DPDs of the form:

$$y^{(PD)} = A^{(PD)}(V_m) \cdot e^{j\Phi^{(PD)}(V_m)} \tag{2}$$

$$\text{AM/AM: } \left|y^{(PD)}\right| = A^{(PD)}(V_m), \quad \text{AM/PM: } \langle y^{(PD)} = \Phi^{(PD)}(V_m) = -\Phi^{(NLA)}(V_m) \tag{3}$$

where $V_m = \left|y^{(mod)}\right|$, and $\Phi^{(PD)}(V_m)$ stands for pre-counter-rotation of the signal by an angle equal to the NLA's AM/PM operation.

1) PD1 with dynamic phase pre-counter-rotation:

$$\text{VMVP: } \quad A^{(PD)}(V_m) = \left|y^{(mod)}\right|, \quad y^{(PD)} = y^{(mod)} \cdot e^{-j\Phi^{(NLA)}(V_m)} \tag{4}$$

2) PD2 with dynamic magnitude/phase pre-counter-rotation:

$$\text{VMVP: } \quad A^{(PD)}(V_m) = A^{(NLA)}(V_m), \; y^{(PD)} = A(V_m) \cdot e^{-j(\Phi^{(NLA)} - \langle y^{(mod)})} \tag{5}$$

this predistortion has an AM/AM conversion function identical with the NLA, while an AM/PM conversion function opposite of the NLA.

3) PD3 with constant magnitude/dynamic phase pre-counter-rotation:

$$\text{CMVP: } \quad A^{(PD)}(V_m) = G, \quad y^{(PD)} = G \cdot \frac{y^{(mod)}}{V_m} \cdot e^{-j\Phi^{(NLA)}(V_m)} = G \cdot e^{-j(\Phi^{(NLA)}(V_m) - \langle y^{(mod)})} \tag{6}$$

note that once the magnitude becomes constant then the corresponding phase rotation also becomes constant, i.e., CMVP=CMCP, which is predistortion PD6.

4) PD5 with average phase (AP) pre-counter-rotation:

$$\text{CMAP: } \quad y^{(PD)} = \frac{y^{(mod)}}{V_m} \cdot e^{-j\bar{\Phi}\,(V_m)} \tag{7}$$

$$\text{VMAP:} \qquad y^{(PD)} = y^{(mod)} \cdot e^{-j\overline{\Phi}\,(V_m)} \qquad (8)$$

where over N symbols $\overline{\Phi}\,(V_m)=\frac{1}{N}\sum_{i=1}^{N}\Phi_i^{(NLA)}(V_m)$, can be implemented using adaptive moving average (MA) calculation.

5) PD6 with constant phase pre-counter-rotation:

$$\text{CMCP:} \qquad A^{(PD)}(V_m) = G, \qquad y^{(PD)} = G \cdot e^{-j(\Phi^{(NLA)}(V_m)-\langle y^{(mod)})} \qquad (9)$$

$$\text{VMCP:} \qquad A^{(PD)}(V_m) = \left|y^{(mod)}\right|, \qquad y^{(PD)} = y^{(mod)} \cdot e^{-j\Phi^{(NLA)}(V_m)} \qquad (10)$$

where in this case $\Phi^{(NLA)}(V_m) = \Phi_{X\ dBm}$ is the rotation angle corresponding to an NLA input V_m with power $X = 10log_{10}|V_m|^2 + 30\ dBm$, for example the rotation angle $\Phi_{30\ dBm} = 22.7^o$ corresponds to input power of 30 dBm. Note that predistortion PD6 becomes a special case of predistortion PD3, when the NLA input has constant magnitude and the AM/PM conversion maps a single input power onto a single-phase shift of the NLA output. For GMSK, since it is a constant magnitude modulation, we only need to consider the CMCP predistortion given by Eq. (9).

In Fig. 5, we show the histogram distributions of the NLA input power and of the corresponding phase shifting by the NLA. Figs. 5c) and 5f) correspond to predistortion cases PD3 and PD6 which produce identical distribution histograms concentrated on a single input power level and single output angle rotation, i.e. CMCP given by Eq. (6) and/or Eq. (9).

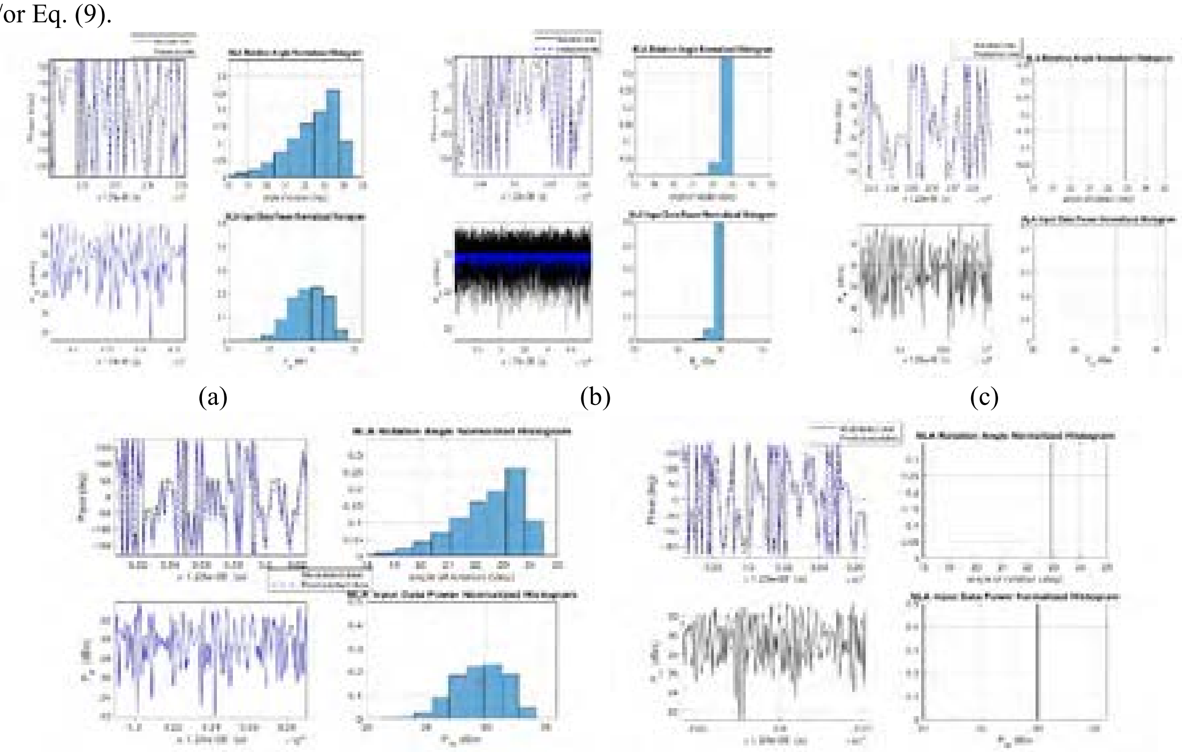

(a) (b) (c)

(d) (e)

Figure 5. NLA input power distribution and the corresponding rotation angle distribution: (a) PD1, (b) PD2, (c) PD3, (d) PD5, (e) PD6.

C. An Analog Predistortion Architecture

Predistortion PD2 implements the exact same conversions performed by the NLA. The observation that DPD2 followed by the NLA produces a constant magnitude amplified output, leads to an equivalent APD architecture of cascading two NLAs in the row which would also produce a constant magnitude amplified output.

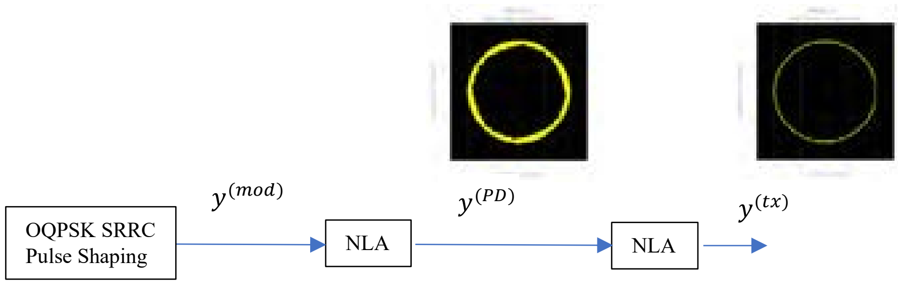

Figure 6. The OQPSK tx-er APD block diagram with cascaded NLAs.

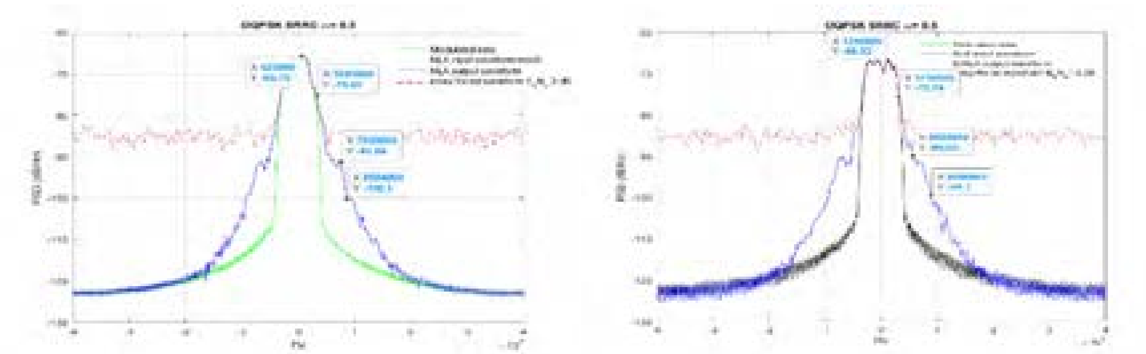

Figure 7. PSDs: (left) DPD2 + NLA; (right) APD: cascaded 2 x NLAs.

From Fig. 7, it is evident that the PSD characteristics of the two architectures are comparable, for example for single NLA with DPD the spectral regrowth starts at 3.281 MHz and -9.29 dB drop, while for the cascaded two NLAs it starts at 3.125 MHz and -8.91 dB drop.

Table 1: SRRC($\alpha = 0.5$): DPD2 vs. APD

bit-rate normalized bandwidth $BW_n = \Delta F \cdot T_b$		
PD 3 + NLA	*2 cascaded NLAs*	
drop (dB) / BW_n	***drop (dB) /*** BW_n	$2 \times NLA$ BW_n *gain*
-9.5 / 0.328	-8.91 / 0.312	0.016*
-25 / 0.75	-23.2 / 0.5625	0.1875
-34 / 0.859	-32.87 / 0.89	-0.031

* *SR starting point*

IV. Characterization of the Nonlinearly Amplified Transmitted Waveforms: PA, PD and SR

Fig. 8, shows the spectral narrowing effect via SRRC filtering, and the narrower OQPSK main lobe compared to the MSK one. At approximately -45 dB attenuation, the theoretical OQPSK spectral gain is approximately 66.66% of the theoretical MSK, while the filtered OQPSK one is the 57.2%. The filtered OQPSK-SRRC($\alpha = 0.25$) has approximately 85% of the spectral width of the OQPSK-SRRC($\alpha = 0.5$) at -32.5 dB attenuation.

Three different operating points for the PA are presented in Fig. 8: a) linear region, b) 1 dB compression point, and c) 0 dB OBO. Note the evident stronger SR effects when the PA is operated at its saturation region due to the introduced nonlinearities. The amplified spectra of OQPSK with rolloff factors $\alpha = 0.25$ and 0.5, have their corresponding crossover at the following points in units [MHz, dB]: a) linear region: [3.9, -27.6], b) 1 dB compression point: [4.2, -24.7], and c) 0 dB OBO: [3.9, -17]. All non-amplified and amplified cases meet after [16 -54.7]. The labels are showing the points complying with both the NTIA and SFCG masks. Specifically, the SFCG mask[8] reaches -30 dB at 14 MHz, and -60 dB at 30 MHz.

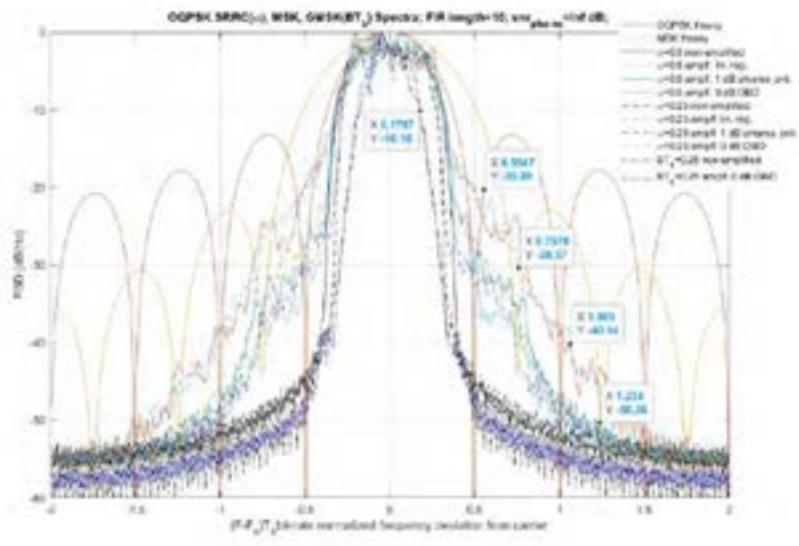

Figure 8. OQPSK-SRRC($\alpha = 0.25, 0.5$), MSK, GMSK($B \cdot T_b = 0.25$): NLA induced SR effects (PD off).

A. SIF for GMSK Over OQPSK-SRRC

The spectral improvement factor (SIF) determines the extra number of spacecrafts that can be accommodated in each bandwidth, via comparing the spectral widths at a certain attenuation level[10]:

$$SIF(\Delta F) = PSD^{(OQPSK)}(\Delta F) - PSD^{(GMSK)}(\Delta F) \tag{11}$$

where $\Delta F = F - F_c$ is the distance of the signal frequency from the carrier frequency. From Fig. 9, it is evident that for OPQSK there is a significantly increasing SR effect with the NLA operating point shifting from the linear region towards saturation, while the corresponding effect on GMSK is negligible. With the PD turned off, the maximum SIF of GMSK over OQPSK is shown in Fig. 9 and some key points are listed in Table 2:

Table 2: SR: OQPSK-SRRC($\alpha = 0.5$) v. GMSK($B \cdot T_b = 0.25$)

PA operating point	snr_{phs_ns} (dB)			
	∞		44.04	
	ΔF (MHz)	$\max_{\Delta F} SIF$ (dB)	ΔF (MHz)	$\max_{\Delta F} SIF$ (dB)
Linear region	-3.3	21.6	-3.4	21.7
1 dB compression point	3.3	21.9	-3.3	22.5
0 dB OBO	4.5	25.3	-4.5	25.2

In the Appendix there is a similar SR comparison study between OQPSK-SRRC($\alpha = 0.25$) and GMSK($B \cdot T_b = 0.25$) (see Figure A1, Table A1). There is also the same comparison when the VMCP-PD given by Eq. (10) is turned on (see Figure A2). The phase noise effect imposed by the PA, was modeled as follows:

$$y^{(tx)} = y^{(NLA)} = \begin{cases} y^{(mod)} \cdot e^{j2\pi\varphi_n}, & PD\ off \\ y^{(PD)} \cdot e^{j2\pi\varphi_n}, & PD\ on \end{cases} \tag{12}$$

where φ_n represents the random phase noise and is modeled as a zero-mean Gaussian variable of variance $\sigma^2_{\varphi_n}$:

$$\varphi_n \propto N(0, \sigma^2_{\varphi_n}) \tag{13}$$

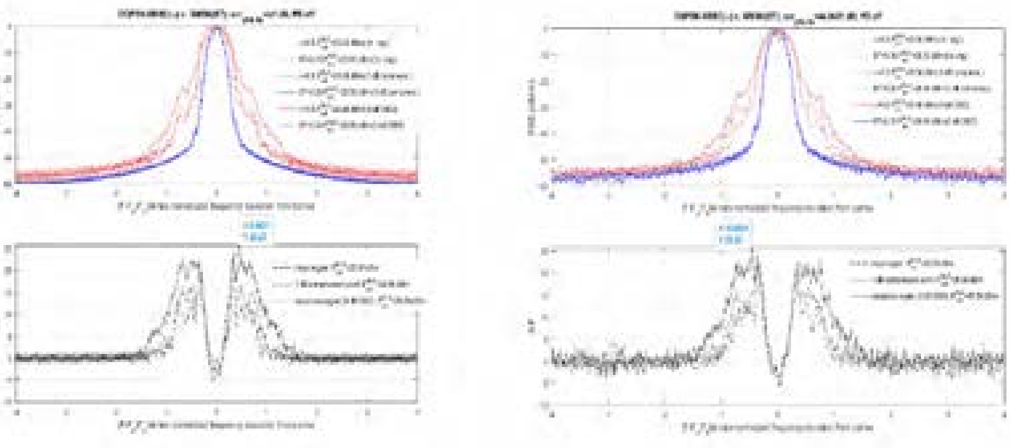

Figure 9. NLA induced spectral regrowth effects (PD off): (left) noiseless; (right) $snr_{phs\_ns} = 44.04\ dB$.

In the following we experiment in identifying the main contributor(s) to SR for OQPSK-SRRC pulse shaping. Therefore, we separated the magnitude operation from the phase operation to reveal their corresponding individual effects. Even though fixing the magnitude to a constant value initially seemed to be the right approach spectrally, it did demonstrate SR effects. Therefore, eventually magnitude variability was allowed while the phase was kept constant.

For the PD1 case, we measured the waveforms' spectral characteristics at various points of the system as is shown in Fig. 10. The spectral regrowth is apparent for both the NLA input at 3.438 MHz with -28.73 dB drop, and the NLA output at 2.5 MHz with -5.32 dB drop. Since the NLA input carries the PD1 effects, which only applies a phase prerotation, we can infer that the "bulk" of the spectral regrowth is due to the NLA's AM/AM conversion. It was explained[5] that when the lowpass filtered modulated signal goes through the NLA's constant amplitude operation, its edges are being sharpened causing SR of its sidelobes. Observing this effect on the spectral characteristics was the motivation to explore various versions of predistortion with different combinations of constant/dynamic magnitude/phase PD conversion functions. In Fig. 10 below, it is shown the spectral advantage of the VMVP-PD and the CMAP given by Eqs. (4) and (7), over the CMCP-PD given by Eq. (9):

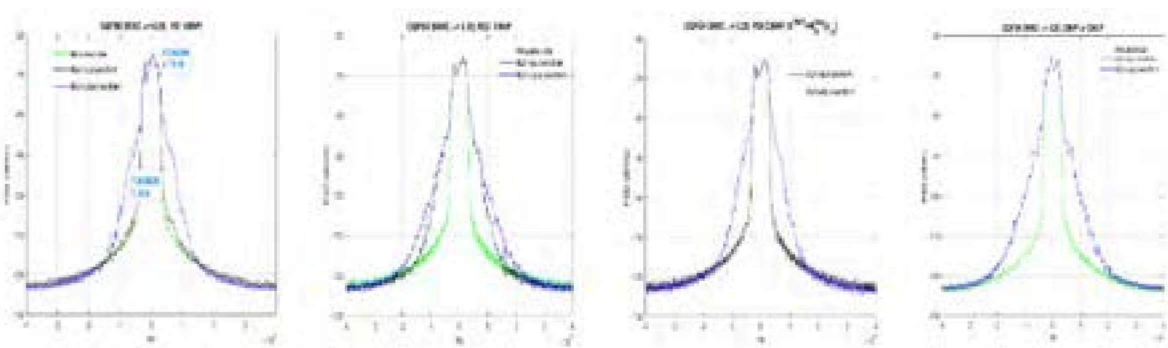

Figure 10. The NLA-induced SR of predistorted OQPSK-SRRC($\alpha = 0.25$).

For GMSK we use a Gaussian filter with bandwidth B so that the time-bandwidth product $B \cdot T_b$ determines the bandwidth efficiency of the GMSK modulation. We considered the following two cases: $B \cdot T_b = 0.25,$ and 0.5. The SIF of GMSK over OQPSK is larger for the CMCP-PD case (Fig. 12, left) where $\max_{\Delta F=-6.7\ MHz} SIF = 22.8\ dB$, than for the VMCP-PD case, (Fig. 12, right), where $\max_{\Delta F=-\ 4.5\ MHz} SIF = 18.27\ dB$.

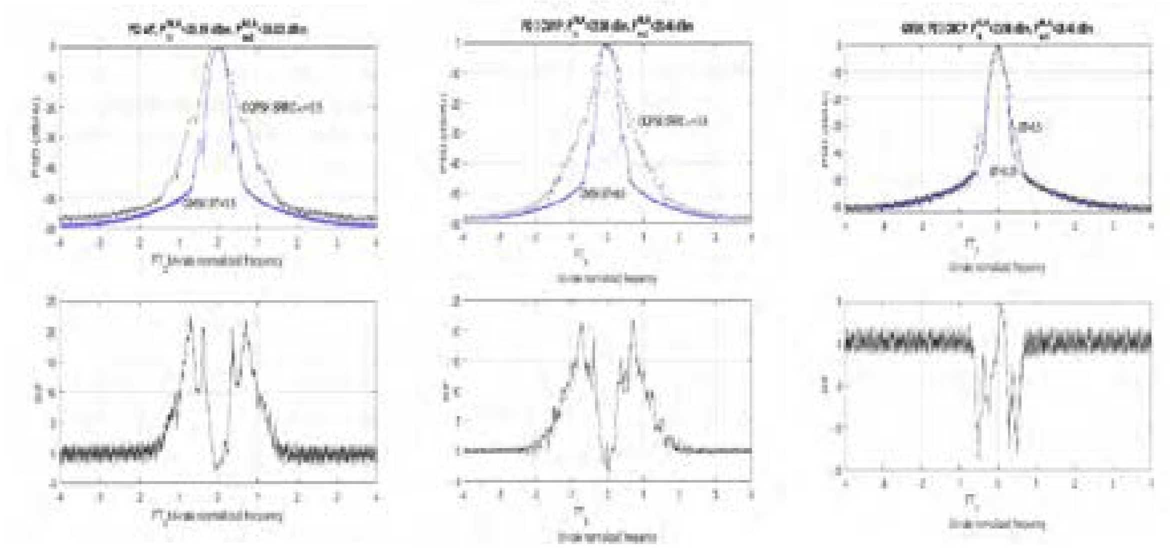

Figure 11. The SIF between GMSK($B \cdot T_b = 0.5$) and OQPSK-SRRC($\alpha = 0.5$), due to NLA and PD type: (left) PD off, PA @ 0 dB OBO; (middle) CMVP-PD, PA @ lin. reg.; (right) CMCP-PD, PA @ lin. reg.

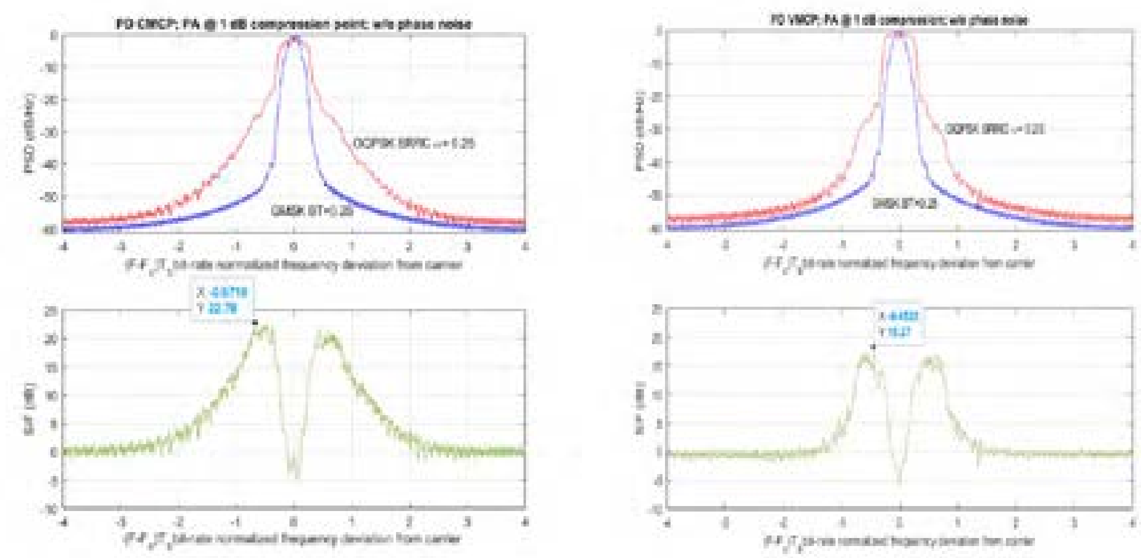

Figure 12. The SIF between predistorted GMSK($B \cdot T_b = 0.25$) and OQPSK-SRRC($\alpha = 0.25$) spectra without phase noise: (left) CMCP-PD Eq. (9); (right) VMCP-PD Eq. (10).

Note that the SIF of GMSK over OQPSK is reduced in the presence of higher levels of phase noise. In Fig. 13, it is shown that for $snr_{phs\_ns} = 44.04\,dB$, the $\max_{\Delta F=5.8\,MHz} SIF = 18.1\,dB$, while for $snr_{phs\_ns} = 24.04\,dB$, the $\max_{\Delta F=-2.6\,MHz} SIF = 14.1\,dB$. OQPSK showed some spectral improvement at higher levels of phase noise, while GMSK remained the same. OQPSK could be the recommended modulation method for more noisy transmitter technologies, while GMSK would be the better choice with the state-of-the-art low-noise transmitters.

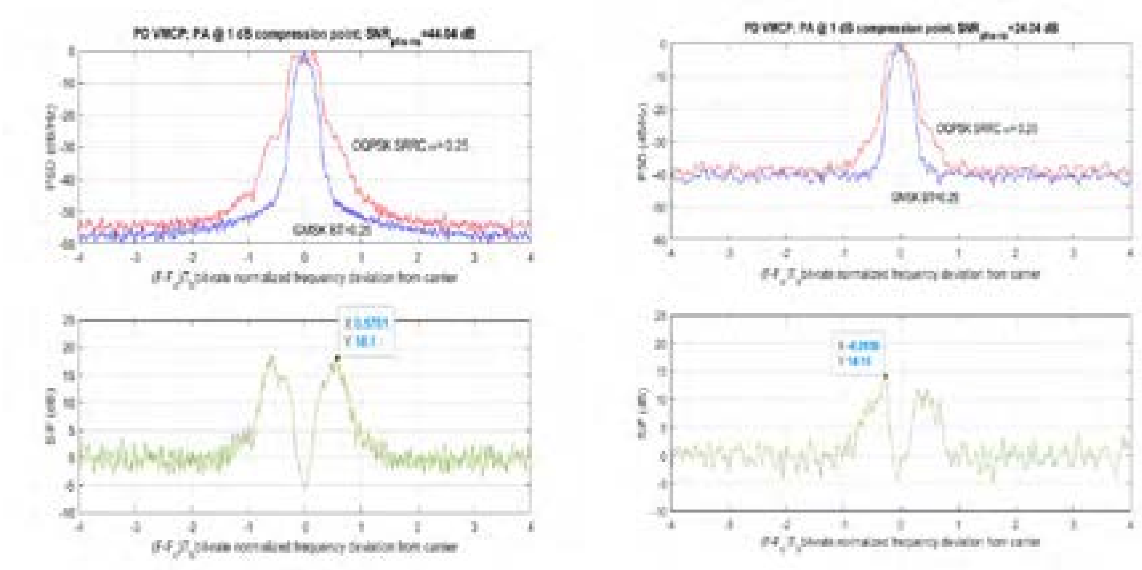

Figure 13. The SIF between predistorted GMSK($B \cdot T_b = 0.25$) and OQPSK-SRRC($\alpha = 0.25$), with phase noise.

B. Power Containment

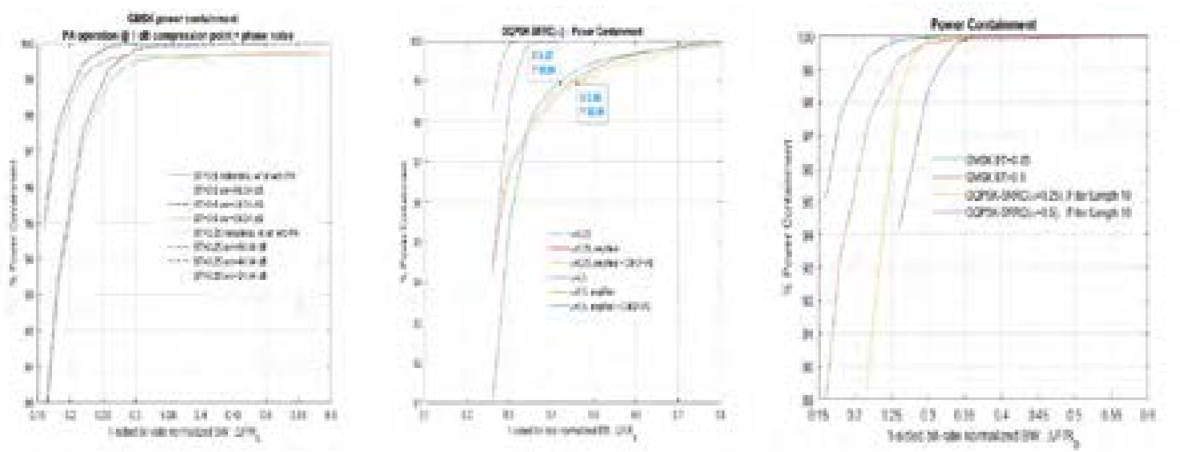

Figure 14. Power containment with PA at 1 dB compression point: (left) GMSK; (middle) OQPSK-SRRC; (right) GMSK v. OQPSK-SRRC w/o amplification.

Note that even though the amplifier does not have significant effect on the GMSK's power containment, it does have a stronger impact on the OQPSK's one. More specifically, the 1-sided bit-rate normalized 99% occupied bandwidth OBW_{99} changes from 3.145 MHz up to 4.2 MHz for rolloff factor $\alpha = 0.5$, and from 2.72 MHz up to 4.5 MHz for $\alpha = 0.25$. This property of very limited SR due to nonlinear power amplification comprises a critical spectral advantage of the GMSK modulation over the OQPSK. Later, in section VII., we provide calculations for "closing down" the OBW_{99} for the sake of obtaining better interference immunity.

C. Phase Noise Spectral Characteristics

In Fig. 15, we are showing the phase noise effects on the transmitted signals via their eye diagrams and constellations, under certain phase noise levels. An upsampling rate of 8 samples/symbol was used for the simulations.

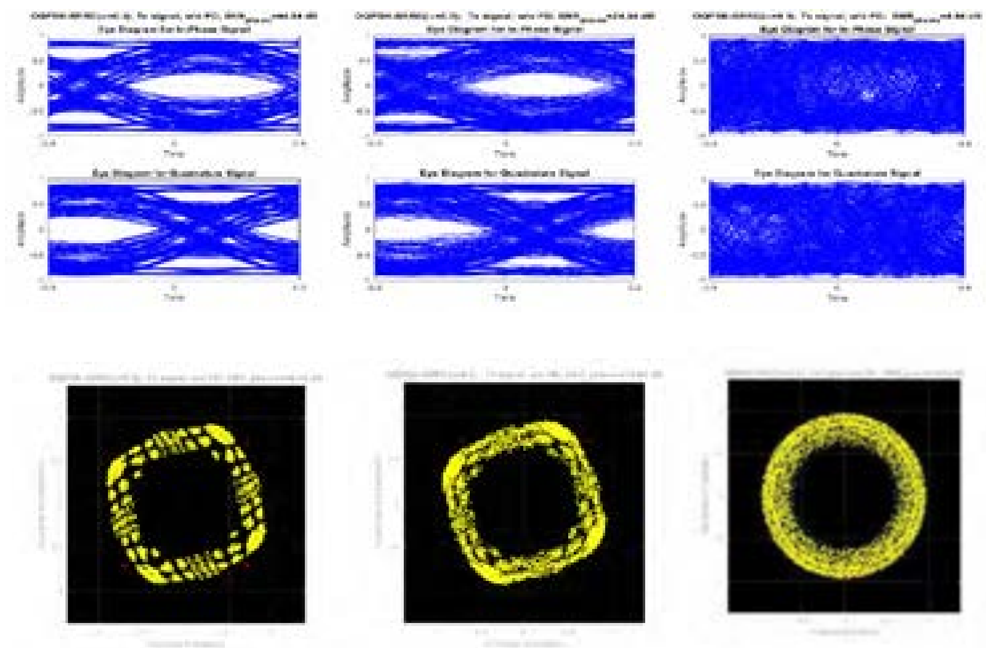

Figure 15. OQPSK-SRRC$(\alpha = 0.5)$ tx-signal $SNR_{phs-ns}(dB)$: (left) 44.04; (middle) 24.04; (right) 4.04.

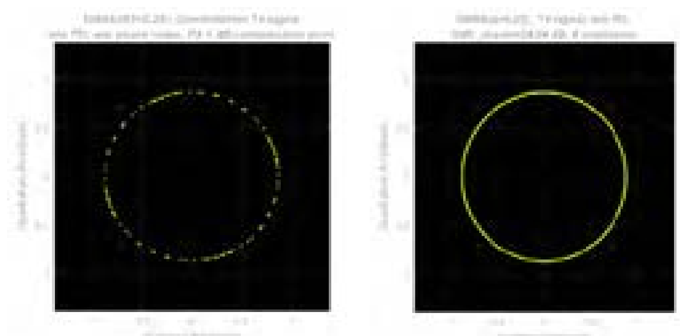

Figure 16. The GMSK$(B \cdot T_b = 0.25)$ tx-signal, $SNR_{phs-ns}\ (dB)$: (left) ∞, (right) 24.04.

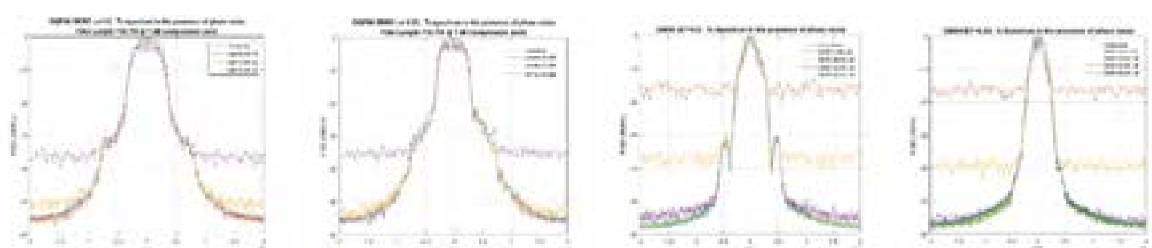

Figure 17. The GMSK and OQPSK-SRRC transmit spectra with and without phase noise and PA operated at the 1 dB compression point.

From Fig. 17, we can infer that GMSK with time-bandwidth product $B \cdot T_b = 0.25$ shows the largest suppression of the sidelobes at approximately -40 dB attenuation for $SNR_{phs-ns} = 24.04\ dB$.

D. Instantaneous Excess Power – PAPR Distributions of PA Input/Output & MF Output Waveforms

For best power efficiency we would like to operate the PA at 0 dB OBO. However, in order to reduce the amount of nonlinearities, we chose to operate closer to the PA's linear region and study the distribution of its input/output instantaneous power P_t^x, at the 1 dB compression point. Fig. 18 (middle), shows the probability of occurrence p distribution that the instantaneous power P_t^x will exceed the average power P_{avg}^x by an excess amount of power equal to ΔP_t^x, for both the PA's input and output. The distribution of the probability of occurrence p, depends on the rolloff factor α, as well as on the PA operating point P_{avg}^x. In our discussion the PA operating point was chosen to be the 1 dB compression point and is notated as P_{1dB}^x.

$$P_t^x(\alpha, P_{1dB}^x) \ = P_{avg}^x(\alpha, P_{1dB}^x) + \Delta P_t^x(\alpha, P_{1dB}^x) \tag{14}$$

$$\text{for} \max P_t^x \rightarrow PAPR_x(\alpha, P_{1dB}^x) = \arg\min_{\Delta P_t^x} p(\alpha, P_{1dB}^x, \Delta P_t^x(\alpha)) = \max \Delta P_t^x(\alpha, P_{1dB}^x) \tag{15}$$

where $x = \text{input, or output}$.

By decreasing α from 0.5 down to 0.25, the PAPR(α) increased from 3.02 up to 4.14 respectively. That was true when the PD was off, as well as when the VMCP-PD from Eq. (10) was on. Note that independent of the value of α, the amplifier's output waveforms produced the average power at $P_{1dB}^{outp} = 1.33\ dB\ OBO$, more frequently than their corresponding input waveforms at $P_{1dB}^{inp} = 5.4\ dB\ IBO$. An estimate of the frequency of occurrence of the 1 dB compression point is provided below by Eq. (16):

$$p\big(\alpha, P_{1dB}^x, \Delta P_t^{inp} = 0\big) = 45\% \ \ < \ \ p\big(\alpha, P_{1dB}^x, \Delta P_t^{outp} = 0\big) = 52\% \tag{16}$$

For GMSK with PD on or off, as well as for all the OQPSK with CMCP-PD on, the PAPR is equal to 0, i.e., the peak power $\max P_t^x$, is always equal to the average one P_{avg}^x:

$$p_{GMSK}\big(\Delta P_t^{inp} = 0\big) = p_{GMSK}\big(\Delta P_t^{outp} = 0\big) = 100\%, \quad \forall\, t,\ \forall\, P_{avg}^x,\ \forall\, B \cdot T_b \tag{17}$$

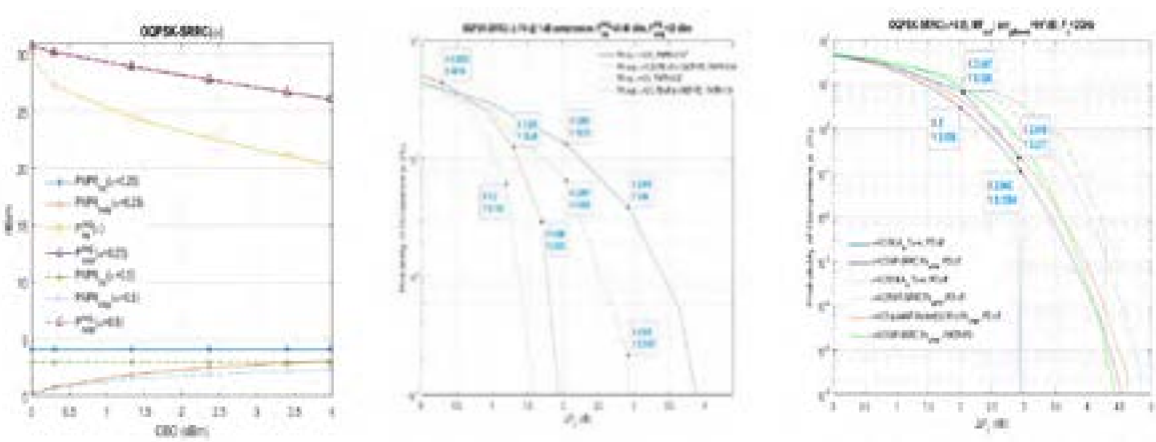

Figure 18. OQPSK-SRRC($\boldsymbol{\alpha}$), $\boldsymbol{\alpha = 0.25, 0.5}$, PA input/output: (left) PAPR as a function of OBO; (middle) $\boldsymbol{p(\Delta P_t^x[0{:}\,PAPR])}$ @ 1 dB compression point; (right) $\boldsymbol{p(\Delta P_t^x[0{:}\,PAPR])}$: Tx PA input, Rx MF output.

The unique signature structure of the probability distribution of the excess power $p(\Delta P_t^x[0{:}\,PAPR])$ for PA input/output and MF output, can be used in more than one way:

1) To monitor the presence of distortions at the transmitter, when the expected $p(\Delta P_t^x[0{:}\,PAPR])$ signature structure is distorted. Early detection of various type of distortions at the transmitter and not depending on their more latent discovery at the receiver's end while wasting large amounts of useful data, enables the system for efficient compensation and recovery. At the transmitter, by producing statistics of the PA input instantaneous power estimates, we can detect the presence of distortion(s) via the observation of significant deviation from some of the key statistics listed in Table 3.

2) There is dual use at the receiver: a) to detect the presence of interference, and b) to perform modulation identification.

In RF communications there is presence of narrowband and/or wideband interference,[10] due to the out-of-band emissions, from the adjacent to the main channels with insufficient frequency-separation. Its early detection is critical to the successful and efficient operation of telemetry data communications. Interference detection could be based on measurements of the stronger deviations from the expected $p(\Delta P_t^x[0{:}\,PAPR])$ signature structure, i.e., violations of certain key points $p(\alpha, \Delta P_t^x)$, on the curves in Fig. 18 and listed in Table 3. On the other hand, for GMSK the peak power does not exceed the average, expressed by Eq. (17). Proper thresholds need to be designed to allow for some tolerance around the expected key points values. This method is particularly useful when the interference is in general "weak" and undetectable via plain power level measurements, but sufficiently strong, and spectrally "colored" to affect the $p(\Delta P_t^x)$ signature structure shape in a detectable way. From Eq. (15) and Fig. 18, we know that the "excess power" distribution $p\left(\alpha, P_{avg}^x, \Delta P_t^x[0{:}\,PAPR]\right)$, depends on P_{avg}^x, which implies that even the "white" interference is detectable.

Second, in order to simplify the receiver hardware, it is preferred to use one flexible cross supporting receiver, capable of accommodating multiple modulation schemes. Having an automated mechanism for identifying an unknown modulation among a set of known modulations of the received waveform is critical for this type of communications, rendering possible a modulation-agnostic receiver. At the receiver, instantaneous power levels of the MF output exceeding P_{avg} by ΔP_t^{MF} =1:3 dB (see Table 3), comprise the best points for modulation identification, between $\alpha = 0.5$ and $\alpha = 0.25$. For example, at the MF output, the OQPSK-SRRC($\alpha = 0.5$) modulated waveforms exceed the average power P_{avg} by approximately 1 dB at an approximate rate of 19%, and by 2 dB at 2.9%. On the other hand the OQPSK-SRRC($\alpha = 0.25$) modulated waveforms exceed the average power P_{avg} by approximately 1 dB at an approximate rate of 29%, and by 2 dB at 11%. These data points can be among the modulation identifiers either at the Tx or the Rx end (Table 3). A critical parameter for this algorithm is the minimum observation time necessary to extract sufficiently reliable power statistics.

Table 3: Key Points $p(\alpha, P_{1dB}^x, \Delta P_t^x)$ for Interference Detection and Modulation Identification

	Tx-er: x = PA input			*Tx-er: x = PA output*			*Rx-er: x = MF output*	
	Probability of occurrence $p(\alpha, P_{1dB}^x, \Delta P_t^x)$ and $p_{GMSK}(P_{1dB}^x, \Delta P_t^x)$ (%)							
ΔP_t^x (*dB*)	$\alpha = 0.5$	$\alpha = 0.25$	**GMSK** $B \cdot T_b = 0.25$	$\alpha = 0.5$	$\alpha = 0.25$	**GMSK** $B \cdot T_b = 0.25$	$\alpha = 0.5$	$\alpha = 0.25$
0	45	45	100	52	52	100	49	46
1	24.5	29	-	11.5	21	-	19	29
2	7	14	-	-	0.044	-	2.9	11
3	$< 10^{-12}$	3.1	-	-	-	-	0.08	1.5
PAPR $p(\alpha, PAPR$	3.02 $p < 10^{-12}$	4.147 p =0.02	0 p =100	1.54 p =0.2	1.94 p =0.1	0 p =100	4.5 $p \cong 10^{-6}$	4.8 $p \cong 2 \cdot 10^{-6}$

V. End-to-End System Performance Simulation Results

Meeting the BER specification at a certain possible $E_b N_o$ level, is the system's ultimate overall performance metric. The transmitter design objective is to use the minimum possible power to obtain the minimum required $E_b N_o$ at the receiver. It might be required to operate the nonlinear PA at the 0 dB OBO for best power efficiency, or it might be preferred and sufficient to operate it at the 1 dB compression point and reduce the amount of induced nonlinearities by the PA, as shown in the signal constellations in Figs. 19-21. It was also shown in Fig. 8, that when the PA is not operated in its linear region, the increased nonlinearities result in spectral broadening. The end-to-end system performance suffers from some filtering losses due to the residual uncompensated ISI introduced by the PA nonlinearities and not counted for by the perfectly chosen MF. However, operating the PA more efficiently compensates for these losses. The eye diagrams in Fig. 20, demonstrate the effective suppression of the ISI from the amplified transmitted waveform, by the VMCP-PD (see Eq. (10)) and VMVP-PD (see Eq. (4)) preamplification counteractions.

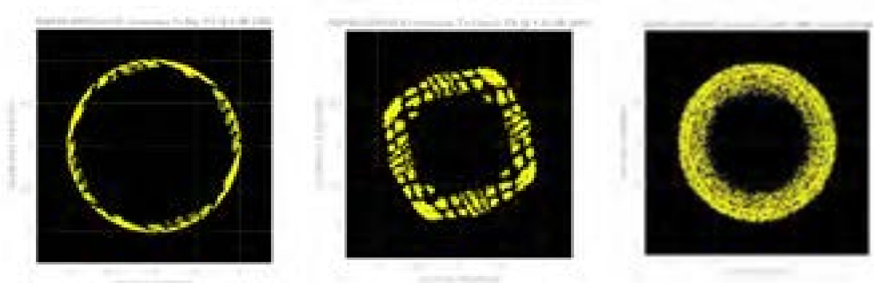

Figure 19. OQPSK-SRRC(α =0.5) tx amplified signal, PD off: (left) noiseless but with higher ISI; (middle) noiseless but with lower ISI; (right) with phase noise $snr_{phs\_ns} = 4.04\ dB$.

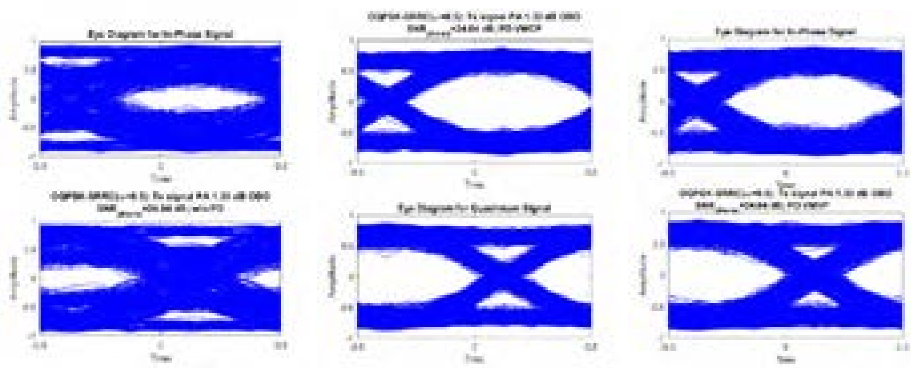

Figure 20. I & Q eye diagrams for the OQPSK-SRRC(α =0.5) tx amplified signal, PA operating @ 1 dB compression point and $snr_{phs\_ns} = 24.04\ dB$: (left) PD off; (middle) VMCP-PD on; (right) VMVP-PD on.

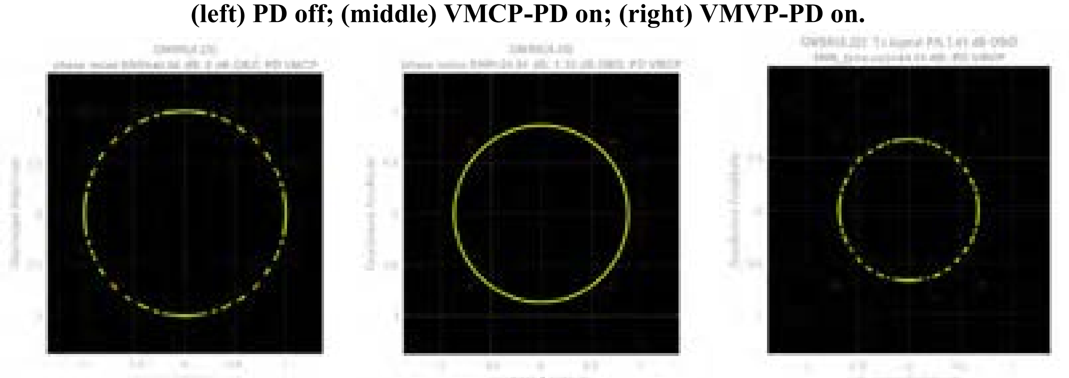

Figure 21. GMSK(BT =0.25) tx amplified signal: PD on, and PA operating @: (left) 0 dB OBO, VMCP-PD, $snr_{phs\_ns} = 44.04\ dB$; (middle) 1 dB compression point, VMCP-PD, $snr_{phs\_ns} = 24.04\ dB$; (right) linear region: 3.41 dB OBO, VMVP-PD, $snr_{phs\_ns} = 44.04\ dB$.

A. Transmitter Initial Calibration with Optional Local Test Receiver

Avoiding the nonlinear operating region for the PA, minimizes the SR effects and consequently the out-of-band emissions. Ideally, by setting the backoff point equal to the PAPR from Eq. (18), it will bring the system's operation entirely in the linear region. By inspection of Table 3 and Fig. 18, and according to Eq. (15), it is evident that in all cases we obtain $PAPR$ for the $min\, p(\alpha) \ll$. However, we would like to trade linearity for efficiency, and reduce that backoff point, in order to approach closer to the PA's highest possible power efficiency, without introducing too many nonlinearities.

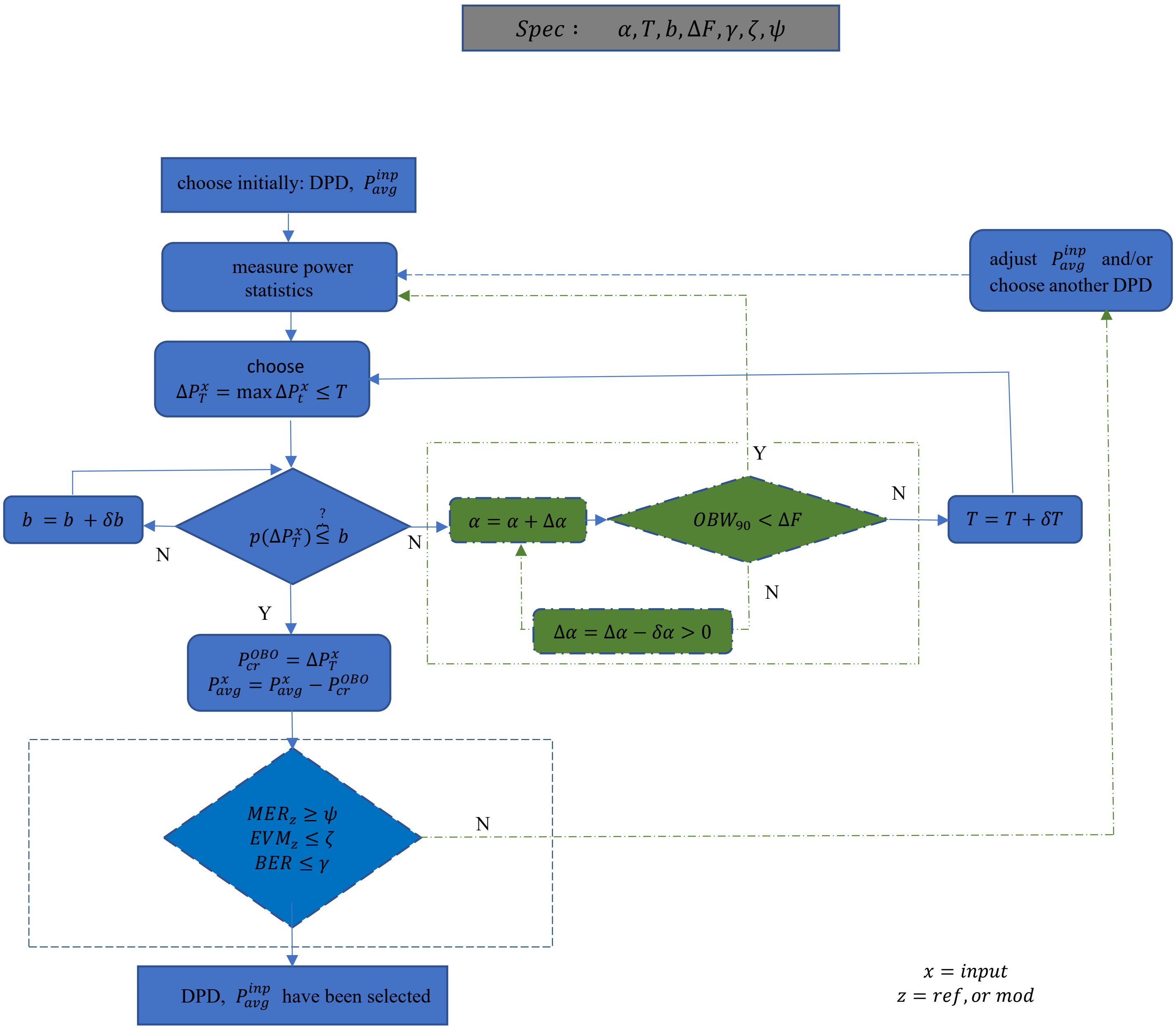

Figure 22. Transmitter initial calibration algorithm flow chart.

$$P^{OBO}_{ideal}(\alpha, P^x_{1dB}) = PAPR_x(\alpha, P^x_{1dB}) = arg_3\left\{\min_{\Delta P^x_t} p(\alpha, P^x_{1dB}, \Delta P^x_t) \ll\right\} = \max \Delta P^x_t(\alpha, P^x_{1dB}) \quad (18)$$

Our design philosophy is that since the $PAPR$ typically occurs with a very small probability $p \ll$, instead of backing off by $PAPR$, it might be more efficient to backoff by the excess amount of power with the second highest probability of occurrence given by Eq. (19), which we call it the effective OBO point, $P^{OBO}_{eff}(\alpha)$. In the case that this choice allows larger than desired amount of nonlinearities, then we consider the third highest, and so forth. For the sake of notation simplicity, in the following discussion we are going to drop the PA's independent parameter P^x_{avg}, its power operating point, and always imply operating at the 1 dB compression point, P^x_{1dB}. In our design, we pursue characterization of the NL power amplifier at P_{1dB}^{x}, and at the same time to bound from above the OBO point by a predetermined finite upper bound *T*. Let us notate the critical needed OBO power as P_{cr}^{OBO}, defined in Eq. (20). The smaller the P_{cr}^{OBO} the higher the power efficiency with lower nonlinearities.

$$P_{eff}^{OBO}(\alpha) = \left\{ arg \max_{\Delta P_t^x > 0} p(\alpha, \Delta P_t^x) \right\} < P_{ideal}^{OBO}(\alpha) \tag{19}$$

There are two design parameters in Eq. (20), the two interdependent upper bounds T, and b, for the excess power $\Delta P_t^x \leq T$, and its probability of occurrence $p(\Delta P_t^x) \leq b$, respectively. First, we need to decide on the value of the upper bound T which describes the system's primary tolerance to nonlinearities. The lower the value of *T*, the higher the system's tolerance and vice versa. Second, we also need to decide on the value of the upper bound b for the accepted probability of occurrence $p(\Delta P_t^x \leq T)$, which describes the system's secondary tolerance to nonlinearities. If the corresponding value of $p(\alpha$,T) cannot be obtained from Fig. 18 or Table 3, i.e., $p(\alpha, T) > b$, then redesign by adjusting the spec parameters as shown in the initial calibration algorithm shown in Fig. 22. Note that the probability of occurrence $p(\alpha, T)$, is inversely proportional to T, i.e., when T decreases (increases) then $p(\alpha, T)$ increases (decreases). Once T, and $p(\alpha,T)$ are found, then P_{cr}^{OBO} can also be determined according to Eq. (20), below:

$$P_{cr}^{OBO}(\alpha, b, T) = \arg_2 \left\{ p(\alpha, \Delta P_t^x(\alpha), T) \underset{\Delta P_{cr}^x = \Delta P_t^x}{\underset{\{\}}{\leq}} b \right\} \leq T \tag{20}$$

From the AM/PM conversion function given by Eq. (1), we can identify the rotation angle of the NLA output and design the DPD producing an output pre-counter-rotated by the same angle but in the opposite direction. We apply "excess power" $\Delta P_t^x(\alpha, P_{1dB}^x)$ analysis (Fig. 18, Table 3, Fig. 22), to identify the critical OBO power $\Delta P_{cr}^x(\alpha, b, T)$ from Eq. (20), and notated the corresponding instantaneous power $P_{cr}^x(\alpha, b, T)$:

$$P_{cr}^x(\alpha, b, T) = P_{avg}^x + \Delta P_{cr}^x(\alpha, b, T) \xrightarrow{Eq.(1)} \Phi_{cr}(\alpha, b, T) \tag{21}$$

Using Eqs. (1), (21), we can calculate the rotation angle $\Phi_{cr}(\alpha, b, T)$ by which the NLA output is rotated when $P_{cr}^x(\alpha, b, T)$ is applied to the NLA input. Then PD-VMCP, from Eq. (10), can be used to pre-counter-rotate the NLA input by $-\Phi_{cr}(\alpha, b, T)$. Alternately, VMVP from Eq. (4), can be used to apply exact pre-counter-rotation for any instantaneous input power to the NLA. Finally, at the receiver side BER and EVM comparisons are conducted in order to evaluate the loss/gain of the former method when compared to the latter.

The block diagram for the initial calibration of the system, in terms of required average power and best DPD option, is given in Fig. 22. The "green subblocks" subsystem which refers to changing the modulation's rolloff factor, is optional, and it can be bypassed, if the modulation parameter(s) cannot change for some reason, or if a spectrum analysis cannot be performed. The system block diagram is partitioned in two subsystems: the upper one (solid lines) can be implemented at the transmitter alone without a supporting local receiver, while the complete system including both subsystems (solid and dashed lines) can be implemented at the transmitter with the support of a local test receiver. The local test receiver can optionally check whether any or all of the following metrics meet spec: MER_z, EVM_z, BER (see subsections *V.B, V.C*).

B. Detection Efficiency for OQPSK

The metrics used to evaluate system performance are the EVM, MER and ultimately the BER. We list below the definitions of those metric**s**[7] as they have been used in our simulations. Let us define the error signals $\boldsymbol{e_{I,n}}$ and $\boldsymbol{e_{Q,n}}$ as the difference between the received symbols $\boldsymbol{I_n}, \boldsymbol{Q_n}$ and a reference signal $\boldsymbol{I_{ref,n}}, \boldsymbol{Q_{ref,n}}$:

$$e_{X,n} = X_n - X_{ref,n-D}, \quad \text{where } X = I, Q, \text{ and } D \text{ is the relative alignment delay} \tag{22}$$

$$EVM(I_{ref,M}, Q_{ref,M}) \quad = \left[\frac{M^{-1}\sum_{m=1}^{M}\left(e_{I,m}^2+e_{Q,m}^2\right)}{M^{-1}\sum_{m=1}^{M}\left(I_{ref,m}^2+Q_{ref,m}^2\right)}\right]^{1/2} \tag{23}$$

$$MER(I_{ref,M}, Q_{ref,M}) = \frac{\sum_{m=1}^{M}\left(I_{ref,m}^2+Q_{ref,m}^2\right)}{\sum_{m=1}^{M}\left(e_{I,m}^2+e_{Q,m}^2\right)} \tag{24}$$

In Eqs. (22)-(24) we can substitute $I_{ref,n}$ and $Q_{ref,n}$ with the ideal values $\hat{I}_n$, and $\hat{Q}_n$ from the corresponding reference constellation to produce : $EVM_{ref}(\hat{I}_M, \hat{Q}_M)$, and $MER_{ref}(\hat{I}_M, \hat{Q}_M)$. In Eqs. (22)-(24) we can substitute the $I_{ref,n}$ and $Q_{ref,n}$ with the $I_M^{y^{(mod)}}$, $Q_M^{y^{(mod)}}$ from the modulated data $y^{(mod)}$, and the I_n, Q_n with the $I_{n+D}^{MF_{out}}$, $Q_{n+D}^{MF_{out}}$ from the MF output to produce : $EVM_{mod}(\hat{I}_M, \hat{Q}_M)$, and $MER_{mod}(\hat{I}_M, \hat{Q}_M)$. In order to produce an estimate of the channel's SNR_{est}, substitute in Eq. (24) the $I_{ref,M}$ and $Q_{ref,M}$ with the transmitted waveform's orthogonal substreams $I_M^{y^{(tx)}}$, $Q_M^{y^{(tx)}}$:

$$SNR_{est} = MER(I_M^{y^{(tx)}}, Q_M^{y^{(tx)}}) \tag{25}$$

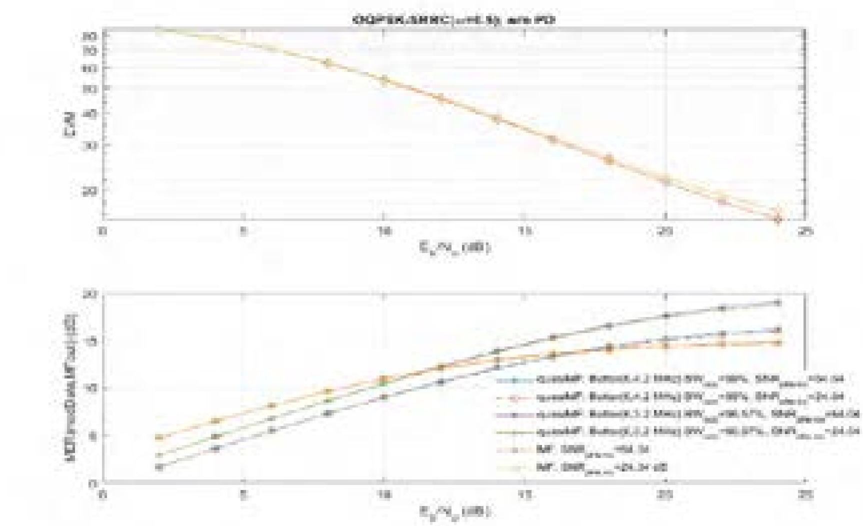

Figure 23. OQPSK-SRRC($\alpha = 0.5$) performance comparisons before the detector: (top) EVM; (bottom) MER.

Among other, some of the RF impairments included are free space path loss, thermal noise from the receiver's front end and phase noise (transmitter components such as oscillators, amplifier, and solar noise). Below we show our calculation of the $\frac{E_b}{N_o}$ in dB for uncoded data:

$$SNR_{dB} = 10 \cdot \log_{10}\left(\frac{1}{\sigma_{ns}^2}\right) = \frac{E_s}{N_o} = \frac{E_b}{N_o} + 10 \cdot \log_{10}(\log_2 M) - 10 \cdot \log_{10}\left(\frac{samples}{symbol}\right) \tag{26}$$

where $M = 4$ for OQPSK, MSK, GMSK.

C. Detection Efficiency for GMSK

GMSK with time-bandwidth product $BT_b = 0.25$ shows an E_bN_o advantage of approximately 3 dB over the OQPSK-SRRC($\alpha = 0.5$), with or without phase noise (see Fig. 24). Increasing the phase noise in GMSK did not hurt the performance for the following two cases: the CMCP-PD from Eq. (9), and the VMCP-PD from Eq. (10), but it did have an impact on the performance of the system when PD was turned off. Therefore, PD proves to be more effective for GMSK in the presence of higher levels of phase noise. Also, the OQPSK VMCP-PD case held its performance better than the CMCP-PD case, in the presence of higher levels of phase noise. Note that with "PD off" an ideal post-correction occurring at the receiver counteracts the data rotation by the transmitter's NLA. That yields an ideal BER performance which otherwise would have some losses in its real implementation.

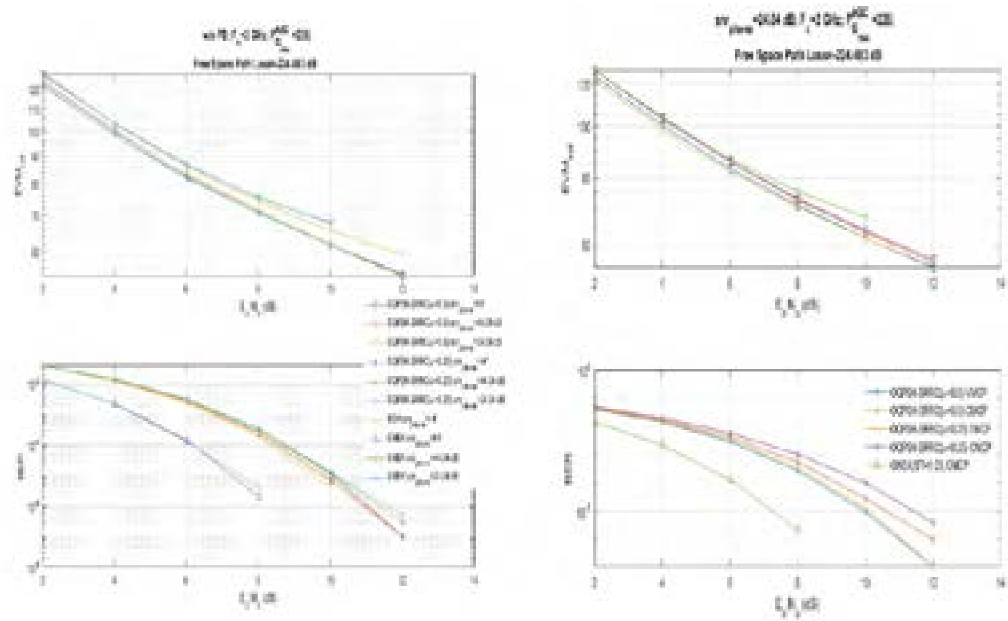

Figure 24. BER performance comparison: (left) GMSK v. MSK v. OQPSK-SRRC without PD; (right) GMSK v. OQPSK-SRRC with CMCP-PD, VMCP-PD.

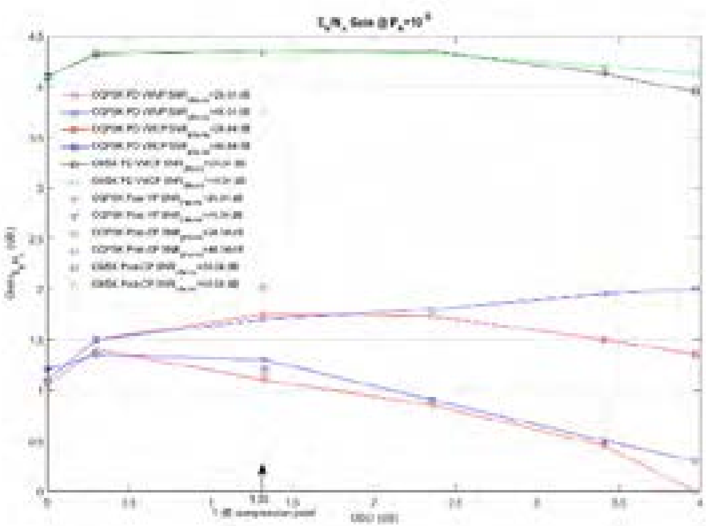

Figure 25. E_b/N_o gain as a function of the PA OBO operating point for OQPSK-SRRC(α =0.5) and GMSK(BT=0.25) with and without PD.

In Fig. 25, it is shown that for OQPSK VMCP-PD, when PA operates at the 1 dB compression point, corresponding to 1.33 dB OBO, there is approximately a 0.7 dB $E_b N_o$ gain over the 0 dB OBO PA operating point. This result corroborates with the constellations shown in Fig. 19, whereby the 0 dB OBO case shows clearly higher levels of ISI than the 1 dB compression one. In Fig. 20, there are three PD cases whereby the PA is operated at the characteristic 1 dB compression point with higher levels of phase noise producing $snr_{phs\_ns} = 24.04\ dB$. It is shown that the transmit amplified signal is subject to more severe degradation when PD is off as compared to when VMVP-and/or VMCP-PD cases are being used instead. On the other hand, VMCP-PD shows lower jitter levels than the VMVP-PD case. In Fig. 25, we can clearly see that as the OBO point decreases the $E_b N_o$ gain of the lower phase noise cases is shrinking as the nonlinearities start dominating the performance and therefore diminishing the phase noise effect.

D. OQPSK Performance Robustness on PA Parameters Variability, and Rotation Angle Correction Offset

In Fig. 26 (left), it is shown how robust is the BER and EVM performance in terms of varying PA parameters such as the β_a, β_φ from Eq. (1). It can be clearly seen that the robustness increases as the PA operating point moves towards the lower range of the linear region which is in agreement with the approximation given in Eq. (1a), whereby the dependence on the β_a, β_φ has been completely eliminated. Also according to Eq. (1c), for the higher operating points for the PA, i.e., in the saturation region, we expect not to have a significant impact on the performance, when the ratios $\frac{\alpha_\alpha}{\beta_\alpha}$, and $\frac{\alpha_\varphi}{\beta_\varphi}$ remain constant.

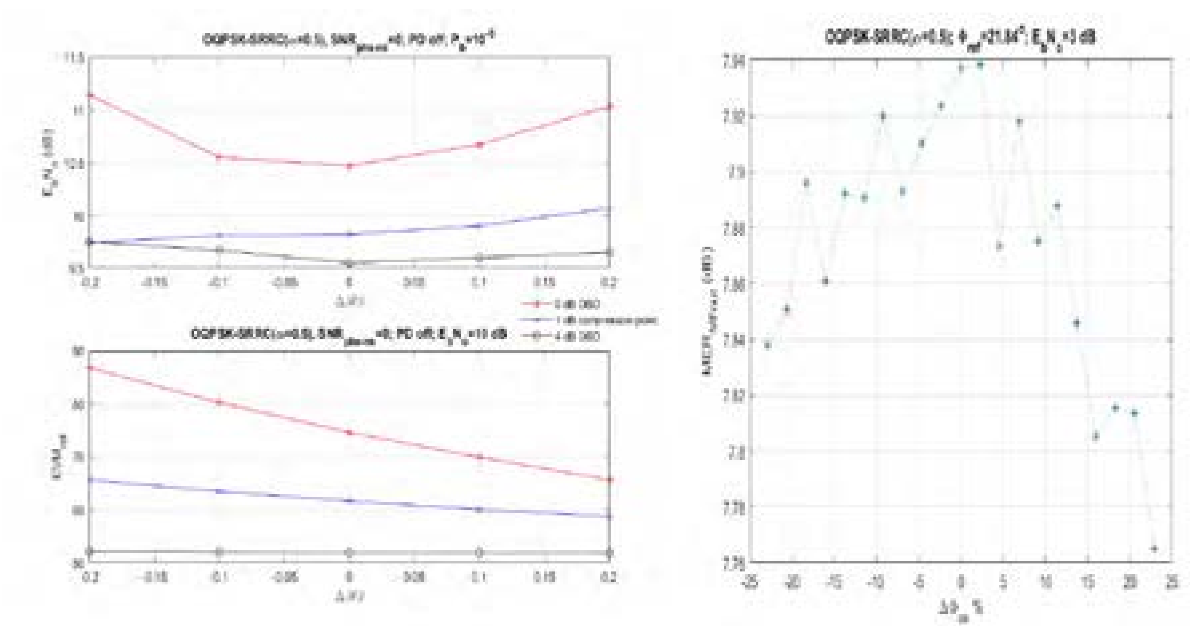

Figure 26. OQPSK-SRRC(α =0.5) performance robustness on variability of: (left) PA parameters β_a, β_φ: (top) BER; (bottom) EVM$_{\mathrm{ref}}$; (right) phase rotation correction offset.

Fig. 26 (right), shows evaluation, using an MER type of metric at the MF output, of the performance sensitivity on the presence of a phase offset $\Delta\Phi_{os}$ during predistortion correction of the rotation angle by the power amplifier, i.e., let us assume that the current rotation on the data caused by the PA due to an input voltage V is equal to $\Phi^{(NLA)}(V)$, but the pre-couter-rotation by the PD was equal to the angle corresponding to the same voltage with a small deviation of its value $V + \Delta V$:

$$\Phi^{(PD)}(V) = -\Phi^{(NLA)}(V) \pm \Delta\Phi_{os} \overset{\Delta V \ll V}{\triangleq} -\Phi^{(NLA)}(V + \Delta V) \quad (27)$$

VI. An EVM / BER - based New Low-Resolution Ranging Algorithm

In Fig. 23, the algorithm is using modulated data-based EVM_{mod} calculations which are not implementable in practice, since they are not available to the receiver in general. Fig. 28, shows a second version of the same algorithm using the EVM_{ref} which is based on the reference constellation which is realistic and implementable in practice. Careful calibration of the AGC parameters such as the AGC maximum power gain $P_{G_{max}}^{AGC}$, is critical. The BER performance remains more or less the same up to an $E_b N_o$ of $10\ dB$. It is the combination of the identical BER performance with the proportional to the distance *D, EVM* performance deviation, and the proper AGC settings, which form the basis for this novel ranging method. Furthermore, the algorithm can be reinforced when combined with applying PAPR measurements of the MF output (Fig. 29). Note that this ranging algorithm remains active continuously and simultaneously with telemetry on too.

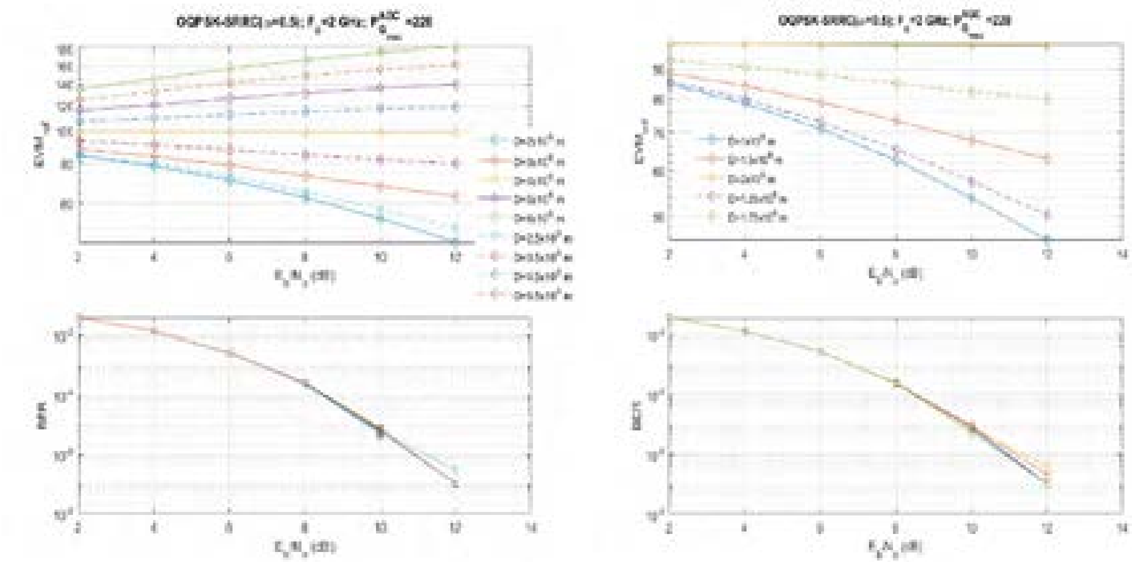

Figure 27. EVM and BER for PA operating @ 1 dB compression point for 2 different AGC maximum power gains: (left) $P_{G_{max}}^{AGC}$=226; (right) $P_{G_{max}}^{AGC}$=220.

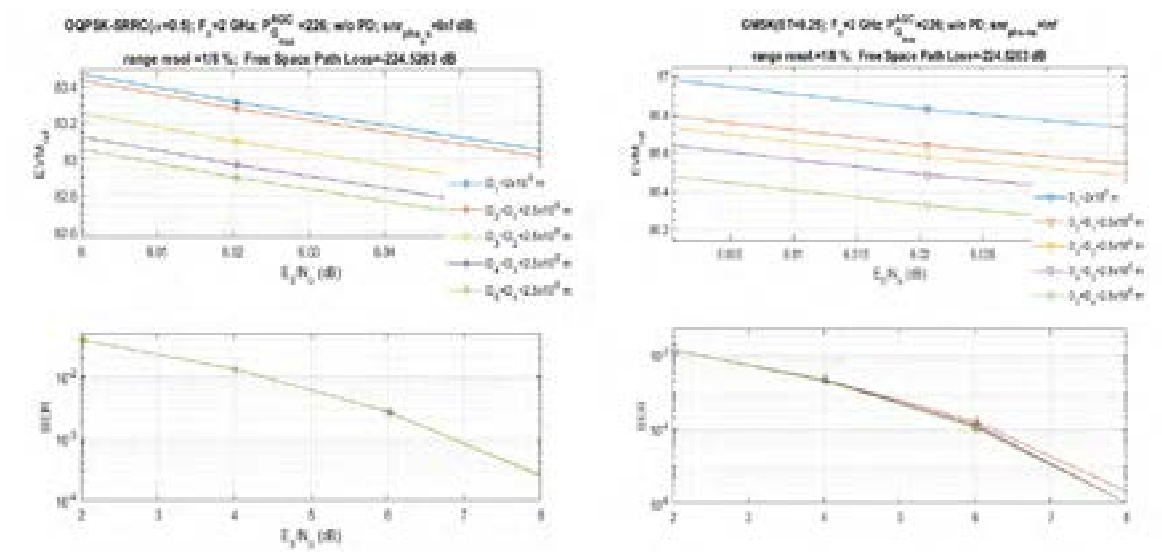

Figure 28. Range resolution estimate for the new implementable real-time receiver ranging algorithm via EVM_{ref} measurement at $\frac{E_b}{N_o} = 6\ dB$.

One advantage of this proposed new algorithm is that there is no need to deactivate the telemetry operation when ranging is activated, in contrast to the current ΔDOR ranging algorithms[11] whereby deactivation is necessary.

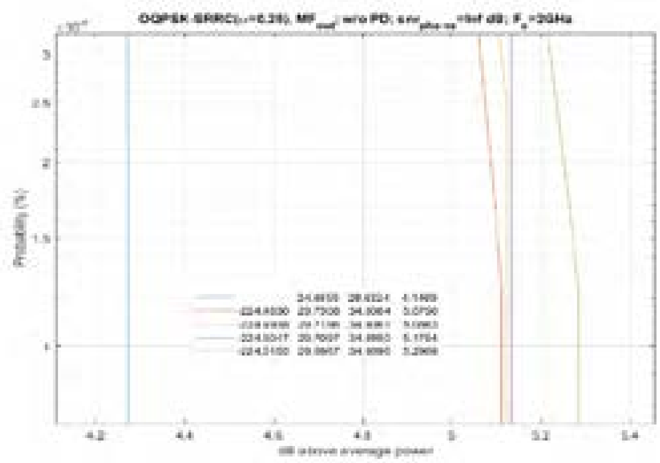

Figure 29. Range resolution estimate for the new implementable real-time receiver ranging algorithm via $PAPR_{MFout}$ measurement at $\frac{E_b}{N_o} = 16\ dB$.

VII. Adjacent Channel Separation/Interference Immunity

In this interference immunity study, boresighted antenna is assumed for the adjacent spacecrafts, such that the ground station receives equal power from the adjacent spacecrafts. Interference immunity assumes[10] no spectral overlap among adjacent channels' spectra above -20 dB. Significant reduction of the interference susceptibility could be obtained[10] by reducing the power containment bandwidth from 99% down to 90%. For amplified OQPSK-SRRC(α) that change would correspond to closing down at the receive front end, the 1-sided BPF bandwidth F_{bw}^{99} (Fig. 14) from $0.45 \cdot R_b$ down to $0.23 \cdot R_b$ respectively for α=0.25, and from $0.42 \cdot R_b$ down to $0.25 \cdot R_b$ for α=0.5. For the amplified and with phase noise GMSK($B \cdot T_b = 0.25$), the corresponding change is (Fig. 14), from $F_{bw}^{99} = 0.22 \cdot R_b$ down to $F_{bw}^{90} = 0.14 \cdot R_b$. In all cases the received signal energy loss is approximately equal to 0.45 dB. Despite the signal energy loss there exists an overall SINR net gain due to the significant suppression of adjacent interference, since any interference existing within the frequency band $[F_{bw}^{90} \quad F_{bw}^{99}]$ will be eliminated.

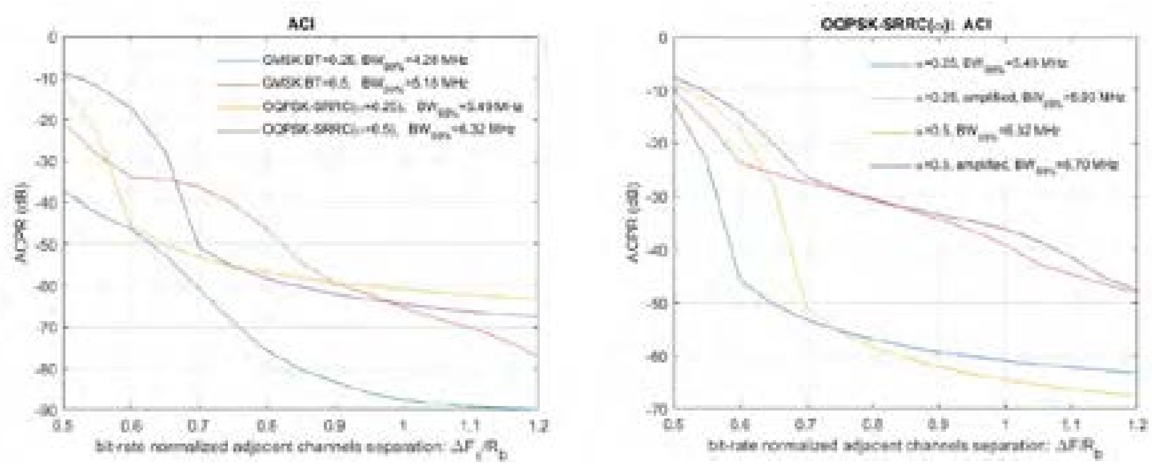

Figure 30. ACPR for: (left) GMSK v. OQPSK-SRRC without tx amplification; (right) noiseless OQPSK-SRRC without and with amplification.

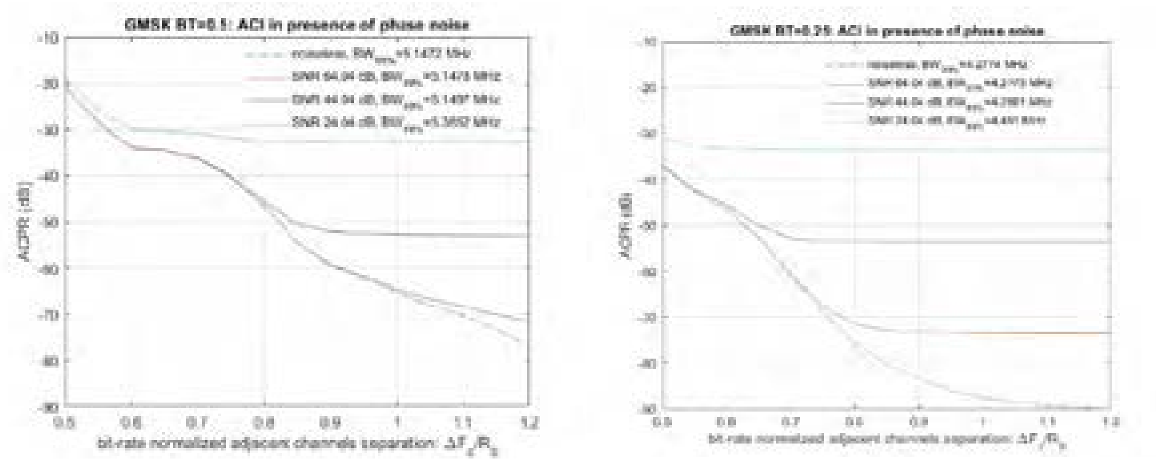

Figure 31. ACPR for amplified GMSK: (left) $B \cdot T_b = 0.5$; (right) $B \cdot T_b = 0.25$.

For GMSK, the noiseless and the highest (64.04 dB) cases reach ACPR=-60 dB at 9 MHz and 7 MHz for $B \cdot T_b = 0.5$ and 0.25 respectively.

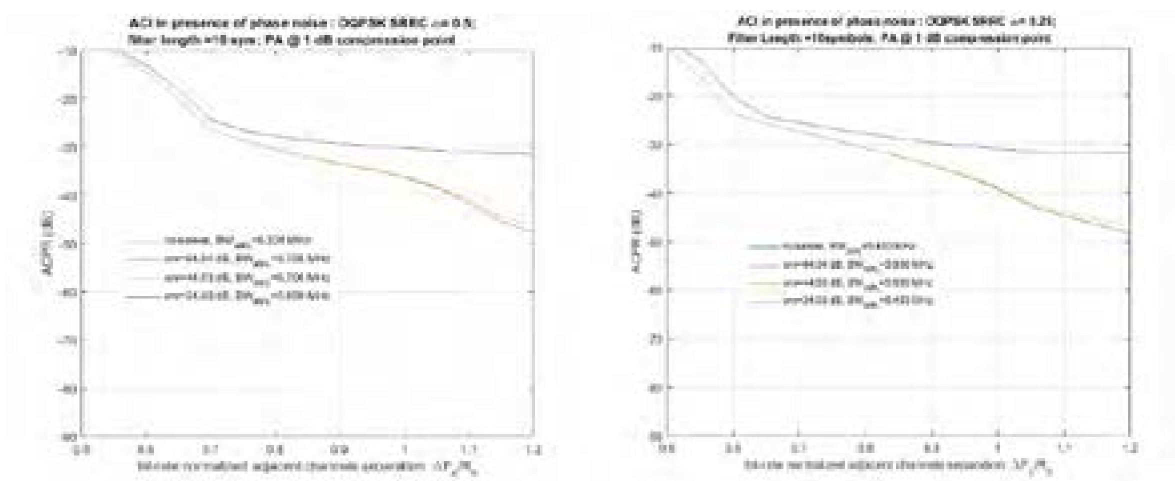

Figure 32. ACPR for amplified $\mathbf{OQPSK - SRRC(\alpha)}$: (left) $\alpha = 0.5$; (right) $\alpha = 0.25$.

VIII. Conclusion

In this work we studied and compared two basic types of modulations and some of their variations: OQPSK and GMSK. More specifically the OQPSK with SRRC baseband pulse shaping for rolloff factors $\alpha = 0.25$ and $\alpha = 0.5$. GMSK showed superior end-to-end system BER performance, and better spectral containment in the presence of a nonlinear amplifier. Even though GMSK was originally designed[12] for mobile communications applications whereby the signal is strong but the available bandwidth very limited, the aforementioned two main properties render GMSK a better modulation choice also for transmitting telemetry data from the spacecraft to the ground stations, whereby the signal is in general weak and the bandwidth relatively limited.

We also introduced predistortion algorithm(s) for OQPSK and GMSK. In the presence of higher levels of phase noise, DPD proved to be more effective for GMSK. For OQPSK with predistortion, the VMCP-PD method outperformed the CMCP-PD. It was also shown that the transmit amplified signal is subject to more severe degradation when PD is off as compared to when VMVP- or VMCP-PD is turned on, with the latter showing lower jitter levels too.

In the future we would like to conduct a similar type of analysis and design for SSPA type of nonlinear power amplifiers, which are also used in category A missions. We would also like to investigate simple feedback mechanisms at the transmitter deploying sensors to better control and render the nonlinear PA to be more efficient.

Appendix

In Fig. A1, we show the SRRC filter frequency and impulse responses for different rolloff factors:

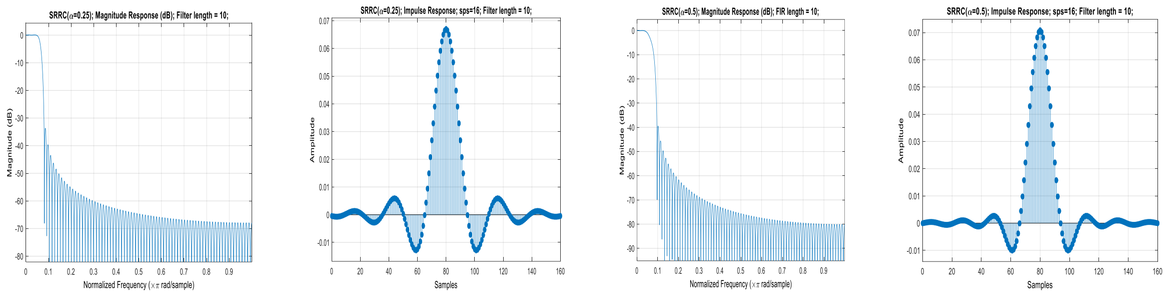

Figure A1. SRRC(α) filter frequency and impulse responses: (left) $\alpha = 0.25$; (right) $\alpha = 0.5$.

From Fig. A2, it is evident that for OPQSK there is a significantly increasing SR effect when the NLA operating point shifts from the linear towards the saturation region. On the other hand, the corresponding effect on GMSK is negligible due to its constant magnitude property. Without applying PD, the maximum SIF of GMSK over OQPSK is shown in Fig. A2 and some key points are listed in Table A1:

Table A1: SR: OQPSK-SRRC($\alpha = 0.25$), v. GMSK($B \cdot T_b = 0.25$)

PA operating point	snr_{phs_ns} (dB)			
	∞		44.04	
	ΔF (MHz)	$\max_{\Delta F} SIF$ (dB)	ΔF (MHz)	$\max_{\Delta F} SIF$ (dB)
Linear region	5.5	15.2	6.4	13.9
1 dB compression point	4.4	17.5	5	17.9
0 dB OBO	5.2	23.4	6.1	24.6

Next, in Fig. A.3 we show same comparisons when VMCP-PD is activated. Note that for GMSK with activated PD at -60 dB attenuation and without any phase noise, there are more than 2 MHz savings. From Fig. A.3, the VMCP-PD produces a finite double sideband bandwidth equal to 6 MHz, while when the PD is off, the corresponding double sideband bandwidth is greater than 8 MHz.

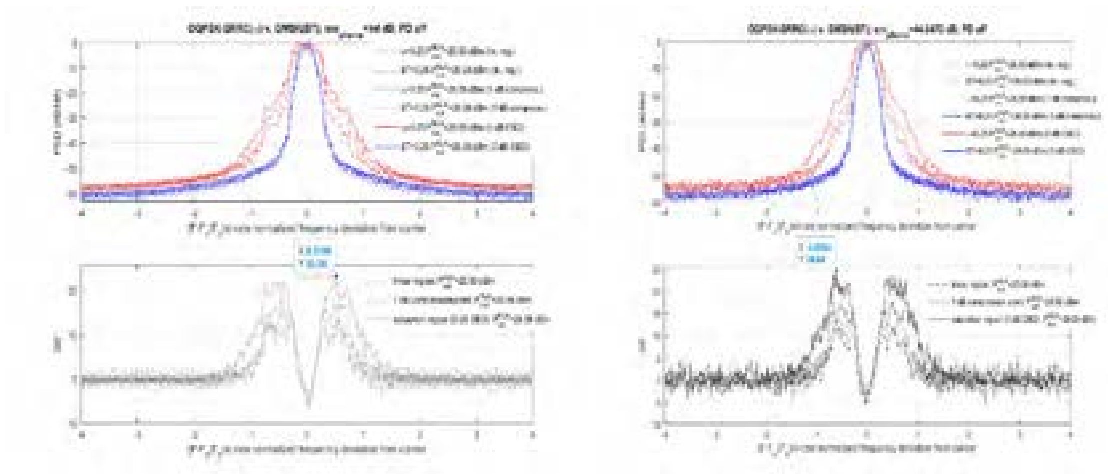

Figure A2. NLA induced SR effects (PD off): (left) noiseless; (right) $snr_{phs\_ns} = 44.04\ dB$.

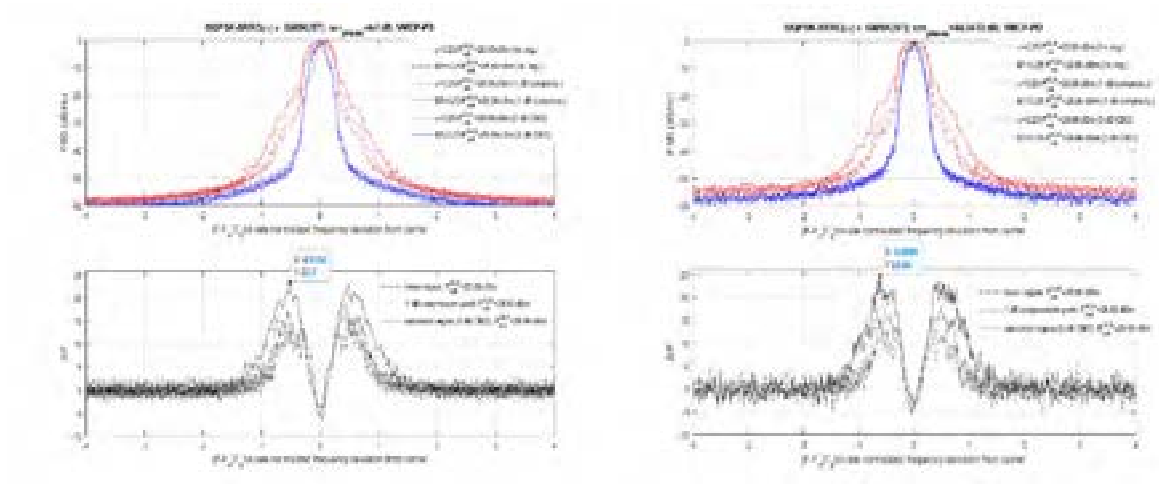

Figure A3. NLA induced SR effects with VMCP-PD:(left)noiseless;(right) $snr_{phs\_ns} = 44.04$ dB

Some more results on ACI evaluation for OQPSK and GMSK are presented in Figs. A4-A5:

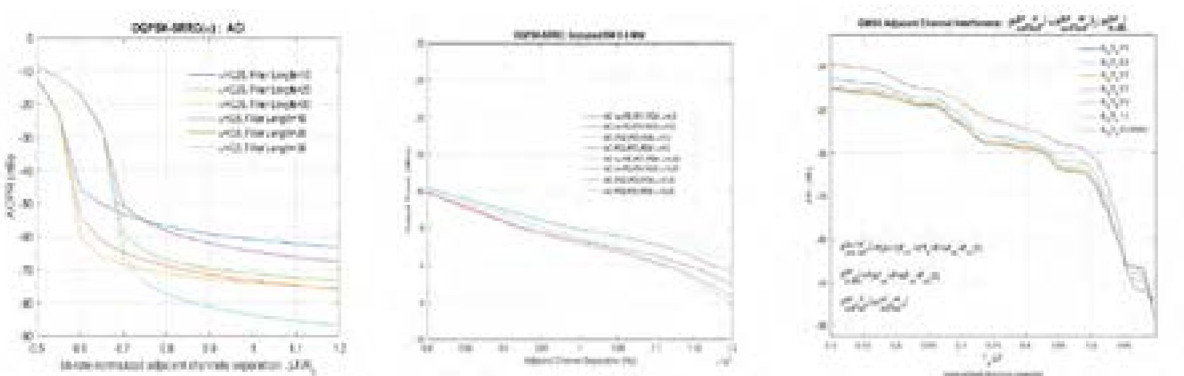

Figure A4. $\mathbf{OQPSK - SRRC(\alpha)}$: (left) not amplified, varying Tx filter length; (middle) noiseless; (right) ACI for GMSK with various $B \cdot T_b$ values[12].

In the following, some more examples of signal constellations are presented at both systems ends the transmitter (Fig. A6) and the receiver (Figs. A7-A8). In Figs. A7-A8, the effect of the sampling the MF and quasi-MF outputs with a phase offset, is demonstrated under various snr conditions.

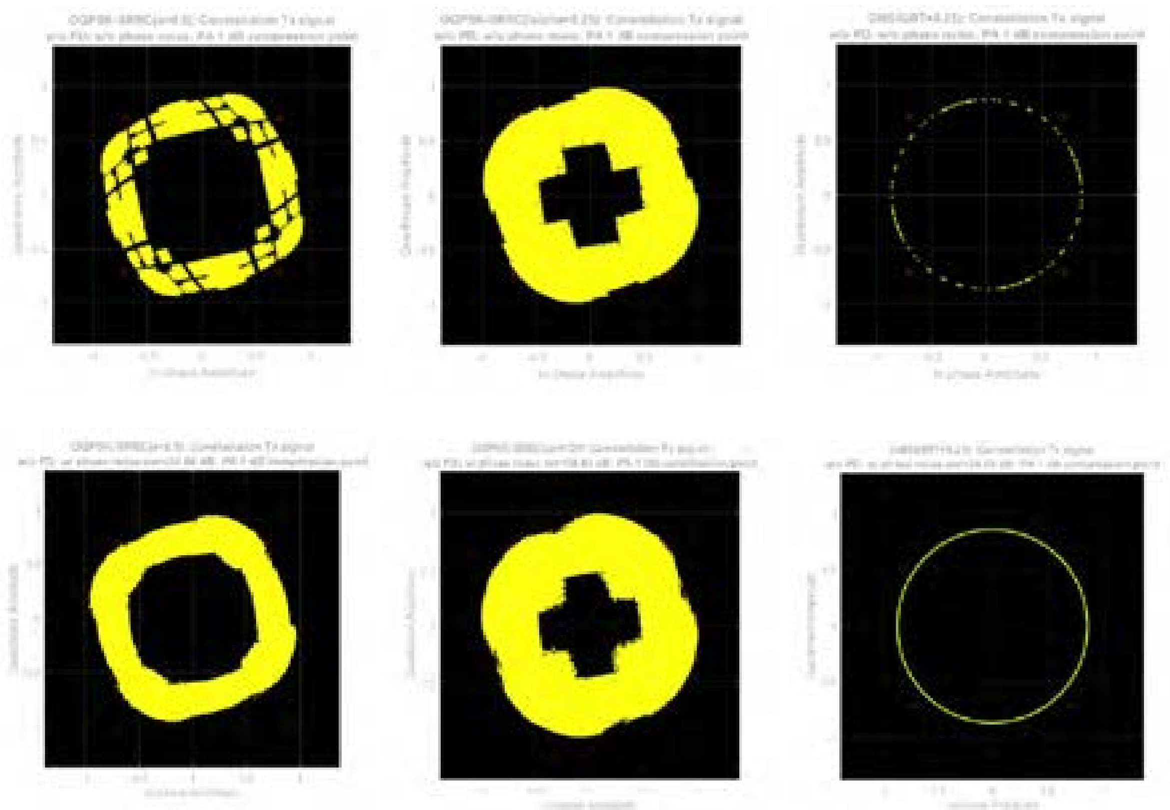

Figure A6. OQPSK, GMSK Tx signal constellations, with PD off, PA @ 1 dB compression point: (top row) w/o phase noise; (bottom row) $snr_{phs-ns} = 24.04\ dB$; (left column) $\alpha = 0.5$; (middle column) $\alpha = 0.25$; (right column) $B \cdot T_b = 0.25$.

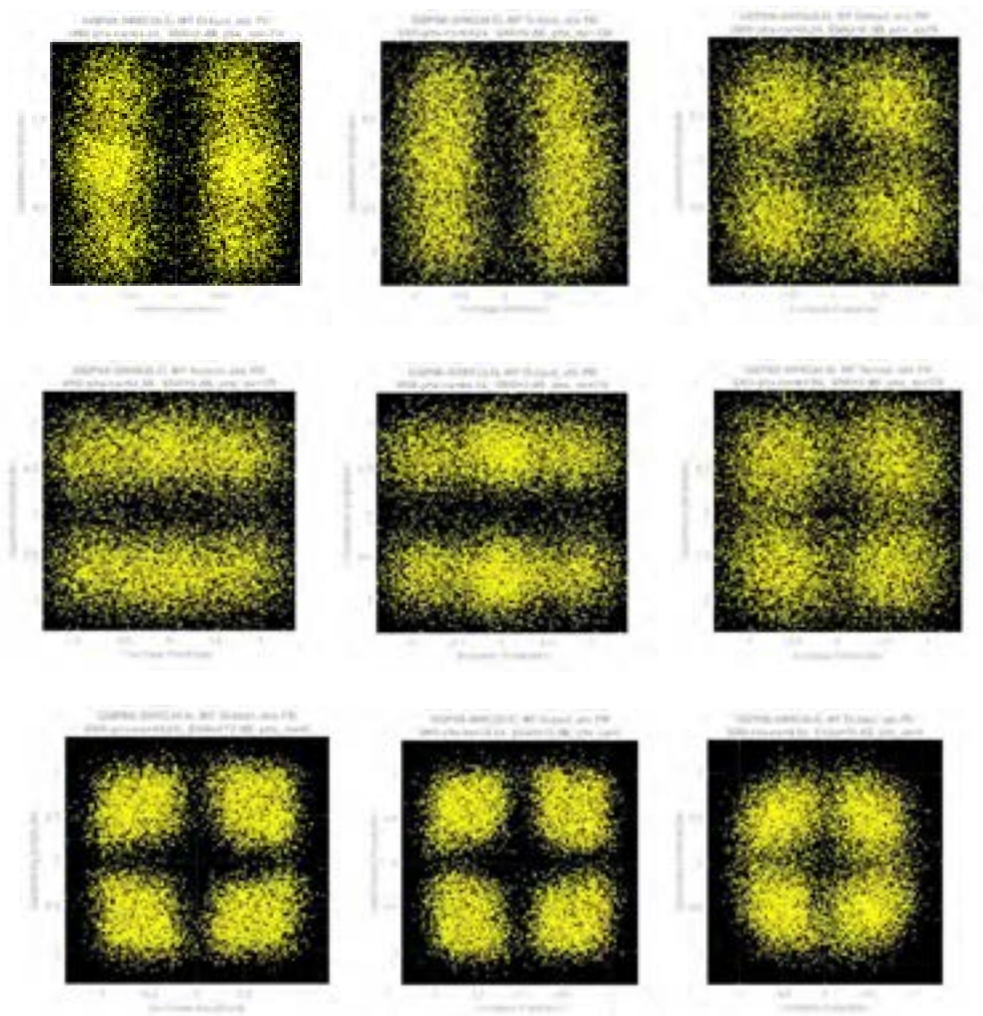

Figure A7. OQPSK-SRRC($\alpha = 0.5$), MF output, varying sampling offset, $snr_{phs\_ns} = 64.04\ dB$: ($top\ 2\ rows$) $snr = 0\ dB$; (bottom row) $snr = 6\ dB$.

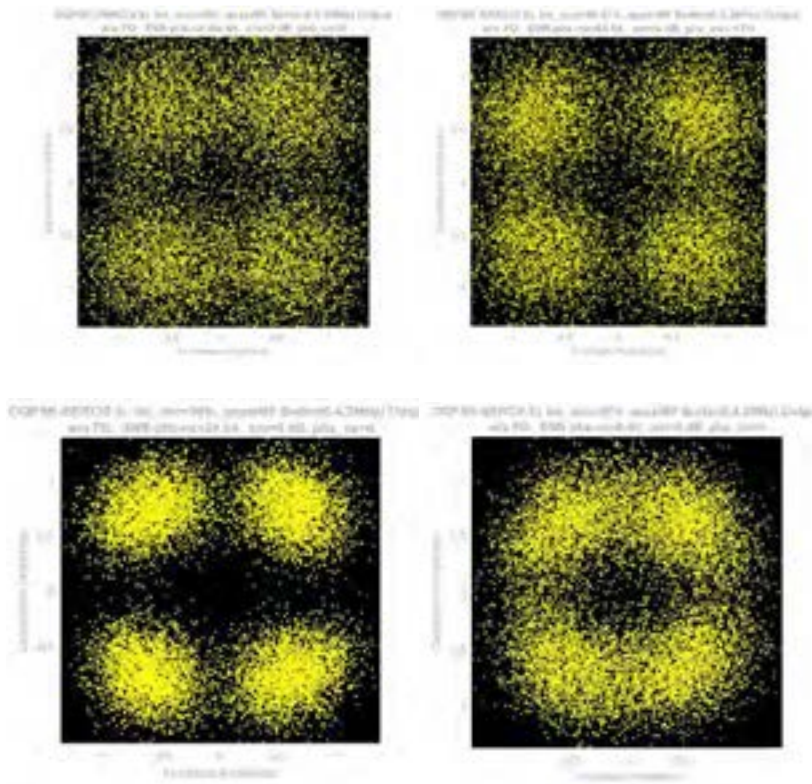

Figure A8. OQPSK-SRRC($\alpha = 0.5$), quasi-MF output (Butterw. order 6, and 99% bandwidth 4.2 MHz), varying sampling offset, $snr_{phs\_ns} = 64.04\ dB$: (top row) $snr = 0\ dB$; (bottom row) $snr = 6\ dB$.

Acknowledgments

The authors would like to thank RF Engineers, Joseph L. Bell and John Reese for their useful input.

References

[1]Sklar, B., "Designing Digital Communications Systems", 2002, pp. 1-29.

[2]Gronemeyer, S.A., and McBride A. L., "MSK and Offset QPSK Modulation", *IEEE Transactions on Communications*, vol. COM-24, no. 8, Aug. 1976, pp. 809–820.

[3]Prabhu, V.K., "MSK and Offset QPSK Modulation with Bandlimiting Filters", 1981, *IEEE Transactions on Aerospace and Electronic Systems,* vol. AES-17, no. 1, January 1981, pp. 2-8.

[4]Simon, M.K., "A generalization of minimum-shift-keying-MSK-type signaling based upon input data symbol pulse shaping," *IEEE Transactions on Communications,* vol. COM-24, Aug. 1976, pp. 845-856.

[5]Morais, D. H., and Feher, K., "The Effects of Filtering and Limiting on the Performance of QPSK, Offset QPSK, and MSK Systems", *IEEE Transactions on Communications*, vol. COM-28, Dec. 1980, pp. 1999-2009.

[6]G. Karam, G., and Sari, H., "Analysis of predistortion, equalization, and ISI cancellation techniques in digital radio systems with nonlinear transmit amplifiers," *IEEE Transactions on Communications*, vol. COM-37, no. 12, Dec. 1989, pp. 1245–1253.

[7]Saleh A.A.M., "Frequency-independent and frequency-dependent nonlinear models of TWT amplifiers," *IEEE Transactions on Communications*, vol. COM-29, no. 11, Nov. 1981, pp. 1715–1720.

[8]The Mathworks, Inc.

[9]CCSDS Green Book 413.0-G-3: *Bandwidth-Efficient Modulations*, Feb. 2018.

[10]Martin, W., et al. "CCSDS-SFCG Efficient Modulation Methods Study at NASA/JPL, Phase 4: Interference Susceptibility." In *Proceedings of the CCSDS RF and Modulation Subpanel 1E on Bandwidth-Efficient Modulations*, 1-171–1-212. Issue 2. CCSDS B20.0-Y-2. Washington, D.C.: CCSDS, June 2001.

[11]*TMOD* No. 810-005, Rev. E, Nov. 30, 2000, JPL D-19379, Rev. E.

[12]Murota, K., and Hirade, K., "GMSK Modulation for Digital Mobile Radio Telephony." *IEEE Transactions on Communications* 29, no. 7, pp. 1044-1050, July 1981.

Deep Space Systems Health Management

Emmanuel des-Bordes*

Blue Ridge College, Weyers Cave, VA, 24486 USA

Charles Dischinger† and Tanya Andrews‡ and Brooke Allen§ and Mariea Dunn Brown, Ph.D.¶

NASA George C. Marshall Space Flight Center EV74, Huntsville, AL 35812 USA

The National Aeronautics and Space Administration (NASA) impressive series of human space exploration missions have inspired the agency to develop several key habitation capabilities into deep space destinations such as Mars. However, deep space mission (DSM) to multiple destinations will face enormous challenges due to the complexity of the mission and light time-delays, and thus prevents complete authority of habitat systems from the ground. The DSM will tend towards a higher level of onboard autonomy and further require teamwork between the vehicle and crew in addition to the impact it will have on operational decisions. In this paper, we develop and implement a framework based on a network representation of function allocation for studying the transition of traditional control systems from the ground to onboard resources. We further expand our network model by proposing levels of adjustable autonomy to ensure increased situational awareness through ground-vehicle-crew interactions. Our extensive analysis shows the path towards increased space autonomy, which further improves system selection and effectiveness for mission operations. We also perform sensitivity analysis to research the impacts of sensitive system parameters failure on the survivability of mission and crew. Our result also explains that many of the variables included in the model require further research to understand the numerical value that represents the vehicle-crew interactions. Furthermore, our network model may well be used to study other function allocation problems in several domains of application to enhance policy requirements for human-system interactions.

Nomenclature

A(ACS)	= Advanced (Autonomous Control Systems)
ADAS	= Advanced Driver Assist System
AES	= Advanced Exploration Systems
AMCM	= Advanced Missions Cost Model
AOS	= Autonomous Operation of Systems
AR	= Atmosphere Revitalization
ATM	= Air Traffic Management
CCCA	= Command, Control, & Communication Architecture
CHeCS	= Crew Health Care System
CIS	= Communications Interface System
CLARAty	= Coupled Layer Architecture for Robotic Autonomy
DCC	= Data Computation Complex
DCS	= Display and Control System
DDT&E	= Design, Development, Test, and Evaluation
DRM	= Design Requirement Mission
DSH	= Deep Space Habitat
DSM	= Deep Space Mission
DSS	= Deep Space System
ECLSS	= Environmental Control & Life Support System

*Assistant Professor, Department of Mathematics

†Human Factors Engineer, Human Factors Engineering Team Lead

‡Human Factors Engineer, Human Factors Engineering Team

§Human Factors Engineer, Human Factors Engineering Team

¶Human Factors Engineer, Human Factors and Integrated Logistics Engineering Team Lead

EDL	= Entry, Descent, and Landing
EPS	= Electrical Power System
EVA	= Extra Vehicular Activity
FD&GRCS	= Food Production & Gas Recycling Capabilities System
FDIIR	= Fault Detection Identification Isolation Recovery
FMEA	= Failure Modes and Effect Analysis
FSM	= Future Space Mission
GNC	= Guidance, Navigation, & Control
HDU	= Habitat Demonstration Unit
HDSA	= Human-Centered Deep Space Automation
LoA	= Level of Autonomy (Authority)
LEO	= Low Earth Orbit
LCC	= Life Cycle Cost
MBR	= Model Based Reasoning
MER	= Mars Exploration Rover
MCC	= Mission Control Center
MOCET	= Mission Operations Cost Estimation Tool
MOCM	= Mission Operations Cost Model
MPR	= Mars Pathfinder Sojourner Rover
MTTF	= Mean Time To Failure
NAFCOM	= NASA–Air Force Cost Model
PRICE-H	= Parametric Review of Information for Costing and Evaluation Hardware
SC	= System Coordination
SHTA	= System Health Trend Analysis
SMC	= System Monitoring Capabilities
SSC	= Station Support Computers
TOCA	= Total Organic Carbon Analyzer
TMS	= Thermal Management System
ToA	= Type of Autonomy (Authority)
UAV	= Unmanned Aerial Vehicle
USNSP	= United States National Space Policy
WRM	= Water Recovery and Management
M	= million
kg	= kilogram

I. Introduction

A. Motivation and Background

DURING the past decades' human spaceflight exploration missions by NASA to multiple destinations beyond low Earth orbit (LEO) has proven successful, for which the agency is inspired to embark on several future explorations to several key-habitation capabilities and crewed long-duration missions.[1] This includes NASA's 2010 lunar moon ARTEMIS (Acceleration, Reconnection, Turbulence, and Electrodynamics) space mission.[2] Currently, NASA's effort is in the process of developing future human asteroid and Mars missions by the year 2025 and mid-2030s time frame, respectively, as described in the United States National Space Policy (USNSP).[3] NASA's previous spacecraft missions to LEO did not face any communication time-delays due to the distance between Earth and the destination.[4] This type of space mission gives the onboard crews the luxury and the ability to communicate efficiently with the ground-control through the course of their mission operations and with reduced onboard autonomy resources. Such space habitation capability in LEO missions will become risky to sustain in deep space due to communications light time-delays, travel distance to Mars, and length of duration on Mars.

Based on existing data and earlier space missions, future long-term mission operations will, therefore, require the use of complex automated or autonomous decision-making systems with fewer onboard crew and ground-control authority. The accomplishment of such missions demands the acquisition of highly complex and reliable spacecraft systems, big-data technology, and robotic systems which could impact the entire architecture, operations, and management of the habitat.[5] Most importantly, the safety and security of complex control systems for DSM depend on their continuous operations and maintenance. This consideration will impose a higher reliance on the degree of the crew or vehicle or a mixture of both (high level of independent separation from the ground-control)[6] leading to increased automated or autonomous operation of onboard systems and increased exploration mission tasks.[4,7] In order to succeed and sustain systems in an extended-duration of DSM, the size of the crew will play a significant role, which will be comparatively small, as described earlier, of approximately four to six members.[8] With increased autonomous mission operations, there's a requirement to understand crew-system interactions and consequently the advanced user interface to promote situational awareness. It will be necessary to incorporate long-duration effective crew-system interaction and crew performance together as one of the criteria during the crew selection for DSM.

Studies also show that other challenges and risks that DSM will encounter include crew confinement and isolation, and the exposure to hostile space environment. In addition to increased onboard autonomy, other research models are investigating the complexity of the crew workload becoming overwhelmingly large with fatigue-related and decreased system performance that appears to be more significant with missions into long-duration destinations.[9–11] On the other hand, the microgravity condition during which the crew members need to perform their research duties will pose health and physiological risk. Therefore, research is developing a series of measures such as the mental model of the situational awareness of the system operation and interactive space programs for the crew to avoid problems of workload-fatigue.[12,13] Additional analysis further suggests that appropriate restructuring and further shifting several of the system operations and management to onboard spacecraft vehicles while reducing the workload of onboard crew members and ground-control management.[5,14]

To minimize the impact of the space constraints, the design of the DSH requires robust, light-weight, and small vehicle based on the design of the international space station (ISS), to further promote operations of the communication systems and data handling management.[8] On the other hand, while real-time communications will not be readily available to support crew work performance and EVA operations, mission control centers (MCC) will effectively continue to monitor mission operations and maintain onboard resources for human-system interactions.[15] Results from recent studies indicate that different scenarios for the design of vehicles for future human DSM will be cost-effective and reduce mission risk.[16] The most important aspect of mission planning and preparing for a long-duration destination involves determining and developing the best strategies for choosing the control systems. The habitat control systems are critically needed for NASA to achieve its goal to succeed in these long-duration destinations. The agency requires that: (*i*) the onboard crew availability and productivity for mission operations are maximized and (*ii*) the functional requirements of the ground-vehicle-crew interactions are well-managed for continuous system operations.

Furthermore, the small, isolated, and the confined environment in the habitat for the crew to stay for a prolonged duration in space will have psychological and stress impact on the crew. Thus, the proposed deep space system (DSS) will provide the necessary solution to minimize risks space: environmental control and life support system (ECLSS),[4] crew health care system (CHeCS),[17] guidance, navigation and control (GNC),[18] command, control, communication architecture (CCCA),[19] temperature management system (TMS),[20] electrical power system (EPS),[21] and extra-vehicular activity (EVA).[22] The subsystems with functional requirements for the DSH have been provided and explained in Section D. While the impact of microgravity and loneliness is severe on crew performance, the failure of system parameters could potentially result in the loss of crew or mission.[23] To understand the failure of system parameters in space, we assume that a primary malfunction may occur due to: (*i*) system operational failure, (*ii*) technical failure, and (*iii*) external impacts, while a secondary failure may occur as a result of (*iv*) failure of back-up or recovery attempts. Thus, for these systems to operate autonomously onboard the DSH, we refer to areas of applications where automation systems have been developed and implemented.

The concept of human-automation function allocation problem has extensively been studied to determine the dynamic allocation of roles and capabilities between humans, who used to be in complete control now being represented as passive operators and autonomous or automated systems as well as their complementary interactions.[10,24] There are many great examples of applications of function allocation in systems relatively ranging from flight management systems in aviation,[14] ADAS technology in vehicles,[10] military robots and automated control UAV systems,[25] ATHEANA application in nuclear power plants,[26] to autonomous medical devices in healthcare system for surgery and to aid physically disabled patients to gain independence.[27–29] Similarly, NASA has long developed and adopted this new generational approach of designs based on autonomous or automated systems. NASA's continuous research into crew activities has prompted ongoing research aimed to maximize crew performance and crew-centered systems during onboard autonomy resources for DSM exploration tasks, thereby reducing dependency on ground controllers.[30]

The primary objective of this paper is to develop a dynamic function allocation approach for the distribution of DSS between ground authority and vehicle-crew autonomy to meet NASA's mission goals for travel into deep space destinations including Mars. Thus, we specifically focus on the autonomy operation of complex control systems.

The remainder of the paper is structured as follows: Section II motivates the need for understanding autonomous system design and summarizes NASA's autonomy for space exploration. Then we illustrate a graphical approach to improve and optimize the allocation of DSS to determine type and level of autonomy (authority) for ground-control, space vehicle, and onboard crew. Section III is a baseline economic study of control systems and a presentation of functional requirements and distinct components of systems. Section IV is a discussion of the results of the dynamic function allocation and identification of potential areas of the systems for autonomous operations, and an explanation of sensitivity analysis of key driving elements of DSS and how they impact mission success and the well-being of crew and vehicle. Finally, Section V is the conclusion and summary of future studies.

II. A Literature Review on the Effects of Autonomy on the Performance of Systems

In this section, we review the literature on function allocation between humans and systems with an emphasis on the autonomous or automated operation of systems and a summary of selected autonomy on space missions.

A. The Role of Humans in Automated and Autonomous Systems

We review methods and approaches that have been implemented and developed to solving function allocation problems in the setting of human-system interaction with allowable technology that exhibits adjustable levels of autonomy. The traditional concept of function allocation first identifies the full functional capability of the human or system, and second assigns the functions individually to be completed to accomplish the goals.[31] The earlier approach to function allocation eliminates the possibility that humans and systems could interact to complete the same function to achieve optimum goals.

Function allocation models have received considerable attention to providing an efficient method for allocating functions to competing agents. For example, Ref. 32 provides the three types of traditional allocation approach: (*i*) the comparison allocation is when system functions are allocated based on the human or system capability, (*ii*) the left-over allocation involves the dynamic shift of system functions (automation) that can not be completely performed by a human, and (*iii*) the economic allocation relatively determines the approach which gives the most benefits to the output of the process. As human-system interaction can be challenging enough, other studies have also examined that dynamic function allocation with the process of human and system working together as a team in a consistent and constant environment to reach a consensus on objectives.[24,33] Many researchers have studied other areas of human-system interaction including the function performance,[34,35] limited resources and cost function,[36] dynamics of work,[37] human-system interaction,[38] and levels of autonomy (automation).[39]

The dynamic human-system or human-in-the-loop system interaction that facilitates situational awareness is a major advantage approach in automated and autonomous systems benson2003experimental. Early examples of human-centered automation research studies have been described as adjustable autonomy in Ref. 40. The report describes adjustable autonomous systems in three areas as having (*i*) full authority over all functions, (*ii*) supervisory control over human operation, and (*iii*) the ability to balance workload between human and system based on situational awareness. Following similar model studies, the dynamic human-system interaction or automation refers to the distribution of functional roles and capabilities of the human to a system in a balanced approach to attain situational and global awareness.[41] In addition, this definition, a system on the other hand is autonomous if it has the ability to perform its functions with no human intervention. Thus, autonomous systems can aid humans to perform functions effectively while drastically reducing the chances for human error.[42] Such systems have achieved the potential to gather, analyze, synthesize large amounts of information, and then manage their limited resources to implement real-time actions. Moreover, the interaction between the human and systems or vehicle is increasingly becoming complex and difficult to assess as more of human-controlled functions are dynamically allocated to machines.[9]

Many industrial domains, including the military, automobile industry, manufacturing industry, and telecommunication, have coordinated numerous efforts to focus on the integration of high technology automated or autonomous systems to assist them in maintaining consistency and flexibility of system processes. The long-awaited need is for industries to maximize revenue and savings while minimizing cost and labor. For instance, the advanced driver assist system (ADAS) technology in self-driving helps with the longitudinal and lateral control of vehicles,[10] while air traffic management (ATM) in aviation largely supports the pilot and, in most cases replaces the roles of the ground-control authority.[14] Another significant aspect is the use of the AeroVironment Puma or the unmanned aerial vehicle (UAV) technology by the military to provide search assistance for tracking and rescuing missing colleagues, and carrying out another military operations, as explained.[43] In addition to these automation innovations and evaluations, Boeing company highly incorporates robotic systems to assemble and build many advanced aircraft for the US military during missions in complex operational territories, together with autonomous airplanes for assuming operations traditionally done by previous pilots.[44]

Automation also brings extensive benefits to the human and system, including elevated safety and reliability, enhanced systems response time, diminished workload, along with high acquisition and operation costs. Yet it also presents a set of challenging issues including searching for the right balance of work performance between humans and the system, a vital preparation concept for the journey to Mars.[45] In searching for the right balance of human-system performance, there have been numerous research studies conducted in an attempt to discuss and analyze the dynamic function allocation and autonomy level for advanced systems integration. Ref. 14 in their study of aviation safety and human-system interaction demonstrates the transition of air traffic system from the ground-control to onboard resources using the Braham approach on a case study of the Überlingen accident to examine flight collisions. The study also discusses the significance of early identification and immediate recovery of human errors. Besides, the work of Ref. 46 analyzes four areas of system functional capability to facilitate efficient human-system operations such as the following: avoidance, robustness, recovery, and reconstruction and its potential impact on systems.

NASA has previously used numerous autonomous systems and also recently engaged in several autonomous space systems, as summarized in Table 1 (See Appendix B). As research studies collectively continue to become increasingly interested in DSM and operations, Ref. 47 illustrates some challenges to developing a DSH for autonomous crew operations and communication time delays leading to mission recommendations and technological infrastructure. For example, in their analysis of a crew-size of 12 for human space mission scenarios to Mars, $1,125$ different activities were developed, ranging from successful launching, mission operations to smooth landing.[48] According to the report Ref. 49, the one-way speed of light is approximately 1.3 seconds from the moon and $1,337.6$ seconds from Mars, a critical challenge and a risk-related issue currently being assessed by NASA for its future DSM. The additional obstacles that crew members face include high environmental radiation and excessive microgravity exposure, further impacting the attention and performance leading to onboard crew members.[8]

Several authors have also proposed measures to challenges in deep space such as a weightless DSH control system based on near LEO missions using the ISS design and a balance between crew autonomy and the autonomous vehicle to release pressure and fatigue from the MCC. For example, in the analysis of Ref. 4 on the autonomous mission operations (AMO) software onboard the ISS, crew members autonomously operated and managed two ECLSS control systems traditionally handled by MCC. The two systems, total organic carbon analyzer (TOCA) and the station support computers (SCC) were well-chosen as they provide yardsticks for future DSM needs. The results of the seven months experiment over 22 missions show an overall success rate of 88%. Using an ISS based simulation in a NASA's Advanced Exploration Systems (AES) AMO project, Ref. 49 examines the impact of communication time delays on human space missions under three baseline scenarios – the lunar, the near-Earth object, and the Mars missions. Their findings show that long time delays offer the potential of increasing the crew members and flight control team workload. To improve the understanding of AES(AMO) project and its extensions, the authors describe and develop the concept of using an autonomous fluid transfer system in a single-button crew for detection, isolation, and recovery procedures without any intervention from the MCC.[50]

In addition to different approaches to shift system functions to onboard autonomy or resources as test-beds for DSH preparation, Ref. 51 focuses on the function allocation of system controls to four design reference missions (DRM) to study the interactions between human-automation-robotic technology for future DSM. The authors extensively demonstrate the significant importance of a weightless DSH for future human explorations in a 60-day and 500-day two-manned missions based on an ISS habitation system. In conclusion, the authors present a long-term useable robust design configuration for DSH in Ref. 52. There is also an extension to the general idea for advanced research regarding concepts for DSH structural design is formulated by the research work of Ref. 8. Other studies such as those of (as seen in Ref. 53) consider the role of the habitat demonstration unit (HDU) multiple research projects managed by NASA in the architectural design of the DSH.

B. Summary of Autonomy For Space Exploration

The selected summary of autonomy for previous and current missions overall LoA in Table 1 improves the understanding of autonomy for space exploration as a basis for extension to DSH. We analyze the gradual incorporation of the role of autonomy in spacecraft automation with an increasing approach towards autonomous control systems in DSH. Developing an appropriate understanding of system autonomous control demands dynamic levels of authority or cooperation between human and system according to the system performance and awareness, human cognitive capabilities and experience, and functional and situational requirements.[9] The concept of types and levels of autonomy (authority) has been extensively investigated in the literature with wide applications in many domains of industries.[7,38,54–56]

Table 1 shows selected examples of autonomy that NASA has implemented for space explorations. As shown in Table 1, column 1 represents the model or the innovative approach used to study the autonomy for the specific space exploration mission. Column 2 indicates the objective of the study or the experiment, and column 3 presents the autonomous control system for improving the mission. Column 4 lists the reference to the literature reviewed.

Table 1. Role of Autonomy for Space Exploration

Model Formulation	Objective of the Study	Autonomous Control System	Reference
1999 Remote Agent Architecture	Describe NASA's first full autonomous control system onboard the deep space one spacecraft	• Nominal operations with goal-oriented • Failure diagnosis and recovery • onboard planning and scheduling	57
2003 CLARAty Decision Layer	Focus on increased autonomy for Mars exploration rover missions	• onboard data analysis • Automated planning • Model-based fault diagnosis	58
2007 Robotic Lunar Survey System	Design a procedural concept for a systematic autonomous survey with rovers at Haughton Crater	• 3D scanning lidar	59
2012 Analog Mission Method	Consider procedures for managing onboard control systems operations while addressing the effects of light time-delay on long-term destinations including Mars with increased crew autonomy	• onboard systems for increased crew autonomy	60
2012 Dynamic Function Allocation	Evaluate allocation of functional requirements between human-operator and future air traffic control system (automation)	• Standard terminal automation replacement system	61
2013 Advanced Autonomous Navigation	Study autonomous map- and feature-based localization navigation system for the planetary rover mission	• Get the localized orbiter map • Assess the position	62
2015 AMO Software Design	Present crew autonomy through assisted operations and management of selected control systems onboard the ISS	• Mission operations functions • Fault management • Data display	4
2018 Astrobee Space Robot	Analyze the free-flying robotic system intended to facilitate ISS mission operations	• Autonomous intra-vehicular activity onboard the ISS • Ground-control remote operations • Interactions between human-robot and onboard crew members	63

While we acknowledge extended studies in the area of function allocation from control systems and levels of autonomy (authority) in many research projects and workshops using simulation-based models and other decision-making methods for human and system interaction, an in-depth investigation into function allocation within deep space systems health management is needed. Thus, our extensive literature review has provided the tools and strategies for this project:

- First, we present a comprehensive study of function allocation between human and system and its applications ranging from aviation to military and then to manufacturing by reviewing several studies to examine the balance of human-system cooperation in the work-place. We also study the benefits and limitations involved in the human-system interaction and transitioning this to the study of DSH. We also define various elements and characteristics of deep space that will impact the functional requirements of systems.

- Second, we develop a graphical method to allocate control systems functions to ground control, space vehicle, and onboard crew to identify their role of autonomy (authority), while we consider the physical constraints and limitations such as light time-delays, safety and capabilities for all control displays on the ground, as well as challenges due to advanced software technologies.

- Third, we further demonstrate our approach to build upon the foundation of our function allocation to a dynamic allocation model that is of utmost importance to ground-control, space vehicle, and onboard crew for facilitating situation and global awareness of DSS operations. Meaning one of the three agents of authority could step in and intervene if necessary, depending on its level of autonomy. Establishing this adaptive relationship between ground-vehicle-crew and systems will achieve the following:
  – Control systems could benefit immensely from dynamic automation software technologies to improve the mission exploration task of the crews in deep space.

  - Control systems will readily be available for autonomous operations to provide high performance, safe, reliable, and cost-effective environment. The automation performance includes the ability to switch between system functions and adapts to the situational awareness.
  - Control systems could prompt an additional crew to support onboard resources for potentially managing excessive deep space workload.

- Finally, we explore the impact of sensitive mission parameters on space vehicle regarding the survival and success of the mission, and the long-term health and performance of onboard crew autonomy.

III. Deep Space System Health Management for Autonomous Operation

In this section, we describe the three types of autonomy agents for our control systems and also provide information on the economic study of control systems. We then propose network representation to determine the control systems for ground-control, onboard crew, and space vehicle autonomy, based on parameters that influence system interactions and other constraints and challenges. Based on the functional requirements and elements of control systems for autonomous operations, we then examine specific components of the system. Furthermore, we develop six LoA to augment the three ToA to render system situational knowledge to all three agents. This process provides valuable insights into the appropriate design and selection of control systems for the habitat.

A. Analyzing Ground-Vehicle-Crew Centered Interaction

We describe the autonomy of each of the three agents that is adjustable based on the situational awareness of system operations through interactions to enhance the flow of information for system management.

1. Ground-control Authority

The ground-control center is an essential facility responsible for planning, operating, managing, and controlling NASA's spacecraft missions (Gemini, Apollo, and Skylab) that has been in existence since 1965. Major systems in the ground-control center include the communications interface system, data computation complex, and the display of the control system.[64] The primary responsibility for MCC during the future long-duration missions will be required to monitor and operate limited version of the autonomous and automated systems from the ground with limited personnel, in areas where the space vehicle and crew are unable to handle. With increased considerations for advanced automation for DSS, traditional control systems on the ground will also be migrated to onboard autonomy with intervention capability from the ground if necessary.[65]

2. Space Vehicle Autonomy

NASA traditionally has named space vehicles according to their missions which are also labeled according to payloads and other mission elements. The space vehicle designed for DSM will consider an increased level of autonomy by incorporating advanced technology including adaptive GNC system, ATM system for flight operations, and mission planning with decreased dependence on ground authority for O&M.[66] Thus, future space vehicles must have the key driving capabilities to operate autonomously in order to accomplish long-term destination missions. On the other hand, a microgravity environment will be difficult to predict during DSM for entry, approach, and landing of space vehicle.[16] This has led to the discussion of splitting heavy space vehicles for future Mars missions into two smaller ones.

3. Onboard Crew Autonomy

Recently ground-control has been assisted by or delegated operations and management to onboard autonomy.[4,67] Given the long-term trip into deep space and the presence of light time-delays, onboard crews will be required to assume increased autonomy and increased system performance using automation resources.[68] According to recent studies, the onboard crew will spend more time monitoring autonomous systems and interacting with ground-control and other automated systems. Remarkably, increased autonomy over extended-duration may result in possible instances of a fatigue-related issue and decreased performance in some crew-system interaction. Thus, sustaining a high level of automation and performance in space ought to be well-defined.

B. Evaluating Baseline Economic Study of Deep Space Control Systems

The DSH for future exploration missions must consist of multiple high-performance and high-reliability systems and subsystems. Therefore, we propose to understand the methods used to analyze the life cycle cost (LCC) of DSH major systems as part of the tool for determining type and level of autonomy selection (software technology). NASA agency-wide requirements for mission-specific methods of cost estimation has always been a highly monitored approach using well-detailed engineering analysis. We define the significant software and hardware expenses and costs involved in DSH, identified as design, development, test, and engineering, launch, and operations and maintenance.[69,70]

Total DDT&E Cost

The DDT&E is the overall cost associated with the design, development, test, and evaluation of systems and subsystems. The costs for deep space DDT&E are estimated to be much higher due to its high performance and high-reliability mission functional requirements and limitations, as well as the weight of the space vehicle. Many estimation methods have implemented in the calculations of DDT&E cost such as the Advanced Missions Cost Model (AMCM), Parametric Review of Information for Costing and Evaluation (PRICE–H) Hardware Cost Model, and the NASA-Air Force Cost Model (NAFCOM).[71]

- The AMCM is an easy and quick technique to use, determined from mission-specific cost inputs: dry mass, the number of units, type of mission, amount of design generations, software technology, and unforeseen technical difficulty to estimate overall DDT&E cost for future mission control systems. The AMCM tool is modeled for long-term predictions.[71] For instance, the DDT&E cost for a Mars surface mission project is determined to be approximately $1.82M per kg, a much larger budgetary estimate for DSM.[71]

Mission Operations & Maintenance (O&M) Cost

The Operations and maintenance cost forms part of every spacecraft mission, and for a future long-duration mission, this cost is likely going to be expensive. The O&M cost requirement for a successful DSM will consist of extensive type and level of autonomous control systems for monitoring, crew training, integration of software technologies, and ground-control support. Methods previously used are Mission Operations Cost Model (MOCM) and Mission Operations Cost Estimation Tool (MOCET).[72]

- The MOCET tool is one of the methods used in developing and predicting the O&M baseline scenario cost from historical economic data for future destination mission operations such as Mars. The procedure is to split the mission operations into separate segments. For example, out of 14 planetary space missions, the technique has been seen used to observe 18 different stages within the mission operations.[72] This model can be improved to highly estimate the O&M cost for DSH.

Total Launch Cost

Typically, the total cost in launching a DSH for a Mars mission will include the accompanying crew, system payloads, and other unforeseen eventualities, based on the undertaken space mission.

C. Functional Requirements and Elements of Control System for Autonomous Operation

Understanding the functional requirements and identifying potential elements of control systems for autonomous systems, as well as meeting guidelines and structural obstacles, are necessary for a successful long-term destination space missions.

1. During a DSM, crew members must learn to adjust to changes in the space environment and surroundings beyond LEO missions[73] in addition to loneliness and separation from the Earth. These effects on crew members will have an impact on the health management and performance of systems. These systems are an integral part of the habitat to fully support and address the mission needs of crew members and payloads survival. The focus is the proposed seven key areas for DSS including the ECLSS, CHeCS, GNC, CCCA, TMS, EPS, and EVA based on the concept of the ISS configuration.[74]

2. We remark the two main features of a long-duration space mission, that are the reaction time of control systems and one-way communication time-delay between Mars and Earth.[49] As we know, reaction time varies significantly in different situations depending on the type of control system function, resulting in many potential design options and autonomy strategy decisions. Light time-delays in long-term destinations into deep space have been carried out by many authors.[75–77] One solution to the time-delay problem, Ref. 78 analyzes two levels of autonomy for onboard crew members and concluded that crew members with high autonomy performed extremely well

than their counterpart in a lower autonomy space travel mission. Similarly, according to the simulation report of Ref. 79, a seven-phased 520-day trip into deep space presents the following scenario. Phase one observed direct communication between ground-control and onboard crew, but later shifted to video messages and finally to high autonomy in the remaining mission phases. Other studies have also implemented self-scheduling software called playbook for flight crews during communication time delays.[80]

3. There are discussions of sending a crew size of between four to six to Mars,[8,81] who will assume an increased level of autonomy (authority); therefore, the habitat will need vehicle autonomy and other onboard resources for high system performance. Also, the space environment for crew members to work in will call for psychological and work performance issues due to prolonged isolation, health risk, and radiation exposure, further impacting crew interactions. Several solutions have been presented for both physiological and psychological problems in space to enhance the success of DSM.[82,83]

4. Safety and reliability defined in the graphical approach refer to the ground-control being capable and skillful enough to assume new roles of control systems, to provide a reduced operational workload for onboard crews. Therefore, the autonomous vehicle and ground-control authority will provide the necessary support of the mission operations for performance improvement in human mission exploration.[84]

5. The architectural engineering design and analysis of the future autonomous vehicle or habitat for a long-term trip requires a series of mission must-have concepts. The space vehicle must be environmentally friendly and completely meet the payloads, safety, and reliability guidelines to accommodate a crew size of four and more, based on lessons learned from the previous spacecraft. Additionally, the future vehicle (habitat) needs to be weightless, cost-effective, cater to the well-being of crews and mission, and thus must immediately assume autonomy if the need arises either from the flight crews or ground control. Yet, the use of some autonomous systems in vehicles could present challenges or risks to structural engineering design.[16,85]

6. As autonomous operations of software technologies are increasingly becoming an integral part and critical component of space transportation, it is of utmost importance to know that advanced technology will provide the ability and platform for DSS to benefit.

D. Examining Components and subsystems of Deep Space System

The safety and reliability of DSS are carried out with vast improvement, but, other key challenges remain in the implementation of autonomous operation of systems (AOS) and advanced software technologies in the DSH:

- first, system functional requirements for fully autonomous operations with minimal to no ground-control or onboard crew intervention is needed and
- second, system expectation requirements that involve challenging areas and mission must-have concepts such as software complexity must be technically detailed during the initial mission analysis.

Control systems form extreme features of the DSH which are designed to be adequately reliable, well-maintained, and safe as well as its being capable of the environmental system in the space environment. For example, first, the life support in DSH is expected to provide approximately 98% of its water from onboard systems, more than 75% of oxygen from carbon dioxide, and mean time to failure (MTTF) of systems for over 30 months for more than 1,100 days.[86] Second, the EPS is the primary source of power to all systems and subsystems for maintaining continuous operations and management of DSS. Thus, in order to optimize the output and also expand the role of the systems for uninterrupted service during future human long-term mission destinations to Mars, we examine to understand their respective components.

1. The ECLSS

The six major subsystems of the ECLSS and their respective functions provide a conducive and habitable environment for the health management of payloads and onboard crews. Advancing some of these human-health critical activities for DSH will potentially require the autonomous operation of specific areas of the ECLSS with software technology, making crew and ground-control productive for other time-sensitive mission assignments.

2. The CHeCS

The CHeCS system is primarily responsible for the health and the well-being of onboard crew members during space travel. The current CHeCS system needs to be upgraded and optimized for a typical long-duration mission with microgravity conditions. A considerable amount of studies have shown many of the possible increase in health risk in a DSH as it is an essential component of the mission with autonomous innovations.

3. The GNC

The GNC system involves three main processes for space mission requirements according to its name could benefit : (*i*) space vehicle current location, (*ii*) space vehicle desired travel course, and then (*iii*) space vehicle control to the exact destination. As shown in Fig. 1, the vital role of the GNC in mission-specific operations and procedures could benefit immensely from in-flight automation.

4. The CCCA

The CCCA system provides a collective approach for space communication and data handling for all control systems and payload operations in space travel missions, invaluable support, and capabilities for the long-duration space mission.

5. The EPS & TMS

Future human long-duration space mission operations will require a continuous flow of power using EPS to manage the health and strength of onboard systems and subsystems. The TMS will be responsible for regulating and maintaining temperature and humidity ranges of systems over specific intervals through the removal of waste heat produced by systems operations. According to Fig. 1, it appears that some of the components of the EPS and TMS systems are potential vehicle automation candidates.

6. The EVA

The EVA system is an essential part of onboard crew activities that consist of science and exploration activities conducted in space. Many authors have conducted investigations over the years to discuss software technology that can adjust and optimize the human-robot interaction behavior in human mission space,[22] highly needed for DSM.

E. Network Representation of Decision and Analysis of Deep Space System for Autonomous Operation

The network illustration presented in Fig. 1 (see Appendix A) is used as a basis to represent decision and analysis for the selection of the type of control systems to be designed and integrated into a DSH for autonomous operation. We describe the network illustration over five stages: gathering, analyzing, synthesizing systems function data, managing system resources, and then implementing system action. Each selection step within the network is examined and then considered for each of the ToA. Ultimately the process will contribute to the importance of system automation motivated by human-safety, well-being and health, and cost- and service-effectiveness of DSS. Thus, each arc defines a feasible decision of yes or no, while each arc length represents the direction.

As shown in Fig. 1, the first and second stages of the network indicate the gathering and arrangement of economic data and system-related benefits, followed by an in-depth system analysis, to make merit-based selections on the ratio of mission benefit to economic study. At the same time, selected crew-members for future deep space exploration missions who will be in long-term isolation and confinement should undergo psychological evaluation and training. The objective of crew psychological assessment is to identify the impact of outer space isolation and confinement.

The third and fourth phases involve the synthesis of all the analyzed data-set leading to the management of limited resources. Physical constraints and challenges for the operation of autonomous systems can be summarized in the synthesis sequence stage as follows: (*i*) effect of control systems time-delays, (*ii*) challenges of vehicle automation engineering design, (*iii*) benefits from software technology, (*iv*) safe and reliable ground-control capabilities to perform some mission operations, and (*v*) psychological assessment of selected onboard crews.

For example, a GNC control system, which requires an instant response time, could be impacted by communications time-delays and decisions must be autonomously made by onboard resources. Following this trend, we consider an additional crew or a knowledge-based expert system. The selection process then gives rise to a trade-off between software technology benefits and intensive training for increased crew autonomy. If an expert system is selected based on its enormous benefits from software, then an advanced crew assistance autonomous-based interface system must be designed to assist crew leading to a vehicle autonomy selection. On the other hand, if GNC software integration is not beneficial and also unsafe for ground-control capabilities, then increased crew autonomy is selected else ground-control will continue to operate the system.

F. Defining Levels of Adjustable Autonomy for Crew-Centered Autonomous System

In this section, we study the network illustration in Fig. 1 to determine the type of autonomy (authority) (ground-control, space-vehicle, onboard crew) and also identify prime areas for a potential automation process. We can achieve this by implementing software and human-robotic technologies in addition to innovative controls and displays on the ground. With the selection of the type of DSH autonomous control system in Fig. 1, the process continues to identify the corresponding desired degree of autonomy (authority) proposed in Table 2 (see Appendix B) to keep crew well-informed of system operations. Table 2 defines two distinct numerical values, with the first representing ground-control level of authority and the second both the vehicle-crew level of autonomy (level of autonomy between vehicle and crew must be critically determined by ground-operator or crew member during mission planning). The numerical value ranges from $1 - 0$ (full ground-control autonomy with no vehicle-crew intervention) to $0 - 1$ (full vehicle-crew autonomy with no ground intervention), adjustable in steps of 0.2. Column 1 gives the adjustable levels of autonomy or authority, and columns 2, 3, 4, 5, and 6 represent the dynamic allocation of functions with five stages: gather, analyze, synthesize, manage system resources, and implement system actions, respectively. Column 7 describes the autonomous control systems.

For example, given the graphical network in Fig. 1 for a vehicle or crew ToA (selection of the type of autonomy) or a mixture of both, then Table 2 identifies or assigns the LoA as follows level G_4 ($0.4 - 0.6$), level G_5 ($0.2 - 0.8$), and level G_6 ($0 - 1$). Furthermore, autonomy operations under dynamic function allocation: gather, analyze, synthesize data, and manage resources stages within levels $G_2 - G_5$ are controlled by all three: ground, vehicle, and crew combination, with the exception of action implementation at level G_2, which is fully determined by the ground-control. Additionally, the autonomy operations under all stages of the dynamic function allocation at levels G_3 and G_4 are determined by all three: ground, vehicle, and crew combination. On the other hand, the combined vehicle-crew autonomy will determine DSS at the implementation stage at level G_5.

IV. Summary of Results and Sensitivity Analysis

In this section, we summarize the results of our study and then study sensitivity analysis to analyze the impact of system failures, behavioral challenges, and space environment on the success of the mission based on our efficient model formulation.

A. Summary of Results of Deep Space System Health Management With Potential Automation Candidates

This section briefly describes the design of the study and details of the process and analysis implemented to arrive at the results. We focus on the discussion of a summary of our findings from the extensive studies into the dynamic allocation of systems functions for autonomy (authority) integration into DSH capability, which ultimately requires functional requirements of control systems and light time-delays to be considered and analyzed. Obviously, the existence of high vehicle-crew autonomy with the support of software technology is clearly needed for overall accomplishments of crew and payload operations in deep space. Our goal for this project is to create system performance ToA for ground-control, vehicle, and crew autonomy (authority) by setting-up a network illustration of decision and analysis over five domains (stages) to consider the role and type of autonomy under system integration constraints and challenges of the space environment, as well as long-duration missions. Given the static outcome and the lack of interactions for the ToA, we then propose an intermediary six LoA to involve the dynamic interactions of ground, vehicle, and crew and also to provide the onboard crew with centralized situation-awareness of control systems, ranging from G_1 to G_6.

We determine the degree of authority for DSS and present our results in Table 3 (see Appendix B), where columns 1 and 2 provide the seven major systems with associated several subsystems. Then column 3 further explains the main functions of the DSH control systems and proposed future functional requirements for DSM. Columns 4 and 5 describe the essential part of the research studies, adjustable types, and levels of automation of operation of control systems, respectively. Column 6 presents integral parts of the DSH control systems that are potential candidates for automation precess based on recent studies on DSH autonomous control systems. The following points show our overall analysis for potential candidate areas for systems automation.

- First, we gain further insights into the functional requirements and constraints of the DSS by splitting them into two major categories: stage-one and stage-two systems.

Stage-one System

Stage-one systems have the advantage of effective operation from the ground with minimal vehicle-crew intervention over-ride due to its response time. For this reason, stage-one systems are going to be less vulnerable to system failure to reduce mission risks and more expensive to operate than stage-two systems.

Stage-two System

Stage-two systems include systems that will allow high vehicle-crew autonomy requirements with some intervention from the ground because of its fast response time and software technology integration. The stage-two system is needed as a ground-control representation for communication and system recovery. Another area is the DDT&E cost for a stage-two system that will increase due to the necessity for advanced software technology and user interface hardware.

This procedure practically supports the distinction and design of software and hardware technologies integration in addition to the training and functional requirements for onboard crews and ground-control. Hence, the procedure can, therefore, be seen as a decision-making model for choosing appropriate autonomy for future systems.

- Second, we observe that the subsystems and functional requirements of the ECLSS and CCCA control systems are inter-related and must work together in a balanced manner. Ground-control handled these systems during previous space missions, however, for DSM, it is intended for some parts to be migrated to onboard resources at level G_3 with a 0.6 authority, and over-ride ability from vehicle-crew. This is because:
  - Continuous operations and maintenance of ECLSS is very critical to the well-being and safety of the vehicle, onboard crew, mission, and payloads. However, the effects of time-delays on some aspects of the trend analysis and monitoring are negligible as the ground has the software capabilities to handle them.
  - Uninterrupted communications with the ground-control are essential for keeping situation awareness of the system processes and global awareness of the entire mission.
- The level G_1 to G_3 are classified as stage-one systems due to its high ground-control capability with minimal vehicle-crew intervention from assistance to the delegation. The system functions belong to the ground-control framework, whereas the remaining specific features are controlled by the combined vehicle-crew. Accordingly, G_1 – G_3 have already been employed in previous and recent NASA's space mission operations.[4,14,87]

1. The ECLSS

The long-term reaction period of the ECLSS system functions and other constraints will assign the system to a centralized ground-control autonomy with possible vehicle-crew override according to the developed network process. The prime areas of the ECLSS for autonomous operation can be attributed to the complexity and interactive ability of the system as follows: (*i*) subsystems monitoring capabilities (SMC), (*ii*) subsystems coordination abilities (SC), (*iii*) management of fault detection-identification-isolation-recovery (FDIIR) methods, (*iv*) subsystems health trend analysis (SHTA), long-duration food production, and gas recycling capabilities system (FP&GRCS). Previous research shows that autonomous advanced monitoring software called the model-based reasoning (MBR) for portable WRM, hygiene WRM, and AR subsystems and the knowledge acquisition for automatic failure modes and effect analysis (FMEA) software for FDIIR just-in-time has been developed for ECLSS systems.[88] Recently many authors have proposed autonomous operations of WRM subsystem using an artificial intelligent control,[89] and centralized automated ECLSS by considering a Bayesian networks approach[90] are recent ECLSS system upgrades for long-term destinations.

2. The CCCA

The automation system update for the CCCA must include advanced software technology for communication link subsystems, FDIIR methods using redundant systems, advanced DSM plan of action from launching to docking are designed, and integrated.[19,91] The process will lead to full automation for ground-control, vehicle, and onboard crew-members according to the network illustration.

- Third, considering the recent system functions and current software upgrades for the EVA system in a DSH demands a higher crew autonomy of 0.6 with ground-control supervision due to its capabilities for system preparation time and extensive monitoring for future risks to support vigorous EVA activities.
- G_4 to G_6 are classified as stage-two systems. These are systems that are highly controlled or influenced by the mixture of vehicle-crew autonomy with minimal to no ground-control interference. The concept of G_4 – G_6 have been implemented in recent NASA's mission operations.[62,63]

3. The EVA

Developing and designing a full autonomous teleoperational activity to manage and operate EVA in a deep space environment requires the combined effort of the ground-control and crew-autonomy. Since the EVA system takes too much time for preparation and operational tasks in the range of 3 to 4 hours, creating possible challenges within the management of the FDIIR subsystem.[21] Therefore, the graphical process and decision based on Fig. 1 suggests a crew-member autonomy with minimal intervention from the ground-control. An additional example is the EVA robotic assistant (ERA) software technology that can be updated into the DSH for human-robot interaction behavior.[22]

- Finally, we notice that the following control systems, CHeCS, GNC, EPS, and TMS, which has a fast reaction time concerning the light time-delays, increased software technology ability, and human-robotic systems will assume increased vehicle-crew autonomy with little to no intervention from ground-control in a future human long-duration planetary mission. These systems function operational requirements will have a 0.8 degree of vehicle-crew autonomy with over-ride capabilities from ground-control for monitoring, planning, and interruption in case of any imminent failure.

4. The CHeCS

The specific areas for CHeCS to benefit from onboard autonomy include advanced telemedicine and surgical robotic technologies. We observe that fast response time and structural challenges to engineering design will require subsystems for increased crew-member autonomy, with ground-control supervision or an onboard physician allowed by NASA policies. A considerable amount of studies have addressed many of the increased health risks in a DSM, as it is a vital component of the mission. Software technology for autonomous CHeCS system includes advanced telemedicine and surgical robotic technologies.[17,92]

5. The GNC

It is highly achievable and flexible to have a centralized full vehicle system-model autonomy with assisted control-displays capabilities to ground-control and crew-members for GNC rendezvous and docking systems, as a result of its fast response time, and no limitations to structural engineering and software technology. Recent studies which indicate that autonomous navigation for deep space missions using onboard GNC software technologies could possibly include AutoNav and AutoGNC have been considered.[18,93]

6. The EPS & TMS

The software technological potential of the TMS and EPS to develop advanced autonomous software technology to enable future human long-duration space missions is being analyzed every day. Major areas of the EPS as well as the TMS identified for vehicle autonomy with reduced ground-control intervention are the continuous monitoring of operational conditions of subsystems, management of the FDIIR methods of subsystems, and power supply in addition to the thermal control systems of the EVA. This is because of their fast reaction period and previous EPS failure rates of 0.06 mission days and 0.5 mission days for Skylab and Space Shuttle, respectively.[21] Thus for a DSH, EPS and TMS software technologies can be optimized for their multifunction requirements in addition to minimal structural engineering challenges.

B. Single Parameter Sensitivity Analysis of Deep Space System Failure

Studies show that NASA's human space exploration missions have encountered some mission-related injuries and crew losses in the past.[94,95] This problem looks complex and difficult to tackle as the space agency is considering measures to minimize such situations that result in unsuccessful missions as they plan for future human missions into deep space including Mars.[23] Studies also show that mission fatalities in the past have occurred during ascent, entry, and landing of a space vehicle, described as the difficult part of space missions.[96] We, therefore, study the autonomous operation of DSS to identify prime areas for advanced software technologies to be developed, essential for supporting human presence on Mars. This can be easily achieved through the studies of one parameter sensitivity analysis of mission success to system failure parameters in deep space.

We outline in this section, an approach for analyzing sensitive elements of the DSH systems that remarkably will impact the success of human mission explorations in deep space. We investigate how the dynamic function allocation decision analysis are impacted as we examine the individual failure of system components and the hostile space environment, while we assume uninterrupted operations of the remaining systems. This study is very important as a policy recommendation to NASA decision-making into deep space in addition to the integration of autonomous control systems in DSH. Reliability and understanding of the parameters and constraints in deep space demand sensitivity analysis to illustrate the impact of failures of DSM parameters and space environment on the survivability of crew, vehicle, and mission as discussed. We represent the possible DSM system failures with a network illustration, shown in Fig. 2 (see Appendix A). This network is drawn over five stages of the Mars space travel to identify where fatalities or failure are encountered during the long-term space trip. In Fig. 2, each node is presented by either an outer space issue-related diamond, solution or action proposed or unfortunate-related rectangle.

- Each diamond represents various uncertainties and challenges that onboard crew could face during the five stages, namely, launch, cruise, orbit, surface, and operations of the Mars mission exploration trip.
- Each arc from a diamond defines a yes approach for a temporary deep space mission issue or system parameter failure which is easily solved whereas a no approach leading to a loss of mission or crew or vehicle. Others also lead to possible solutions or eventual fatalities in the long run. Beyond the issues, the rectangles represent the solutions or the unrecoverable instances from mid-course issues.

The system failure sensitivity analysis presented in Table 4 (see Appendix B) analyzes the potential occurrences of system failures and space environment during human space explorations and subsequent emergency ranging from temporary to permanent distress or health challenges to crew or vehicle, thus impacting the success of the mission. In Table 4, column 1 represents the potential failures of DSM parameters and the the hostile outer space while column 2 indicates the consequences endured from the system failures, possibly leading to the assumption of temporary or permanent loss of crew or mission. Finally, column 3 presents an immediate solution or action to system fatality in deep space.

In the description of our sensitivity analysis network illustration, we provide detailed example of potential system failures and radiation exposure as this is the ability to learn about emergencies in space travel. We assume that crew members for DSM have undergone extensive mission training, and a thorough inspection of DSS and other protocols have been properly done. During the launch phase, supposing an ascent of a launch vehicle experiences an initial system failure, redundant (recovery) system steps in with a call routed to the ground-control. If the issue remains unresolved, this could lead to mission-delayed or a quick return to Earth, to possible loss of vehicle, and eventually a loss of mission. On the other hand, the issue could easily be recovered for the mission to progress as scheduled, assuming it's a temporary problem. In the cruise to the Mars phase, other challenging issues could be encountered including control system failure which must be quickly investigated and solved upon deployment of redundant systems. Also, ground-control will be involved for instant system recovery, assuming light time-delays has not set in yet. If all these actions fail, the system is likely going to be unrecoverable resulting in a loss of mission.

During the Mars orbit, Mars surface, and Mars operation phase of the mission, system failures including the EDL component of GNC and prolonged communication loss will have a key noticeable impact on the success of the mission and the crew. This can be attributed to reduced crew concentration as a result of increased autonomy, reduced ground control supervision due to light-time-delays, and psychological issues from isolation. Emergency from GNC could be catastrophic, and without any access to easily return to Earth. Beyond the issues from system failures, extended exposure to space environment can have a dire effect on the well-being of the crew and consequently EVA activities. Exposure to space radiation remains one of the challenging aspects which must be considered during any space travel into deep space. Crew members' activities must be planned for minimum exposure in the space environment as prolonged exposure could result in serious illness. Our studies reveal that system failures are a major concern and must form a critical component of the AOS. The risk during space travel remains inevitable, however, there are policies that can be recommended including accidents case-studies to avoid failures of future human space explorations.

V. Conclusions and Future Study

In this studies, we present a deep space system health management, especially, we develop a network representation model formulation and approach of function allocation for studying the shift of previously managed mission control systems from the ground to onboard automation. We focus on the ground-control, onboard crew, and space vehicle autonomy operations to determine system ToA for every of the proposed DSS. We accomplish the function allocation through the use of allowable autonomy software technologies within a DSH across five stages of operations of autonomous control systems. In an attempt to expand on the effectiveness of the ToA, we develop an in-depth LoA under systems functional requirements and mission complexity leading to the introduction of numerical assignment for adjustable autonomy. In summary, our study provides the subsequent guidelines:

(*1*) The LoA model approach improves the distribution of system functions specifically between (*i*) ground-control autonomy and (*ii*) combined vehicle-crew autonomy with levels starting from $1 - 0$ (G authority) to $0 - 1$ (V$-$C autonomy). We evaluate the function allocation process on the idea that the vehicle and crew are onboard autonomy.

(*2*) We also demonstrate the ground-control authority that has control over the DSS with relatively slow reaction time and safe for ground-control capability. Vehicle-crew autonomy, on the other hand, has higher control over the DSS with fast response time and benefits from software technology.

(*3*) We divide the control systems into two groups. We illustrate and classify the ECLSS and CCCA systems as a stage-one system, and while the CHeCS, GNC, TMS, EPS, and EVA systems as a stage-two system with minimal intervention from both agents.

(*4*) Our findings show that the proposed model provides understanding and guidelines for agency-wide decision-makers on the health and strength of a deep space system.

Furthermore, we perform one parameter sensitivity analysis to assess the impact of the DSS failure parameters and space environment on the success of the mission under the proposed five phases of a long-term Mars mission: launch, cruise, orbit, surface, and operations using a graphical approach. We examine the following points and provide potential action for immediate recovery:

(*5*) Our findings show that the entry, descent, and landing part of the GNC and TMS are one of the system failure points, that may result in structural failure leading to the of LoV and LoC that subsequently results in LoM. We suggest that the agency must design space vehicles in such a way that they will survive and sustain on the Mars terrain during the EDL process and operation.

(*6*) On the other hand, the hostile space environment and isolation challenges possess less risk to LoM due to increased software technology. However, these challenges and changes possess other fatalities such as respiratory diseases and bone loss to crew-members leading to LoC. We suggest an onboard physician for a regular check-up.

(*7*) We also address other system failures such as the impact of the explosion of the vehicle oxygen leading to rapid depressurization in the habitat causing the LoV and potentially in some cases, the crew may escape the emergency.

(*8*) Finally, our model also assumes that temporary systems failure in DSS may recover with just-in-time redundancy options built into the systems. Therefore, NASA agency can meet its goals for future mission intervention through the choice of the best strategy for redundancy and other system capabilities.

For future study, we could expand the trade-offs among dynamic function allocations of control systems to incorporate diverse representations of data. Many of the system variables within the network model require further research to know the role of autonomy within the vehicle-crew interaction. The model formulation can also be applied to other function allocation problems in several domains and also to analyze accident-related case-studies for future allocation of systems functions. Finally, we could perform multiple parameter sensitivity analysis by dynamically varying all other parameters to have a will be of major importance to the agency.

Appendix

Appendix A

A. List of Figures

The network illustration of decision and analysis of function allocation and effects of deep space system failures on mission success are presented in Fig. 1 and Fig. 2, respectfully.

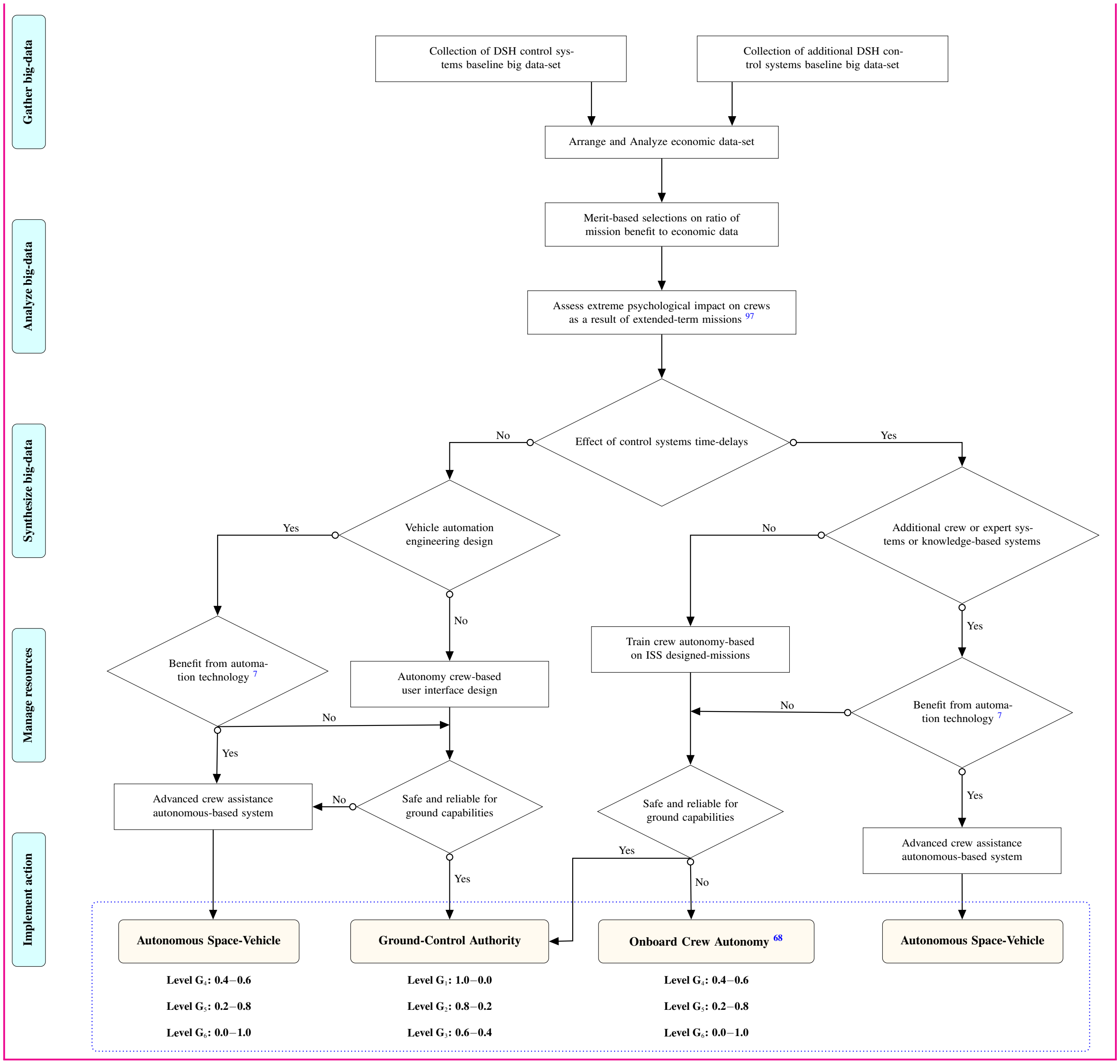

Figure 1. Network Representation of Decision and Analysis of Control Systems for Autonomous Operation

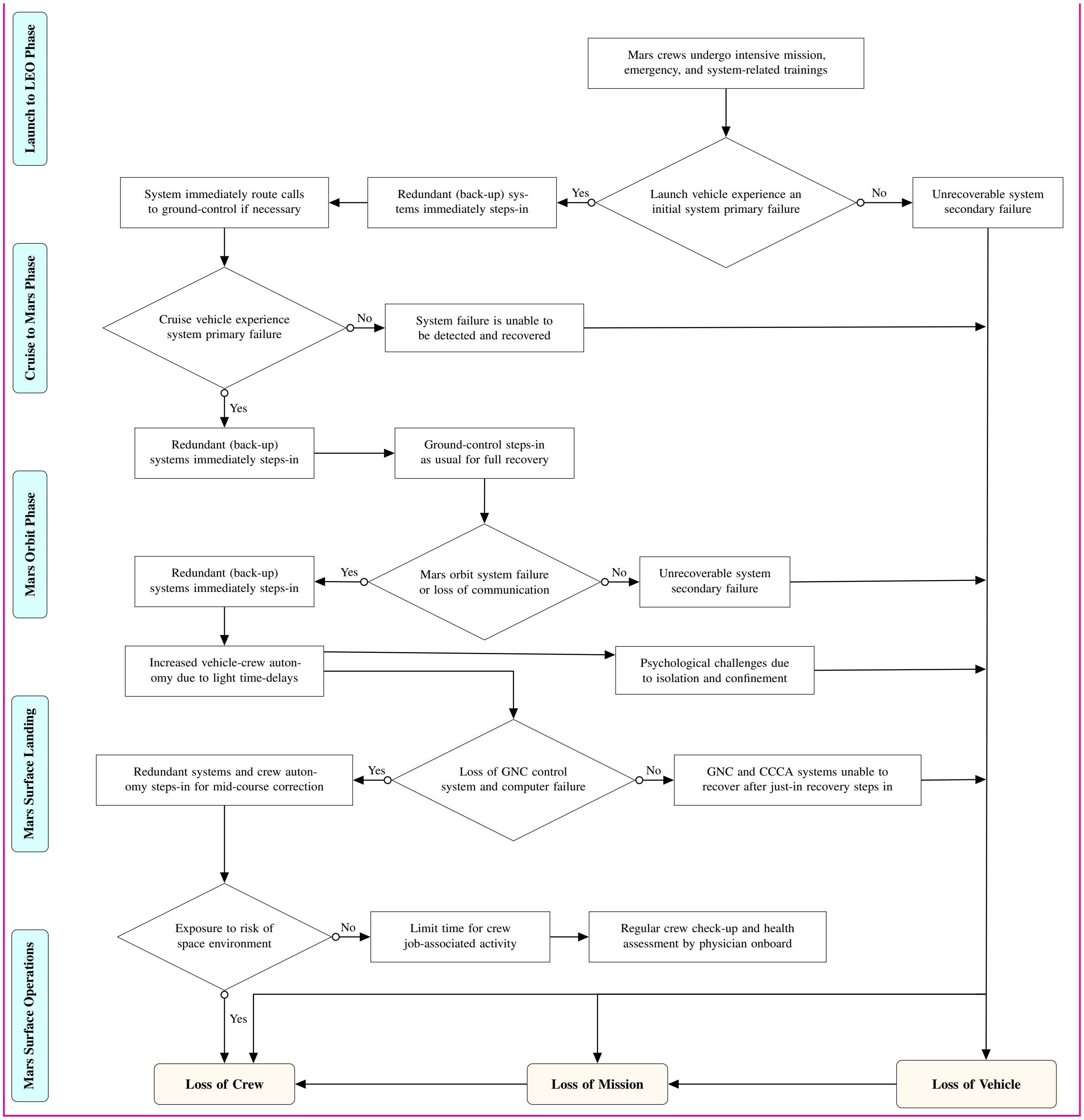

Figure 2. Network Representation of the Effects of Deep Space System Parameter Failure

Appendix B

B. List of Tables

The dynamic level of autonomy (authority) for deep space system, deep space habitat autonomous system design and capabilities, and deep space habitat single parameter sensitivity analysis are presented in Table 2, Table 3, and Table 4, respectfully.

Table 2. Dynamic Level of Autonomy (Authority) for Deep Space System[38,39]

Level of DSS Autonomy	Dynamic Allocation of Function					Description & Capability of ToA & LoA
	Gather	Analyze	Synthesize	Manage Resources	Implement Action	
Full Ground Authority[1] Level G_1: (1.0 – 0.0)	G	G	G	G	G	• Ground-control allocates function-specific to vehicle-crew autonomy over the gathering, analyzing, synthesizing system data, and managing resources stages, but it implements the system action.
Ground Allocation[2] Level G_2: (0.8 – 0.2)	G – V – C	G – V – C	G – V – C	G – V – C	G	• Ground-control allocates function-specific to vehicle-crew autonomy over the gathering, analyzing, synthesizing system data, and managing resources stages, but it implements the system action.
Ground Delegation[3] Level G_3: (0.6 – 0.4)	G – V – C	G – V – C	G – V – C	G – V – C	G – V – C	• Ground-control delegates controlled functions to vehicle-crew autonomy over the gathering, analyzing, synthesizing system data, managing resources, and implementing action stages.
Ground Supervision[4] Level G_4: (0.4 – 0.6)	G – V – C	G – V – C	G – V – C	G – V – C	G – V – C	• Ground-control supervises limited functions performed by vehicle-crew autonomy over the gathering, analyzing, synthesizing system data, managing resources, and implementing action stages.
Ground Engagement[5] Level G_5: (0.2 – 0.8)	G – V – C	G – V – C	G – V – C	G – V – C	V – C	• Vehicle-crew autonomy performs major functions with minor ground-control intervention including gathering, analyzing, synthesizing system data, managing resources, and implementing action.
Full Vehicle – Crew Autonomy[6] Level G_6: (0.0 – 1.0)	V – C	V – C	V – C	V – C	V – C	• Vehicle-crew executes all mission operations autonomously without ground-control intervention including gathering, analyzing, synthesizing system data, managing resources, and implementing action.

[1] Level G_1 – Ground-control with no vehicle-crew intervention. Numerical value assigned as follows: ground-control authority: 1.0 vehicle-crew autonomy: 0.0

[2] Level G_2 – Ground-control with assistance from vehicle-crew autonomy. Numerical value assigned as follows: ground-control authority: 0.8 vehicle-crew autonomy: 0.2

[3] Level G_3 – Ground-control with partial vehicle-crew autonomy. Numerical value assigned as follows: ground-control authority: 0.6 vehicle-crew autonomy: 0.4

[4] Level G_4 – Ground-control supervision with conditional vehicle-crew autonomy. Numerical value assigned as follows: ground-control authority: 0.4 vehicle-crew autonomy: 0.6

[5] Level G_5 – Ground engagement with high vehicle-crew autonomy. Numerical value assigned as follows: ground-control autonomy: 0.6 vehicle-crew authority: 0.8

[6] Level G_6 – Full vehicle-crew autonomy with zero ground-control intervention. Numerical value assigned as follows: ground-control authority: 0.0 vehicle-crew autonomy: 1.0

Table 3. Deep Space Habitat Autonomous Operation of System Design and Capabilities

DSH System	Major subsystems	Function	ToA[8]	LoA[9]	Potential Prime Areas for Autonomous Operation
ECLSS[1]	• Atmosphere revitalization • Atmospheric control and supply • Water recovery and management • Metabolic waste management • Thermal and humidity control • Fire detection and suppression	• Implement artificial ecosystem for regenerating life support.	Ground Authority	G_3 (0.6−0.4)	Onboard oxygen and water recovery, autonomous system trend analysis, and high MTTF.
CHeCS[2]	• Exercise countermeasures system • Health maintenance system • Food storage and management	• Permit long-duration onboard health equipment and food system to sustain the health, well-being, and performance of crews.	Crew Autonomy	G_5 (0.2−0.8)	Ability to have long-term food system and onboard medical human-robotic system.
GNC[3]	• Guidance • Navigation & Control	• Locates the present position and execute the desired location of the vehicle to its destination.	Vehicle Autonomy	G_5 (0.2−0.8)	Advanced autonomous navigational system capabilities (entry, descent, & landing).
CCCA[4]	• Flight operations • Ground support system • Communication & • Data management system	• Allows ground control to monitor and maintain DSH systems • Keeps down-and-uplink between ground control and crew activities	Ground, Vehicle, & Crew Autonomy	G_3 & G_4	Advanced onboard real-time data processing and return system.
TMS[5]	• Thermal protection • Thermal control • Cryogenic systems	• Maintains required temperatures within specific ranges.	Vehicle Autonomy	G_5 (0.2−0.8)	Effective TMS architecture
EPS[6]	• Energy storage • Power generation • Power management and distribution	• Provides electrical power for activities in space and during the space mission.	Vehicle Autonomy	G_5 (0.2−0.8)	Advanced EPS technologies, advanced long-term batteries.
EVA[7]	• Mobility • Science and exploration	• Activity and operations performed in a space environment.	Crew Autonomy	G_4 (0.4−0.6)	Teleoperations

[1] ECLSS – Environmental Control & Life Support System
[2] CHeCS – Crew Healthcare System
[3] GNC – Guidance, Navigation & Control
[4] CCCA – Command, Control, and Communication Architecture
[5] TMS – Thermal Management System
[6] EPS – Electrical Power System
[7] EVA – Extra Vehicular Activity
[8] ToA – Type of Autonomy (Authority)
[9] LoA – Level of Autonomy (Authority)

Table 4. Deep Space Habitat Single Parameter Sensitivity Analysis: The Effects of Deep Space System Failure[81,98]

Potential DSS Parameter Failure	Consequences to Mission	Description of Proposed Solution & Immediate Action
• Integral Components of CCCA System Failure With Ground-Control or Light Time-Delays	• Temporary loss of data management and system trend-analysis for crew, further leading to loss of mission. • Permanent loss of essential communication between ground and crew during EVA and crew activity resulting in loss of crew.	• Increased vehicle-crew autonomy and automated control systems with redundancy. • Allow human-robotic system onboard to take over ground-control mission assignment. • Trained crew-members with communication- and data management-related challenges during mission planning must quickly step in. • Crew can abort mission and return to Earth after prolonged period of no communication.
• Essential Parts of ECLSS System Failure	• Impact of carbon-dioxide removal, oxygen generation, and water processing cause loss of consciousness and major health problems in crew. • Prolonged ECLSS problem and challenges leading to potential loss of crew or mission.	• Back-up spare parts and just-in repair process should begin. • Advance FDIIR capability onboard to resolve issues can assist. • Autonomous solar panels onboard for uninterrupted electricity can be deployed. • NASA must invest in advance software technology for ECLSS.
• Failure Components in GNC System During Ascent, Descent, or Landing	• Temporary loss of navigation can cause interruption of mission or vehicle. • Permanent loss of orbit control will further lead to loss of crew or vehicle.	• Immediate return to Earth if possible. • Ground-control supervision will be needed to help switch to secondary systems. • Full autonomous onboard GNC back-up system integrated into the vehicle takes over.
• Integral Parts of TMS & EPS Systems Failure	• Will significantly impact EVA activity and research work. • Life-support and food systems will largely be affected, further impacting lives of crew and mission. • Operations and system management will gradually be failing and permanently stop.	• Advance FDIIR-inherent systems with just-in time parts for quick recovery. • Advance source of power for maintaining uninterrupted electric flow if it's power issue. • Loss of crew resulting to loss of mission success if challenges persists.
• Travel Time to Deep Space Long-Duration Deep Space Mission	• Psychological challenges due to living in isolation and confinement. • Impact crew well-being (sleep deprivation) and work performance.	• Crew can spend less time and reduce work-load in space environment. • Crew must receive regular psychological assessment in deep space. • Develop advance propulsion system to reduce travel time.
• Exposure to Risk of Space Environment	• Long periods in radiations lead to loss of bone density and fatal diseases. • Dust particles in deep space can cause human respiratory problems and contaminate spacesuits seals.	• Regular crew check-up and health assessment by physician onboard. • onboard system to provide accurate weather of deep space environment and advanced technological rays to counteract planetary radiations. • Time-frame for crew job-associated activity in space environment must be chosen with care.
• Failure of secondary components (back-up) of control systems during middle of mission	• Loss of mission if not successful • Loss of crew and vehicle if all attempts fail	• Attempt to contact ground-control in the middle of mission if possible or abort mission and return to Earth.

Acknowledgments

The information and recommendations expressed in this article are primarily those of the author and do not necessarily define any official position of NASA. The NASA Marshall Space Flight Center Aerospace Fellowship Program extensively supports the studies in this report. The author of this report is also pleased to acknowledge the extensive support of the Human Factors Branch at the MSFC especially those of Charles Dischinger, Tanya Andrews, Brooke Allen, and Mariea Dunn Brown, PhD.

References

[1]Katz, D. S. and Some, R. R., "NASA advances robotic space exploration," *Computer*, Vol. 36, No. 1, 2003, pp. 52–61.
[2]Angelopoulos, V., "The ARTEMIS mission," *The ARTEMIS mission*, Springer, 2010, pp. 3–25.
[3]Crotts, A., *The new Moon: Water, exploration, and future habitation*, Cambridge University Press, 2014.
[4]Pohlkamp, K. M., Mauldin, J., and Frank, J. D., "Demonstrating autonomous mission operations onboard the International Space Station,"

AIAA SPACE 2015 Conference and Exposition, 2015, p. 4646.

[5]Simon, M., Latorella, K., Martin, J., Cerro, J., Lepsch, R., Jefferies, S., Goodliff, K., Smitherman, D., McCleskey, C., and Stromgren, C., "NASA's advanced exploration systems Mars transit habitat refinement point of departure design," *2017 IEEE Aerospace Conference*, IEEE, 2017, pp. 1–34.

[6]Sipes, W. and Beven, G., "Human Cognitive Performance in Spaceflight and Analogue Environments," *Aviation, Space, and Environmental Medicine*, Vol. 85, 2014, pp. 1033–1048.

[7]Frost, C. R., "Challenges and opportunities for autonomous systems in space," https://www.nap.edu/read/13043/chapter/17, 2010, Accessed July 10, 2020.

[8]Smitherman, D. V. and Griffin, B. N., "Habitat concepts for deep space exploration," *AIAA Space 2014 Conference and Exposition*, 2014, p. 4477.

[9]Maurer, M., Christian Gerdes, J., Lenz, B., and Winner, H., *Autonomous driving: technical, legal and social aspects*, Springer Nature, 2016.

[10]Pacaux-Lemoine, M.-P., Simon, P., and Popieul, J.-C., "Human-machine cooperation principles to support driving automation systems design," *3rd International Symposium on Future Active Safety Technology Toward zero traffic accidents*, 2015, p. 9.

[11]Cheruvu, R., "Big Data Applications in Self-Driving Cars," *Retrieved July*, Vol. 18, 2015, pp. 2016.

[12]Gander, P. H., Mangie, J., van den Berg, M. J., Smith, A. A. T., Mulrine, H. M., and Signal, T. L., "Crew fatigue safety performance indicators for fatigue risk management systems," *Aviation, space, and environmental medicine*, Vol. 85, No. 2, 2014, pp. 139–147.

[13]Whitmire, A., "Fatigue Management in Spaceflight Operations," https://ntrs.nasa.gov/search.jsp?R=20110015940, 2011, Accessed July 25, 2020.

[14]Rungta, N., Brat, G., Clancey, W. J., Linde, C., Raimondi, F., Seah, C., and Shafto, M., "Aviation safety: modeling and analyzing complex interactions between humans and automated systems," *Proceedings of the 3rd international conference on application and theory of automation in command and control systems*, 2013, pp. 27–37.

[15]Board, S. S., Council, N. R., et al., *Recapturing a future for space exploration: life and physical sciences research for a new era*, National Academies Press, 2012.

[16]Salotti, J. M., "Simplified scenario for manned Mars missions," *Acta Astronautica*, Vol. 69, No. 5-6, 2011, pp. 266–279.

[17]Haidegger, T. and Benyo, Z., "Surgical robotic support for long duration space missions," *Acta Astronautica*, Vol. 63, No. 7-10, 2008, pp. 996–1005.

[18]Bhaskaran, S., "Autonomous Navigation for Deep Space Missions," https://trs.jpl.nasa.gov/bitstream/handle/2014/42469/12-1876.pdf?sequence=1, 2012, Accessed July 1, 2020.

[19]Yuen, J. H., *Deep space telecommunications systems engineering*, Springer Science & Business Media, 2013.

[20]Patel, V. P., Winton, D., and Ibarra, T. H., "A selected operational history of the internal thermal control system (ITCS) for international space station (ISS)," Tech. rep., SAE Technical Paper, 2004.

[21]Erickson, J. D., "Manned spacecraft automation and robotics," *Proceedings of the IEEE*, Vol. 75, No. 3, 1987, pp. 417–426.

[22]Burridge, R. and Graham, J., "Providing robotic assistance during extra-vehicular activity," *Mobile Robots XVI*, Vol. 4573, International Society for Optics and Photonics, 2002, pp. 22–33.

[23]Hall, J. L., "Columbia and Challenger: organizational failure at NASA," *Space Policy*, Vol. 19, No. 4, 2003, pp. 239–247.

[24]Norman, D. A., "Stages and levels in human-machine interaction," *International journal of man-machine studies*, Vol. 21, No. 4, 1984, pp. 365–375.

[25]Lin, P., Bekey, G., and Abney, K., "Autonomous military robotics: Risk, ethics, and design," Tech. rep., California Polytechnic State University, San Luis Obispo, 2008.

[26]Cunningham, M., Barriere, M., Bley, D., Cooper, S., Forester, J., Kolaczkowski, A., Luckas, W., Parry, G., Ramey-Smith, A., Thompson, C., et al., "A Technical Basis and Implementation Guidelines for a Technique for Human Event Analysis," 2000.

[27]Hirschbein, M. J., Collins, S., Jean, W. C., Chang, S. D., and Adler Jr, J. R., "Treatment of intraorbital lesions using the Accuray CyberKnife system," *Orbit*, Vol. 27, No. 2, 2008, pp. 97–105.

[28]Allaf, M., Patriciu, A., Mazilu, D., Kavoussi, L., and Stoianovici, D., "Overview and fundamentals of urologic robot-integrated systems," *Urologic Clinics*, Vol. 31, No. 4, 2004, pp. 671–682.

[29]Carlson, M. S., Drury, J. L., Desai, M., Kwak, H., and Yanco, H. A., "Identifying factors that influence trust in automated cars and medical diagnosis systems," *2014 AAAI Spring Symposium Series*, 2014, pp. 20–27.

[30]Johnston, M. D., Tran, D., Arroyo, B., Sorensen, S., Tay, P., Carruth, B., Coffman, A., and Wallace, M., "Automating Mid-and Long-Range Scheduling for NASA's Deep Space Network," *Space Operations: Experience, Mission Systems, and Advanced Concepts*, 2013, pp. 327.

[31]Fitts, P. M., "Human engineering for an effective air-navigation and traffic-control system," *Committee on Aviation Psychology*, 1951.

[32]Rouse, W. B. and Rouse, W. B., *Design for success: A human-centered approach to designing successful products and systems*, Vol. 2, Wiley-Interscience, 1991.

[33]Boy, G. A., *The handbook of human-machine interaction: a human-centered design approach*, CRC Press, 2017.

[34]Bailey, R. W., *Human performance engineering: A guide for system designers*, Prentice Hall Professional Technical Reference, 1982.

[35]Hollnagel, E. and Bye, A., "Principles for modelling function allocation," *International Journal of Human-Computer Studies*, Vol. 52, No. 2, 2000, pp. 253–265.

[36]Dearden, A., Harrison, M., and Wright, P., "Allocation of function: scenarios, context and the economics of effort," *International Journal of Human-Computer Studies*, Vol. 52, No. 2, 2000, pp. 289–318.

[37]Ockerman, J. and Pritchett, A., "A review and reappraisal of task guidance: Aiding workers in procedure following," *International Journal of Cognitive Ergonomics*, Vol. 4, No. 3, 2000, pp. 191–212.

[38]Beer, J., Fisk, A., and Rogers, W., "Toward a Framework for Levels of Robot Autonomy in Human-Robot Interaction," *Journal of Human-Robot Interaction*, Vol. 3, 2014, pp. 74.

[39]Hart, J. and Valasek, J., "Methodology for prototyping increased levels of automation for spacecraft rendezvous functions," *2007 AIAA Conference and Exhibit*, 2007, p. 2797.

[40]Dorais, G. and Kortenkamp, D., "Designing human-centered autonomous agents," *Pacific Rim International Conference on Artificial Intelligence*, Springer, 2000, pp. 321–324.

[41]Parsons, H. M., "Automation and the individual: Comprehensive and comparative views," *Human Factors*, Vol. 27, No. 1, 1985, pp. 99–111.

[42]Kaber, D. B. and Endsley, M. R., "The effects of level of automation and adaptive automation on human performance, situation awareness and workload in a dynamic control task," *Theoretical Issues in Ergonomics Science*, Vol. 5, No. 2, 2004, pp. 113–153.

[43]Chamseddine, A., Akhrif, O., Charland-Arcand, G., Gagnon, F., and Couillard, D., "Communication relay for multiground units with unmanned aerial vehicle using only signal strength and angle of arrival," *IEEE Transactions on Control Systems Technology*, Vol. 25, No. 1, 2016, pp. 286–293.

[44]Bogue, R., "The growing use of robots by the aerospace industry," *Industrial Robot: An International Journal*, 2018.

[45]Cullen, R., Rogers, W., and Fisk, A., "Human performance in a multiple-task environment: Effects of automation reliability on visual attention allocation," *Applied Ergonomics*, Vol. 44, 2013, pp. 962–968.

[46]Vaneman, w. K. and Triantis, K., "Designing resiliency into critical infrastructure systems," https://ndiastorage.blob.core.usgovcloudapi.net/ndia/2014/system/16881ThursTrack2Vaneman.pdf, 2014, Accessed July 5, 2020.

[47]Wu, S.-C. and Vera, A. H., "Supporting Crew Autonomy in Deep Space Exploration: Preliminary Onboard Capability Requirements and Proposed Research Questions," https://humansystems.arc.nasa.gov/publications/NASA_TM-2019_220345.pdf, 2019, Accessed June 26, 2020.

[48]Stuster, J. W., Adolf, J. A., Byrne, V. E., and Greene, M., "Human Exploration of Mars: Preliminary Lists of Crew Tasks," https://ntrs.nasa.gov/archive/nasa/casi.ntrs.nasa.gov/20190001401.pdf, 2018, Accessed June 26, 2020.

[49]Frank, J., Spirkovska, L., McCann, R., Wang, L., Pohlkamp, K., and Morin, L., "Autonomous mission operations," *2013 IEEE Aerospace Conference*, IEEE, 2013, pp. 1–20.

[50]Haddock, A. T. and Stetson, H. K., "Advancing Autonomous Operations for Deep Space Vehicles," *Space Operationss 2014 Conference*, 2014, p. 1782.

[51]Marquez, J. J., Adelstein, B. D., Ellis, S., Chang, M. L., and Howard, R., "Evaluation of human and automation/robotics integration needs for future human exploration missions," *2016 IEEE Aerospace Conference*, IEEE, 2016, pp. 1–9.

[52]Smitherman, D., Russell, T., Baysinger, M., Capizzo, P., Fabisinski, L., Griffin, B., Hornsby, L., Maples, D., and Miernik, J., "Deep space habitat configurations based on international space station systems," https://ntrs.nasa.gov/archive/nasa/casi.ntrs.nasa.gov/20120014530.pdf, 2012, Accessed June 26, 2020.

[53]Kennedy, K., "NASA Habitat Demonstration Unit Project-deep space habitat overview," *41st International Conference on Environmental Systems*, 2011, p. 5020.

[54]Onnasch, L., Wickens, C. D., Li, H., and Manzey, D., "Human performance consequences of stages and levels of automation: An integrated meta-analysis," *Human factors*, Vol. 56, No. 3, 2014, pp. 476–488.

[55]Kaber, D. B., "Issues in human–automation interaction modeling: Presumptive aspects of frameworks of types and levels of automation," *Journal of Cognitive Engineering and Decision Making*, Vol. 12, No. 1, 2018, pp. 7–24.

[56]Miller, D., Sun, A., and Ju, W., "Situation awareness with different levels of automation," *2014 IEEE International Conference on Systems, Man, and Cybernetics (SMC)*, IEEE, 2014, pp. 688–693.

[57]Rajan, K., Bernard, D., Dorais, G., Gamble, E., Kanefsky, B., Kurien, J., Millar, W., Muscettola, N., Nayak, P., Rouquette, N., et al., "Remote Agent: An autonomous control system for the new millennium," *Proceedings of the 14th European Conference on Artificial Intelligence*, IOS Press, 2000, pp. 726–730.

[58]Estlin, T., Castano, R., Gaines, D., Bornstein, B., Judd, M., Anderson, R. C., and Nesnas, I., "Supporting increased autonomy for a Mars Rover," https://www.researchgate.net/publication/255663139_Supporting_Increased_Autonomy_for_a_Mars_Rover, 2008, Accessed June 29, 2020.

[59]Fong, T., Allan, M., Bouyssounouse, X., Bualat, M. G., Deans, M., Edwards, L., Flückiger, L., Keely, L., Lee, S. Y., Lees, D., et al., "Robotic site survey at Haughton Crater," *Proceedings of the 9th International Symposium on Artificial Intelligence, Robotics and Automation in Space (iSAIRAS), Los Angeles, CA*, 01 2008, pp. 26–29.

[60]Reagan, M., Janoiko, B., Johnson, J., Chappell, S., and Abercromby, A., "NASA's analog missions: Driving exploration through innovative testing," *AIAA SPACE 2012 Conference & Exposition*, 2012, p. 5238.

[61]Prevot, T., Smith, N. M., Palmer, E., Callantine, T. J., Lee, P. U., Mercer, J., Martin, L., Brasil, C., and Cabrall, C., "An overview of current capabilities and research activities in the Airspace Operations Laboratory at NASA Ames Research Center," *14th AIAA Aviation Technology, Integration, and Operations Conference*, 2014, p. 2860.

[62]Pham, B., Maligo, A., and Lacroix, S., "Absolute map-based localization for a planetary rover," *12th Sympusium on Advanced Space Technologies and Automation in Robotics*, 2013, pp. 1–8.

[63]Bualat, M. G., Smith, T., Smith, E. E., Fong, T., and Wheeler, D., "Astrobee: A new tool for ISS operations," *2018 SpaceOps Conference*, 2018, p. 2517.

[64]Kearney, M., "The evolution of the mission control center," *Proceedings of the IEEE*, Vol. 75, No. 3, 1987, pp. 399–416.

[65]Rouff, C. A., Hinchey, M. G., Rash, J. L., Truszkowski, W., and Sterritt, R., "Towards autonomic management of NASA missions," *11th International Conference on Parallel and Distributed Systems*, Vol. 2, IEEE, 2005, pp. 473–477.

[66]Karidhal, R., Harinath, N., Robert, P., and Kesavaraju, V., "Mission automation and autonomy for the Mars Orbiter Mission," *Current Science*, 2015, pp. 1070–1075.

[67]Stetson, H. K., Frank, J. D., Haddock, A., Cornelius, R., Wang, L., and Garner, L., "AMO EXPRESS: A command and control experiment for crew autonomy," *AIAA SPACE 2015 Conference and Exposition*, 2015, p. 4448.

[68]Love, S. G. and Harvey, R. P., "Crew autonomy for deep space exploration: Lessons from the Antarctic Search for Meteorites," *Acta Astronautica*, Vol. 94, No. 1, 2014, pp. 83–92.

[69]Jones, H., "Methods and Costs to Achieve Ultra Reliable Life Support," *42nd International Conference on Environmental Systems*, 07 2012, p. 3618.

[70]Wertz, J., "Reducing Mission Cost, James Wertz and Wiley Larson Editors," *Space Technology Series, Space Technology Library*, 1996.

[71]Jones, H. W., "Estimating the life cycle cost of space systems," *45th International Conference on Environmental Systems*, 07 2015, pp. 1–13.

[72]Hayhurst, M., Eftekharzadeh, S., Wood, B., Jyothindran, V., Kellogg, R., Daniels, C., Jordin, L., and Sasamoto, W., "Mission Operations Cost Estimation Tool (MOCET): 2015 NASA Cost Symposium," https://www.nasa.gov/sites/default/files/files/20_MOCET_NASA_Cost_Symposium_Briefing_2015-08-21_tagged.pdf, 2015, Accessed July 12, 2020.

[73]Fiedler, E. R. and Harrison, A. A., "Psychosocial adaptation to a Mars mission," *Journal of Cosmology*, Vol. 12, 2010, pp. 3685–3693.

[74]Rucker, M. A. and Thompson, S., "Developing a habitat for long duration, deep space missions," https://ntrs.nasa.gov/archive/nasa/casi.ntrs.nasa.gov/20120008183.pdf, 2012, Accessed June 28, 2020.

[75]Love, S. G. and Reagan, M. L., "Delayed voice communication," *Acta Astronautica*, Vol. 91, 2013, pp. 89–95.

[76]Rader, S. N. and Reagan, M. L., "Human-in-the-loop operations over time delay: lessons learned," *43rd International conference on environmental systems*, 2013, p. 3520.

[77]Coderre, K., Edwards, C., Cichan, T., Richey, D., Shupe, N., Sabolish, D., Ramm, S., Perkes, B., Posey, J., Pratt, W., et al., "Concept of Operations for the Gateway," *Space Operations: Inspiring Humankind's Future*, Springer, 2019, pp. 63–82.

[78]Kanas, N., Saylor, S., Harris, M., Neylan, T., Boyd, J., Weiss, D. S., Baskin, P., Cook, C., and Marmar, C., "High versus low crewmember autonomy in space simulation environments," *On Orbit and Beyond*, Springer, 2013, pp. 231–244.

[79]Gushin, V., Shved, D., Ehmann, B., Balázs, L., and Komarevtsev, S., "Crew-MC interaction during communication delay in mars-500," *Proceedings of the International Astronautical Congress*, Vol. 1, 2012, pp. 11–17.

[80]Marquez, J. J., Hillenius, S., Kanefsky, B., Zheng, J., Deliz, I., and Reagan, M., "Increasing crew autonomy for long duration exploration missions: self-scheduling," *2017 IEEE Aerospace Conference*, IEEE, 2017, pp. 1–10.

[81]Manzey, D., "Human missions to Mars: new psychological challenges and research issues," *Acta Astronautica*, Vol. 55, No. 3-9, 2004, pp. 781–790.

[82]Tripathi, R., Wilson, J., Cucinotta, F., Nealy, J., Clowdsley, M., and Kim, M.-H., "Deep Space Mission Radiation Shielding Optimization," *Age*, Vol. 25, No. 35, 2001, pp. 45.

[83]Taylor, E. R., "Human deep-space travel and colonization: technical issues," *New Space*, Vol. 3, No. 3, 2015, pp. 154–164.

[84]Dempsey, D. L. and Barshi, I., "Towards Crew-Centered, Mission-Oriented Space Flight Training," https://ntrs.nasa.gov/archive/nasa/casi.ntrs.nasa.gov/20190018054.pdf, 2020, Access July 25, 2020.

[85]Crawford, J. M. and Weisbin, C. R., "Autonomous Operations for the Crew Exploration Vehicle-Trade Study Design Considerations," *AIP Conference Proceedings*, American Institute of Physics, 2005, pp. 1145–1152.

[86]Anderson, M. S., Macatangay, A. V., McKinley, M. K., Sargusingh, M. J., Shaw, L. A., Perry, J. L., Schneider, W. F., Toomarian, N., and Gatens, R. L., "NASA environmental control and life support technology development and maturation for exploration: 2018 to 2019 overview," *48th International Conference on Environmental Systems*, 07 2019, p. 297.

[87]Ezell, L. N., *NASA Historical Data Book*, Vol. 3, NASA, 1988.

[88]Dewberry, B. S., Carnes, J. R., Lukefahr, B. D., Rogers, J. S., Rochowiak, D. M., Mckee, J. W., and Benson, B. L., "The ECLSS advanced automation project evolution and technology assessment," https://ntrs.nasa.gov/archive/nasa/casi.ntrs.nasa.gov/19930018534.pdf, 1990, Access July 7, 2020.

[89]Bonasso, R. P., Kortenkamp, D., and Thronesbery, C., "Intelligent control of a water-recovery system: three years in the trenches," *AI magazine*, Vol. 24, No. 1, 2003, pp. 19–19.

[90]Stapleton, T., Heldmann, M., Schneider, S., O'Neill, J., Samplatsky, D., White, K., and Corallo, R., "Environmental control and life support for deep space travel," *48th International Conference on Environmental Systems*, 2018, p. 343.

[91]Fisher, F., Chien, S., Paal, L., Law, E., Golshan, N., and Stockett, M., "An automated deep space communications station," *1998 IEEE Aerospace Conference Proceedings*, Vol. 3, IEEE, 1998, pp. 153–162.

[92]Stewart, D. F., "Medical care delivery in the US space program," https://ntrs.nasa.gov/archive/nasa/casi.ntrs.nasa.gov/19940007334.pdf, 1991, Accessed July 2, 2020.

[93]Beauchamp, P. M., Cutts, J. A., Quadrelli, M., Wood, L., Riedel, J. E., McHenry, M. C., Aung, M., Volpe, R., and Cangahuala, L., "Guidance Navigation and Control Technology Assessment for Future Planetary Science Missions," *AIAA SPACE 2013 Conference and Exposition*, 2013, p. 5411.

[94]Jones, H. and Ewert, M., "Ultra reliable closed loop life support for long space missions," *40th International Conference on Environmental Systems*, 2010, p. 6286.

[95]Stromgren, C., Terry, M., Mattfeld, B., Cirillo, W., Goodliff, K. E., Shyface, H. R., and Maxwell, A. J., "Assessment of Maintainability for Future Human Asteroid and Mars Missions," *AIAA SPACE 2013 Conference and Exposition*, 2013, p. 5328.

[96]Adler, M., Wright, M., Campbell, C., Clark, I., Engelund, W., and Rivellini, T., "Draft entry, descent, and landing roadmap," *National Aeronautics and Space Administration*, 2010.

[97]Kaber, D. B. and Endsley, M. R., "The combined effect of level of automation and adaptive automation on human performance with complex, dynamic control systems," *Proceedings of the Human Factors and Ergonomics Society Annual Meeting*, SAGE Publications, 1997, pp. 205–209.

[98]Linck, E., Crane, K. W., Zuckerman, B. L., Corbin, B. A., Myers, R. M., Williams, S. R., Carioscia, S. A., Garcia, R., and Lal, B., *Evaluation of a Human Mission to Mars by 2033*, IDA Science and Technology Policy Institute, 2019.

A Hybrid Consensus Technique for SVGS Camera Sensor in Multi-Agent Robotic Guidance, Navigation & Control

Hadi Fekrmandi *
Research Associate, NASA Marshall Space Flight Center, Martin Rd SW, Huntsville, AL 35808, USA

A distributed state estimation technique is developed for the smartphone video guidance system (SVGS) in multi-agent autonomous robotic mission applications. The SVGS camera sensor was implemented as primary measurement model to obtain relative pose estimation from other agents of interest and the landmarks. The proposed technique is based on the hybrid of the Metropolis-Hasting Markov Chains (MHMC) and the Iterative Covariance Intersection (ICI) methods. The MHMC method computes the consensus over information updates, and the ICI method reaches consensus over the priors. The Robot Operating System (ROS) and Gazebo physics simulator were used to conduct a study on the hybrid consensus technique for SVGS system as camera sensor. The results for a scenario involving a group of three robots operating with a consensus algorithm, shows that the proposed method for the SVGS system improves the measurement accuracy, robot perception, network reliability, and computational efficiency.

I. Introduction

The application of autonomous robots in space exploration missions reduces safety concerns and extends the possible mission distance since return transportation is not necessary [1]. In addition, the use of robots decreases complexities and costs because there is no need for on-board life-support systems as robots can withstand and operate in harsh conditions, such as extreme temperature, pressure, and radiation, where humans cannot survive [2]. The National Aeronautics and Space Administration (NASA) Artemis program aims to land on the moon by the year 2024 to evaluate establishing a sustainable exploration by 2028 [3]. NASA is investigating robotic solutions with new mobility concepts in operating scenarios that require access to extreme terrain categories. This may include fluffy/high-porosity regolith expected at the lunar poles, steep, rugged slopes, and uneven terrain with possible ice content at the bottom of deep-shadowed craters, subterranean features, such as caves, lava tubes, and pits [4]. Due to multiple challenges in space domain, teleoperation becomes inefficient or infeasible, and robot autonomy is identified as a key aspect for future planetary exploration missions. Therefore, in addition to developing the novel mobility concepts, these technologies must be presented as an integrated part of a robotic platform with a significant level of sensing and autonomy [5]. Furthermore, these must be feasible for operation in the targeted environments, i.e., mechanisms resistant to fault/failures due to lunar dust, extreme temperatures, and power restrictions in shadowed lunar craters. To advance technologies needed to live on and explore the Moon, NASA's Space Technology Mission Directorate (STMD) established the Lunar Surface Innovation Initiative (LSII) [6].

In an effort to succeed in lunar human habitation, NASA is investigating many novel robotic technologies with advanced autonomy to help understand, explore, map, and potentially harvest resources on the lunar surface. The plan portrays the overall vision of autonomous systems with four signature capabilities to support the Artemis mission [7]. Among many others, these systems include an ice-mining drill for the lunar surface, a system that could unpack and assemble into an antenna or small habitat on its own, or small robots that can autonomously explore the lunar surface as a team [8]. One such solution in development is the Volatiles Investigating Polar Exploration Rover (VIPER) [9]. It will prospect water-ice on human scales, creating water resource maps of the polar regions [10]. However, deploying complex and large robotic systems creates many single points of failure for a mission [11]. Robotic swarm rover explorers are being investigated by NASA where they envision multiple low cost, small robots for lunar exploration [12]. Alternative mobility explorers are being considered including low cost, high-reliability hopping/cartwheeling/tumbling platforms referred to as CubeBot [13, 14]. This is a different kind of robot designed to overcome the challenges of traversing small bodies in space by hopping and tumbling on the surface instead of rolling on wheels [15]. NASA's Jet Propulsion Laboratory in southern California is developing the robotic scouts, Cooperative Autonomous Distributed Robotic Explorers (CADRE) [16], designing them to explore as a group and collect data in hard-to-reach places such as craters and caves on the Moon. The CADRE project is developing a network of shoe-box-sized mobile robots that could

*Assistant Professor of Mechanical Engineering, South Dakota School of Mines & Technology, Email: Hadi.Fekrmandi@Gmail.com

enable future autonomous robotic exploration of the Moon, Mars, and beyond. The CADRE robots are the latest version of NASA's Autonomous Pop-Up Flat-Folding Explorer Robot (A-PUFFER) technology [17]. Each robot contains an onboard computer with a wireless radio for communication and a stereo camera, which has multiple lenses and image sensors for sensing the front-facing environment and capturing 3D imagery.
Any coordinated autonomous or semi-autonomous operation in challenging environments requires up-to-date localization estimates for all robots in a team and a joint map to operate on. While centralized visual based navigation and control of a swarm are suitable for certain space applications, for example, small satellites in an on-orbit servicing mission [18], the uncertainties of communication at scientifically interesting places such as craters, canyons, or caves require a decentralized approach. This demands developing a resilient yet computationally efficient distributed framework, with robustness to communication failure characteristics for reliable operation in cooperative autonomous missions. To tackle these challenges, this study aims developing a framework for localization and state estimation of heterogeneous multi-robot teams. The product can be used for autonomous guidance navigation and control, for example, in exploration scenarios where the robots have to travel through previously unknown, unstructured, or rough terrains. The results offer a reliable, scalable, and computationally efficient solution for swarm of autonomous robots who are using relative pose-based estimation, such as, the Smartphone Video Guidance System (SVGS) [19], to enable operating in an environment without external methods for localization, such as global navigation satellite systems.

II. Methods and Modeling

A. Problem Formulation

We assume a team of N mobile robots explore a 2D environment, $\mathbf{E} \subset \mathbf{R}^2$, in search of an unknown number of targets. At each time step, robot i collects a set of local relative measurements, given by

$$\mathbf{z}_{\mathrm{i}}(k) = \left[\mathbf{z}_{\mathrm{i,j_1}}(k), \mathbf{z}_{\mathrm{i,j_2}}(k), \cdots, \mathbf{z}_{\mathrm{i,j}_{\mathcal{N}_\mathrm{i}}}(k)\right]^T \tag{1}$$

where $\mathcal{N}_i$ indicates the number of measurements by robot i at time step k. In an environment with noise and clutter, the number of measurements varies over time. Moreover, in multi-robot systems, the relative motion of robots may cause targets to enter or leave the sensor's field of view (FOV). The state of robot i at time k is $\mathbf{x}_{\mathrm{i}}(k)$. The team seeks to estimate the probability distribution over the vector containing the states of the targets (i.e. robot agents and waypoints) given by

$$\mathbf{x}(k) = [\mathbf{x}_1(k), \mathbf{x}_2(k), \cdots, \mathbf{x}_{\mathrm{N}}(k)]^T \tag{2}$$

where each $\mathbf{x}_{\mathrm{N}}(k) \in \mathbf{E}$. Note that this set encodes both the number of targets (i.e., the cardinality of the set $|X_t|$) and the state of each target.

B. Robot Motion Model

We consider agents with a constant-velocity target tracking model also known as a nearly-constant-velocity model [20]. In this model, presented in equation 4, accelerations along x and y directions are modeled as small white noise since agents don't communicate their control inputs. The robot's state dynamics are given by:

$$\mathbf{x}_{\mathrm{i}}(k+1) = \boldsymbol{F}\left(\omega_i(k)\right)\mathbf{x}_{\mathrm{i}}(k) + \boldsymbol{Q}\boldsymbol{w}_i(k) \tag{3a}$$

$$\boldsymbol{\omega}_i(k+1) = \boldsymbol{\omega}_i(k) + \Delta u_i(k) \tag{3b}$$

where $\boldsymbol{w}_i(k) \sim \mathcal{N}(0, \boldsymbol{\sigma^2} I)$ represents additive white noise used to model unknown perturbations. $\omega_i(k)$ is the turn rate, by the robot i at time step k, and matrices F and Q are given by:

$$\boldsymbol{F} = \begin{bmatrix} 1 & 0 & \frac{sin(\omega\Delta)}{\omega} & -\frac{1-cos(\omega\Delta)}{\omega} \\ 0 & 1 & \frac{sin(\omega\Delta)}{\omega} & \frac{1-cos(\omega\Delta)}{\omega} \\ 0 & 0 & cos(\omega\Delta) & sin(\omega\Delta) \\ 0 & 0 & sin(\omega\Delta) & cos(\omega\Delta) \end{bmatrix} \tag{4}$$

$$
\boldsymbol{Q} = \begin{bmatrix} \frac{\Delta^2}{2} & 0 \\ 0 & \frac{\Delta^2}{2} \\ \Delta & 0 \\ 0 & \Delta \end{bmatrix} \tag{5}
$$

C. Observation Model

Vision-based pose estimation is the determination of transformation between the measured data coordinate frame and the model data coordinate frame [21]. Pose estimation algorithms developed in literature are typically categorized as either analytical or iterative [22]. The SVGS sensor processes the input image with an iterative algorithm to obtain a 6-dimensional pose estimation of the target (shown in Fig 1). To develop a stochastic model of SVGS camera sensor, assume each robot's SVGS camera sensor produces noisy observations that are a function of the state of the robot. In our research, the SVGS sensor is modeled as a function of the target robot's state $\mathbf{x}_\text{i}(k)$, the vision sensor noise $\boldsymbol{v}_i(k)$, and the observer robot's position. The measurement model of the i^th robot is:

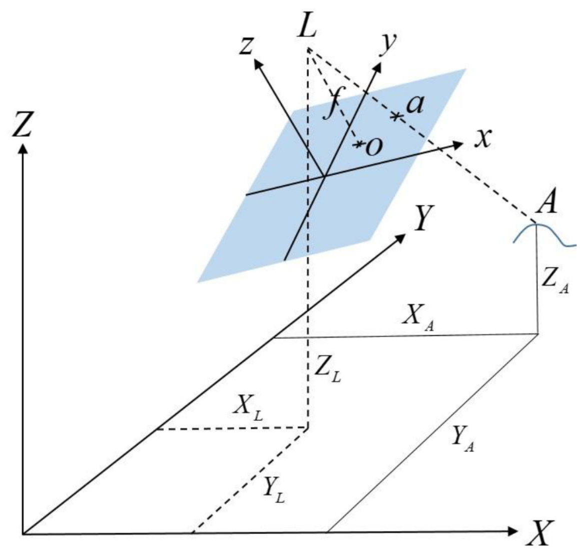

Figure 1 Object and camera frames illustrating projection of a point on a 2D image from 3D space used in SVGS sensors [23]

$$
\mathbf{z}_\text{i}(k+1) = \boldsymbol{H}_i(k)\mathbf{x}_\text{i}(k) + \boldsymbol{v}_i(k) \tag{6a}
$$

$$
\boldsymbol{v}_i(k) \sim \mathcal{N}(0, \boldsymbol{R}_i(k)) \tag{6b}
$$

where $\boldsymbol{v}_i(k) \sim \mathcal{N}(0, \boldsymbol{\sigma}^2 I)$ represents additive noise used to model uncertainty in SVGS pose estimations. In this research, agents play the role of observers and make noisy observations. The SVGS sensor measures the relative pose of agents and target waypoints in the sensor's FOV. We assume each agent's SVGS sensor produces noisy observations that have magnitudes that are linearly dependent on the range and the type of the target according to interpolation obtained from Table 1:

The observation Jacobian $\boldsymbol{H}$ converts a state to an expected observation $z = \boldsymbol{H}(\boldsymbol{X})$. The measurement of the target from the camera is the target transformed from the global coordinate system into the local coordinate system of the camera. The state estimated by each agent is in the global coordinate system, so each measurement must be computed from these global coordinates:

$$
z = R^T p_\text{camera} - R^T p_\text{target} \tag{7}
$$

Table 1 Range-based 3σ error values for SVGS LED targets [24]

Operating Range (meters)	*Operating Range (meters)*	*Z Range (meters)*	*X, Y Lateral (meters)*	*Roll (degrees)*	*Pitch/Yaw (degrees)*
SRT short range targets	0-3	0.02	0.02	0.3	0.3
	3-10	0.13	0.16	2.0	2.0
	10-20	0.23	0.5	2.0	2.0
	20-30	0.47	1.5	3.0	3.0
LRT long range targets	30-50	0.5	0.03	0.3	1.5
	50-100	1.7	0.06	0.5	2.5
	100-300	15.0	0.2	1.5	7.0

where R is the camera's global transformation matrix, and the points p_{target} and p_{camera} are the global positions of the target and camera, respectively. Then, $\boldsymbol{H}$ can be computed as

$$\boldsymbol{H}_{i,j} = \begin{bmatrix} \frac{\partial \mathbf{z}_{\mathrm{i,j}}(k)}{\partial x_i[0]} & \frac{\partial \mathbf{z}_{\mathrm{i,j}}(k)}{\partial x_i[1]} & \frac{\partial \mathbf{z}_{\mathrm{i,j}}(k)}{\partial x_i[2]} \end{bmatrix}. \tag{8}$$

D. Network Topology

Assume there are N homogeneous agents represented with nodes of a graph. Graph methods have proven reliable in multi-agent networks as an approach for addressing the challenges of designing, analyzing, and controlling multi-agent robotic systems [25]. These agents can communicate with each other under a communication network with time-varying connectivity. At each time step, the network topology is $G(k) = \langle \mathcal{V}(k), \mathcal{E}(k) \rangle$ where $\mathcal{V}(k)$ and $\mathcal{E}(k)$ are the set of graph nodes and edges, respectively. If agents i and j are connected at time step k, they are considered as $(i, j) \in G(K)$, which means they can communicate directly. The node corresponding to the i^{th} agent is denoted by v_i. Neighbors of node v_i are defined as the union of the node v_i and

$$\mathcal{N}_i = \{v_i\} \cup \{v_j \in \mathcal{V} | (i, j) \in \mathcal{E}\}. \tag{9}$$

Also, $|\mathcal{N}_i|$ is the cardinality of $\mathcal{N}_i$.

Each agent has a sensory system and an embedded processor on-board. Sensors make observations every Δt seconds. Processors and the network are fast enough to handle calculations based on messages passing among agents every δt seconds. We assume that $\delta t \ll \Delta t$. We also assume that the communication channel that agents exchange their information over the is free of delay or error.

III. Distributed Filtering

A. Recursive Estimation

An estimator computes the posterior probability of a random dynamic process $\mathbf{x}(k)$ conditioned on a sequence of measurements $\{\mathbf{z}(0), \ldots, \mathbf{z}(k)\}$, where $\mathbf{z}(k)$ denotes the observation vector at the time-step k. When the Gaussian distribution is chosen to represent the probability distribution of $\mathbf{x}(k)$, the tuple $(\hat{\boldsymbol{x}}(k), \boldsymbol{P}_x(k))$ uniquely identify the posterior that we are trying to compute, where $\hat{\boldsymbol{x}}(k)$ and $\boldsymbol{P}_x(k)$ are the mean vector and the covariance matrix corresponding to the Guassian posterior at step k.

A recursive estimator such as the Kalman Filter (KF) performs the posterior calculation recursively based on the current observation, $\mathbf{z}(k)$, the estimation at the previous step, $(\hat{\boldsymbol{x}}(k-1), \boldsymbol{P}_x(k-1))$, and the motion and observation models. Following the common terminology of the recursive estimation, we denote the predicted and estimated mean and covariance at time k by $(\hat{\boldsymbol{x}}^-(k), \boldsymbol{P}_x^-(k))$ and $(\hat{\boldsymbol{x}}(k), \boldsymbol{P}_x(k))$.

B. Information Filter

The Information Filter (IF) is a transformed version of the Kalman Filter (KF), returning an identical output, yet having a simpler update step. Since this update step will be run multiple times in a consensus algorithm, it is the filter of choice for this application. When using the IF, the state vector and covariance matrix are not quite the same as the KF, but can be easily transformed as follows:

$$\boldsymbol{y}(k) = \boldsymbol{P}_{\mathbf{x}}^{-1}(k)\mathbf{x}(k), \tag{10a}$$

$$\boldsymbol{Y}(k) = \boldsymbol{P}_{\mathbf{x}}^{-1}(k). \tag{10b}$$

These variables are called the information vector and information matrix, respectively. The prediction step of the IF can then be written as

$$\boldsymbol{M}(k) = (\boldsymbol{F}^{-1})^T \boldsymbol{Y}(k-1)\boldsymbol{F}^{-1}, \tag{11a}$$

$$\boldsymbol{P}_{\mathbf{x}}(k) = \boldsymbol{M}(k) + \boldsymbol{Q}(k)^{-1}, \tag{11b}$$

$$\boldsymbol{Y}^{-}(k) = \boldsymbol{M}(k) - \boldsymbol{M}(k)\boldsymbol{P}_{\mathbf{x}}(k)^{-1}\boldsymbol{M}(k), \tag{11c}$$

$$\boldsymbol{y}^{-}(k) = \boldsymbol{Y}^{-}(k)\boldsymbol{F}\boldsymbol{Y}(k-1)\boldsymbol{y}(k-1). \tag{11d}$$

If a central node can obtain the information from all agents, then the IF update step is as simple as summing the information from all measurements and adding that to the IF prediction. The information update ($\delta \boldsymbol{I}(k)$ and δi) contains the information from all measurements:

$$\delta \boldsymbol{I}_j(k) = \boldsymbol{H}_j{}^T \boldsymbol{R}_j{}^{-1} \boldsymbol{H}_j \tag{12a}$$

$$\delta i_j = \boldsymbol{H}_j{}^T \boldsymbol{R}_j{}^{-1} \mathbf{z}_{\mathrm{j}}(k), \tag{12b}$$

and the priors ($\boldsymbol{y}^{-}(k)$ and $\boldsymbol{Y}^{-}$) contain the state information from previous estimations:

$$\boldsymbol{y}(k) = \boldsymbol{y}^{-}(k) + \textstyle\sum_{j=1}^{N} \delta i_j(k) \tag{13a}$$

$$\boldsymbol{Y}(k) = \boldsymbol{Y}^{-}(k) + \textstyle\sum_{j=1}^{N} \delta \boldsymbol{I}_j(k). \tag{13b}$$

The information filter functions well when the information update and prior contain data from all agents. When this is not the case, and agents can only communicate with their neighbors, a different method is required. This new method should take in only the priors and information updates of neighboring agents and, with time, converge to the same estimations as the information filter. To create a distributed information filter estimation, agents need to compute a consensus over both the information updates as well as the priors. Here, a hybrid consensus method is used, using two separate methods, first introduced in [26].

Each time the consensus is run, the first step is to compute the priors ($\boldsymbol{y}^{-}(k)$ and $\boldsymbol{Y}^{-}(k)$) and the information updates ($\delta \boldsymbol{I}(k)$ and $\delta i(k)$). Then, for each consensus step l, agents send and receive the priors and information updates with all connected agents. The process then runs one step of the Metropolis-Hasting Markov Chains (MHMC) and ICI methods.

C. Consensus Over Information Updates (MHMC)

The distributed averaging sensor fusion [27] uses MHMC to reach a consensus over the uncorrelated information (the measurements). One can use the message passing protocol of the form $\boldsymbol{x}^{l+1} = \sum_{j=1}^{|\mathcal{N}^l|} \gamma_{ij}^l x_j^l$ to calculate the average of the values on the graph nodes in which $d_i^l = |\overline{\mathcal{N}}_i^l|$ is the degree of the node v_i, i.e. the number of agents that it is connected to, and

$$\gamma_{ij}^l = \begin{cases} \frac{1}{1+\max\{d_i^l, d_j^l\}} & \text{if } (i,j) \in \mathcal{E}^l, \\ 1 - \sum\limits_{(i,m)\in\mathcal{E}^l} \gamma_{im}^l & \text{if } i = j, \\ 0 & \text{otherwise.} \end{cases} \tag{14}$$

MHMC works excellently for uncorrelated information but cannot be used with the priors, since they may contain correlated information.

D. Consensus Over Priors (ICI)

For the correlated information buried in the priors, a different estimation method is needed. In this case, that is Iterative Covariance Intersection (ICI). As discussed in [28], in the ICI method at initial iteration $l = 0$, for each agent, the local estimate, $[\boldsymbol{Y}_j{}^0, \boldsymbol{y}_j{}^0]$ is assigned as:

$$\boldsymbol{y}_j{}^0 = \boldsymbol{y}_j{}^0 + \delta i_j{}^0, \quad \boldsymbol{Y}_j{}^0 = \boldsymbol{Y}_j{}^0 + \delta i_j{}^0. \tag{15}$$

Then, for each iteration afterward, solve for ζ^* such that

$$\begin{aligned} \zeta^* &= \underset{\zeta}{\operatorname{argmin}}\ \mathcal{J}\left([\textstyle\sum_{j \in \mathcal{N}_i^l} \zeta_j y_j{}^l]^{-1}\right), \\ s.t. \quad &\textstyle\sum_{j=1}^{|\mathcal{N}_i^l|} \zeta_j = 1, \quad \forall j \quad \zeta_j \geq 0, \end{aligned} \tag{16}$$

where $\mathcal{J}(\cdot)$ is an optimization objective function (here, the determinant is used).

IV. Results

In this study, a hybrid consensus method was implemented for the autonomous multi-agent systems in a collaborative guidance, navigation, and control mission. Each agent has their own limited local views of the world and a limited communication range while their overall task is to fuse their relative measurements from landmarks and agents to generate a perception of entire world. One can easily see the improvement of the state estimation when MHMC and ICI is implemented. Our results indicated that using the proposed decentralized method, agents were able to obtain state estimation of the entire swarm. Moreover, upon losing the direct measurement, they were able to quickly obtain a consensus on all the estimations. Agents are allowed to communicate with each other, and the network is fully connected. SVGS camera sensors obtained a relative state estimate from the visual markers in their point of view. First, the distributed state estimation for global state estimation was implemented using the hybrid of MHMC and ICI methods. Figure 2 shows the start of the simulation with 3 agents and 4 visual markers. The agents start at x = 0 m, and the visual markers are in two groups of 20m apart pairs located at distances of 5m and 25m from the origin, respectively. The agents accelerate to 0.2 m/s and travel past the visual markers, estimating both the state of the visual markers and each of the three agents. Since the camera on each agent cannot see the other agents traveling beside them, the only method for estimating the state of the other agents is communication of the information matrix and information vectors. In this study the agents are using the hybrid consensus algorithm to fuse each agent's estimation of the swarm where the pose estimation of the landmarks are obtained by a simulated SVGS system using the data from Table 1.

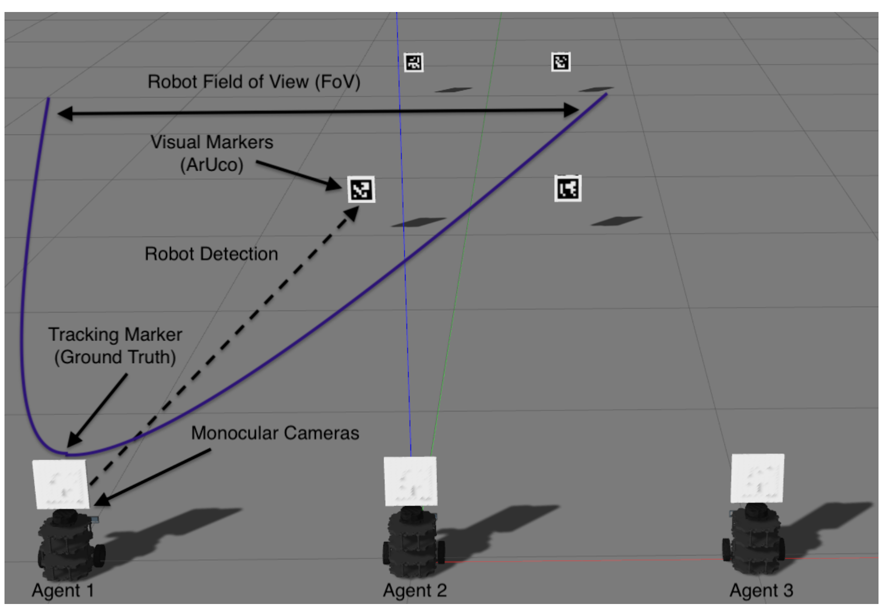

Figure 2 Sketch of multi-robot simulation setup with the SVGS targets represented by ArUco markers

The current report presents results from a similar scenario reported in [29] where three agents each traversed to two individual waypoints and the numerical simulation of agent trajectories was implemented in the OpenMAS toolbox [30]. The new results are obtained by the hybrid consensus method implemented in a Robot Operating System (ROS) framework with Gazebo physics simulator. The methods and modeling described in the previous sections are used to achieve this. Each agent measures their relative pose to its waypoints and the pose's of the visual markers in its FOV. In Figure 2, the first agent, shown with the black trail in the following results, attempts to travel to its two waypoints at (10, 20) and (30, 5). The second and the third agents, shown with the red and yellow trails have waypoints at (10, 0) and (30, 0) for the second and (10, -20) and (30, -5) for the third agent. All three agents start at (0, 5), (0, 0), and (0, -5) with legends used as agent-0, Agent-1, and agent-2 in the results, respectively. The measurements made by each agent have errors obtained by linearizing the error versus range data for the SVGS sensor in Table 1 into an equation for error versus distance. Then, a covariance matrix is created at each time step using the distance to the measured object. The motion model error is modeled as 5% of the traveled distance in a time step, $Q = 0.05dt\sqrt{dx^2 + dy^2}$. The controller for these agents assigns a forward velocity of 0.2 m/s, and sustains a settling time of 0.5 s for adjustments. The state publisher node computes and publishes the state for each turtle bot with a frequency of 50 Hz. With this starting point, three simulations were launched. In the first, agents had an infinite communication radius, shown in Figure 3. They sent data between themselves and conducted 20 consensus steps at each time step. In the second simulation, agents had their communication range reduced to 25m, so information was not fully shared between them, shown in Figure 4. Instead, *agent-0* could communicate with *agent-1* but not *agent-2*. Therefore, *agent-1* acted as a middle man and shared *agent-2*'s pose information with *agent-0*. In the third simulation, agents' communication radius was set to 15m, so the communication network was disconnected for a large period of simulation time, and agents estimate others solely by their own model of other agents in the group, shown in Figure 5. Figures 3a, 4a, and 5a are plots of the true trajectory and estimations made by the other agents. Figures 3b, 4b, and 5b are plots of the difference between each estimate and the true trajectory. This error is plotted as distance ($\sqrt{x^2 + y^2}$), where the solid line is showing the mean and the error bars represent the standard deviation. Due to the symmetry in design for scenario of the simulations in this study, the estimations and errors of *agent-2* and *Agent-3* are similar to those of *agent-1*, so they are not shown here.

(a) Estimated position

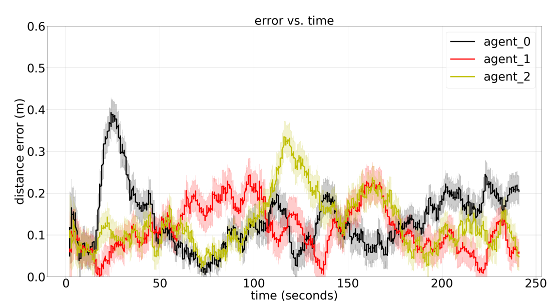

(b) Error in estimation

Figure 3 ***agent-0* estimating itself, *agent-1*, and *agent-2* in a fully connected network**

V. Discussion

In Figure 3, *agent-0* has full communication with *agent-1* and *agent-2*. This results in a small estimation error, shown in Figure 3b. In contrast to Figure 5, where there is a section of no communication with *agent-1* and *agent-2*, *agent-0* attempts to estimate the path taken by *agent-2*, but, due to its large distance (40m away when *agent-2* hits the first waypoint and turns sharply up and to the right), the error is large. The hybrid consensus method is used in Figure 4. *agent-0*'s long-distance measurement can be combined with *agent-1*'s short-range measurement, resulting in a significantly improved estimation. This can also be seen in the error plots themselves, where the mean error from *agent-0* in Figure 5b goes off the figure, while the error with the consensus in Figure 4b peaks at 0.65m. The consensus enabled results have lower maximum error than non-consensus results and have slightly lower error over the whole simulation.

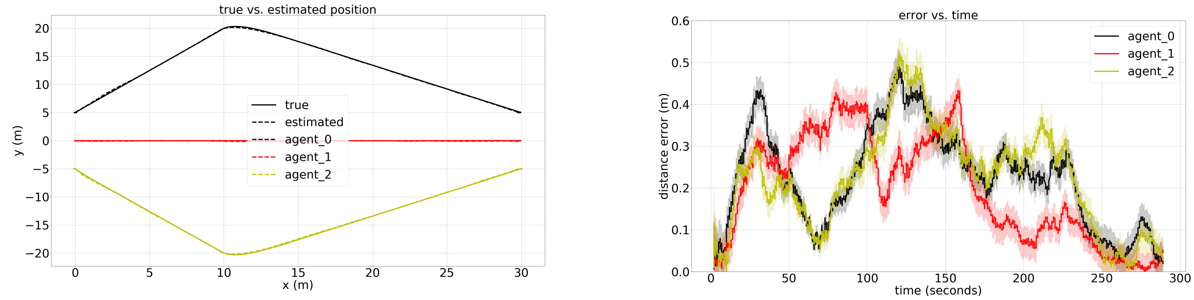

(a) Estimated position **(b) Error in estimation**

Figure 4 ***agent-0*** **estimating itself,** ***agent-1*****, and** ***agent-2*** **in a connected network**

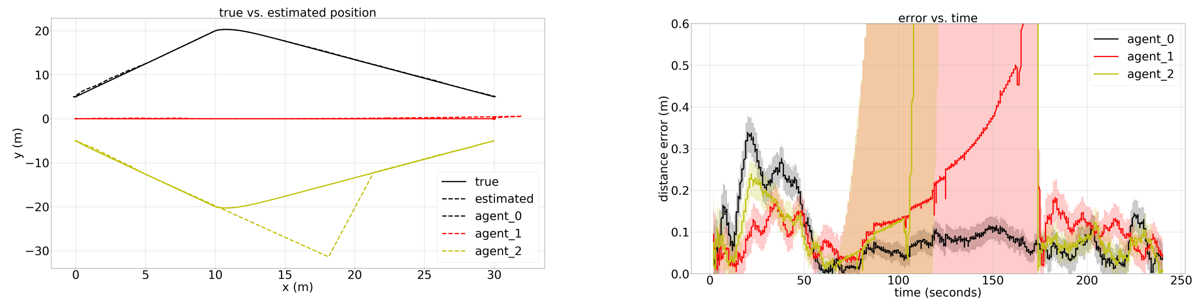

(a) Estimated position **(b) Error in estimation**

Figure 5 ***agent-0*** **estimating itself,** ***agent-1*****, and** ***agent-2*** **in a partially connected network**

VI. Conclusion and Future Work

The results of this study introduces the hybrid consensus technique for the SVGS camera sensor deployment in robotic and autonomous systems. The method is developed and implemented in ROS platform and the performance is validated by the computational resources of turtle bot robots in Gazebo physics simulator. While the results of the current preliminary study are promising, further study is required for experimental validation and verification of the proposed method in real-time robotic with constraints similar to those encountered in the space. Specifically, the unique challenges of lunar surface environment, with limited power, measurement and communication range of the multi-agent robots, and challenging lunar dust need further investigation of SVGS camera sensor in the swarm robots that are engaging the hybrid distributed framework for state estimation. The Gazebo world simulator for the lunar surface developed by NASA Ames center can be utilized for creation of more realistic world models to evaluate robot perceptions against the actual camera poses and agents ability in tracking SVGS targets in the presence of persisting lunar dust. While the measurements were obtained from a single type of pose estimation sensor, the technique is suitable for heterogeneous agents operating in a decentralized and dynamic communication network. The computational efficiency of the proposed hybrid consensus technique along with the better performance compared to competing algorithms are important characteristics that motivate pursuing future studies to extent the current decentralized framework of the hybrid consensus method to the Internet of Federated Things (IFoT) based swarm of intelligent robots. Recent advances in decentralized machine learning approaches known as Federated Learning offer a significant opportunity for capitalizing the improvements observed for state estimation of swarm robots in this study for multiple autonomous robot mission objectives of the Artemis program including exploration, mapping and service activities.

Funding Source

This work is supported by the aerospace fellowship program at NASA George Marshall Space Flight Center's control systems design and analysis branch.

Acknowledgments

I would like to express appreciation to Frank Six for supporting and inspiring space research at the NASA MSFC. Author greatly acknowledges Brooke Graham, coordinator of the summer fellowship program and John Rakoczy, director of the MSFC division EV-41. I greatly acknowledge Edward Duke, director of the South Dakota EPSCoR program and the NASA SD Space Grant Consortium. I sincerely appreciate Kyle Houchin and Amanda Messegee, students at Advanced Intelligent Mechatronics laboratory of South Dakota Mines for their contributions towards preparation and submission of the report.

References

[1] Roman, M. C., Vetcha, N., Fiske, M., Carrato, P., and Leucht, K. W., "Overview of NASA's Break the Ice Lunar Challenge," *ASCEND 2020*, 2020, p. 4196.

[2] Li, T. Y., and Liu, S., "Enabling commercial autonomous robotic space explorers," *IEEE Potentials*, Vol. 39, No. 1, 2019, pp. 29–36.

[3] Seedhouse, E. L., and Llanos, P., "Science and exploration of the moon enabled by surface telerobotics," *Journal of Space Safety Engineering*, 2021.

[4] National Aeronautics and Space Administration, "NASA's BIG Idea Challenge," , 2018.

[5] Austin, A., Sherwood, B., Elliott, J., Colaprete, A., Zacny, K., Metzger, P., Sims, M., Schmitt, H., Magnus, S., Fong, T., et al., "Robotic lunar surface operations 2," *Acta Astronautica*, Vol. 176, 2020, pp. 424–437.

[6] Clinton, R. G., Edmunson, J. E., Fiske, M., Effinger, M. R., Jensen, E., and Ballard, J., "Overview of NASA's Moon-to-Mars Planetary Autonomous Construction Technology (MMPACT)," *ASCEND 2021*, 2021, p. 4072.

[7] Wedler, A., Schuster, M. J., Müller, M. G., Vodermayer, B., Meyer, L., Giubilato, R., Vayugundla, M., Smisek, M., Dömel, A., Steidle, F., et al., "German Aerospace Center's advanced robotic technology for future lunar scientific missions," *Philosophical Transactions of the Royal Society A*, Vol. 379, No. 2188, 2021, p. 20190574.

[8] Vickers, J., "Lunar Infrastructure and Surface Operations," *Annual ISS Research and Development Conference (ISSRDC)*, 2019.

[9] Vaughan, R., "VIPER–Volatiles Investigating Polar Exploration Rover: Mission Overview," *International Small Satellite Conference*, ????

[10] Fong, T., "Volatiles Investigating Polar Exploration Rover," *Australasian Conference on Robotics and Automation*, 2020.

[11] Toupet, O., Biesiadecki, J., Rankin, A., Steffy, A., Meirion-Griffith, G., Levine, D., Schadegg, M., and Maimone, M., "Terrain-adaptive wheel speed control on the Curiosity Mars rover: Algorithm and flight results," *Journal of Field Robotics*, Vol. 37, No. 5, 2020, pp. 699–728.

[12] Wilcox, B. H., Nayar, H., and Howe, A. S., "Autonomous Mars ISRU robotic excavation: characteristics and performance targets," *2019 IEEE Aerospace Conference*, IEEE, 2019, pp. 1–19.

[13] Shen, H.-X., Zhang, T.-J., Li, Z., and Li, H.-N., "Multiple-hopping trajectories near a rotating asteroid," *Astrophysics and Space Science*, Vol. 362, No. 3, 2017, p. 45.

[14] Fagan, A. F., "Annual Meeting of the Lunar Exploration Analysis Group (LEAG): August 31–September 2, 2021, Virtual," , 2021.

[15] Cheng, B., Yu, Y., and Baoyin, H., "Numerical simulations of the controlled motion of a hopping asteroid lander on the regolith surface," *Monthly Notices of the Royal Astronomical Society*, Vol. 485, No. 3, 2019, pp. 3088–3096.

[16] Vitug, E., "Cooperative Autonomous Distributed Robotic Explorers (CADRE)," , ???? URL `https://www.nasa.gov/directorates/spacetech/game_changing_development/projects/CADRE`.

[17] Karras, J. T., Fuller, C., Carpenter, K. C., Buscicchio, A., and Parcheta, C. E., "Puffer: pop-up flat folding explorer robot," 2018.

[18] Sabatini, M., Volpe, R., and Palmerini, G., "Centralized visual based navigation and control of a swarm of satellites for on-orbit servicing," *Acta Astronautica*, Vol. 171, 2020, pp. 323–334.

[19] Becker, C., Howard, R., and Rakoczy, J., "Smartphone Video Guidance Sensor for Small Satellites," *27th Annual AIAA/USU Conference on Small Satellites*, AIAA, Logan, UT, 2013.

[20] Li, X. R., and Jilkov, V. P., "Survey of maneuvering target tracking. Part I. Dynamic models," *IEEE Transactions on aerospace and electronic systems*, Vol. 39, No. 4, 2003, pp. 1333–1364.

[21] Fekrmandi, H., Rutan-Bedard, S., Frye, A., and Hoover, R., "Validation of vision-based state estimation for localization of agents and swarm formation," *USCToMM Symposium on Mechanical Systems and Robotics*, Springer, 2020, pp. 216–224.

[22] Maidi, M., Didier, J.-Y., Ababsa, F., and Mallem, M., "A performance study for camera pose estimation using visual marker based tracking," *Machine Vision and Applications*, Vol. 21, No. 3, 2010, pp. 365–376.

[23] Hariri, N., Gutierrez, H., Rakoczy, J., Howard, R., and Bertaska, I., "Performance Characterization of the Smartphone Video Guidance Sensor as Vision-Based Positioning System," *Sensors*, Vol. 20, No. 18, 2020, p. 5299.

[24] Carter, C., "Robust Targeting for the Smartphone Video Guidance Sensor (SVGS)," 2017.

[25] Mesbahi, M., and Egerstedt, M., *Graph theoretic methods in multiagent networks*, Vol. 33, Princeton University Press, 2010.

[26] Tamjidi, A., Chakravorty, S., and Shell, D., "Unifying consensus and covariance intersection for decentralized state estimation," *2016 IEEE/RSJ International Conference on Intelligent Robots and Systems (IROS)*, IEEE, 2016, pp. 125–130.

[27] Xiao, L., Boyd, S., and Lall, S., "A scheme for robust distributed sensor fusion based on average consensus," *IPSN 2005. Fourth International Symposium on Information Processing in Sensor Networks, 2005.*, IEEE, 2005, pp. 63–70.

[28] Chen, H., Wang, J., Wang, C., Shan, J., and Xin, M., "Distributed diffusion unscented Kalman filtering based on covariance intersection with intermittent measurements," *Automatica*, Vol. 132, 2021, p. 109769.

[29] Fekrmandi, H., Frye, A. J., Tamjidi, A., Rakoczy, J., and Hoover, R. C., "Autonomous Multi-agent Systems Using SVGS Camera Sensor for Lunar Surface Mobility Applications," *2021 IEEE Aerospace Conference (50100)*, IEEE, 2021, pp. 1–10.

[30] Douthwaite, J. A., and Mihaylova, L. S., "OpenMAS - An open-source multi-agent simulator for MatLab," , Mar. 2020. https://doi.org/10.15131/shef.data.11954418.v1, URL https://figshare.shef.ac.uk/articles/OpenMAS_-_An_open-source_multi-agent_simulator_for_systems_with_complex_and_arbitrary_decision_mechanics_and_dynamic_behaviour/11954418/1.

A Compact Model to Predict Heat Leak Into a Cryogenic Storage Tank

Michael S June
Christian Brothers University, Memphis, TN, 38104, USA

Ali Hedayat
Marshall Space Flight Center, Huntsville, Al, 35808, USA

Joseph C. Leahy
Marshall Space Flight Center, Huntsville, Al, 35808, USA

Stored cryogens are essential for long-term space travel. Due to external heating from the environment, ullage temperature increases, and with it, pressure. When ullage pressure reaches a specified limit, strategies including venting must be employed to reduce the pressure. A compact model is proposed, which uses an Ohm's Law analogy, with thermal resistances to build 1-D resistor networks which predict heat leak into a cryogen tank. Results showed good correlation to data sets. For one data set where 20.2 W was measured, the model predicted 20 W.

I. Nomenclature

A	=	area
h	=	convective coefficient
I	=	electrical current
k	=	conductive coefficient
L	=	length of conductive path for conductive resistance calculation
Q	=	heat power
R_{cond}	=	conductive thermal resistance
R_{conv}	=	convective thermal resistance
T_w	=	temperature of warm radiating body
T_c	=	temperature of cold radiating body
ϵ_w	=	emissivity of warm radiating body
ϵ_c	=	emissivity of cold radiating body
σ	=	Stefan-Boltzman constant

II. Introduction

For long-term space travel, cryogens need to be stored over long periods of time. The cryogens are stored at a low enough temperature, typically in the low 20s K, that heat tends to flow from the environment into the cryogen. The dominant mode of heat transfer in the absence of significant gaseous atmosphere for convection, is radiative heat transfer. The cryogen will reach saturation temperature and pressure due to the heat leak, and the gaseous phase in the headspace (Ullage) will continue to increase in temperature and pressure until the physical limits of the container are reached. This necessitates strategies for maintaining the pressure at or below the safe structural limit of the vessel

(Ref. 1, 2) Ultimately, the pressure must be released by venting, which causes loss of the cryogen and possibly an unwanted thrust vector (Ref. 2).

To understand and quantify the need for pressure reducing strategies including venting, the heat leak into the container must be calculated. This paper describes a thermal resistance calculation based on the Ohms Law Analogy, to predict heat leak.

III. Procedure

A 1-dimensional resistor network was modeled for the ullage, and another was modeled for the liquid. Hydrogen was assumed to be the cryogen. The tank and insulating strategy was based on the Multipurpose Hydrogen Test Bed (MHTB), which is located at the Marshall Space Flight Center (MSFC), in Alabama. (Ref. 1, 2, 3). The resistance model was validated and compared to data from the MHTB, including measured heat leak. The insulation strategy on the MHTB is typical, and well characterized, such that it was expected to yield a model that would be applicable to other tank geometries, fill levels and cryogens by simply changing the surface area used in the calculations and thermodynamic properties, notably saturation conditions at the safe pressure limit of the vessel.

Thermal resistance is typically derived from Newton's Law of cooling for convection, and from Fourrier's Law for conduction. Radiative heat transfer is often lumped in with convection as an observed phenomena and part of the measured convective coefficient, h.

$$R_{cond} = \frac{L}{kA} \quad (1)$$

$$R_{conv} = \frac{1}{hA} \quad (2)$$

There is simple convection from the ullage and liquid to the walls of the tank, and simple conduction through the tank walls and SOFI layer.

Since radiative heat transfer is the dominant form of heat transfer from the environment to the tank, a radiation-only resistance was calculated based on the MacIntosh model of radiative heat transfer through the MLI Layers (Ref. 4).

$$\frac{Q}{A} = \frac{\sigma\{T_W^4 - T_C^4\}}{\left(\frac{1}{\epsilon_W} + \frac{1}{\epsilon_C} - 1\right)} \quad (3)$$

To get thermal resistance in units of C/W or K/W, Eq. (3) was rearranged as follows.

$$R_{rad} = \frac{T_W - T_C}{\left[\frac{\sigma\{T_W^4 - T_C^4\}}{\left(\frac{1}{\epsilon_W} + \frac{1}{\epsilon_C} - 1\right)}\right]} A \quad (4)$$

While not considered in this study, a simple convective model, such as MacIntosh's model for convection under various pressures, can be used in a similar way to evaluate ground hold conditions (explain?).

Ohm's law states

$$V = IR \quad (5)$$

Ohm's law analogy for thermal systems replaces Voltage with Temperature, Current with Heat Energy, and Electrical Resistance becomes Thermal Resistance. Voltage is analogous to temperature since they are both gradients driving the phenomena and behave similarly in a circuit analysis. Current is analogous to Heat Energy since they are both treated like a flow across a gradient, and behave similarly in a circuit analysis. As well, both Electrical Resistance and Thermal Resistance will act similarly in a circuit analysis. Herein lies the convenience of Ohm's Law Analogy. A simple resistor network can be built with thermal resistances and analyzed like an electrical resistor network. Thermal resistances acting in series are added like series resistors in an electrical circuit and parallel thermal resistances add like parallel electrical resistances. Once all the individual resistances are obtained, they are simply added to yield one equivalent resistance. If the thermal gradient from the liquid or the ullage and the outermost boundary temperature, say the skin temperature of the enclosure, one can quickly find the heat leak. A spreadsheet or MatLab program can be made which calculates the heat leak for various tank sizes, SOFI insulation thicknesses, and with added complexity, varying numbers of MLI layers with varying distances between the layers.

$$\Delta T = QR \quad (6)$$

IV. Results

Figure 1 shows temperatures at the interfaces, determined from the thermal resistances calculated. Since the calculation of the MLI layer resistances relied heavily on empirical data, it was expected that the calculated temperatures would be in good agreement with measured data. The calculation for thermal resistance across the SOFI layer relied on an assumption of thermal conductivity from (Ref. 1) of 0.000866 W/mK.
It is apparent from the calculated temperatures that this is not a good assumption for this particular test. Figure 2 shows the same data against an adjusted assumption of 0.002 W/mK for the thermal conductivity of the SOFI layer.

With the adjustment to the thermal conductivity of the SOFI layer, the model returned the result of 18.8W for a dataset with a measured heat leak of 18.7W. Once again, a good result was expected since the model was based on the actual temperatures measured across the layers.

The model was then compared to results obtained and reported in previous papers (Ref. 3) and shown in Table 1.

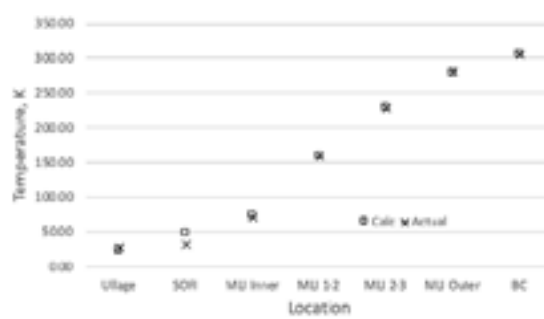

Figure 1. Calculated and actual temperatures assuming k=0.000866 W/mK

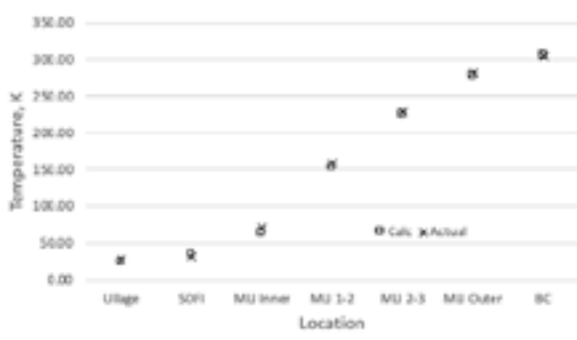

Figure 2. Calculated and actual temperatures assuming k=0.002 W/mK

Fill Level %	Reported Heat Leak W	Calculated with current model W
90	20.2	20.0
50	18.7	19.3
25	18.8	18.8

Table 1. Comparison of model to previous reported data.

The previous comparisons are with data considered to be low heat leak conditions. Other data, referred to as high heat leak data, includes heat leak through penetrations in the insulation, such as through the legs of the tank. The legs had active heat guards which were de-activated during the high heat leak tests. A simple calculation based on Newton's law of cooling, knowing the temperature gradient along the legs, the geometry and the material properties, suggests that the heat leak through the legs alone could be as high as 20 W. Figure 3 shows data from a high heat leak test compared to the model. The heat leak through the legs and other penetrations can be accounted for by increasing the thermal conductivity of the SOFI layer. This is since it is a 1-D model with all heat leak through the SOFI layer lumped together and spread over the layer. This value can be found by iterating the value until the predicted temperatures match the actual temperatures within a reasonable error. For the data in Figure 3, the value of the thermal conductivity of the SOFI layer that gave the best results was k=0.004 W/mK. This resulted in a calculated heat leak of 59.2 W, as compared to a measured value of 54.7 W.

Table 2 compares model results to previously reported high heat leak data (Ref. 3).

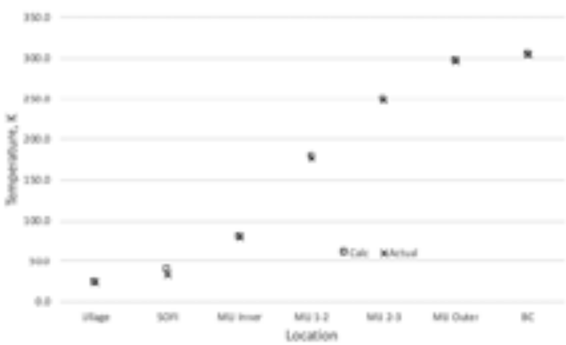

Figure 3. Calculated and actual temperatures for high heat leak and k=0.004 W/mK

Fill Level %	Reported Heat Leak W	Calculated with current model W
90	54.1	59.2
50	54.0	60.9
25	--	60.4

Table 2. Comparison of model to previous reported data.

V. Conclusion

Use of thermal resistance modeling and Ohm's law analogy yielded a good compact model, that can be applied to cryogenic tanks with similar insulation strategies. A model was created to account for more ideal conditions of a well thermally isolated tank. The model can be adjusted to account for heat leak through penetrations and support structures. The ideal model can also be used and the result added to calculated heat leak for specific structures, such as legs, knowing the thermal gradient and geometry of the legs.

The key to the accuracy of these models was comparison to and adjustment based on real data.

Acknowledgments

The author would like to thank Marshal Space Flight Center, University of Alabama, Huntsville, the National Space Grant Foundation, and the Marshall Faculty Fellowship Program. As well, thank you to Ali Hedayat and Joseph Leahy for their support and technical contributions. Finally, thank you to Frank Six, and Brooke Graham for pulling together this great experience under tough circumstances.

References

Periodicals

[1] Martin, J. J., Hastings, L., "Large-Scale Liquid Hydrogen Testing of a Variable Density Multilayer Insulation With a Foam Substrate," *NASA/TM-2001-211089*, Marshall Space Flight Center, Al, June 2001.

[2] Hastings, L.J., Flachbart, R.H., Martin, J. J., Hedayat, A., Fazah, M., Lak, T., Nguyen, H., Bailey, J.W., "Spray Bar Zero-Gravity Vent System for On-Orbit Liquid Hydrogen Storage", *NASA/TM-2003-212926*, Marshall Space Flight Center, Al, October 2003.

[3] Hastings, L., Hedayat, A., Brown, T.M., "Analytical Modeling and Test Correlation of Variable Density Multilayer Insulation for Cryogenic Storage", *NASA/TM-2004-213175*, Marshall Space Flight Center, Al, May 2004..

[4] McIntosh, G.E., "Layer by Layer MLI Calculation Using a Separated Mode Equation", *Advances in Cryogenic Engineering*, Plenum Press, New York, Vol. 39B, 1994, p. 1683

NASA-Torch-MSU
LiDAR-IMU Navigation and Mapping System

Seongjai Kim*
Mississippi State University, Mississippi State, MS, 39762.

Michael R. Zanetti†
NASA Marshall Space Flight Center

From the summer, 2020, we are developing a real-time system for navigation and mapping using range, velocity, and angular rotation measurements gathered from a LiDAR and an IMU. The problem is challenging because errors in estimations can introduce drift that increases proportional to the square of the acquisition time and in turn cause mis-registration of the resulting LiDAR point cloud. This report summarizes what we have developed during the summer and what research activities we are planning in near future.

Nomenclature

GPS	=	Global Positioning System
IMU	=	Inertial Measurement Unit
LiDAR	=	Light Detection and Ranging
SLAM	=	Simultaneous Localization and Mapping
ICP	=	Iterative Closest Point
RANSAC	=	RANdom SAmple Consensus
ΔT	=	the time period for SLAM
A_x, A_y, A_z	=	Raw acceleration measurements along each axis (m/s^2)
G_x, G_y, G_z	=	Raw gyroscope measurements about each axis (rad/s), usually referred to as p, q, and r, respectively.
ϕ, θ, ψ	=	Euler angles in radian (roll-pitch-yaw)
$\widehat{\phi}$, $\widehat{\theta}$, $\widehat{\psi}$	=	Estimates of the Euler angles

I. Introduction

Light Detection and Ranging (LiDAR) has become an established procedure for obtaining dense point cloud data sets over geospatial regions [1–4]; its mapping is an approved method of producing accurate information about the shape and surface characteristics of the Earth [5–8]. Data acquisition using LiDAR has several advantages over most other techniques, particularly due to its higher resolution, centimeter accuracy, and ground detection in forested terrain [9].

LiDAR is an active remote sensing system; light is emitted from a rapidly firing laser. This light travels to the ground and reflects off of things like foliage and buildings. The reflected light energy then returns to the LiDAR sensor. A LiDAR system measures the time which takes for the emitted light to travel to the ground and back. That time is used to calculate the distance traveled, which is then converted to a local relative point $\mathbf{x}_r = (x_r, y_r, z_r)$ using the orientation of the emitted light provided by inertial measurement units (IMUs) [9]. In order to accomplish the global positioning of the point on the Earth, the local relative point is then simply added to the source location of the light energy $\mathbf{x}_s = (x_s, y_s, z_s)$, which can be identified by the global positioning system (GPS). That is, the resulting position is

$$\mathbf{x} = \mathbf{x}_s + \mathbf{x}_r. \tag{1}$$

For navigation and terrain mapping of LiDAR-based sensing systems, an essential component is the onboard IMU which produces position and orientation information of the system. However IMUs typically suffer from the

*Department of Mathematics and Statistics, 175 President's Circle. skim@math.msstate.edu
†Martin Rd SW, Huntsville, AL 35808. michael.r.zanetti@nasa.gov

accumulated error due to bias/drift in measurements and typically their measurements must be continually corrected by using positional tracking systems like Global Positioning System (GPS). But GPS is not available everywhere and it will be degraded or fully unavailable in and near buildings, tunnels, and mines on the Earth; off the Earth it is not available at all. Furthermore, supplemental measurements available from magnetometers on the Earth may not be available on other bodies in the Solar System.

In this project, we are investigating a powerful real-time LiDAR-IMU integrated software system, where the IMU accelerometer and gyroscope data are combined with LiDAR data, for autonomous navigation and mapping in GPS-denied environments. This algorithm is applied to the Kinematic Navigation and Cartography Knapsack (KNaCK) LiDAR system which has been developed at NASA MSFC.

The major reason why autonomous navigation is challenging is because many algorithms that currently exist take quite a bit of time to process an optimal trajectory, using a limited onboard computing power [10]. Thus the major issue for real-time LiDAR-IMU navigation systems in GPS-denied environments is to develop innovative powerful computational algorithms. We have developed new computational algorithms, parts of which are modifications of existing methods, while others are completely new. Here we summarize what we have developed.

The report is organized as follows. In the next section, we present a brief review on IMU measurements, data handling, and the iterative closest point (ICP) algorithm, as preliminaries. Section III describes the real-time navigation and mapping system we have been developing. In Section IV, we collect some planned research activities to be accomplished by the end of the year. A new dataset has been made using a crane (Run18); we will work on the dataset for both localization and small object detection.

II. Preliminaries

This section briefly describe IMU measurements, data handling, and the iterative closest point algorithm.

A. IMU measurements

Accelerometer: The accelerometer measures accelerations around each axis with respect to the body frame. When the accelerometer is at rest, it measures gravitational acceleration only. Therefore, by resolving forces using simple trigonometry, we can calculate an estimate of pitch and roll from the raw accelerometer data:

$$\begin{aligned} \widehat{\phi}_{Acc} &= \arctan\Big(\frac{A_y}{\sqrt{A_x^2 + A_z^2}}\Big), \\ \widehat{\theta}_{Acc} &= \arctan\Big(\frac{A_x}{\sqrt{A_y^2 + A_z^2}}\Big). \end{aligned} \tag{2}$$

Gyroscope: The gyroscope measures angular rates of change around each axis with respect to the body frame. Assuming that the measurements are noise-free, we could integrate these raw measurements to get the angular position relative to the body frame. Unfortunately, as usual we will have a fair amount of noise present in the gyroscope readings. If we were to integrate this, we would add up all the small errors due to noise, which then would accumulate over time and become large in magnitude, which is known as *gyroscopic drift*.

As aforementioned, the gyroscopes measure angular rates of change in the body frame. However, we cannot simply integrate the raw angular rates of change to get our roll, pitch, and yaw angles in the *inertial frame*. For example, let's start from rest and pitch up to 60 degrees, then yaw to either side by rotating 90 degrees about the yaw body frame axis; this will decrease the pitch angle in the inertial frame, simply by yawing in the body frame! The observation implies that the rates of change of Euler angles depend on more than one body frame angular velocity. Indeed, *in order to get the rates of change in the inertial frame*, we need to transform our states as follows:

$$\begin{bmatrix} \dot{\phi} \\ \dot{\theta} \\ \dot{\psi} \end{bmatrix} = \begin{bmatrix} 1 & \sin\phi\, \tan\theta & \cos\phi \tan\theta \\ 0 & \cos\phi & -\sin\phi \\ 0 & \sin\phi\, \sec\theta & \cos\phi \sec\theta \end{bmatrix} \begin{bmatrix} G_x \\ G_y \\ G_z \end{bmatrix}. \tag{3}$$

We can then integrate the transformed states of angular change rates, $[\dot{\phi}, \dot{\theta}, \dot{\psi}]$, to get the inertial attitudes.

B. Data fusion: the complementary filter

The principle behind sensor fusion, as the name says, is to combine the data acquired from two or more imperfect sensors to find an improved and more reliable estimate of a state. A simple method is to use the so-called *complementary filter*. The complementary filter works by combining the desirable low-frequency characteristics of the accelerometer with the desirable high-frequency characteristics of the gyroscope. The method is as follows.

1. Choose a constant α, $0 < \alpha < 1$. A reasonable choice is $\alpha = 0.05 \sim 0.1$.
2. Initialize the states $(\widehat{\phi}_0, \widehat{\theta}_0) = (\widehat{\phi}, \widehat{\theta})|_{t=0} = (\phi_0, \theta_0)$.
3. For each timestep t (sampling time Δt):
   (3.a) Retrieve raw accelerometer and gyroscope readings from the IMU.
   (3.b) Compute an estimate of angles $(\widehat{\phi}_{Acc}, \widehat{\theta}_{Acc})$ from accelerometer data, using (2).
   (3.c) Combine the estimates with the integral of the transformed gyroscope in (3):

$$\begin{bmatrix} \widehat{\phi}_{t+1} \\ \widehat{\theta}_{t+1} \end{bmatrix} = (1-\alpha)\left(\begin{bmatrix} \widehat{\phi}_t \\ \widehat{\theta}_t \end{bmatrix} + \Delta t \begin{bmatrix} \dot{\phi} \\ \dot{\theta} \end{bmatrix} \right) + \alpha \begin{bmatrix} \widehat{\phi}_{Acc} \\ \widehat{\theta}_{Acc} \end{bmatrix}. \tag{4}$$

The final step ((3.c)) is a difference equation which performs the actual filtering. The accelerometer measurements are low-pass filtered, while the gyroscope measurements are high-pass filtered. These signals are then combined, depending on the constant α, to form the final state estimates. ***Code****: The complementary filter is in* `angle_inertia_comp.c`*.*

C. The iterative closest point (ICP) algorithm

The ICP algorithm is very popular because of its simplicity and clarity. However, in order to the algorithm work for various real cases, further modifications and improvements are required. Here we briefly describe its mathematical background.

Let $\mathcal{S}$ and $\mathcal{M}$ are two finite sets in finite dimensional real vector space $\mathbb{R}^d$ that contain N_S and N_M points, respectively. The goal is to determine the rigid or non-rigid transformation $T : \mathbb{R}^d \to \mathbb{R}^d$ which minimizes the distance between given sets:

$$\mathrm{dist}(T(\mathcal{S}), \mathcal{M}) = \sum_{\mathbf{s}\in\mathcal{S}} \sum_{\mathbf{m}\in\mathcal{M}} \|T(\mathbf{s}) - \mathbf{m}\|_w^2, \tag{5}$$

where $\|\cdot\|_w$ is the L^2-norm involving weights w. In particular we are interested in a transformation of the form

$$\begin{aligned} T : \mathbb{R}^d &\to \mathbb{R}^d \\ \mathbf{s} &\mapsto T(\mathbf{s}) = \mathcal{R}\mathbf{s} + \mathbf{t}, \end{aligned} \tag{6}$$

where $\mathcal{R}$ and $\mathbf{t}$ represent the rotation matrix and the translation vector, respectively. Thus the objective to be minimized is defined as

$$E(\mathcal{R}, \mathbf{t}) = \sum_{i=1}^{N_S} \sum_{j=1}^{N_M} \|w_{ij}[(\mathcal{R}\,\mathbf{s}_i + \mathbf{t}) - \mathbf{m}_j]\|^2, \tag{7}$$

where w_{ij} denote weights, having a value of either 0 or 1.

Now, let $\mathbf{m}_i \in \mathcal{M}$ be the nearest points to $(\mathcal{R}\,\mathbf{s}_i + \mathbf{t})$ for $\mathbf{s}_i \in \mathcal{S}$. Then, with a certain choice of w_{ij}, the objective in (7) can be rewritten as

$$E(\mathcal{R}, \mathbf{t}) = \frac{1}{N_S} \sum_{i=1}^{N_S} \|(\mathcal{R}\,\mathbf{s}_i + \mathbf{t}) - \mathbf{m}_i\|^2. \tag{8}$$

The objective can be minimized iteratively, beginning with an initialization $(\mathcal{R}_0, \mathbf{t}_0)$. Now we summarize the ICP algorithm as in Fig. 1. ***Code****: The ICP algorithm is implemented in* `icp_iteration.c` *and* `image_register.c`*.*

The most costly component of the ICP algorithm is Step 1, which finds the nearest point $\mathbf{m}_i \in \mathcal{M}$ for every point $\mathbf{s}_i \in \mathcal{S}$ using (9). Various computational strategies can be employed in order to improve its efficiency and accuracy; see e.g. [11].

The ICP Algorithm

- Set a threshold $\tau > 0$.
- Initialize $(\widehat{\mathcal{R}}, \widehat{\mathbf{t}}) = (\mathcal{R}_0, \mathbf{t}_0)$
- For $k = 1, 2, \cdots$
  1. Set $(\mathcal{S}_k, \mathcal{M}_k)$, by finding the nearest point $\mathbf{m}_i \in \mathcal{M}$ for every point $\mathbf{s}_i \in \mathcal{S}$:

$$\mathbf{m}_i = \arg\min_{m \in \mathcal{M}} \|(\widehat{\mathcal{R}}\,\mathbf{s}_i + \widehat{\mathbf{t}}) - \mathbf{m}\|. \tag{9}$$

  2. If $\|\mathbf{s}_i - \mathbf{m}_i\| > \tau$, discard $(\mathbf{s}_i, \mathbf{m}_i)$ from $(\mathcal{S}_k, \mathcal{M}_k)$.
  3. Compute the rotation matrix $\mathcal{R}$ and translation vector $\mathbf{t}$ using the least square method for distance minimization:
     (3.a) Compute the centroids of both point sets:

$$C_{\mathcal{S}_k} = \frac{1}{N_k} \sum_{\mathbf{s}_i \in \mathcal{S}_k} \mathbf{s}_i, \quad C_{\mathcal{M}_k} = \frac{1}{N_k} \sum_{\mathbf{m}_i \in \mathcal{M}_k} \mathbf{m}_i, \tag{10}$$

     where $|\mathcal{S}_k| = |\mathcal{M}_k| = N_k$.
     (3.b) Align all of the points in $(\mathcal{S}_k, \mathcal{M}_k)$, using corresponding centroids:

$$\mathcal{S}'_k = \{\mathbf{s}'_i \mid \mathbf{s}_i - C_{\mathcal{S}_k},\ \ \mathbf{s}_i \in \mathcal{S}_k\}, \quad \mathcal{M}'_k = \{\mathbf{m}'_i \mid \mathbf{m}_i - C_{\mathcal{M}_k},\ \ \mathbf{m}_i \in \mathcal{M}_k\}. \tag{11}$$

     (3.c) Compute covariance matrix $H_k = \mathcal{S}'_k(\mathcal{M}'_k)^T \in \mathbb{R}^{3\times 3}$ and get its singular value decomposition (SVD):

$$H_k = U_k \Lambda_k V_k^T. \tag{12}$$

     (3.d) Then the rotation matrix and the translation vector are given by

$$\mathcal{R}_k = V_k U_k^T, \quad \mathbf{t}_k = C_{\mathcal{M}_k} - \mathcal{R}_k C_{\mathcal{S}_k}. \tag{13}$$

  4. Update $(\widehat{\mathcal{R}}, \widehat{\mathbf{t}})$:

$$\widehat{\mathcal{R}} = \mathcal{R}_k \widehat{\mathcal{R}}, \quad \widehat{\mathbf{t}} = \mathcal{R}_k \widehat{\mathbf{t}} + \mathbf{t}_k. \tag{14}$$

  5. If convergent, return $(\widehat{\mathcal{R}}, \widehat{\mathbf{t}})$; otherwise continue.

Fig. 1 The iterative closest point (ICP) algorithm.

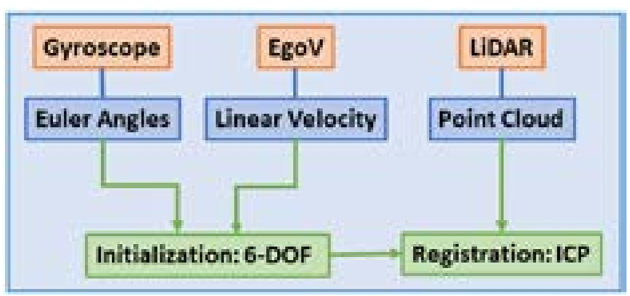

Fig. 2 Illustration for the localization scheme, in each time interval ΔT.

III. Real-time Navigation and Mapping System

A. Navigation and mapping system

Our algorithm for real-time navigation and mapping involves localization for each time period; See Fig. 2, where the localization algorithm, to be performed in each time interval ΔT, is depicted. The algorithm is implemented and being processed as follows.

- **Code**: A code is written in C.
- **Datasets**:
  - An Aeva A2 LiDAR scanner is used for point cloud, and EgoV is provided from the LiDAR scanner.
  - Datasets are generated, moving and scanning around the Torch building; point cloud is produced in 10Hz.
- **Processing**:
  - Acquired datasets are *not* well synchronized among point cloud, Euler angles, and linear velocities. As a result, the initialization step is not fully tested.
  - LiDAR odometry (using LiDAR data only) is occasionally erroneous for the given datasets.

It has been experimentally verified that an accurate initialization is very important for the registration step to obtain estimates, both accurately and efficiently. Also it has been verified that the ICP algorithm is occasionally erroneous.

B. Registration

In order to improve accuracy in the registration step, one may compute the rotation matrix and the translation both forward and backward; then compare their feasibility to fuse. Let L_t and L_{t+1} be the LiDAR datasets to be registered. Then, the registration can be performed either forward or backward.

$$\begin{cases} \mathcal{R}_f L_t + \mathbf{t}_f = L_{t+1} & \text{(FWD)} \\ \mathcal{R}_b L_{t+1} + \mathbf{t}_b = L_t & \text{(BWD)} \end{cases} \tag{15}$$

Then the rotation matrices and the translation vectors are related as

$$(\mathcal{R}_b,\, \mathbf{t}_b) \approx (\mathcal{R}_f^{-1},\, -\mathbf{t}_f). \tag{16}$$

They are *not exactly* the same, but quite well approximating each other.

To understand how to fuse information included in rotation matrices, let's consider extract angles from the rotation matrix. In general, Euler angles can be extracted from any rotation matrix, regardless of how many rotations were used to generate it. For a typical x-y-z rotation sequence, we end up with the rotation matrix:

$$\mathcal{R} = R_z(\psi)R_y(\theta)R_x(\phi) = \begin{bmatrix} c_\psi c_\theta & c_\psi s_\theta s_\phi - s_\psi c_\phi & c_\psi s_\theta c_\phi + s_\psi s_\phi \\ s_\psi c_\theta & s_\psi s_\theta s_\phi + c_\psi c_\phi & s_\psi s_\theta c_\phi - c_\psi s_\phi \\ -s_\theta & c_\theta s_\phi & c_\theta c_\phi \end{bmatrix}, \tag{17}$$

where (ϕ, θ, ψ) are roll-pitch-yaw angles and $c_a = \cos a$ and $s_a = \sin a$ for an angle a.

To get roll-pitch-yaw angles out of any given numeric rotation matrix, we need to relate the matrix elements to extract the angles based on simple trigonometry. Re-writing the rotation matrix in (17) reads:

$$\mathcal{R} = \begin{bmatrix} r_{11} & r_{12} & r_{13} \\ r_{21} & r_{22} & r_{23} \\ r_{31} & r_{32} & r_{33} \end{bmatrix}. \tag{18}$$

Then, comparing this and (17), we can come up with the following expressions to extract the angles:

$$\begin{aligned} \tan\phi &= \frac{r_{32}}{r_{33}}, \\ \sin\theta &= -r_{31}, \\ \tan\psi &= \frac{r_{21}}{r_{11}}, \end{aligned} \tag{19}$$

where $\tan\eta = x/y$ can be solved for η, using the function `atan2` implementing such as `eta=atan2(x,y)`. ***Code**: It is utilized in the function* `estimate_A_trans` *defined in* `utils_others.c`.

A strategy for fusing forward and forward estimates

a) Find $(\mathcal{R}_f,\, \mathbf{t}_f)$ and $(\mathcal{R}_b,\, \mathbf{t}_b)$ which satisfy (15).

b) Extract angles using (19):

$$\begin{aligned} \mathcal{R}_f &\Rightarrow (\phi_f,\, \theta_f,\, \psi_f) \\ \mathcal{R}_b &\Rightarrow (\phi_b,\, \theta_b,\, \psi_b) \end{aligned}$$

c) If $(\phi_f,\, \theta_f,\, \psi_f,\, \mathbf{t}_f)$ is similar to $-(\phi_b,\, \theta_b,\, \psi_b,\, \mathbf{t}_b)$, then average them; otherwise use the initialization.

***Code**: This is not explicitly implemented yet; however, there are functions implemented to do it easily.*

Remark. The motion model is traditionally defined as in (15): a rotation and followed by a translation. However, it may not represent real motion, because the rotation and the translation may happen simultaneously. This concern can be resolved easily. Consider the following model of rotation-centered motion:

$$\mathcal{R}(L_t + \mathbf{t}/2) + \mathbf{t}/2 = L_{t+1}, \tag{20}$$

which may represent motions much more accurately. For this model, the corresponding ICP can be implemented by modifying the ICP algorithm in Fig. 1. The difference will happen only in (9) and $\mathbf{t}_k$ in (13).

To derive a mathematical formula for $\mathbf{t}_k$, let $(\mathcal{S}, \mathcal{M})$ be the corresponding nearest data points obtained from (L_t, L_{i+1}). Then it follows from the model (20) that the centroids $(C_{\mathcal{S}}, C_{\mathcal{M}})$ of $(\mathcal{S}, \mathcal{M})$ are related as

$$\mathcal{R}(C_{\mathcal{S}} + \mathbf{t}/2) + \mathbf{t}/2 = C_{\mathcal{M}}, \tag{21}$$

from which we can conclude

$$\mathbf{t} \;=\; 2(\mathcal{R} + I)^{-1}(C_{\mathcal{M}} - \mathcal{R}C_{\mathcal{S}}). \tag{22}$$

Of course, for the new motion model, $(\widehat{\mathcal{R}}\,\mathbf{s}_i + \widehat{\mathbf{t}})$ in (9) must be replaced by $(\widehat{\mathcal{R}}\,[\mathbf{s}_i + \widehat{\mathbf{t}}/2] + \widehat{\mathbf{t}}/2)$. Note that $(\mathcal{R} + I)$ is a 3×3 matrix, and its inverse can be found using a formula-like program. ***Code**: The inverse of* 3×3 *matrices can be computed using the function* `inverse3x3`, *which is in* `utils_matrix_algebra.c`.

C. Further developments

As a part of LiDAR data processing, we may have to detect small objects, where objects can be viewed as perturbations from a background model. For example, small objects on the ground can be detected as perturbations from a ground plane. In such object detection, the major step is to find a plane which best fits point cloud. A *RANdom SAmple Consensus* (RANSAC)-based algorithm can be applied to estimate the best-fitting plane. The basic idea of RANSAC is as follows.

The RANSAC algorithm

1. Select randomly the minimum number of points, required to determine the model parameters.
2. Solve for the parameters of the model.
3. Determine how many points from the set of all points fit with a predefined width η (inliers).
4. If the fraction of the number of inliers over the total number points in the set exceeds a predefined threshold τ, re-estimate the model parameters, using all the identified inliers and stop.
5. Otherwise, repeat steps 1–4 (maximum of N times).

The RANSAC algorithm is simple to implement and efficient; however, it is erroneous. We have develop an iterative algorithm, called the *iterative partial regression* (IPR) algorithm.

The Iterative Partial Regression (IPR)

0. Initialize the model parameters, using either the whole point cloud or its randomly selected subset.
1. Determine inliers from the whole point cloud that fit with a predefined width η from the estimated model.
2. Solve for a new set of model parameters, using all the identified inliers.
3. If the new estimates are *near* to the old ones, by a predefined tolerance τ, return the new estimates and stop.
4. Otherwise, repeat steps 1–3.

The IPR is implemented and compared with RANSAC. Fig. 3 depicts typical results of RANSAC and IPR. In the figure, the line in blue is the one obtained from point cloud without noise and considered as the true best-fitting line, the red line is the fitting line for all the points including noise, and the cyan line is estimated line by algorithms. The RANSAC occasionally produces erroneous parameters, while the new algorithm results in consistent accurate parameters.

Their performances are compared qualitatively in Table 1, where each algorithm is run 1000 times for each datasets to find the standard deviation of the error. For the model $y = a + bx$, let $(\widehat{a}, \widehat{b})$ be the true best-fitting parameters, while (a_i, b_i) be the i-th estimate. Then, we define

$$\sigma(a - \widehat{a}) = \Big(\frac{1}{N}\sum_{i=1}^{N}(a_i - \widehat{a})^2\Big)^{1/2}, \quad \sigma(b - \widehat{b}) = \Big(\frac{1}{N}\sum_{i=1}^{N}(b_i - \widehat{b})^2\Big)^{1/2}, \quad N = 1000. \tag{23}$$

(Data=1; RANSAC)

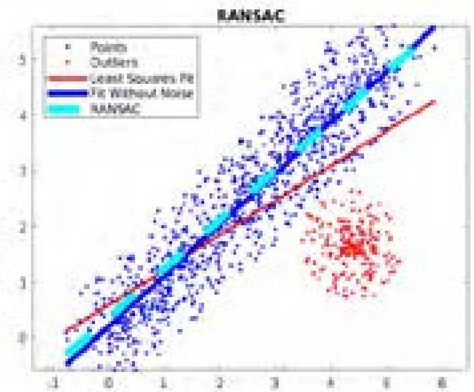

(Data=1; IPR)

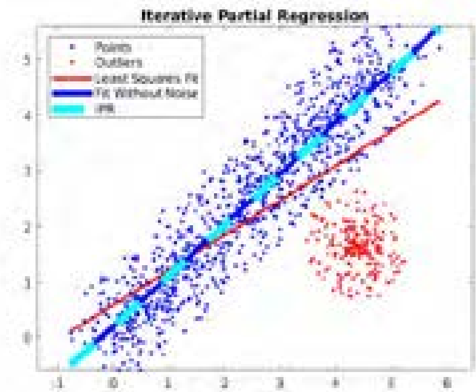

(Data=2; RANSAC)

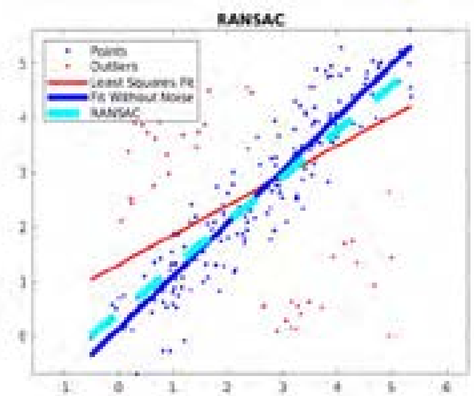

(Data=2; IPR)

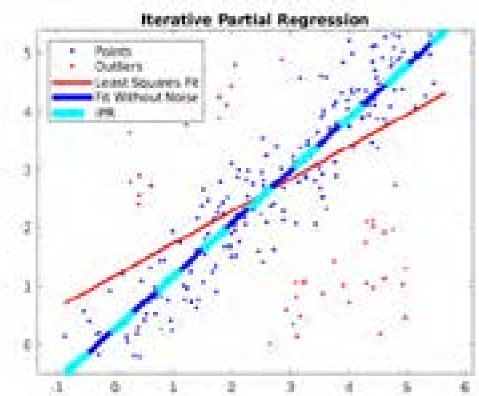

Fig. 3 RANSAC and IPR for synthetic datasets.

Table 1 Model fitting $y = a + bx$, for parameters (a, b). The algorithms RANSAC and IPR are run 1000 times for each dataset to find the standard deviation of the error: $\sigma(a - \widehat{a})$ and $\sigma(b - \widehat{b})$, where $(\widehat{a}, \widehat{b})$ is the true best-fitting parameters. E-time indicates the whole elapsed time for the algorithms to run 1000 times, of which each run is carried out with a new randomly-generated points of the same size.

Data	Algorithm	$\sigma(a - \widehat{a})$	$\sigma(b - \widehat{b})$	E-time (sec)
1	RANSAC IPR	0.1812 0.0291	0.0694 0.0255	3.9813 1.8354
2	RANSAC IPR	0.1634 0.0187	0.0547 0.0046	3.9813 1.8754

As one can see from the table, the IPR outperforms the RANSAC in both accuracy and efficiency; the IPR is more accurate and twice more efficient than the RANSAC.

IV. Planned Research

A new dataset has been made using a crane (Run18), for which a LiDAR scanner hung on a crane acquired point cloud, shooting lasers downward. Run18 is now being analyzed.

- **Localization**: For the dataset, we will work on localization as usual.
- **Flatness and object detection**: we will try to figure out (a) how flat the ground is and (b) what small objects are.

This section presents planned research which we will complete by the end of the year. The code will be expanded and implemented for general purpose, although it is being tested for Run18.

A. Localization

Localization begins with an accurate initialization of the sensor location and orientation, followed by a drift correction by using a registration algorithm. The most popular registration method is the ICP due to its robustness and efficiency; see Section II.C. However, the ICP is erroneous unless (a) *the initialization is accurate* and (b) *data pre-processing is appropriate*. By an appropriate data pre-processing, we mean that the LiDAR point cloud must be pre-processed for a subset of points with which the ICP produces accurate registration. Such a pre-processing step is quite dependent on the data environments, particularly, the scenes the data is representing. We will develop various strategies for localization.

B. Flatness and object detection

As aforementioned, small objects can be viewed as perturbations from a background plane. Thus, for Run18, the major step of object detection is to find a plane which best fits point cloud. We will apply the IPR described in Section III.C for the processing.

Acknowledgment

I, Seongjai Kim, deeply appreciate Dr. Michael R. Zanetti for his help and concerns. The research was a great opportunity for me to recognize real-world. We together will make a publication soon and hopefully work on various challenging real-world problems.

References

[1] Brock, J. C., and Purkis, S. J., “The Emerging Role of LiDAR Remote Sensing in Coastal Research and Resource Management,” *Journal of Coastal Research*, Vol. 53, 2009, pp. 1–5.

[2] Johnson, K. M., and Ouimet, W. B., “Rediscovering the lost archaeological landscape of southern New England using airborne light detection and ranging (LiDAR),” *Journal of Archaeological Science*, Vol. 43, 2014, pp. 9–20.

[3] Wulder, M. A., Bater, C. W., Coops, N. C., Hilker, T., and White, J. C., “The role of LiDAR in sustainable forest management,” *The Forestry Chronicle*, Vol. 84, No. 6, 2008, pp. 807–826.

[4] Wulder, M., Coops, N., Hudak, A., Morsdorf, F., Nelson, R., Newnham, G., and Vastaranta, M., “Status and prospects for LiDAR remote sensing of forested ecosystems,” *Can. J. Remote Sensing*, Vol. 39, No. S1, 2013, pp. S1–S5.

[5] Kim, H., Willers, J. L., and Kim, S., “Digital elevation modeling via curvature interpolation for LiDAR data,” *Electronic Journal of Differential Equations, Conference Special Issue*, Vol. 23, 2016, pp. 47–57.

[6] Kim, H., Willers, J. L., and Kim, S., “Curvature Interpolation Method for Surface Reconstruction for Geospatial Point Cloud Data,” *International Journal of Remote Sensing*, Vol. 41, No. 4, 2020, pp. 1512–1541.

[7] Tang, L., and Shao, G., “Drone remote sensing for forestry research and practices,” *Journal of Forestry Research*, Vol. 26, No. 4, 2015, pp. 791–797.

[8] Wulder, M. A., White, J. C., Nelson, R. F., Næsset, E., Ørka, H. O., Coops, N. C., Hilker, T., Bater, C. W., and Gobakken, T., “LiDAR sampling for large-area forest characterization: A review,” *Remote Sensing of Environment*, Vol. 121, 2012, pp. 196–209.

[9] Dong, P., and Chen, Q., *LiDAR Remote Sensing and Applications*, CRC Press, Boca Raton, 2017.

[10] Steiner, T. J., Truax, R. D., and Frey, K., “A vision-aided inertial navigation system for agile high-speed flight in unmapped environments: Distribution statement A: Approved for public release, distribution unlimited,” *2017 IEEE Aerospace Conference*, 2017, pp. 1–10.

[11] Procházková, J., and Martišek, D., “Notes on iterative closest point algorithm,” *Proceedings of the 17th Conference on Applied Mathematics (APLIMAT 2018)*, 2018, pp. 876–884.

Interfacing Astrophysical Simulations with Data Analysis Infrastructure

Shane L. Larson[1]

Center for Interdisciplinary Exploration and Research in Astrophysics (CIERA), Northwestern University, Evanston, IL 60201

Gravitational wave astronomy is an observational discipline in its infancy, with the first detections only 5 years in the past. As such, the scientific community is transitioning from a community of small independent research groups into a larger, collaborative community that works under the auspices of common data, common conventions, and shared scientific tools. Here we outline the beginning effort to interface a mature astrophysical code for population synthesis of galactic stellar populations (COSMIC) maintained by the Northwestern astrophysics community, with the development gravitational wave analysis pipeline (LDAsoft) maintained by the Marshall Space Flight Center gravitational wave group.

I. Introduction

The Laser Interferometer Space Antenna (LISA) [1] is the selected L3 mission for the European Space Agency's Cosmic Visions program, currently in Phase A development and scheduled for launch in the early 2030s. It is also part of NASA's program of record, ranked in the 2010 Decadal Survey ("New Worlds, New Horizons"). NASA is a junior partner in the ESA program, and supports the effort in the United States through a LISA Study Team managed out of the Goddard Space Flight Center (the author is a member of this study team; the author's MSFC sponsor, Tyson Littenberg, is a Core NASA member of the study team).

LISA is a laser interferometric gravitational wave observatory, comprised of three spacecraft arranged in an equatorial constellation with 2.5 million kilometer separations between spacecraft. Each spacecraft is in an independent solar orbit, phased and oriented such that the time-dependent relative motion makes the trio appear as a stable triangular constellation, following the Earth around its orbit. The plane of the constellation is inclined to the ecliptic by 60 degrees, and as viewed from the sun makes a complete clockwise rotation over the course of a year; the nominal configuration is shown in Figure 1.

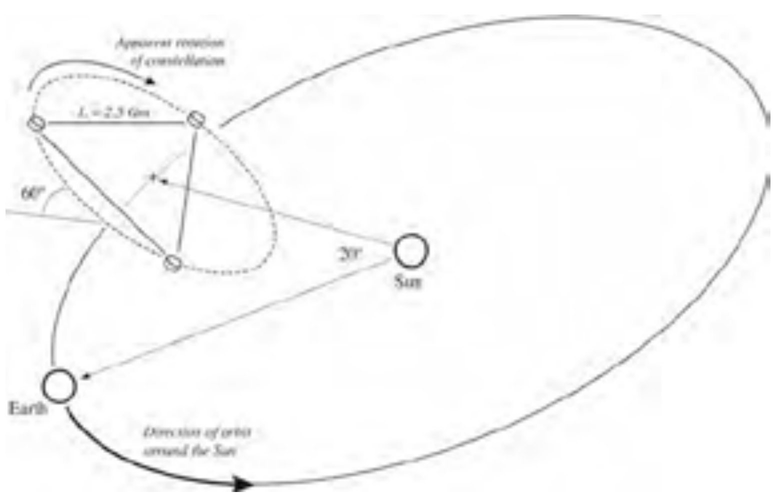

Fig. 1 Apparent configuration of LISA constellation, relative to Earth.

---

1 Associate Director of CIERA; Research Professor, Department of Physics & Astronomy, Northwestern University.

II. LISA Science

LISA is a broadband, interferometric gravitational wave observatory, with baseline sensitivity across more than four decades of frequency in the gravitational wave spectrum from $10^{-4}\text{Hz} \lesssim f \lesssim 1\text{Hz}$. The expected instrumental capability is displayed as a sensitivity curve in Fig. 2 [2], plotting the threshold strength of a source required for detection against the frequency. Roughly speaking, the frequency at which a source emits gravitational waves is inversely proportional to the astrophysical timescales one which masses more dynamically in the system. LISA's peak sensitivity is around $f \sim 10^{-3}\text{Hz}$, so the relevant astrophysical timescales are $t \sim 1000\text{sec}$.

At such timescales, the primary astrophysical sources are massive black hole binaries at the centers of galaxies, small compact objects falling into massive black holes, and ultra-compact binary star systems (UCBs) formed of stellar remnants in the Milky Way galaxy. Our work is primarily focused on the UCBs.

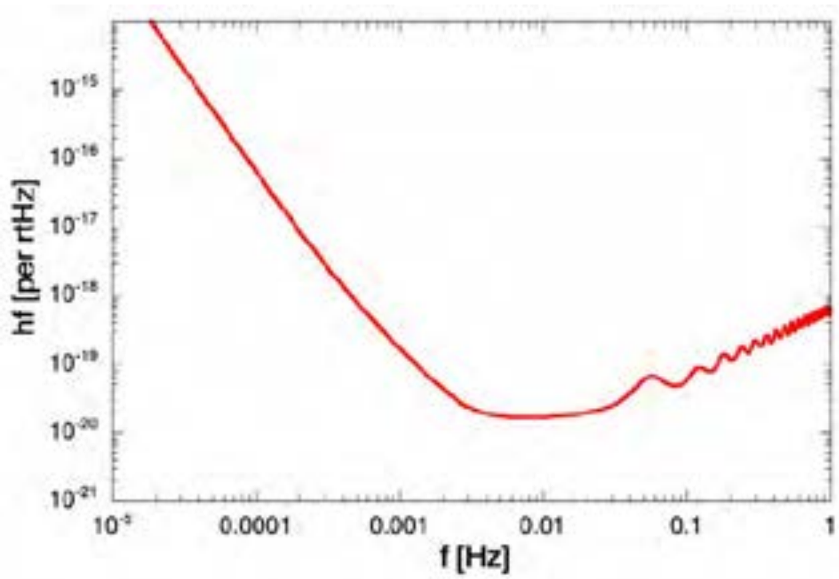

Fig. 2 The baseline LISA sensitivity, plotted as gravitational wave amplitude spectral density (a measure of gravitational wave strength) vs. gravitational wave frequency.

III. White Dwarf Binaries

Our current understanding of the ultra-compact binary population in the Milky Way is founded on observations of known systems, coupled with analytic models, and massive numerical simulations that model the evolution of stars systems across the history of the galaxy ("population synthesis"). The expectation is there will be a total of $\sim 10^7$ galactic UCBs in the LISA band. The signals from the vast majority of these will be overlapping and indistinguishable from another forming a confusion foreground. There will $\sim 10^4$ individually resolved sources that will be loud enough to stand out above the confusion and cataloged by LISA. This resolved population will be the single largest catalog of gravitational wave sources from any gravitational wave observatory, representing an unprecedented opportunity to understand the history of stellar evolution in the Milky Way and probe the processes that drive stellar evolution.

A. COSMIC SYNTHESIS

Our group at Northwestern has developed a rapid population synthesis code for creating realizations of galactic stellar populations, known as COSMIC [3]. COSMIC is a publicly available [4] population synthesis code based on BSE [5], that provides a suite of utilities to build the underlying statistical properties of a stellar population, and rapidly Monte Carlo draw from those statistical distributions to make full populations. It uses updated formalisms to incorporate modern understanding of binary evolution. For user-defined initial parameters that define the properties of the stellar system being modeled, COSMIC returns a population of binaries at the current day, and keeps the evolution history of each binary.

COSMIC has the flexibility to simulate populations piecewise, either by population type or by spatial distribution. In large stellar systems like a galaxy, most systems evolve in isolation ("in the field") independent of dynamical interactions with other systems. The properties of the stellar population then depend on just a few large bulk properties, such as the metallicity and star formation history, so galaxy realizations can be built up by simulation that focuses on single system evolution. The basic strategy of COSMIC's inner workings is as follows:

1) Generate a finite number of binary systems in a ``fixed population," evolving each system for the entire 13.7 Gyr age of the galaxy, given the initial properties of the galaxy. For this study, we use metallicities consistent with the known properties of the stellar halo. The fixed population is built up in stages, until the statistical distribution of the successively larger populations stabilizes, representing the correct correlated parameter distribution of DWDs for the input galaxy parameters.
2) Systems are drawn from the statistical distribution represented by the fixed population, which captures the distributions of system parameters and their interdependencies and degeneracies. For a galaxy realization, the total population is scaled to the desired mass of the galaxy, a free parameter specified to identify a particular stellar system of interest.
3) Each binary is randomly drawn from the distributions of the fixed population, and randomly assigned a birth time based on the star formation history adopted for the simulation.
4) The positions of the individual star systems in the realization are randomly assigned following a spatial model based on stellar observations outlined in [6]

A profile view of the production COSMIC galaxy for this work is shown in Fig. 3, viewing the galactic plane edge on.

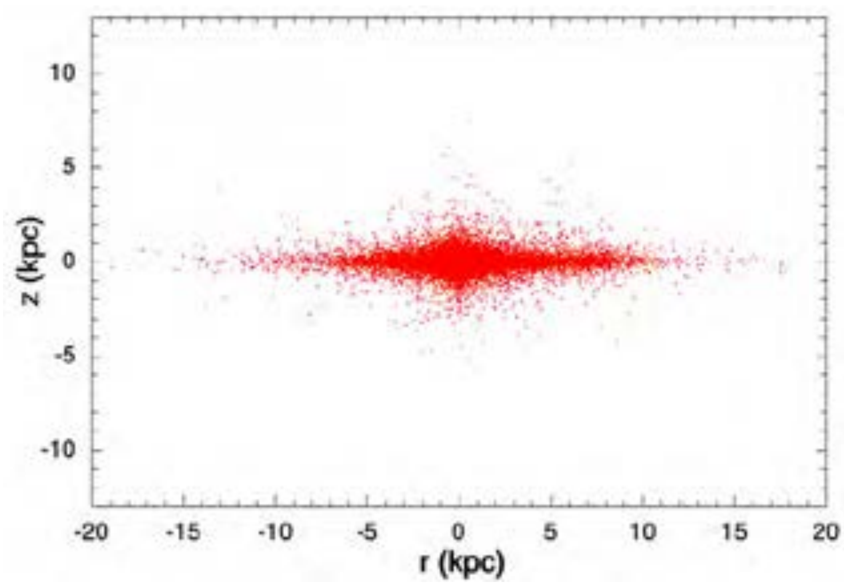

Fig. 3 A COSMIC galaxy, output with baseline parameters to describe the Milky Way, viewed edge on.

B. Synthesized Galaxy

The goal in the current project is to build infrastructure that makes COSMIC output accessible by the developing suite of LISA data analysis pipelines being developed at MSFC (see Sec. C: LDAsoft, below), and provide a more realistic view of LISA's astrophysical measurement capabilities. Currently, especially in the astrophysics community, the assessment of observability by LISA is done in a very ad hoc way, which is computationally expedient by virtue of being reduced to an algebraic operation, making it ideal for massive computational simulations. The information such ad hoc views gives of LISA capabilities are sufficient for current astrophysical needs, since the uncertainties introduced by an imperfect LISA analysis do not begin to approach the uncertainties in the astrophysical models themselves. The ad hoc analysis approach relies on a simple calculation of the "signal-to-noise ratio" (SNR) which is formally defined by

$$(SNR)^2 = \rho^2 = \int df \, \frac{|\tilde{h}(f)|^2}{S_n(f)} \tag{1}$$

where $\tilde{h}(f)$ is the Fourier transform of the gravitational wave signal, and $S_n(f)$ is the power spectral density of the noise, well approximated for our needs by the square of the sensitivity curve $h_f(f)$shown in Fig. 2. For most of the ultra-compact binaries, they are stationary in frequency (their orbital periods do not evolve substantively during the expected LISA observation time), so the frequency dependence in $\tilde{h}(f)$ can be approximated as a delta function, which collapses the integral in Eq. (1) leaving

$$(SNR)^2 = \rho^2 = \left(\frac{h_o \sqrt{T_{obs}}}{h_f(f)} \right)^2 \tag{2}$$

where h_o is the gravitational wave amplitude of the binary given at quadrupole order [7]. Using this approach, a simple cut can be quickly made on an entire galactic simulation to generate an approximate Catalog of individual sources that LISA will be able to measure in the Milky Way. The gold standard for data analysis is a threshold SNR = 8 is required for a source to be detectable; in practice we take a lower threshold of SNR = 5, since it is well known that the ultimate SNR obtained for a source is a strong function of the data analysis procedure used. Choosing a slightly lower threshold insures that sources near the edge of detection, which is where many astrophysical inferences have been historically made, are kept. Fig. 4 shows a polar view of the Milky Way looking down on the galactic plane, with the full stellar population plotted in red, and the binaries in a LISA catalog selected by this SNR method. Note the strong clustering of sources around the location of the Sun, on the right-hand side of the plane. This is the gravitational wave equivalent of *Malmquist bias* where brighter sources are preferentially detected.

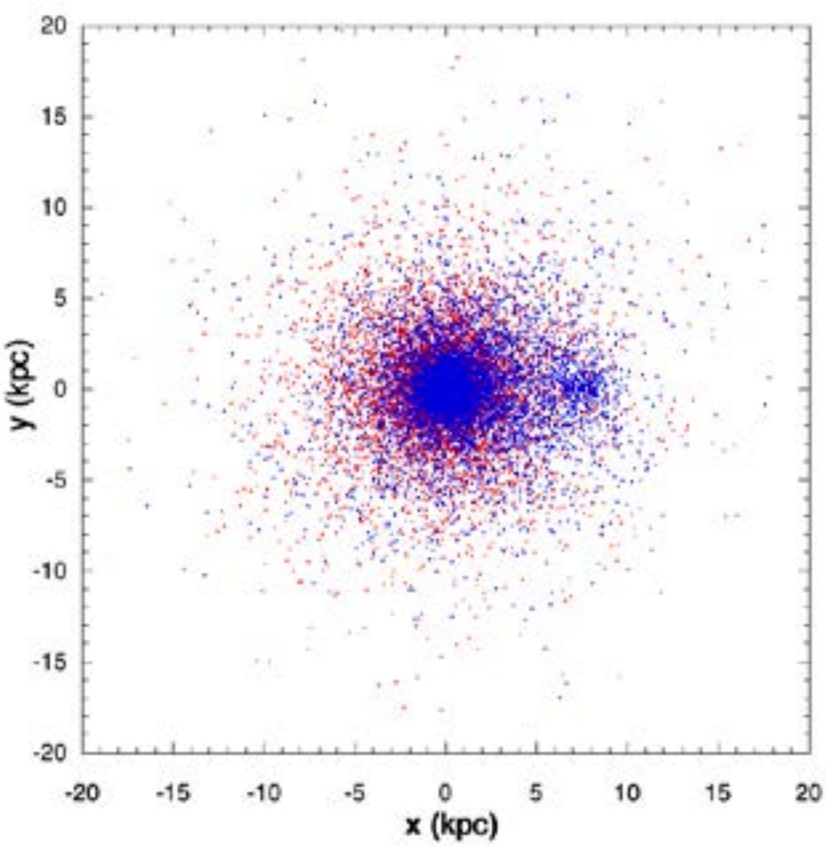

Fig. 4 Our COSMIC galaxy (red) with LISA resolved sources (blue), as viewed from the galactic north pole. Note the clustering of sources around the Earth at r = +8 kpc (gravitational wave Malmquist bias).

Ultimately in analysis, the quantities of interest are not the parameter values themselves, but rather the errors, which characterize the quality of the measurement and bound the ability to interpret or extract astrophysical inferences from the data. At the level of computing the SNR, simple fits to errors as scaling laws against the SNR are used [8]. This scaling is generally sufficient for making broad astrophysical assessments. An example of such an ad hoc error analysis applied to the same COSMIC galaxy used above is shown in Fig. 5 below, showing the errors in sky location against the errors in the source amplitude, both direct measurables by LISA. This is a particularly relevant example for the UCBs, as they are the most numerous *multi-messenger* source. Currently there are some 50 known systems that have been observed with telescopes and are expected to be strong LISA sources [9], and there will be hundreds to thousands more, depending on the aperture of telescopes dedicated to finding electromagnetic counterparts.

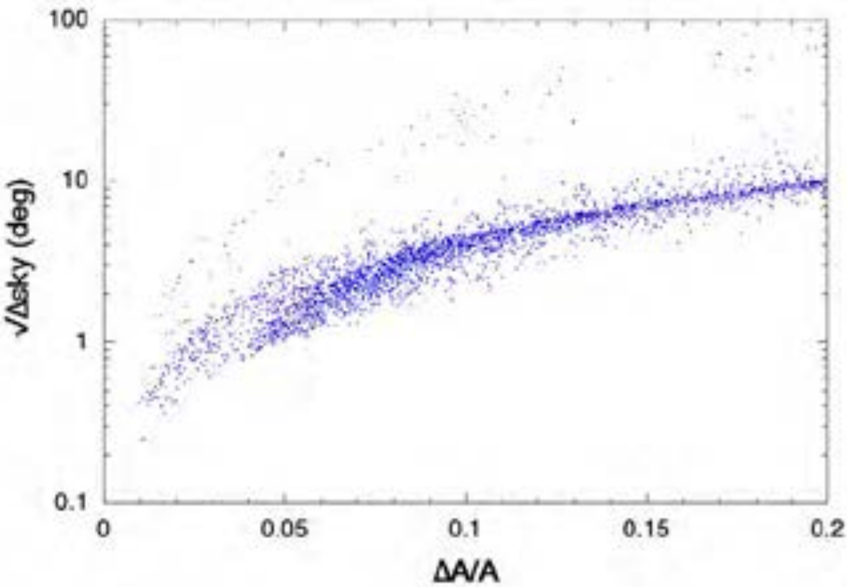

Fig. 5 Ad hoc error analysis of our COSMIC galaxy, showing sky location errors vs. fractional gravitational wave amplitude errors for resolvable sources in a LISA catalog.

C. LDAsoft

The group at MSFC maintains a nascent software pipeline for LISA data analysis known as LDAsoft [10]. The package is built around the philosophy of piecewise improving the simulation and analysis of LISA data, taking incremental steps that constantly move our techniques forward toward more realistic assessments of LISA data. LDAsoft in particular can make a major improvement over the ad hoc analysis shown above by improving the estimates of LISA errors using a Fisher-matrix analysis [11]. Fisher-matrix analysis is not perfect [12], but it can be done for low computational cost, making it an ideal tool to use in massive simulations like the galaxies produced by COSMIC.

The LDAsoft pipeline proceeds from baseline of assuming data inputs that approximate LISA data in some way (i.e. measured gravitational wave signal $h(t)$ or interferometric variables). By contrast, the infrastructure typically used in our group, similar to that used in most astrophysical modelling scenarios, begins from the parameters of the source, notably the stellar masses and orbital parameters. A pre-processor API has been prototyped to consume COSMIC galaxies and output LDAsoft input files. This is not without challenges, and requires new modifications and changes in both codes to be implemented that reflect the new purposes they are being used for. As described in Section IV, the ultimate application of this work is to develop theoretical inference studies, so the provenance of simulated sources from COSMIC must somehow be maintained and identifiable with the source outputs from LDAsoft.

The LDAsoft pipeline has been successfully applied to the LISA Data Challenge galaxy known as *Radler*, and work is proceeding on utilizing COSMIC galaxies in the same framework. One of the strengths of COSMIC is that it does not have fixed parameters that describe the galaxy; they can be varied to reflect the astrophysical constraints or assumptions used to build the galaxy. The initial LDAsoft analysis of our COSMIC galaxy shows variances at odds with the *Radler* output, which has been tracked down to differences in the assumptions about the underlying galaxies passed to LDAsoft. As can be seen in Fig. 6 below, the *Radler* vs. COSMIC PDF for source outputs is shown, with significant difference in support at different parameter values. The most substantive and obvious difference is in the number of sources present in the two galaxies -- *Radler* has only 29.8 million systems, whereas

COSMIC has 39.4 million systems. Both populations are consistent with the Milky Way, but represent different ways of scaling the population synthesis that was used -- the *Radler* realization targeted the traditional expected number of binaries, based on extant observational constraints, whereas the COSMIC galaxy produced here targets the expected *mass* in binaries. However, a simple difference in number of systems cannot account for the different distributions between the two galaxies. Amplitude distributions are highly dependent on the spatial model for the galaxy used, which includes assumptions both about the galactic components (halo, bulge, thick disk, and thin disk) and their respective scale heights. Orbital period distributions are a strong function of binary evolutionary physics, which different population synthesis codes treat differently. Understanding and calibrating these differences is ongoing work.

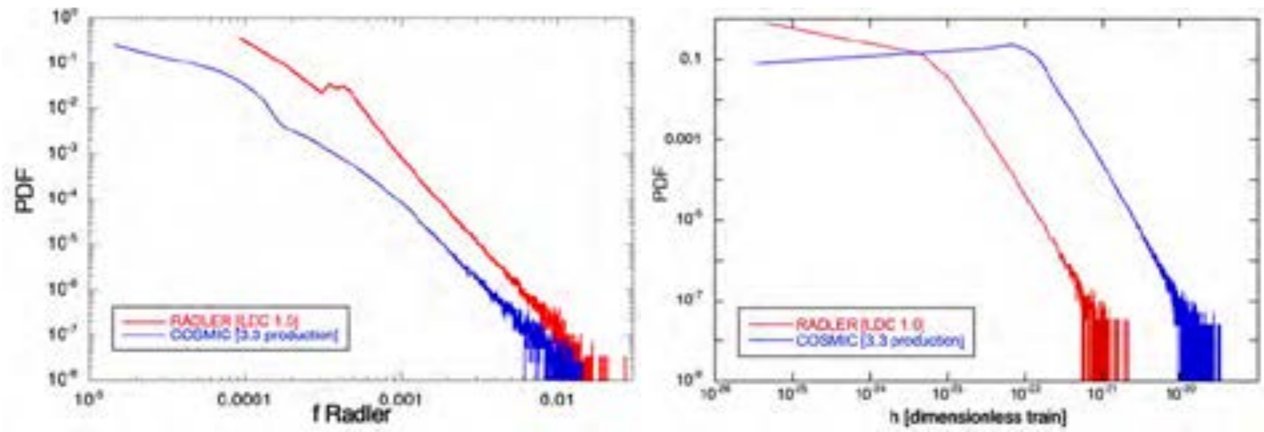

Fig. 6 Comparison between the distribution functions for COSMIC output against the *Radler* output, used to baseline the LDAsoft operations. [Left Panel] Comparison of the distribution functions for gravitational wave frequency (proxy for orbital periods). [Right Panel] Comparison of the distribution functions for dimensionless train (proxy for spatial distributions).

IV. FUTURE: AN ANALYSIS CHAIN FOR ASTROPHYSICS

Our goal is to produce efficient pipelines that link LISA data analysis with astrophysical simulation work. This has two important outcomes. First, it will build stronger links to the astrophysical simulation community. By and large over the multi-decade history of LISA, this connection has been focused on gravitational wave *rate predictions*. However, as the astronomical community becomes more adapted to having access to gravitational wave data, attention will increasingly turn toward constraining theories and speculations about astrophysical processes. This will require higher fidelity treatments of gravitational wave data that is closer to what the actual LISA data products will be. Second, the development of simulation pipelines need to be built and tested using reasonable approximations of what the real astrophysical signals may be, to be prepared for real LISA data. Fig 7. shows the current collaboration effort, and how the output data of these efforts will flow back to the assessment of astrophysical problems.

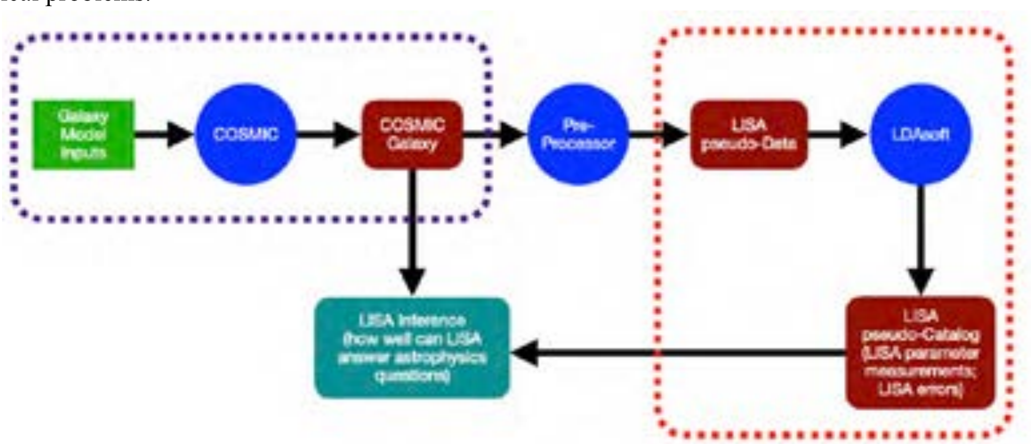

Fig. 7 COSMIC (purple dashed) and LDAsoft (red dashed) common workflow.

As a particular concrete example of how improved analysis tools like LDAsoft will inform astrophysical problems, consider the confusion foreground signal shown in Fig. 8. The ultimate measured shape of the spectral foreground will depend on the precise analysis pipeline capabilities, but also on the underlying astrophysical populations in the galaxy. The ability to resolve and fit the shape of the foreground depends on the analysis pipeline that produces the foreground to start with. The ability to interpret the shape of the foreground and infer what information it encodes about the galactic binary population will be intimately tied to the ability to theoretically simulate it. This will be part of our ongoing work.

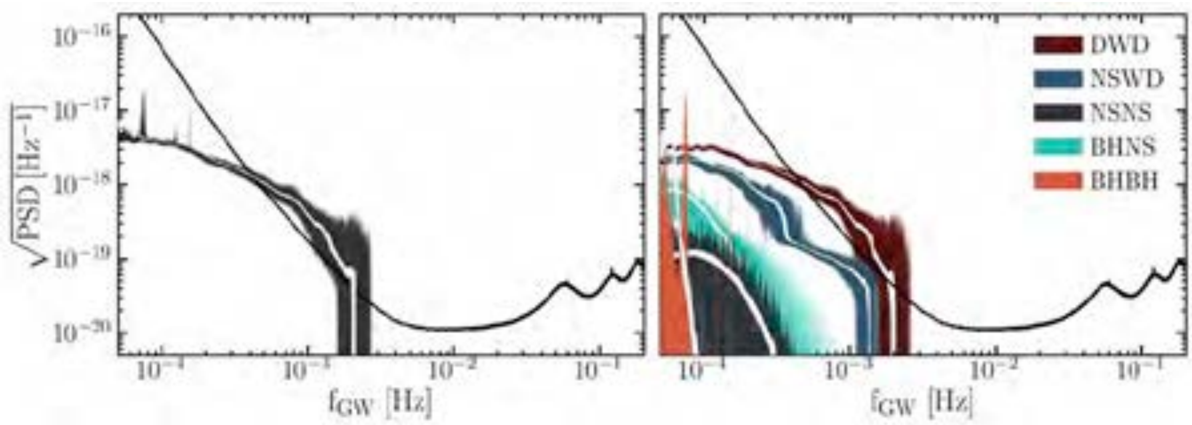

Fig. 8 Examples foreground spectra from COSMIC. The full spectrum is shown in the left panel, and the contributions in the right panel. The color bands are the expected range of astrophysical amplitudes for the foreground, based on our current understanding of the underlying populations. This represents the range of possible foregrounds LISA may have to contend with.

Acknowledgments

This collaboration was supported by a NASA Summer Faculty Fellowship for the summer of 2020, during the Coronavirus Pandemic. Given the remote nature of the experience, it is impossible to thank everyone at MSFC, NASA, and Space Grant that supported the herculean tasks of making it still possible. I'd like to thank my collaborator, Tyson Littenberg at MSFC, and his group, for hosting me and encouraging this work to proceed. I'm also deeply indebted to the graduate and undergraduate students who work in my group to develop software and produce the galactic simulations we use, particularly Julie Malewicz, Weitan Yu, and Kierstin Sorensen; without their intellectual efforts and work, these projects would not be possible.

References

[1] eLISA Consortium, "The Gravitational Universe," arxiv:1305.5720.

[2] Larson, S. L., Hellings, R. W., Hiscock, W. A., "Unequal arm space-borne gravitational wave interferometers," *Physical Review D*, **66**, 062001 (2002)

[3] Breivik, K., Coughlin, S., Zevin, M., Rodriguez, C. L., Kremer, K., Ye, C. S., Andrews, J. J., Kurkowski, M., Digman, M. C., Larson, S. L., Rasio, F., "COSMIC Variance in Binary Population Synthesis," *Astrophysical Journal*, **898**, 71 (2020); arxiv:1911.00903

[4] "COSMIC: A python package for population synthesis", v3.3, July 2020. http://cosmic-popsynth.github.io/

[5] Hurley, J., Tout, C. A., Pols, O. R. "Evolution of binary stars and the effect of tides on binary populations," *Monthly Notices of the Royal Astronomical Society*, **329**, 897 (2002).

[6] McMillan, P. J., "Mass Models of the Milky Way," *Monthly Notices of the Royal Astronomical Society*, **414,** 2446 (2011).

[7] Peters, P.C., "Gravitational Radiation and the Motion of Two Point Masses" *Physical Review*, **136**, B1224 (1964).

[8] Takahashi, R., Seto, N., "Parameter estimation for galactic binaries by the Laser Interferometer Space Antenna," *Astrophysical Journal*, **575**, 1030 (2002).

[9] Littenberg, T. B., Larson, S. L., Nelemans, G., Cornish, N. J., "Prospects for observing ultra-compact binaries with space-based gravitational wave interferometers and optical telescopes," *Monthly Notices of the Royal Astronomical Society*, **429**, 2361 (2013).

[10] "LDAsoft", Littenberg, T. B., July 2020. https://github.com/tlittenberg/ldasoft/

[11] Cutler, C., Flanagan, E. E., "Gravitational waves from merging compact binaries: How accurately can one extract the binary's parameters from the inspiral waveform?," *Physical Review D*, **49**, 2658 (1994).

[12] Vallisneri, M., "Use and abuse of the Fisher information matrix in the assessment of gravitational-wave parameter-estimation prospects," *Physical Review D*, **77**, 042001 (2008).

Flexible Sensor Modeling and Origami Supercapacitors

Russell W. Mailen*
Auburn University, Auburn, Alabama, 36849, U.S.A.

Zachary C. Jones
NASA Marshall Space Flight Center Huntsville, Alabama, U.S.A.

Curtis W. Hill
NASA Marshall Space Flight Center Huntsville, Alabama, U.S.A.

Additive manufacturing (AM) facilitates the fabrication of diverse products for space applications. AM reduces in-space resource requirements by using a common stock of raw materials and highly customizable fabrication capabilities. We report on two projects related to AM in space worked on this summer by Dr. Russell Mailen, NASA MSFC Summer Faculty Fellow. In the first project, Dr. Mailen utilized finite element analysis to investigate internal stresses generated during the peeling removal of a reusable cortisol sensor. This sensor integrates a Kapton electronics carrier, battery, conductive vias, and spring pins into an RTV630 silicone encapsulant. Cohesive elements were used to model separation of the sensor from a substrate. Locations of high stress resulting from peeling from different locations on the sensor are reported. In the second project, Dr. Mailen experimentally investigated self-folding for origami supercapacitors. A laminated composite concept is developed in which a stack-up of active and passive components is laminated with the printed supercapacitors. Exposure of the initially flat substrate to infrared (IR) light will induce self-folding of the supercapacitor along fold lines that define a compact Miura-Ori fold pattern.

I. Nomenclature

D	=	scalar damage variable
δ_m^{max}	=	maximum value of the effective displacement attained during the loading history
δ_m^f	=	effective displacement at complete failure
δ_m^0	=	effective displacement at damage initiation
E_{nn}	=	tensile stiffness of cohesive layer
G_1, G_2	=	shear stiffness of cohesive layer
N	=	material parameter representing order of Ogden model
t	=	stress components of the traction-separation model affected by damage
$\bar{t}$	=	stress component predicted by elastic traction separation behavior for the current strains without damage
t_n	=	normal traction at which failure initiates
t_s, t_t	=	shear traction at which failure initiates
T_g	=	Glass-transition temperature
α_i	=	exponential parameter for Ogden material model
$\bar{\lambda}_1, \bar{\lambda}_2, \bar{\lambda}_3$	=	deviatoric principal stretches
μ_i	=	parameter for Ogden material model

II. Project 1: Finite Element Modeling of Flexible Sensor

Flexible electronics enable new wearable devices which can be worn for extended periods of time. In a collaboration between NASA and NextFlex, a reusable and flexible sensor, called AstroSense, used for determining astronaut stress levels through the sensing of cortisol levels, is under development. In this project, we use finite element analysis

*Assistant Professor, Department of Aerospace Engineering, Auburn University, 211 Davis Hall Auburn University, Alabama 36849

to determine internal stresses resulting from peeling actions for removal of the sensor from the astronaut's skin. Insight gained by this analysis will facilitate the development of the sensor which is capable of multiple uses without damage to the integrated electronics. The three-dimensional finite element analysis framework uses cohesive elements and linear damage evolution to model peeling of the sensor from a stainless steel substrate.

A. AstroSense by NextFlex

A preliminary geometry and stackup with adhesive layers for the flexible cortisol sensor has been developed by NextFlex (Figure 1).[1] The reusable electronic reader (blue component) is comprised of a Kapton (polyimide) electronics carrier embedded in an RTV630 (silicon) encapsulent material. Spring pins attached to the Kapton layer contact conductive traces on a disposable electrode sensor. The electrode sensor is adhered to the electronic reader using 3M 2477p adhesive film. The disposable electrode sensor consists of 3M 2477p adhesive, Kapton film with conductive traces, and 3M Microfluidic Diagnostic Film 9962.

Fig. 1 Stackup of layers in AstroSense sensor.

B. Finite Element Framework

A three-dimensional, finite element framework is used to model peeling of the reusable electronic reader from a stainless steel substrate. A quasi-static analysis step is employed in which a displacement boundary condition normal to the substrate surface is applied using a linear variation. Cohesive elements at the interface between the electronic reader and a stainless steel substrate represent the silicone layer of the 3M 2477p adhesive tape. The RTV630 encapsulent is modeled using an Ogden hyperelastic model, in which the strain energy potential is expressed as

$$U = \sum_{i=1}^{N} \frac{2\mu_i}{\alpha_i} (\bar{\lambda}_1^{\alpha_i} + \bar{\lambda}_2^{\alpha_i} + \bar{\lambda}_3^{\alpha_i} - 3) \tag{1}$$

All other materials were modeled using a linear elastic material model with representative material properties.

The adhesive layer uses a linear damage model to represent separation from the substrate. The adhesive layer is modeled with an orphan mesh offset from the silicone encapsulant. A mismatched mesh interface with the substrate requires the use of a tie constraint between the adhesive layer and the substrate. In addition, hard normal contact and frictionless tangential contact is applied between the RTV630 layer and the substrate. We employ an uncoupled, maximum stress traction separation law with linear damage evolution as depicted in Figure 2. The stiffness, E_{nn}, and traction separation force, t_n, of the cohesive layer are specified to achieve the peel force reported by the manufacturer. Because normal peeling force is the expected separation mode for the sensor, the shear stiffness, G_1 and G_2, and maximum shear traction, t_s and t_t, of the adhesive layer are set arbitrarily high to help stabilize the solution. Traction separation initiates when t_n is exceeded. This occurs at a separation distance of δ_m^0, which is related to t_n and E_{nn}. As the sensor is separated further from the substrate, the normal traction, t, is updated according to a scalar damage variable, D, according to

$$t = (1 - D)\bar{t} \tag{2}$$

where $\bar{t}$ is the predicted traction without damage and D is updated according to a linear damage law

$$D = \frac{\delta_m^f (\delta_m^{max} - \delta_m^0)}{\delta_m^{max} (\delta_m^f - \delta_m^0)} \tag{3}$$

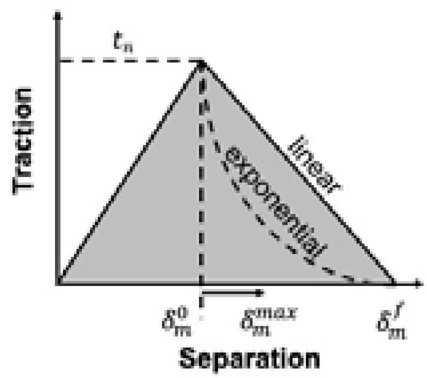

Fig. 2 Illustration of traction separation damage evolution model. The linear damage evolution model is used to update a damage variable D

The finite element model incorporates into the Kapton layer geometry for a CR2032 battery, truncated spring pins (representative of compressing the pins in contact with the substrate), and an array 150 μm diameter vias separated by a distance of $5\sqrt{2}mm$ (Figure 3a,b). Due to complexity of the geometry, linear tetrahedral elements are employed in meshing (Figure 3c). An encastre boundary condition is applied to the stainless steel substrate and the AstroSense geometry is placed in the middle of the substrate (Figure 3d). A displacement boundary condition is applied to the AstroSense geometry in the direction normal to the substrate. Three locations are considered for this displacement boundary: (1) the battery end of the geometry (Figure 3e, red) (2) the middle of the geometry on one side (Figure 3e, blue), and (3) the sensor end of the geometry (Figure 3e, green). The force required to peel the sensor is determined by summing the vertical reaction forces at the nodes in each of these regions.

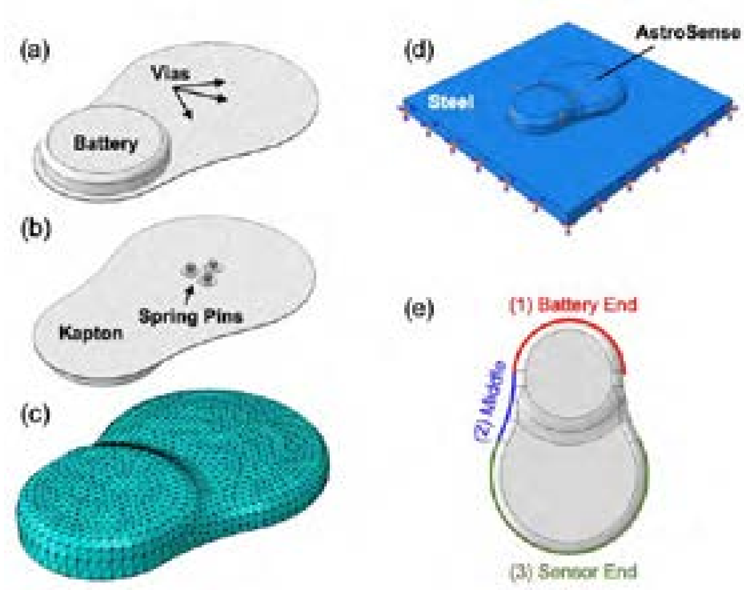

Fig. 3 (a) Top isometric view of Kapton layer showing battery on lower left-hand side and vias (discrete points on right hand side). (b) Bottom isometric view of Kapton layer showing truncated pins. (c) Example mesh applied to AstroSense geometry. (d) AstroSense geometry on top of steel substrate. (e) Locations of applied displacement (peeling) boundary conditions.

C. Material Properties

Material properties were determined with reference to literature values. The properties for the cohesive layer were adjusted to be representative of the data provided by the manufacturer. [2] For this, we modeled a 0.04 mm thick by 25.4 mm wide carrier (Young's Modulus 2e9 GPa) with a .04 mm thick adhesive layer being peeled from a stainless steel substrate as shown in Figure 4, left. One end of the tape layer was displaced vertically at a rate of 5 mm/s, up to 10 mm displacement in a quasi-static analysis step. Representative results from the peel test are shown in Figure 4, right. The legend, indicating $t_n^{(i)}$, represent results from successive analyses in which t_n are iteratively scaled to obtained the target peel force of 110 gms/25.4mm (1.08 N/25.4 mm). Oscillations in the plot result from simultaneous separation of rows of cohesive elements. After separation initiates, the oscillations proceed in a periodic manner. The average of these oscillations was related to the peel force supplied by the manufacturer.[2]

Material properties for the RTV630 were obtained from Jiang *et al*.[3] Material properties for the Kapton film were obtained from DuPont.[4] Other material properties are representative values found on the internet. The material properties used in analysis of AstroSense sensor are summarized in Table 1.

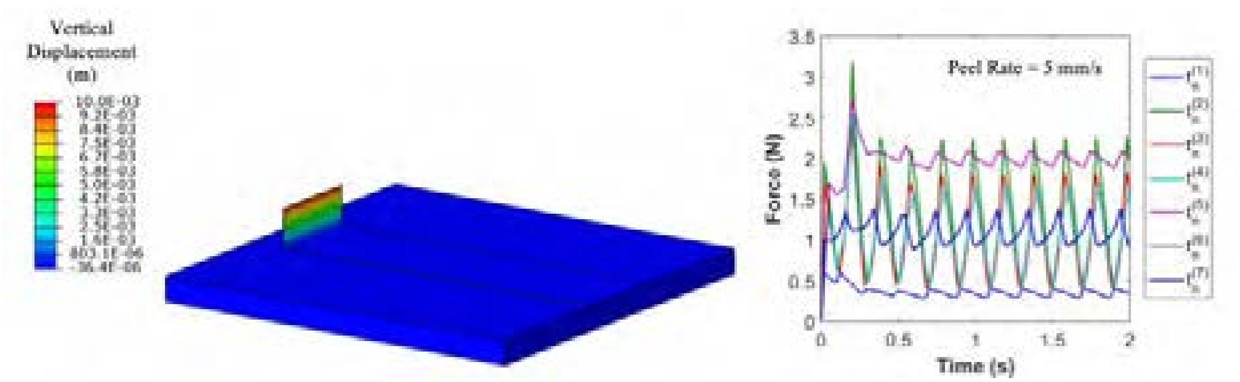

Fig. 4 Left: Peel test with vertical displacement contour. Right: Example results for varying t_n. Oscillations correspond to separation of cohesive layer at each row of elements.

Table 1 Properties used in finite element model.

Material	Density	Modulus	Poisson's Ratio	
Copper (pins)	7764 kg/m^3	110e9 Pa	0.343	
Kapton	1420 kg/m^3	2.76e9 Pa	0.34	
Type 304 SS (substrate)	8000 kg/m^3	200e9 Pa	0.3	
	Density	μ_i	α_i	
RTV630	1070 kg/m^3	-2.77e6 Pa	-2.19	
		6.25e6 Pa	4.93	
		2.20e6 Pa	1.13	
	t_n, t_s, t_t	$\delta_m^f - \delta_m^0$	Modulus	Stabilization
Silicone Adhesive	77,692, 9e6, 9e6 Pa	0.001 m	2e9 Pa	0.001

D. Peeling of AstroSense

After adjusting the traction-separation properties of the silicone tape, peel tests of the AstroSense geometry were evaluated using the locations indicated in Figure 3e. The force displacement results are shown in Figure 5. It is seen that the location of the peeling displacement boundary affects the maximum force required to peel the sensor vertically from the substrate. After the maximum force is exceeded, the cohesive elements exceeding a damage of $D = 1$ are deleted, and the peeling force decreases. The analyses for the sensor and battery peel locations stopped prematurely as the contact area of the remaining cohesive elements decreased rapidly.

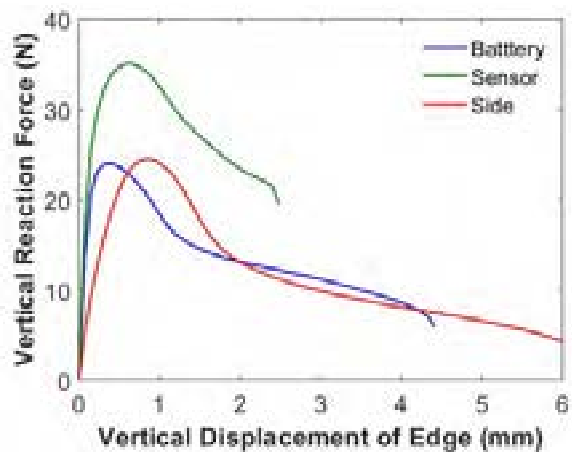

Fig. 5 Force-displacement results for AstroSense geometry peeled from stainless steel substrate using properties in Table 1. Legend corresponds to peel locations indicated in Figure 3

Figures 6 - 8 show the damage evolution variable, D, (top row), von Mises stresses on the top of the Kapton sheet, looking down (middle row), and von Mises stresses on the bottom of the Kapton sheet, looking up (bottom row) for three representative edge displacements for each peel location. Cohesive elements are deleted from the mesh (and turn gray) as the critical separation is exceeded. Comparison of the von Mises contour plots for each load case indicate that the stresses on the bottom surface of the Kapton layer are generally higher than the top layer. Stresses concentrate around the perimeter of the sensor portion and in the transition from the wide, sensor portion to the narrow battery portion of the AstroSense geometry. Asymmetry in the stress results across the plane of symmetry of the sensor is attributed to differences in mesh refinement. For example, in the middle row of Figure 6, the lower half of the contour plot appears more red than the top half. The top half has a higher mesh refinement due to meshing around the 150 μm vias. Refinement of the mesh will be addressed in future investigations. Approximate regions of high stress are illustrated in Figure 9.

E. Conclusions and Recommendations

In this portion of the fellowship, we showed that finite element analysis using cohesive elements could be used to model peeling of the AstroSense geometry from a substrate. The maximum peel force occurs immediately before the initiation of separation of the sensor from the substrate. As the contact area of the remaining cohesive elements decreases rapidly, the solution becomes unstable. The model can be probed to indicate regions of high stress under which separation and failure of electrical components may occur.

Following these preliminary results, the following recommendations are made for future investigations:

1) Experimentally characterize 3M 2477P tape in house to refine cohesive element material model.
2) Refine material model for RTV 630 silicone encapsulent
3) Replace stainless steel substrate with substrate more representative of human skin.
4) Perform detailed characterization of 150 μm vias to better understand conditions under which damage to the electrical circuit occurs.
5) Address solution instability as remaining contact area rapidly decreases.
6) Introduce additional electrical components to geometry.

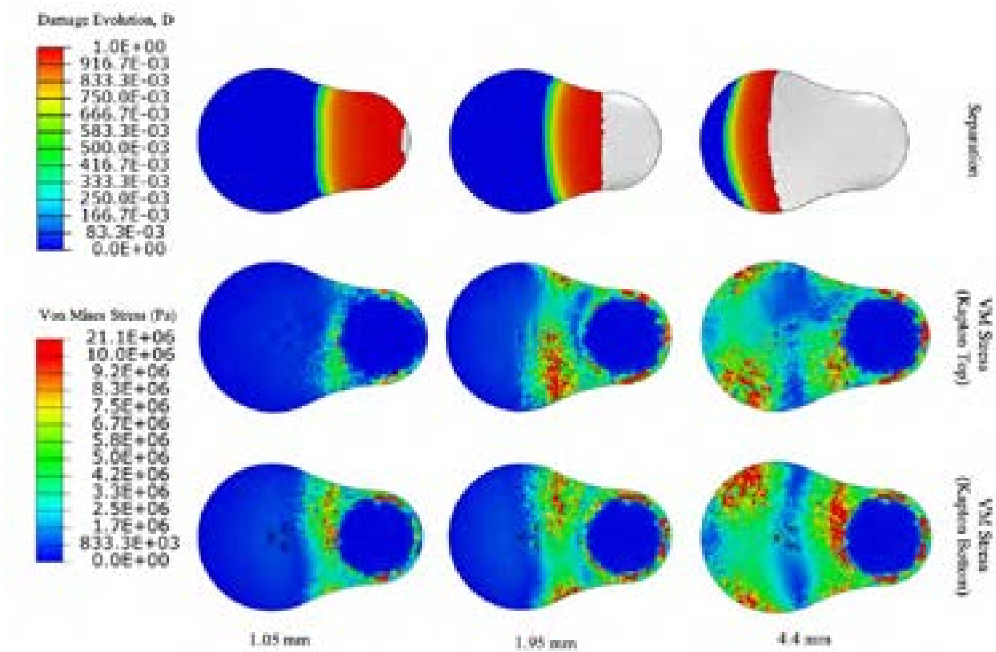

Fig. 6 Contour plots for analysis of AstroSense geometry peeled from battery region. Top Row: Damage evolution variable (looking bottom up). Middle Row: von Mises stresses on top of Kapton sheet (looking top down). Bottom Row: von Mises stresses on bottom of Kapton sheet (looking bottom up). Each column corresponds to increasing vertical displacement of peel location.

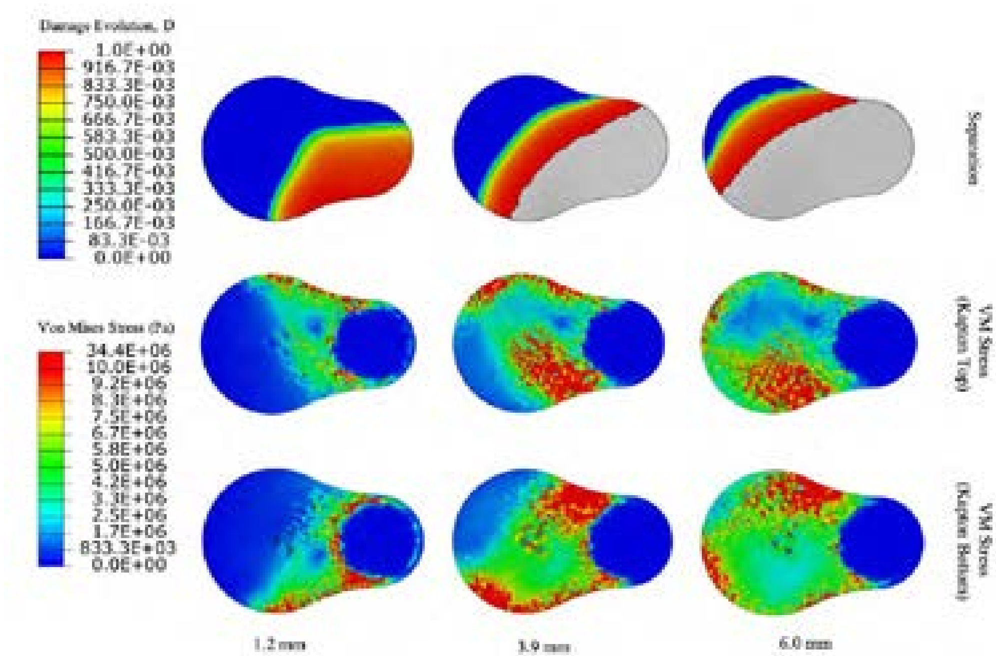

Fig. 7 Contour plots for analysis of AstroSense geometry peeled from side. Top Row: Damage evolution variable (looking bottom up). Middle Row: von Mises stresses on top of Kapton sheet (looking top down). Bottom Row: von Mises stresses on bottom of Kapton sheet (looking bottom up). Each column corresponds to increasing vertical displacement of peel location.

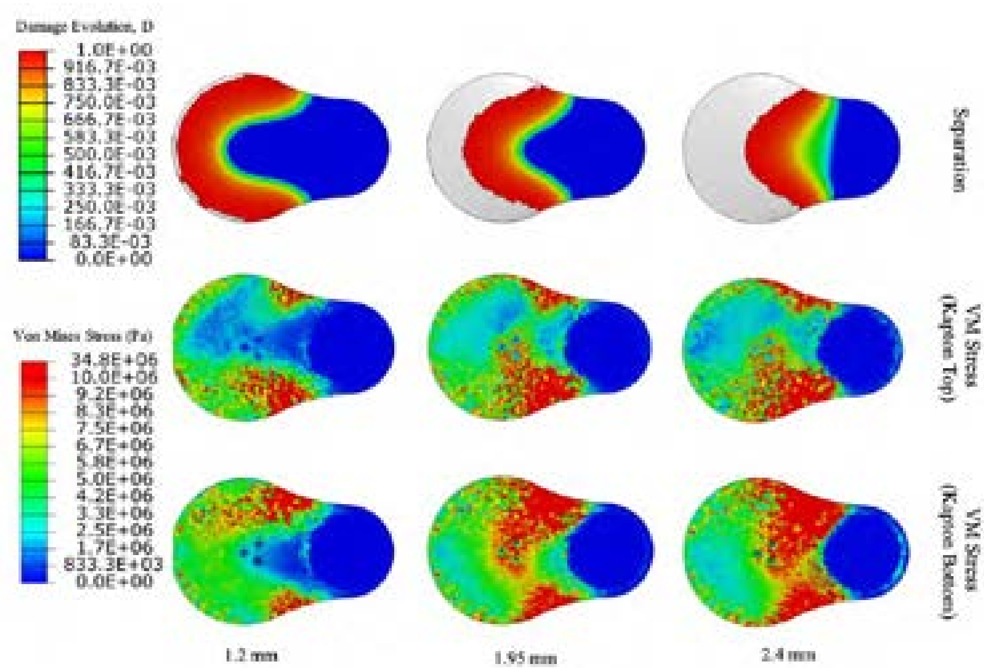

Fig. 8 Contour plots for analysis of AstroSense geometry peeled from sensor region. Top Row: Damage evolution variable (looking bottom up). Middle Row: von Mises stresses on top of Kapton sheet (looking top down). Bottom Row: von Mises stresses on bottom of Kapton sheet (looking bottom up). Each column corresponds to increasing vertical displacement of peel location.

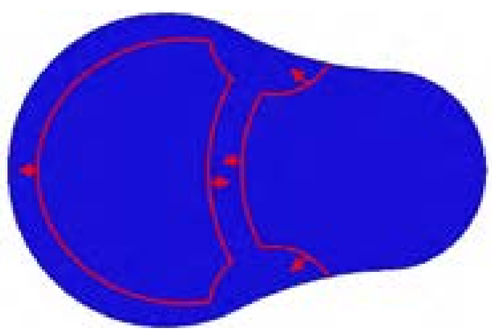

Fig. 9 Depiction of approximate regions of high stress.

III. Origami Supercapacitor

In the second project, Dr. Mailen experimentally investigated the application of self-folding origami to additively manufactured supercapacitors.[5] The fabrication process for the supercapacitor is shown in Figure 10. The process begins by 3D printing an Acrylonitrile butadiene styrene (ABS) and poly(vinyl alcohol) (PVA) substrate. The substrate is placed in a high humidity chamber to reduce the roughness of the PVA layer. Next a silver current collector layer is deposited onto the substrate and annealed at 120°C for 2 hours. An active layer consisting of either (1) activated carbon, carbon black, and PVDF (for electrochemical double-layer capacitors (EDLC)) or (2) graphene/CNTs/Mn_3O_4 dispersed in ethyl-cellulose (for pseudocapacitors (PC)) is deposited on top of the current collector. Finally, a gel polymer electrolyte consisting of PVDF and lithium perchlorate is deposited on the surface of the supercapacitor. A revised version of this supercapacitor replaces the ABS/PVA substrate with a polyimide film.

An array of supercapacitors can be printed to improve charge capacity or discharge rate. It is desired to fold the flat, printed supercapacitor array into a compact shape. This has been demonstrated using manual methods (Figure 11), but the process is labor intensive. To address the labor intensive issue, we recommend the use of self-folding origami

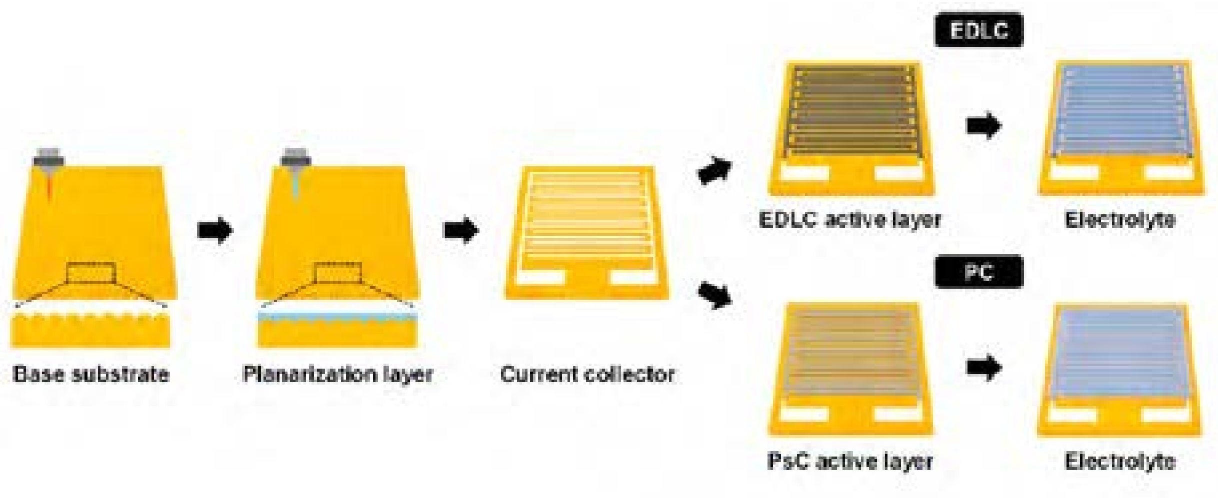

Fig. 10 Fabrication process of prototype substrate. Left to right: additive manufacturing of ABS substrate, chemical treatment for planarization, deposition and annealing of silver current collectors, deposition of active layer, and deposition of electrolyte.

using polystyrene (PS) shape-memory polymer (SMP) sheets. SMP sheets are pre-strained such that they shrink to approximately half of their original dimensions in plane when heated above the glass-transition temperature, T_g. These sheets can be patterned using an opaque marker or ink from an inkjet printer. When exposed to an infrared (IR) light, the patterned regions locally heat due to local light absorption of the ink. This introduces a gradient in temperature and shrinking through the thickness of the sheet, and the sheet folds along the ink pattern (Figure 12).[6–10] The temperature required to initiate folding in the PS SMP sheet ($T \approx T_g = 103°C$) is exceeded by some of the processing temperatures for the 3D printed supercapacitor, thus a laminated approach is suggested.

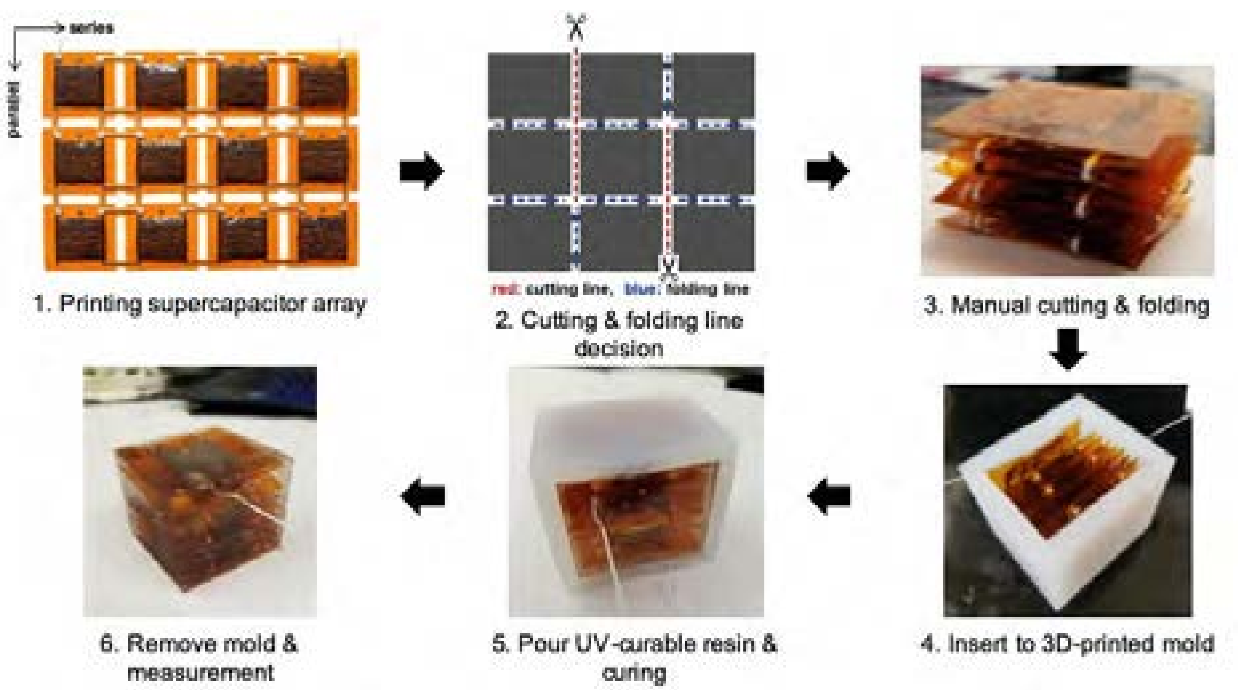

Fig. 11 Processes for manually folding and packaging of printed supercapacitor array. (Figure courtesy of Myeong-Lok Seol.)

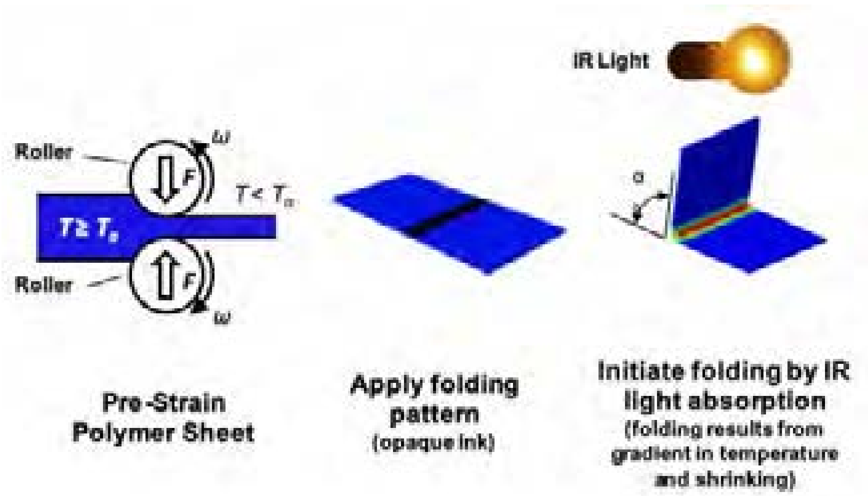

Fig. 12 Self-folding process using shape memory polymer sheets. Left: pre-straining of polymer sheet before acquisition. Middle: patterning of polymer sheet with black ink. Right: Self-folding by exposure to IR light.

A. Materials and Methods

Dr. Mailen began a preliminary investigation using PS SMP sheets commercially available as Graphix® Shrink Film. These sheets were laminated with either aluminized Mylar film (emergency blankets from Staples) or 1 mil thick Kapton tape. The Mylar film was glued to the PS sheets using 3M Super 77 spray adhesive (Lowe's Home Improvement). Ink patterns were manually drawn on the PS sheets using an opaque marker.

B. Results

Samples comprising either the Mylar film or the Kapton tape (passive layers) laminated with the pre-strained PS sheet (active layer) were considered. Variations were considered in which the ink was patterned on the PS sheet either between the active and passive layer, or opposite of the passive layer (Figure 13). It was observed that the Mylar film was thin enough to not influence the folding direction of the PS film, i.e., the sample folded toward the patterned side of the PS sheet. However, the Mylar sheet influenced the rate and maximum angle folded. An example of a Mylar laminated sample with the ink between the Mylar and the SMP is shown in Figure 14, left, where it is seen that the Mylar separates slightly from the ink region during folding. In other samples, it was also observed that the Mylar film was able to block the IR light, and thus prevent folding, for time spans typically required to fold samples (10 seconds). For samples with the Kapton tape, it was observed that the Kapton tape was thick enough to cause the laminated sample folded away from the passive layer, regardless of the location of the ink, with limited influence on the maximum angle folded. This is illustrated by the samples in Figure 14, right. In these samples, the ink on the left is between the active and passive layers (Figure 13A), whereas the ink on the right is on the opposite side of the active layer as the passive layer (Figure 13B). The three samples, from front to back, are comprised of a single active layer of PS laminated with one, two, and three layers of Kapton tape respectively. In all three samples, the PS SMP is the top layer shown.

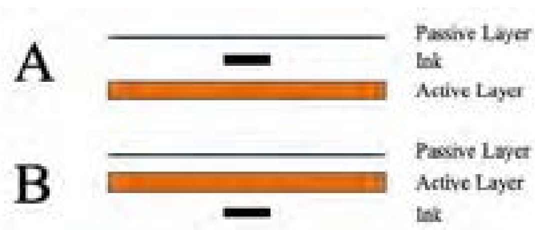

Fig. 13 Orders of lamination of active layer (SMP) with passive layer (Mylar or Kapton) and location of ink. A. Ink between active and passive layers. B. Ink on opposite side of active layer as passive layer.

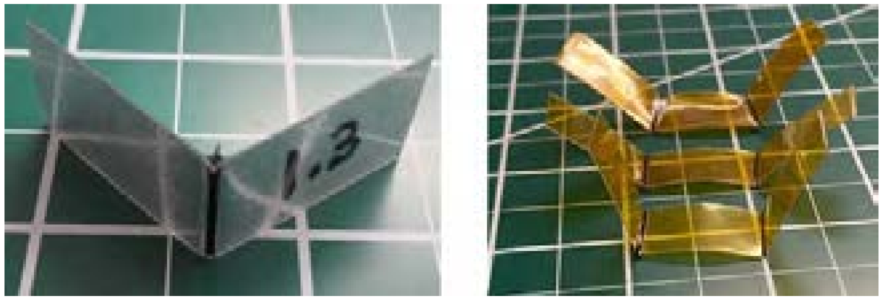

Fig. 14 Left: Laminate Mylar and SMP sheet with ink between the two layers. Right: SMP sheet laminated with (front to back) one, two, or three layers of Kapton tape. The ink patterns on the left of the image are between the active and passive layers, wereas the ink on the right is on the opposite side of the active layer as the Kapton tape. In all three cases, the SMP is the top layer shown.

C. Recommendations for Self-Folding Supercapacitor

Based on the preliminary results described above, it is recommended to laminate the Kapton film-based supercapacitor with the Mylar film and ink patterned SMP layers after printing and cutting the supercapacitor pattern (Figure 15A). Ink patterned on both sides of the SMP sheet allow the supercapacitor to fold into a desirable Miura-Ori pattern upon exposure to IR light (Figure 15B,C).The Mylar film serves to block the supercapacitor from the IR light while still allowing self-folding. Larger single unit-cells of the Miura-Ori pattern were self-folded as part of this preliminary investigation (Figure 15D,E).

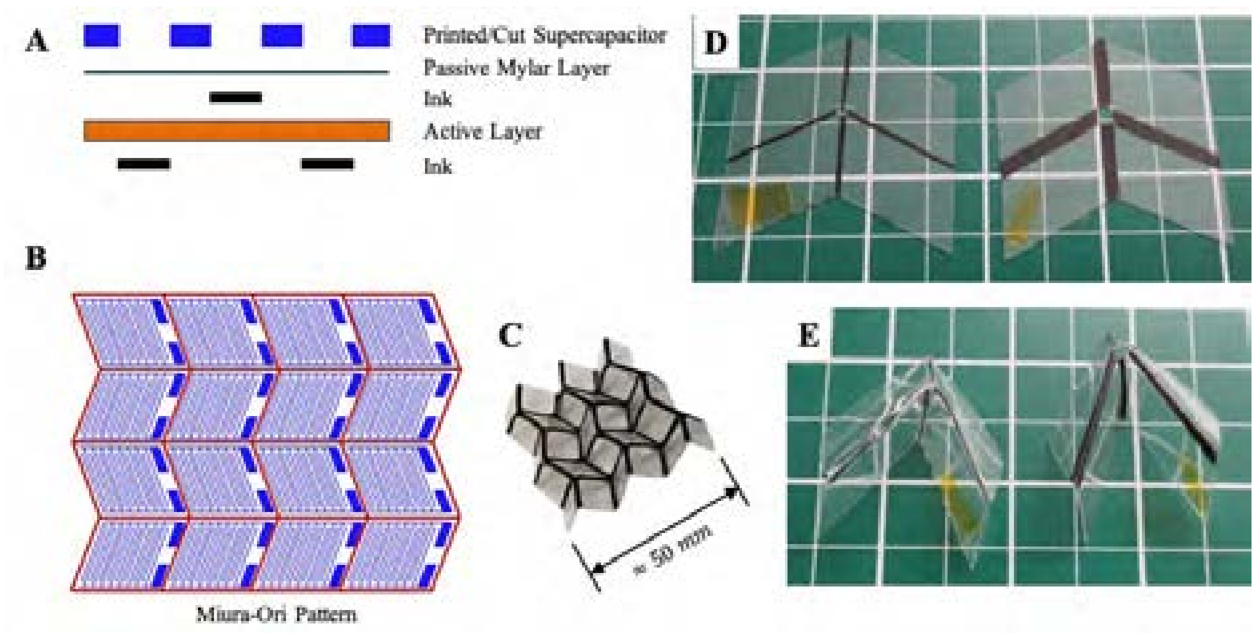

Fig. 15 A. Proposed stack-up sequence for self-folding origami supercapacitor. B. Proposed Miura-Ori pattern containing individual supercapacitors which can be connected in series or parallel C. Miura-Ori pattern self-folded in Dr. Mailen's laboratory at Auburn University. D. Large, single unit cells of Miura-Ori pattern differing only in ink pattern width. The white grid lines in the background are spaced at 12.7 mm intervals) E. Samples from D. after self-folding.

Acknowledgments

The author of this report would like to acknowledge the support of the NASA Marshall Space Flight Center Summer Faculty Fellowship program for supporting the PI throughout the summer 2020.

References

[1] Pantchenko, O., "Development of Flexible Multi-Sensor Device," Quarterly Technical Report, NextFlex, Mar. 2020.

[2] "3M™ Medical Silicone Tape 2477P, Double Sided Silicone/Acrylate Thermoplastic Elastomer, Configurable," , 2020. URL `https://www.3m.com/3M/en_US/company-us/all-3m-products/~/3M-Medical-Silicone-Tape-2477P-Double-Sided-Silicone-Acrylate-Thermoplastic-Elastomer-Configurable/?N=5002385+3294739648&rt=rud`, archive Location: US.

[3] Jiang, T. Z., Xue, P., and Butt, H. S. U., "Pulse shaper design for dynamic testing of viscoelastic materials using polymeric SHPB," *International Journal of Impact Engineering*, Vol. 79, 2015, pp. 45–52. https://doi.org/10.1016/j.ijimpeng.2014.08.016, URL http://www.sciencedirect.com/science/article/pii/S0734743X14002115.

[4] "Kapton® HN General-Purpose Polyimide Film," , 2020. URL https://www.dupont.com/products/kapton-hn.html.

[5] Seol, M.-L., Nam, I., Ribeiro, E. L., Segel, B., Lee, D., Palma, T., Wu, H., Mukherjee, D., Khomami, B., Hill, C., Han, J.-W., and Meyyappan, M., "All-Printed In-Plane Supercapacitors by Sequential Additive Manufacturing Process," *ACS Applied Energy Materials*, Vol. 3, No. 5, 2020, pp. 4965–4973. https://doi.org/10.1021/acsaem.0c00510, URL https://doi.org/10.1021/acsaem.0c00510, publisher: American Chemical Society.

[6] Liu, Y., Boyles, J. K., Genzer, J., and Dickey, M. D., "Self-folding of polymer sheets using local light absorption," *Soft Matter*, Vol. 8, No. 6, 2012, pp. 1764–1769. https://doi.org/10.1039/C1SM06564E, URL http://pubs.rsc.org/en/content/articlelanding/2012/sm/c1sm06564e.

[7] Liu, Y., Mailen, R., Zhu, Y., Dickey, M. D., and Genzer, J., "Simple geometric model to describe self-folding of polymer sheets," *Physical Review E*, Vol. 89, No. 4, 2014, p. 042601. https://doi.org/10.1103/PhysRevE.89.042601, URL http://link.aps.org/doi/10.1103/PhysRevE.89.042601.

[8] Mailen, R. W., Liu, Y., Dickey, M. D., Zikry, M., and Genzer, J., "Modelling of shape memory polymer sheets that self-fold in response to localized heating," *Soft Matter*, Vol. 11, 2015, pp. 7827–7834. https://doi.org/10.1039/C5SM01681A, URL http://pubs.rsc.org/en/content/articlelanding/2015/sm/c5sm01681a.

[9] Mailen, R. W., Dickey, M. D., Genzer, J., and Zikry, M. A., "A fully coupled thermo-viscoelastic finite element model for self-folding shape memory polymer sheets," *Journal of Polymer Science Part B: Polymer Physics*, Vol. 55, No. 16, 2017, pp. 1207–1219. https://doi.org/10.1002/polb.24372, URL http://onlinelibrary.wiley.com/doi/10.1002/polb.24372/abstract.

[10] Mailen, R. W., Dickey, M. D., Genzer, J., and Zikry, M., "Effects of thermo-mechanical behavior and hinge geometry on folding response of shape memory polymer sheets," *Journal of Applied Physics*, Vol. 122, No. 19, 2017, p. 195103. https://doi.org/10.1063/1.5000040, URL http://aip.scitation.org/doi/abs/10.1063/1.5000040.

2020 NASA-MSFF Final Report (abridged):

Recycling In-Space Plastic Waste for Deep-Space Additive Manufacturing: Capability Assessment and Technology Development, Part -II[1]

BHABA R. SARKER, PhD, PE[2]
Louisiana State University, Baton Rouge, LA 70803

and

TRACIE J. PRATER, PhD[3]
CHRISTOPHER E. ROBERTS, PhD[4]
FRANK E. LEDBETTER, III PhD[5]
PHILLIP B. HALL[6]
NASA Marshall Space Flight Center, Huntsville, AL 35812

ABSTRACT

Recycling plastics and other materials in deep space has become a pressing issue for NASA and other international space agencies. These technologies are needed to manage waste on long duration missions. Two main problems, which will be exacerbated with missions beyond low earth orbit, are recycling of waste in space and enhancing additive manufacturing (AM) capabilities to help reduce waste by enabling use of otherwise nuisance material.. While the general problem centers around the recycling process of trash and waste in deep space missions, the specific objective here is to explore the additive manufacturing process, especially the feedstock or filament coil production out of these waste materials, so that the filament coil can be used as feedstock for AM manufacturing of essential tools or other necessary parts. The prevailing environment of the crews, with limited storage space, may drive the need to manufacture the tools and parts out of trash and waste. This research focus on the basic theme of 3R (reusing, recycling or repurposing) processes for the waste in the space station and future habitable volumes in lunar orbit or on a planetary surface. An in-depth analysis of different aspects of the problem has been reported in Part I report (Sarker *et al.* 2020). This abridged report subsequently highlights some general findings and recommendations to enhance the system capability..

Nomenclature

N = number users,
n_{ij} = 1 if the user i completes the task j successfully or 0 otherwise,
p = Probability of unacceptability of filament being unacceptable after the quality control check,
R = number of tasks,
T = Total processing time when no re-feeding is done (i.e., no defective filament is produced),
t_{ij} = the time spent by user i to perform task j, irrespective of completion or quit,
t_p = Processing time (or recycling time taken from the beginning to end),
t_R = Defective filament refeeding time to the shedder,
ξ_E = Effectiveness (i.e., the completion rate expressed in proportion or percentage),
η_R = Overall relative efficiency (ratio of *successfully* completed task time to total time taken., $0 \leq \xi_E, \eta_T, \eta_R \leq 1$,
η_T = Time-based efficiency is measured in terms of task time giving a weighing factor on time.

1. INTRODUCTION

Long-duration human space exploration missions beyond low Earth orbit (LEO) and into deep-space need solutions to effectively manage generated trash and other waste. The generation of such trash and waste causes significant space and technological problems. For the International Space Station (ISS), the storage of foam is an issue (it must be wrapped in Nomex for storage due to flammability concerns and cannot be out/unwrapped where the crew are for an extended

[1] Part I is a 42-page main report with all detailed data, submitted to the research group (all authors).
[2] Elton G. Yates Distinguished Professor, Dept. of Mech. & Industrial Engineering, LSU, Baton Rouge, LA 70803; bsarker@lsu.edu
[3] NASA Marshall Space Flight Center, Materials Engineering Support Office (MSFC-EM04), Huntsville, AL, 35812, tracie.j.prater@nasa.gov
[4] NASA Marshall Space Flight Center, Materials Engineering Support Office (MSFC-EM04), Huntsville, AL, 35812; christopher.e.roberts@nasa.gov
[5] NASA MSFC, Science and Technology Office (MSFC-ST23, MIPSS-SME), Huntsville, AL, 35812; frank.ledbetter@nasa.gov
[6] NASA Marshall Space Flight Center, Science and Technology Office (MSFC-ST23), Huntsville, AL 35812; phillip.b.hall@nasa.gov

period). With Gateway, the logistics and habitation modules will be much smaller relative to ISS and the ability to return "trash" from Gateway in the way Cygnus currently does for ISS is uncertain, so storing large amounts of launch packaging there may not be viable. Therefore, different logistics reduction projects are developing new technologies to mitigate these issues with waste management strategies. Trash takes up space and presents a safety risk to the crew from biological and physical hazards. Lockhart (2018) indicated that four astronauts can generate 2,500 kilograms of waste during a year-long mission. Current waste disposal methods on the International Space Station (ISS) rely on astronauts' manually processing the trash by placing it into bags and then loading it onto a designated container for storage, which, depending on the craft, returns the trash to Earth or burns up in the atmosphere. This logistics model will be difficult for missions beyond LEO.

Generally, reusing, recycling and repurposing (3R) the trash is one way of mitigating it and can also serve to potentially transform waste into sources of other supplies for the mission. For example, crews can process small pieces of trash in a high-temperature reactor which breaks them into water, oxygen, and other gases, which the crew can use or vent as needed; the remaining volume of the waste is reduced in size and is no longer biologically active [Lockhart 2018]. Recycling and repurposing all (or as much of the mass that is launched up as possible) is key for sustainable, long-duration space travel. Waste conversion and volume reduction will increase the available volume for science and exploration tasks, close the manufacturing loop for human spaceflight by reducing reliance on feedstock upmassed from earth, and repurpose nuisance material onboard spacecraft. The general problem lies in the issue of whether any of these processes are at all logistically and economically viable for spaceflight, considering the space the systems will occupy, energy requirements, and the time for crew required to tend them.

The trash and waste materials on space missions could consist of metals, non-metals (plastic, foams and packaging materials) and liquids (water, drinks, chemicals). A significant portion of this waste are plastics. These occupy space and create hazards to crew health and the ISS environment. Therefore, this paper will focus on recycling of plastic materials to some useful purposes onboard the space station.

Additive Manufacturing (AM), also known as 3D printing, is a process for making parts by joining materials layer by layer. While it was initially reserved mainly for producing sample or prototype parts, the technology has evolved over the years to enable manufacturing of fully functional production parts for automotive, aerospace, medical, and a wide range of other markets. AM encompasses a wide range of technologies such as laser sintering, fused filament fabrication, and stereolithography. Recently, injection molders have used this technology both for low-volume production parts made of specialized plastics and for mold-making. Therefore, given the prevailing situation on space missions regarding waste, especially plastics materials, AM for recyclable materials will be an appropriate technology to use the 3R processes within the spacecraft. To date, the fused filament fabrication (FFF) printing technique for polymers has been demonstrated onboard ISS. The ISM project is currently maturing two 3D printing technologies for metals (bound metal deposition and wire arc additive manufacturing) to flight.

2. Problem Description

While plastics and foams are the lightest of all materials used in the space station, the trash and waste are composed mostly of them, occupying valuable space. If trash were repurposed, this volume could be utilized for new science and technologies to advance human knowledge. Reusing and/or recycling creates a tradeoff between economic advantage and technical advancement that needs be assessed for different missions. The work under the recycling/reuse component of the ISM portfolio has historically focused on reuse of plastics and packaging materials:

(a) ***Filament for 3D (3-dimensional) printing*:** Development of manufacturing technology for recycling, specifically the development of systems adaptable to ISS, which can recycle used polymer parts or plastic packaging materials into filament for 3D printing. This also includes development of in-process monitoring capabilities for filament production, which provide an in-line assessment of the diameter of the filament and the flexural modulus.

(b) ***Development of materials which are intended to be reused and recycled*.** This includes development of thermally reversible polymeric materials which can be reprocessed over multiple recycling and printing cycles without significant degradation or a deterioration in processability. Materials may be produced in the form of films or foams which are then pelletized and extruded into a wire form. The plastic wire is spooled into feedstock for 3D printing. An economic assessment and recycling multiplicity can be investigated with respect to its quality and useful life to evaluate feasibility of the process.

2.1 Goal and Objectives:

Given the problems encountered in space missions, NASA's current main goal is to minimize the trash and waste in space station by the 3R processes to mitigate the prevailing issues onboard (storage space, health and hazards, etc.) and repackage and redistribute payloads and supplies at the ground level. To date, the ISM project has only explored very specific materials and application of recycling technology on space missions. Thus, the major objectives are to fulfill the following objectives:

(1) ***Material choice*****:** Assess which materials used as plastic packaging for ISS currently are recycled in industry. Delineate which packaging materials truly represent nuisance material from those for which there is an existing method for reprocessing. Additional information on frequency of use of packaging materials was provided by NASA Johnson Space Center. Categorization of materials, flexibility and usability, cost evaluation and other qualifiers of the materials are the major factors in decision-making processes about recycling which need to be highlighted in the analysis.

(2) **Process planning:** Depending on the properties of the materials for recycling, process plans for making the 3D printing filaments may differ due to types of raw materials (e.g., plastics and other polyesters), quality and form of finished products required (e.g., filament coil) and varying requirements of recycling equipment (e.g., shredder, extruder, and plastic injection molder). When an industrial process for recycling of an existing material used in ISS applications is identified, additional information needs to be provided on: (a) the process steps for recycling, (b) power requirements and physical footprint (dimensions, volume, mass) of systems typically used in processing, (c) assessment of scalability of the process for space applications, (d) yield of the process, and (e) how recycled materials are used in industry. The general recycling process may remain unchanged, but depending on the different types of plastics materials, the processing steps and required time may change.

2.2 General Methodology

As the 3R-process indicates, the recyclable materials on the space station need to be sorted first into different categories or classifications before any additive manufacturing initiative is undertaken. Given the existing inventory of recyclable materials onboard *plus* the potential of incoming trash and waste, this sorting will be an ongoing process. There are several types of plastic materials currently being used in the space station. In a future mission with 3R, nuisance materials are either to be avoided or will need to be disposed of quickly through the AM process to free up space for additional utilization—they should be triaged/prioritized for recycling if multiple materials are accumulating. Once a critical volume of any kind(s) of recycling materials accumulates, especially the ones that occupy more space and/or warrant health hazards and habitat issues, a decision on material choice should be made for one that will mitigate faster the creeping issues for 3R processes within the spacecraft. The classification will be discussed later.

Depending on the properties of the chosen material, a process sequence is planned wherein the material is first shredded/fragmented to small pieces, which is followed by a molding process prescribed for that material and finally drawing it into a filament coil to be used for additive manufacturing. Therefore, at any point in time at the space station, the crews have two basic choices: (a) materials selection, and (b) the corresponding processing plans.

The process plans for most materials on board are mostly the same except in some cases they may differ depending on the material properties and processing capability of the existing facilities. Therefore, it is essential to classify different plastics and know their material properties so that appropriate process plans can be developed for certain type of plastics and special manufacturing facilities (shredder, extruder, etc.) can be selected prior to the mission. Figure 1 illustrates the general pre-recycling process of the plastic materials before they go into the actual recycling process, which will be discussed in subsequent section as pertinent.

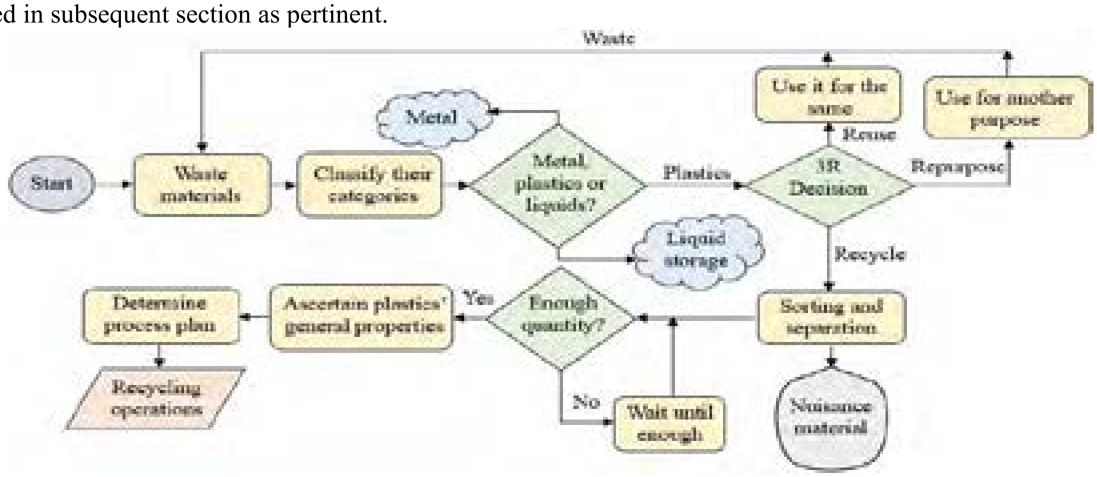

Figure 1. General pre-recycling process flow of plastics

3. Classification of Recycling materials

The waste materials in space could be plastics, metal or ceramics type materials. Based on frequency of use, plastics and light metals (aluminum and its alloys) are the two preferred materials used in space as candidates for recycling. Depending on their material properties and usage, we classify each type of materials into their sub-groups for ease of planning and design of the AM system.

3.1 Plastic Materials Classification

In today's daily life including NASA missions, plastic is an essential component of many items, including water bottles, beverage containers and packaging. Depending the mechanical and chemical properties, the plastics are classified with SPI (Society of Plastic Industry) codes. Most commonly there are several types of plastics which dominate the recycling landscapes. Their physical, material and chemical properties are well known, and they are easily distinguishable to make some informed decisions about their recycling process. Seven categories of plastics that are seen around us quite frequently and are well-studied for recycling include: (1) Polyethylene Terephthalate (PETE or PET), (2) High-Density Polyethylene (HDPE), (3) Polyvinyl Chloride (PVC), (4) Low-Density Polyethylene (LDPE), (5) Polypropylene (PP), (6) Polystyrene or Styrofoam (PS), and (7) Miscellaneous plastics (includes polycarbonate, polylactide, acrylic, acrylonitrile butadiene, styrene, fiberglass, and nylon).

3.1.1 Mechanical and Thermal Properties

The mechanical properties of plastics can be dramatically altered by environmental conditions, and particularly by extreme temperatures. Some plastics may portray normally ductile behaviors, but when exposed to low temperatures may become brittle. It is important to understand the conditions that a product may endure to ensure that those conditions are replicated during testing. For example, if glue tube is too rigid (high modulus of elasticity), it will not allow the user to comfortably or successfully squeeze glue out of the tube. So, a material with a lower modulus of elasticity will help increase the softness or flexibility to dispense the glue better. This may include many layers of thin plastic made up of different grades of HDPE, which allowed the tube to be easily squeezed and easily recycled. Modulus is also a key parameter for enabling the material to be spooled into a form that is compatible with AM.

Table 1 provides the general material properties of these materials so that this information can be used for selecting the plastic waste for additive manufacturing. Packaging materials for different kinds of payloads at the ground level can also be appropriately chosen to ensure compatibility with future recycling processes on the space station. It may be noted that the data presented in Table 1 are collected from different sources which do not report consistently.

Table 1. Material and thermal properties of plastics

SPI Code	Types of Plastics	Density (gm/cm^3)	Elastic Modulus (GPa)	Tensile Strength (MPa)	Flexural Strength (MPa)	Hardness (R)	Melting point ^0C
1	PETE or PET	1.3-1.4	2.0 -2.7	152	3380	50-100	126-135
2	HDPE or PE-HD	0.91-0.96	0.41-1.49	23-29	970 – 1380	33-66	120-140
3	PVC or V	1.41	2.9	52	88	115	100
4	LDPE or PE-LD	0.917-0.930	0.19-0.52	52	151 – 2200	45-59	108-121
5	PP	0.9	1.5-2.0	20-40	8.35-11.04	57-120	200-300
6	PS	1.07	3.35	34	20.60	80	200-250
7	OTHERS	-	-	-	-	-	-

* 1 MPa (Mega-Pascal) ≈ 145.0377 psi and 1GPa = 1000 MPa. = 145,037 psi

With respect to additive manufacturing, material density, modulus of elasticity, flexural and tensile strength, maximum allowable stress, and some chemical properties, such as heat resistance and melting point, play an important role selecting the plastic materials for recycling and processing into AM feedstock. Two commonly used plastics, HDPE and LDPE are thus compared here to reflect their general material characteristics.

3.1.2 Filament quality measure and control: In-line/off-line measurement:

Filament coil, which is the feedstock for a 3D printer is the first output of a plastic recycling process for additive manufacturing. The precision of 3D printing depends on the production quality of the filament. The ability to control the flow of your filament makes printing easier and more consistent. One of the major factors affecting this control is *filament diameter*. If the 3D printer receives the same diameter of filament, it will set the speed, accordingly, extruding a perfect amount. The printer has no way to adjust when it is set to extrude the product, but if the filament diameter fluctuates then the amount it extrudes will be inconsistent—this can lead to blobby prints due to over-extrusion or weak prints due to under-extrusion—perfectly round 3D printer filament prints best. If it has too much ovality, it may cause the filament to twist creating unevenly extrusion or jam in the printer.

3.2. Metal Classification and Recycling:

Another area of interest to ISM and the on-orbit servicing, assembly and manufacturing (OSAM) area is metal recycling. Materials of interest for in-space metals recycling include AA2219, AA6061, AA7075, SS 316 and Ti-64. A more limited, ancillary activity like the above work on polymers would consider any processes which are typically used to recycle these metallic materials in industry and their potential for infusion into space missions. Most fixtures and frames of the stations are richly made of these materials. Thus, scalability of this recycling application will be the overarching consideration for future missions.

The mechanical properties of AA6061 differ based on how it is heat treated or made stronger using the tempering process. Its modulus of elasticity is 68.9 GPa (10,000 ksi)—this value measures the alloy's stiffness, or resistance to deformation. Generally, this alloy is easy to join via welding and readily deforms into most desired shapes, making it a versatile manufacturing material. AA7075 can match most steel alloys in terms of strength. On the other hand, AA7075 is one of the hardest aluminum alloys available. While AA 7075 is less workable than AA6061, if the designer's greatest consideration is strength, then AA7075 may be preferable. The material properties of different aluminum, steel and titanium alloys are shown in Table 2.

Table 2. Properties of aluminum, steel and titanium alloys used in aerospace

Types of Alloy	Density (gm/cm^3)	Elastic Modulus (GPa)	Tensile Strength (MPa)	Flexural Strength (MPa)	Hardness (HRB)	Melting point ^{0}C
AA 2219	2.84	73.8	172-476	-	72	543
AA 6061	2.70	68.9	124-290	299.71	60	585
AA 7075	2.81	71.9	572	30 - 280	87	477
SS 316	7.87	193	290	170	79	1400
Ti-6-4 (Ti-6Al-4V)	4.43	113.8	950	490 - 800	36	1604

3.3 Selecting Plastic for Additive Manufacturing

Additive manufacturing is a low- or no-pressure process compared to the high pressures of injection molding. The AM process often relies on the application of thermal energy to create inter-layer adhesion and layer-to-layer consolidation. Pai-Paranjape (2018) mentions that as heat management systems in AM vary so does the form in which material (filaments, liquids, powders and pellets) is supplied and delivered. The heat profiles in printers and the thermal properties of polymers can influence rheological behavior and affect the way material layers are consolidated, resulting in different properties compared to those of injection-molded parts. Even post-processing techniques for additively manufactured parts, such as support removal, vapor smoothing, sanding and sand blasting, and thermal curing, are different from techniques for injection-molded parts. Nylons have been used for SLS techniques to scale to production batches, but this is typically for aerospace parts where quantities are in the low thousands not mass-produced packaging. Materials traditionally used to print prototypes generally are *not expected* to meet the demand of high-volume production and the requirements of end-use parts, from mechanical properties to aesthetics.

3.4 Guidelines for Process and Material Selection

Although selection ultimately depends upon the requirements of each application and the manufacturing process, the following can be considered general guidelines about candidate materials for major types of additive manufacturing. Some of these processes are (a) fused deposition, (b) laser sintering, (c) large format am, (d) stereolithography: (e) hp multi-jet fusion and (f) carbon CLIP process.

4. IN-SPACE RECYCLING

Plastics recycling is done in a significant scale around the world and there is considerable research conducted to discover the most efficient ways to recycle. Because raw materials have a high value and are a precious resource, the industry makes every effort to recover as much as possible to impart cost savings and reduce environmental impact.

There are two primary methods to recycle plastics, mechanical recycling and feedstock recycling:

(a) *Mechanical recycling* is the simplest method. Mechanical recycling is where the plastics, which soften on heating, are, reformed into molding granules to make new products. The process involves collection, sorting, cleaning/washing, shredding, reduction into flake (film and sheet) or granules which may then need washing and drying. This is then re-compounded with additives and/or more virgin raw material, extruded and chopped into pellets for reuse.

(b) Feedstock *recycling* involves breaking down polymers into their constituent parts using heat or pressure. In turn, these parts can be used to make new plastics and chemicals. Feedstock recycling provides benefits and improvements when the materials being recycled are mixed or contaminated.

The goal of plastic recycling in the spacecraft is to minimize the storage space and health hazards caused by plastics and create a cleaner and greener environment by a 3R process which, in turn, helps produce new plastic products using virgin materials. Plastic is inexpensive, durable, lightweight, and versatile. It can be easily molded and remolded into different products that find use in a plethora of applications. The recovery and recycling of plastic products in the spacecraft will become extremely important on future space missions beyond low earth orbit. New plastic materials can be thermoformed, foamed, coated and extruded into useful products and packages on demand.

4.1 Plastic reprocessing/recycling

Plastic recycling refers to the process of recovering scrap plastic materials and reprocessing them into useful, functional items. These plastic products and packages account for 10% of the total waste produced across the globe. The plastic recycling process utilizes 88% less energy than it requires when producing new plastic products from virgin raw materials (CMC 2020). However, scrap plastic recycling faces many challenges that range from sorting mixed plastics and processing them, to removing residues and recycling the materials.

In the general recycling process, first the collected plastics or polymers on a space mission will be identified by the crew on board. The ground personnel will also remain aware of the inventory of trash and waste in the crew habitat. The habitat will have some adaptable recycling system compatible with the input raw materials (plastics or metals). It is assumed that the recycling process can be completed within the power and other operational constraints of the overall system. The six steps needed to produce filaments from plastics are:

(a) *Collection:* Plastic products and packaging materials like containers, jars, bottles and bags are collected from restaurants, commercial businesses and homes.

(b) *Sorting:* After collecting materials for recycling, they are transported to the recycling facility where they are sorted manually or with machines. Contaminants are removed from the plastic waste. This sorting process may be based on color and resin content.

(c) *Washing:* Plastics are washed to clean and removes all impurities before processing.

(d) *Shredding:* Cleaned plastic wastes are then shredded into small, reusable fragments using plastic shredders—these fragments are re-sorted again by weight to undergo different deconstruction processes where they are cut into small flakes or ground into particles adaptable to the remanufacturing facilities (recyclers).

(e) *Disinfecting:* Plastic is cleaned several times during the plastic recycling process. Recycling centers employ specialized machines to sort and separate freshly washed plastic flakes based on their resin content.

(f) *Manufacturing:* This is the final step of the plastic recycling production process, wherein the plastic particles are smashed and melted into pellets, which are then used for the manufacturing of finished plastic products through an extrusion process or drawn into filament coils for additive manufacturing.

The physical and thermal qualities of filaments (diameter, modulus of elasticity, melting point, etc.) will be monitored through special devices to ensure the filament is manufactured within certain acceptable quality limits. Once it passes the quality tests, the filament coils would then be stocked for AM use on the spacecraft. Any rejected recyclable materials will be fed back to the process again for reprocessing or scrapped to trash permanently. There are many difficulties in fully adopting the terrestrial recycling process flow to a space mission—space station has limited physical space, limited power, crew (processes must be safe to operate in the vicinity of humans), and microgravity (some processes may be gravity dependent). Therefore, operating a new recycling process in microgravity should be undertaken carefully, considering all the physical and environmental factors.

4.2 Compatibilization and Rebuilding of Mixed Plastic Waste Fractions

Mechanical recycling of mixed plastic waste streams such as post-consumer solid waste is a technological challenge, due to the presence of a wide variety of commodity polymers in waste streams. Vilaplana and Karlsson (2008) argue that recycled mixed polymeric blends usually have low compatibility between the different polymeric components, due to limited interfacial adhesion. This leads to polymeric dispersion microstructures with poor mechanical properties. Improvements in the procedures for separating co-mingled waste streams may lead to more effective mechanical recycling, but this procedure is time consuming and never fully effective. The mechanical recycling of mixed waste streams could be enabled by the upgrading of mixed polymeric fractions through the inclusion of suitable additives. These additives could protect the recycled blend components from degradation during reprocessing, improve the interfacial adhesion and dispersion of the blend components, and even enhance the molecular structure of the mixed polymeric system by promoting chemical reactions during melt processing (rebuilding by reactive extrusion).

Many commercial compatibilizers (agents) and impact modifiers are available for upgrading mixed waste polymers during mechanical recycling. These compatibilizing additives base their function on physical or chemical effects; non-reactive compatibilizers improve the interfacial adhesion due to good miscibility with both polymers of the blend, whereas reactive compatibilizers have chemical activity and create effective links among the components of the blend through reactive extrusion.

4.3 Sustainability of System and Process

Sustainability may be defined as the processes and actions through which the natural resources of a system will not be depleted. Natural resources and their allocation are influenced by the way a society is organized. This resource availability maintains an economic and ecological balance so that the society's quality of life does not decrease. In this way, we can say that resource exploitation, manufacturing operations, the direction of investments, technological developments, wealth distribution, and institutional changes, among others, are sustainable if they do not hurt the ecosystem and if they allow for society's quality of life to remain at the same level or increase. In order to maintain a sustainable in-space manufacturing capability, a machine that can both print plastic parts and recycle them back into reusable raw materials to make more and/or different parts will be of utmost interest from a cost perspective.

Astronauts can use this technology to manufacture and recycle some usable items such as food-safe utensils and convert the inconvenient waste into feedstock to help build the next generation of space systems. Reuse of the waste can reduce the cost and risks for NASA and private space exploration missions. By 2024, NASA wants to create a Fabrication Laboratory, or FabLab, to test an integrated, multi-material, on-demand manufacturing system on ISS. The FabLab will allow astronauts to select what they want or need from a catalogue of parts and provide an on-demand manufacturing capability for logistics reduction.

4.4 Power Requirement and Physical Footprint (Dimension, Volume and Mass)

There are many types of 3D printers using various AM processes in the market. Energy consumption in metal AM could not only affect the sustainability of the process itself, but also influence the microstructure and mechanical properties of the fabricated components. A few results on energy consumption are reported here from different perspectives such as material properties, product design, printer's capability, and processing.

(a) *Energy consumption:* Alex Huckstepp of Digital Alloys (Metal AM Guide, March 28, 2019) indicates that almost all metal AM processes consume powder or wire as the feedstock, while machining usually uses billet as the feedstock. Energy is needed to process the metal block into these forms (ingot) from which power is created through a slow and expensive gas atomization process. Wire is drawn through progressive dies. The metal plates formed from rolling an ingot is cut to various billet sizes. This feedstock requires 3-4 times more energy to manufacture the billet used in machining. The wire drawing process is slightly more efficient than the gas atomization of powder and has a higher yield. Manufacturing Joule printing feedstock (for the process used by Digital Alloys) should consume slightly more energy than wire DED because of its thinner wire drawing steps, whereas binder jet feedstock production consumes the highest per-kg energy because of the addition of the binder.

Metal AM is an energy intensive process since laser beams or electron beams with high power density are used to fully melt materials. A fundamental understanding of energy consumption in metal AM could not only better utilize the current limited economic resources more sustainably, but also help improve the quality and extend the service life of AM produced metal components. Energy consumption in metal AM could be categorized into two levels: machine level and process level. Powder bed fusion (PBF) and directed energy deposition (DED) are the two major types of metal AM processes. NASA is currently working to mature DED for a demonstration on ISS. Electron beam melting (EBM), a metal AM process, uses electron beam generated by high voltage as the heat source to melt metal powder materials.

Baumers *et al.* (2011) presented a consistent and reliable absolute measure of energy consumption across several widely adopted additive manufacturing systems. In this section we concentrate on the spectrum of additive technology variants suited to produce end-use parts and products, with an emphasis on metallic additive technologies. The assessed experimentally verified results are reported for selective laser melting (SLM), direct metal laser sintering (DMLS), electron beam melting (EBM), laser sintering (LS) and fused filament fabrication (FFF) of polymers.

(b) *Controlling process to minimize energy consumption:* There are a wide range of factors that affect differences in energy demand. The additive manufacturing processes are categorized in two forms: pre-products and components, each of which consists of process and the properties. The energy demand for producing metallic pre-products depends on the technology, layout of the process chain, and the material properties. Powder will have different shape sizes and di density, on which heat capability, melting enthalpy, and reactivity will depend as well. Thus, the energy demand appears to depend on the level of process integration, (i.e. number of melting cycles). Component production also depends on material properties and the production process.

4.5 Assessment of Recycling Processes

Although the collection, sorting and processing of materials into new products also entails significant negatively environmental impacts, recycling is widely assumed to be environmentally beneficial. Lifecycle assessment quantifies and evaluates the environmental impacts of a product from the acquisition of raw materials, through manufacture and use, to the final disposal. Lifecycle assessment can also provide a framework for the analysis of environmental impacts from systems such as transport or waste management.

Plastic materials can be recycled in a variety of ways and the ease of recycling varies among polymer type, package design and product type. For example, rigid containers consisting of a single polymer are simpler and more economic to recycle than multi-layer and multi-component packages. Thermoplastics, including PET, PE and PP all have a high potential to be mechanically recycled. Thermosetting polymers such as unsaturated polyester or epoxy resin cannot be mechanically recycled, except to be potentially re-used as filler materials once they have been size-reduced or pulverized to fine particles or powders. This is because thermoset plastics are permanently cross-linked in manufacture, and therefore cannot be re-melted and re-formed.

Rigid plastics are typically ground into flakes and cleaned to remove food residues, pulp fibers and adhesives. The latest generation of wash plants use only 2–3 m^3 of water per ton of material, about one-half of that of previous equipment. Innovative technologies for the removal of organics and surface contaminants from flakes include 'dry-cleaning', which cleans surfaces through friction without using water. After size reduction, a range of separation techniques can be applied. Sink/float separation in water can effectively separate polyolefins (PP, HDPE, LDPE) from PVC, PET and PS. Use of different media can allow separation of PS from PET, but PVC cannot be removed from PET in this manner as their density ranges overlap. Other separation techniques such as air elutriation can also be used for removing low-density films from denser ground plastics. One area of innovation has been in finding higher value applications for recycled polymers in closed-loop processes, which can directly replace virgin polymer.

5. Additive Manufacturing

Additive manufacturing (AM) is a technology that allows physical components to be made from virtual three-dimensional (3D) computer-aided-drawing model data by building the component layer-by-layer until the part is complete. The simplest way to visualize any additive manufacturing technique is to think of the process as the opposite of subtractive manufacturing processes such as milling. In additive manufacturing, a part is formed by layer-wise deposition of the materials in a three-dimensional pattern. The process involves slicing a solid model of the part into multiple layers, creating a toolpath to trace the individual layers, and then building the part layer by layer using the feedstock material in a computer-controlled automated machine. Since the process relies on material addition in each layer leading to the final part geometry, it is called an additive process. In contrast, a conventional machining process starts with a block of material and follows a material removal technique to create the final part geometry and therefore is called a *subtractive process* [Dutta *et al.* 2019].

Additive Manufacturing, also known as 3D printing, is a process for making parts by joining materials layer by layer. While formerly reserved mainly for producing sample or prototype parts, the technology has evolved over the years to enable manufacturers to make fully functional production parts for automotive, aerospace, medical and a wide range of other markets. Additive Manufacturing encompasses a wide range of technologies, among them laser sintering, fused deposition modeling, stereolithography and more. Processors—injection molders in particular—are increasingly using this technology both for low-volume production part made of specialized plastics, and for mold-making.

5.1 Scale of Operations (Industrial and Laboratory Operations)

Plastics are the most common materials for producing end-use parts and products, and are used for everything from consumer products to medical devices. Plastics are a versatile category of materials, with many polymer options, each with their own specific mechanical properties. A variety of plastic manufacturing processes have been developed to cover a wide range of applications, part geometries, and types of plastics. For any designer and engineer working in product development, it is critical to be familiar with the manufacturing options available today and the new developments that signal how parts will be made tomorrow. The steps to follow the scale of operations lies in (a) product form, (b) volume/cost, (c) lead time, (d) material, (e) types of plastics, and (f) manufacturing process.

The scale of recycling operations will depend on the above stated factors. For space, small products may be manufactured onboard and large parts would be manufactured using industrial capabilities on the ground. Given the checklist of the above-mentioned factors, the crew must assess capability and availability of recycling facilities and the product form to make an appropriate decision on reuse of a material.

5.2 New Technologies and Knowledge Gap

The plastics recycler is a semi-autonomous manufacturing facility capable of processing raw materials into usable 3D printing filament for an additive manufacturing facility. Deploying such a system on ISS will explore the feasibility of operating recycling capabilities on future expeditions. Research on how to extract oxygen from plastics and metal waste or regolith is also an important idea for long-time survival in the space environment and could also be used to create process pathways for feedstock generation.

A current recycler on ISS is the *Refabricator*, a device designed to accept plastic materials (ULTEM 9085) of various sizes and shapes and turn them into the feedstock used to 3D print items. The process of printing and recycling takes place a single automated machine about the size of a miniature refrigerator. This technology is an important first step toward fabrication, recycling, and reuse of plastic materials in a space habitat.

Recycling systems on ISS will complete the plastic sustainability lifecycle on-orbit by providing astronauts the ability to convert plastic packaging and trash, as well as objects previously fabricated by the 3D printer, into feedstock to be reused by the printer. These systems will facilitate the reusability of materials to solve new problems as they arise, whether on the International Space Station or in future crewed space exploration missions. The invention will improve the autonomy and sustainability of long-duration space missions, while also helping to reduce the cost and weight of payloads carried from earth.

(a) Sustainable Manufacturing in Space: Made In Space (MIS)'s ISS recycling facility, named Braskem Recycler, aims to improve the sustainability of manufacturing capabilities on the ISS. MIS Recycler is creating a closed-loop system for manufacturing in space. MIS Recycler is designed to convert plastic waste and 3D printed objects into feedstock that can be used by additive manufacturing facilities currently on the ISS. Onboard the space station, plastic waste and materials will be loaded into the facility and then reduced into smaller pieces. The reduced pieces are then heated, extruded, and spooled into feedstock that is compatible with the MIS Additive Manufacturing Facility. Aside from material loading, the recycling process is automated and requires minimal crew intervention. Addition of this technology promotes a sustainable supply chain in space that doesn't rely on routinely delivered feedstock from Earth.

(b) Long-Duration Space Missions: The ISS provides a valuable testbed to validate new recycling facility which could have significant implications for future exploration missions to the Moon and Mars. A closed-loop manufacturing process allows explorers to maximize resources by reconstituting existing objects or plastic waste into new tools.

5.3. Yield of the Recycling Process

The yield of a recycling process depends on several aspects of the system such as raw material conversion ratio (i.e., less loss), recycling equipment capabilities and efficiencies, output (filament) quality, processed product reconvertibility (multiplicity), and ambient conditions (temperature, pressure, raw material condition). Crew time is of utmost value in space. Thus, given this situation, the crews would have to estimate their plastic or metal recycling time to make the filament coil and manufacture the required product by additive manufacturing. A general filament coil recycling process is given in Figure 2, wherein the options for both recycling nonconforming product (bad filament) and recyclability of product after a useful life are considered. Multiple recycling and re-feedings of products is studied to enhance the throughput rate of the recycler system.

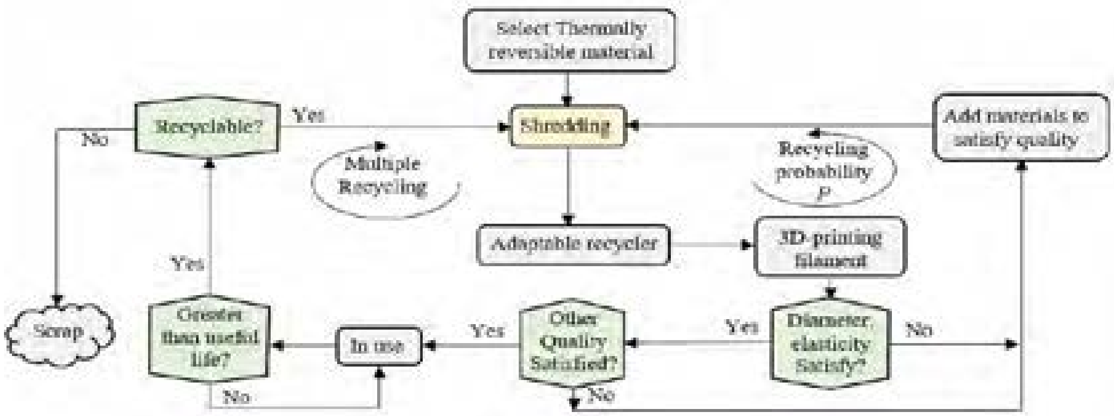

Figure 2. Multiple recycling system

5.3.1 Throughput analysis of the system:

Let the *processing time* (or recycling time), t_p, be defined as the time taken from the beginning of shredding to end of quality checking time of the filament. t_R is defective filament refeeding time to the shedder and p ($0 \le p \le 1$) is the probability of unacceptability of filament after the quality control check. Also assume that *T* is the total processing time when no re-feeding is done (i.e., no defective filament is produced), and T_R is the total re-feeding time. Then, according to Hossain and Sarker (2016), the recycling time can be estimated as follows:

Theorem 1: For a plastic recycling system with single feedback of defective filament, the estimated filament production time, $T_f = t_p + T_R = t_p + pt_R$

Theorem 2: The total feedback-time T_R for *n* feedbacks of filaments is given as $T_R = \frac{p(1-p^n)t_R}{(1-p)}$.

Theorem 3: For an AM system producing defective filament with probability p, the throughput rate for *n*-feedbacks of filaments, the throughput rate R_{Th} can be estimated by

$$\frac{1}{t_p+t_R} \le R_{Th} = 1 / \left(t_p + \frac{p(1-p^n)t_R}{(1-p)} \right) \le \frac{1}{t_p}.$$

Example 1. Computing throughput time and rate.

Let times for different operations in the plastic recycling process under laboratory setup be as given in Figure 3 and Table 3. The processing is not always error-free—assume about 10% of the filament coil produced is defective due to imperfect extrusion or wire drawing or some other mechanical malfunction. Nonconforming output is fed back to the shredder to reprocess the defective quantity. The problem is to estimate the actual recycling time required for the crew to meet their other schedules and manage other mission priorities.

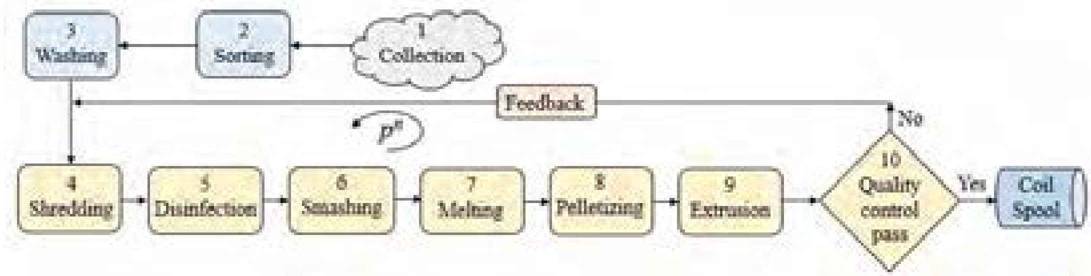

Figure 3. Filament feedback recycling process

Here, the actual processing production time is composed of shredding, disinfection, smashing, melting, extrusion/drawing and quality checking, for which the production time is t_p= 33 minutes. The reprocessing time t_R, is the feedback time t_b *plus* the remaining (forward) reprocessing time t_f: that is, t_R= t_b+ t_f. Here, t_f = 33, 29, 24 (if the nonconforming coil is fed to the shredder, disinfection chamber, or smasher, respectively), and so on (theoretically), but smashing is the last process for any feedback or incoming materials. After smashing, the wire-making process (melting-pelleting, extrusion) starts.

Table 3. Assumed time-data for plastic recycling process to manufacture filament coils †

Process:	Collection	Sorting	Washing	Shredding	Disinfection	Smashing	Melting	Pellet	Extrusion	Quality	Feedback
Operation time:	-	30	20	5	4	5	4	5	6	4	5
Time remaining				33	29	24	-	-	-	-	

† Hypothetical data.

So, assuming the refeeding starts at shredding operation, t_R= t_b+ t_f = 5 + 33 = 38 minutes. The estimated filament coil production time, by Theorem 1, is actually $T_f = t_p + pt_R$.= 33 + 0.1 (38) = 36.80 minutes. If the filament is fed back 3 times (for example), then the estimated total production time is given by Theorem 2 as T_R = $p(1-p^n)t_R/(1-p)$ = $0.1(1-0.1^3)38/(1-0.1)$ = 4.218 minutes and the filament coil production time is $T_f = t_p + T_R$ = 33+4.218 = 37.218 minutes for 3 feedbacks instead of 36.80 minutes. By Theorem 3, the throughput rate with n = 3 feedbacks is $R_{Th} = 1/\left(t_p + p(1-p^n)t_R/(1-p)\right)$ = 1/ 37.218 = 0.0268687/min = 1.61 filament coils/hour. □

5.3.2. Yield of different recycle materials:

The postconsumer plastic bottle recycling industry experienced a difficult year in 2018 with less growth in pounds collected than in pounds of bottles on store shelves. Package designers continue to decrease the amount of material used by light-weighting and reducing the size of PET and HDPE bottles. Light-weighted containers continue to be at high risk of misdirection into the paper stream at material recovery facilities. Many consumer products are being sold in smaller bottles as household demographics change with smaller households. The sales of PET for bottles rebounded dramatically compared to 2017 sales while sales of HDPE for bottles decreased slightly.

5.4 Benefits of Additive Manufacturing

AM and CM (conventional manufacturing) face different trade-offs, with each process likely to play a role in future manufacturing capabilities. AM has the potential to minimize materials and energy usage, reduce waste, accelerate innovation, and compress supply chains. Some benefits of AM technology based on USDOE (2015) reports are: (a) innovation (b) part consolidation (c) lower energy consumption (d) less waste (e) reduced time to market (f) light weighting, and (g) agility of manufacturing operations.

5.5 Impacts of Additive Manufacturing

It is observed that there is a comparatively large amount of plastic and packaging materials in ISS cargo. The packaging materials are a "step increase" in total mass of the system—they occur at the beginning of a mission and then do not increase beyond that (until there is another resupply and a new mission increment begins). If we consider events that correspond to a change in the amount of packaging material available on ISS, there are two that occur with some regular cadence: *upmass* (which occurs with cargo resupply or arrival of new crew, every few months) and *downmass* (also occurs once every few months when Cygnus departs station or—with an accompanying smaller decrease in material—when crew depart station). For a long duration mission beyond LEO, we would expect to have an initial large step increase in waste material with launch of initial supplies and then a smaller, more infrequent increase with cargo resupply. Thus, the overall accumulation rate of the waste materials is higher at the beginning of the crew's operational time in space for a long-duration mission. Hence, the collecting and processing raw material preparation for AM will be assumingly intense at the beginning of a mission to minimize the apparent storage volume. Moreover, the packaging and nonreturnable payloads are to be planned such that they can be convertible to feedstock for an AM process.

5.6 Usability of Systems

A *metric* is a standard of measurement in units that can be used to describe a system with multiple attributes and quantifies the *usability* of the system. There are several reasons in measuring it: (a) to effectively communicate with the stakeholders of the system, and (b) to compare the *usability* of multiple products and to quantify the severity of a *usability* problem. Ultimately, the primary objective of *usability* metrics is to assist in producing a system or product that is neither under- nor over-engineered. The ISO 9241-11 standard defines *usability* as the extent to which a product can be used by users to achieve specified goals with *effectiveness, efficiency* and *satisfaction* in a specified context of use.

Basically, *effectiveness* (ξ_E) calculates the completion rate, which can also be expressed in proportion or percentage, whereas *time-based efficiency* (η_T) is measured in terms of task time giving a weighing factor on time. These usability measures are shown in Table 4, wherein N = number users, R = number of tasks, n_{ij} = 1 if the user i completes the task j successfully or 0 otherwise, and t_{ij} = the time spent by user i to perform task j, irrespective of completion or quit. Another measure called the *overall relative efficiency* (η_R) uses the ratio of the time taken by the users who successfully completed the tasks with respect to the total time taken by all users. Obviously, all these measures are scaled on $0 \le \xi_E, \eta_T, \eta_R \le 1$ and closer is the value of these metrics to 1, better is the usability or performance of the system.

Table 4. Effectiveness and efficiency metrics of any system.

Measures:	Effectiveness (ξ_E)	Time-based Efficiency (η_T)	Overall Relative Efficiency (η_R)
Metric:	$\frac{\sum_{i=1}^{N}\sum_{j=1}^{R} n_{ij}}{NR}$	$\frac{\sum_{i=1}^{N}\sum_{j=1}^{R} n_{ij}/t_{ij}}{NR}$	$\frac{\sum_{i=1}^{N}\sum_{j=1}^{R} n_{ij}t_{ij}}{\sum_{i=1}^{N}\sum_{j=1}^{R} t_{ij}}$
Unit:	Proportion	goals/unit time	Proportion

Example 2: Efficiency and effectiveness

To elucidate the problem, let's assume there are N = 4 crews to complete R = 5 tasks. The completion or interruption times (in seconds) and the computational measures are reported in Table 5 wherein the value of n_{ij} in $n_{ij}(t_{ij})$ indicates the task completion status (1: completed, and 0: incomplete) and the time t_{ij} in parentheses.

Table 5. Computational data and the efficiency measures.

	Data: $n_{ij}(t_{ij})$					Computational results		
	j					$\sum_{j=1}^{R} n_{ij}$	$\sum_{j=1}^{R}(n_{ij}/t_{ij})$	$\sum_{j=1}^{R}(n_{ij}t_{ij})$
i	1 (12)	0 (7)	1 (14)	1 (10)	1 (15)	4	0.32143	51
	1 (10)	1 (6)	0 (12)	1 (15)	1 (14)	4	0.40476	45
	1 (16)	1 (9)	1 (15)	1 (6)	1 (17)	5	0.46577	63
	0 (15)	1 (5)	1 (8)	1 (14)	1 (12)	4	0,47976	39
$\sum_{i=1}^{N}$=						**17**	**1.67172**	**198**

The general effectiveness measure, $\xi_E = \sum_{i=1}^{N}\sum_{j=1}^{R} n_{ij}/NR$ = 17/20 = 0.85 and obviously, for a single crew, $\xi_E = \sum_{j=1}^{R} n_{ij}/R$ as N→1. The time-based efficiency, $\eta_T = (\sum_{i=1}^{N}\sum_{j=1}^{R} n_{ij}/t_{ij})/NR$ = 1.67172/4(5) = 0.083586 goals/sec, and for the total time spent $T = \sum_{i=1}^{N}\sum_{j=1}^{R} t_{ij}$= 232, the overall relative efficiency, $\eta_R = \frac{\sum_{i=1}^{N}\sum_{j=1}^{R} n_{ij}t_{ij}}{\sum_{i=1}^{N}\sum_{j=1}^{R} t_{ij}}$ = 198/232 = 0.85345. It may be further noted that the average task time/crew/task is *T/NR*= 232/20 = 11.60 seconds and $\eta_T(T/NR)$ = 0.083586 (11.60) ≡ 96.96% of the goal can be completed. These measures can help estimate the crew time in the spacecraft to accommodate other options. □

5.7 Economics: Reduction of Costs

Recycling is part of an ethic of resource efficiency where products are used to their fullest potential. When a recycled material, rather than a raw material, is used to make a new product, natural resources and energy are conserved. This is because recycled materials have already been refined and processed once; manufacturing the second time is much cleaner and less energy-intensive than the first. For example, manufacturing with recycled aluminum cans uses 95 percent less energy than creating the same amount of aluminum with bauxite.

If we look at the big picture of what it takes to create a product from scratch—to get the raw materials, transport them, process them and manufacture them—making goods with recycled material like paper, plastic, glass, and metal is a major energy saver. Manufacturing one ton of office and computer paper with recycled paper stock can save nearly 3,000 kilowatt hours over the same ton of paper made with virgin wood products. A ton of soda cans made with recycled aluminum saves an amazing 21,000 kilowatt-hours by reducing the virgin bauxite (bozite) ore that would have to be mined, shipped, and refined—that's a 95% energy savings. A ton of PET plastic containers made with recycled plastic conserves about 7,200 kilowatt hours. San Diego County Office of Education has reported that recycling one glass bottle saves enough energy to light a 100-watt light bulb for four hours

6. Logistics Systems: Plastic Packaging and Source Materials

NASA's current future exploration missions are focused on destinations beyond LEO. These missions include a progressive increase in the time that humans will be required to spend away from Earth vicinity. Potential mission scenarios range from human exploration of cis-lunar space, requiring durations of around 60 days, to Mars destination exploration, requiring mission durations of up to 1000 days or more.

Lopez *et al.* (2015) provided a summary requirement for logistics systems used for deep space missions. The authors described a process and calculations used to estimate mass and volume requirements for crew logistics, including consumables such as food, personal items, gasses, and liquids. Determination of logistics requirements are based on crew size, mission duration, and the degree of closure of the *environmental control life support system* (ECLSS). Details are provided on the consumption rates for different types of logistics and how those rates were established. Results for potential mission scenarios are presented, including a breakdown of mass and volume drivers. Opportunities for mass and volume reduction are identified, along with potential variables that could increase requirements.

6.1 Assessment of Mass

The current mission architectures assume the transit habitat will carry complete survival capabilities for the entirety of the mission duration. Pre-emplaced Mars assets are unavailable in the Mars vicinity when 30 days of contingency consumables are included in an open-loop configuration. Contingency consumables cover periods of system downtime/repair and allow for slight growth in the crewed mission duration. For this reason, volumetric requirements for the dry goods, along with total CTBE loading and volumes are given in Sarker *et al.* (2020).

Lopez *et al.* (2015) reported that food mass constituted about 52% and 66% of the total dry consumables' masses for the cis-lunar and Mars missions, respectively. Two areas of interest for reducing total food mass are lowered hydration rate and reduced packaging mass. These areas may present some opportunities for improvement, but the benefits will likely be limited. Reduced hydration rates below the 28% used on ISS may compromise palatability. Lower levels of food hydration will also limit ECLSS water yield such that, at some point, any reduced food mass will be offset by increased water delivery requirements or increased ECLSS closure. Current packaging methods for ISS meals allow for excess food and packaging mass. Improved containment systems could potentially be used to reduce this mass. More innovative food preparation and improved storage systems may mitigate this problem and reduce plastic usage.

6.2 Sources of Materials & Payloads

While plastics are found in all major MSW categories, the containers and packaging category had the most plastic tonnage at over 14 million tons in 2017. This category includes bags, sacks and wraps; other packaging; polyethylene terephthalate (PET) bottles and jars; high-density polyethylene (HDPE) natural bottles; and other containers. Plastics are also found in nondurable products, such as trash bags, cups, utensils, medical devices and household items such as shower curtains. The plastic food service items are generally made of clear or foamed polystyrene, while trash bags are made of high-density polyethylene (HDPE) or low-density polyethylene (LDPE). A wide variety of other resins are used in other nondurable goods. Plastic resins are also used in a variety of container and packaging products, such as PET beverage bottles, HDPE bottles for milk and water, and a wide variety of other resin types used in other plastic containers, bags, sacks, wraps and lids. This wide range of usage of plastics also has an influence on the recycling systems for space missions, as they must be able to process some portion of the amount of packaging material which is initially upmassed and accommodate a mixed-material input stream.

6.3 Styrofoam and other packaging materials

There are various types of foams that are currently used for packaging items for space missions or multi-modal transportation with high potential damage to products. Some of the commonly used types of foams are: charcoal foam, eggcrate foam, poly foam, polyethylene, and custom packaging. Foams used in NASA and International Space Station (ISS) are specially manufactured for this application.

Harris *et al.* (2014) mentioned that limited available data regarding types of foam used on the ISS are from foams that were launched to the ISS on ATV3, HTV3, SpX-D, and SpX-1 flights. On the average, 37% of the cargo volume was foam, predominantly Minicel and Zotek. Small amounts of Plastazote and very small amounts of Pyrell were also present. In the future, Plastazote is expected to make up most packing foams on flights to the ISS; Zotek will be the second-most common packing foam. Plastazote is 98-99% polyethylene with 1-2% carbon black. Zotek is lightweight, closed cell polyvinylidene fluoride (PVDF) foam. Plastazote has flame retardant capabilities. Further, the volume reduction and densification of Zotek, Minicel, Plastazote LD 24FR and LD45FR were tested at 150ºC. The volume reduction factor v_r and the densification factor ρ_f are defined as $v_r = v_F/v_0$ and $\rho_f = \rho_F/\rho_0$, respectively, where v_0 is the initial volume and v_F is the final volume and ρ_0 is the initial density and ρ_F is the final density.

6.4 In-Situ Resource Utilization (ISRU) Efforts

To live and work in deep space for months or years may mean astronauts have less immediate access to supplies. NASA will send cargo to the Gateway in lunar orbit to support expeditions to the surface of the Moon. However, the farther humans go into deep space, the more important it will be to generate products with local materials, a practice called *in-situ resource utilization* (ISRU). *Reversible thermoset* (RVT) materials, developed by Cornerstone Research Group under a Small Business Innovative Research (SBIR) contract, may provide a path for reclamation or repurposing of materials in support of ISRU-initiatives which focus on using launch packaging as feedstock. Also, automated in-process quality control of recycled filament will help to ensure part consistency and provide property information when using ISRU packaging materials.

NASA’s current interests center around two main overarching themes: new technology to venture into deep space and technology to encourage a self-sustained environment that will reduce the ever-increasing cost burden of total exploration missions. These goals can be achieved in part by reducing the launch mass through use of limited parasitic cargo material. Snyder *et al.* (2019) view the objective of this ISRU as reducing supply or resupply needs and achieving reduced payload mass. ISRU can also reduce the mission risk, increase crew flexibility and extend the deep space mission duration.

Prater *et al.* (2020) provides a summary of NASA’s 3D Printed Habitat Centennial Challenge, which spurred the development of new printing methods and creation of new robotic hardware for material delivery, extrusion and control. This effort focused on development of AM technologies that benefit both Earth-based construction and NASA’s robotic precursor planetary missions. Large format AM technologies may be needed to establish a sustained human settlement on Moon and Mars.

7. Current Status and Advancement of AM in Space

Recycling in-space waste for deep-space mission has become a pressing problem for space agencies, especially for long duration missions. In recent aerospace research and technology, plastics have become an inseparable part of spaceflight hardware, supplies, and payloads. In commercial planes, launch vehicles, ISS and other spacecraft, plastic has become an important light material to minimize the cost and payload mass alongside other light metals such as aluminum and titanium. Between 1970 and 2000, the cost to launch a kilogram to space remained fairly steady, with an average of $18,500 per kilogram. When the Space Shuttle was in operation, it could launch a payload of 27,500 kilograms for $1.5 billion, or $54,500 per kilogram. For a SpaceX Falcon 9, a rocket used to access the ISS, the cost is reported to be just $2,720 per kilogram, which is a drastic cost reduction relative to other launch vehicles [see Cobb 2019]. Though the unit cost per kilogram of the payload has decreased recently, the facilities and science experiments demand more payload experimental setups and longer duration mission time, which increases other mass such as consumable and non-consumable supplies that ultimately create the waste stream.

(a) Physical limitations: In order to mitigate this problem of waste management in the space station, additive manufacturing has been adopted as a driver to the waste elimination process. The output of the waste recycling is the feedstock (filament coils), which is then the input to the actual AM process that creates a new product or reproduces broken or lost parts or tools. What we may be able to manufacture on the ground may not be possible to produce in the space environment because of many resource and environmental constraints, such as physical space, temperature, safety and crew time. Therefore, crews may have limited opportunities in the near term to mitigate waste accumulation through recycling processes which lead to additive manufacturing of parts and tools. It is important to note that if a part cannot be produced on a space mission using the same materials and design as on earth, there is also the opportunity to redesign the part to be compatible with a space-based manufacturing system. Use of ISM on space missions requires

coordination between those developing the manufacturing systems and the designers who would eventually use these capabilities for on-demand manufacturing to support sparing and repair.

(b) Economics and yield advantages for single and multiple missions: Recycling waste to manufacture feedstock for AM empties the physical space that trash and waste occupy. Therefore, on future missions it could help free up space to perform other necessary science experiments. The initial investment for a new technology is always significant. After the initial capital investment of a recycler and AM equipment for space missions, these capabilities can be used by the crews of the subsequent missions. The initial investment is depreciated over several mission to defray the initial cost, resulting in economic benefit to NASA.

(c) Knowledge gap: There are three major issues relating to the knowledge gap in this undertaking: the recycling process, recycling technology, and recycling system design. All three aspects are nearly independent.

First, the *recycling process* has been elaborately discussed in previous sections. Recycling in industry typically consists often steps: collection, sorting, washing, shredding, disinfecting, smashing, melting, pelletizing, extrusion and quality evaluation. Innovative recycling processes may be developed, depending on the raw materials (waste types), to minimize the processing time or to improve the quality. This may involve new combinatorial process sequences to accelerate the sequence and/or eliminate/incorporate some new process(es).

Second, in *recycling technology*, new products are being introduced in the market to perform the desired process more effectively. Such a new product (equipment) may be adapted to ISS to take advantage of the new technology.

Third, the *recycling system* presents another perspective. Filament coil will go through a quality control check after the extrusion process to identify sections with nonconformances. It has been discussed earlier (in throughput analysis) that if filament does not meet quality standards, the filament is fed back into the system (i.e., at shredder, disinfector or smasher, depending on the feeding product quality in the previous pass). This will further minimize the crew time and improve the process quality.

There are host of 3D printers in the market and users of AM technologies have many choices. There is a need to carefully evaluate the quality and capability of these systems before adapting them to ISS for specific applications. Most systems use standard virgin filament. For recycling processes operated on ISS, the filament quality may not be as good as terrestrially recycled filament if the recycling process is significantly impacted by operation in a microgravity environment or if significant changes must be made to the process to scale it for operation onboard a spacecraft.

8. General finding and recommendations

In our general findings, we have highlighted different use environments for recycling (with an emphasis on ISS), physical and material properties of the waste, volume and mass statistics of different materials, elemental analysis of the waste materials, human biostatistics (crew consumables and requirements) and several other key considerations that will inform use of recycling systems on space missions. The following are the highlights on those findings: (a) process plan, (b) plastic classification, (c) material and thermal properties, (d) throughput analysis, (e) usability evaluation, (f) logistics planning: and (g) packaging materials.

8.2 Recommendations

Several new approaches to measure the efficiency and effectiveness of systems, including the crew time and equipment, have been discussed with exemplifications. If the process is well defined and the time data of activities for recycling different materials are known, the system can be evaluated to improve it for future missions. The impact of this currently proposed approach will potentially improve and enhance crew and system performance. The following recommendations are made to enhance future system architectures and improve the performance of recycling processes for waste in space:

(a) *Payload mass:* Total mass of the payload should be reduced to minimize the carrier load and the total mass on the space station.

(b) *Throughput analysis:* Process and throughput analyses on board the station will help better estimate the crew time and the total processing time. The metrics proposed in evaluating different functions are also helpful to measure the system performance.

(c) *Packaging materials:* Procedures for packaging consumables and non-consumable products taken to the ISS through payloads are known, but assessment of mass and volumetric measures of these materials will help pack the products more effectively, considering crews' personal and metabolic needs. The choice of packaging materials (to align with materials compatible with recycling systems) is also critical to achieving the mission benefits of recycling for logistics reduction.

9. Concluding remarks

The primary goal of the research was to explore minimizing the trash and waste on space missions using the 3R processes that will work within the prevailing constraints for operation on ISS. These constraints include storage space, crew safety, power, mass, volume, and operation in a microgravity environment. To date, the ISM project has only explored very specific materials and application of recycling technologies on space missions and the work does not span the full range of recycling options/approaches available.

The current research surveyed and critically reviewed different databases, open literature and online information. In some instances, data sets are not consistently reported either because of a lack of information or because of proprietary rights pertaining to the data. Some data cited are not well attributed to sources such as NASA, NIST, AIAA, ARO, ONR, NSF and other international agencies. Therefore, careful attention has been given to select and cite references. Numerous data have been cited in the academic literature and some of this information is also included partially in tabular form in this report. Several findings and recommendations derived from this study have been highlighted above—applications or implementation of some these propositions will potentially improve the AM initiatives for demonstration on ISS or on other space missions.

Acknowledgement:

Professor Bhaba Sarker is thankful to Dr. N. Frank Six, University Affairs Officer of NASA Office of STEM Engagement and Ms. Brooke Graham, NASA-EPSCoR Program Manager, for their continued cooperation and support.

REFERENCES:

Baumers, M., Tuck, C., Wildman, R., Ashcroft, I. and Hague, R. (2011), Energy inputs to additive manufacturing: Does capacity utilization matter? *Working paper:* Loughborough University, Loughborough, LE11 3TU, UK.

CMC (Compact Management Company) (2020), 6 Steps of the Scrap Plastic recycling process, https://www.norcalcompactors.net/scrape-plastic-recycling/ (July 16, 2020)

Cobb, W. W. (2019), How Space X lowered costs and reduced barriers to space, *The Conversation*, May 1, 2019; https://theconversation.com/how-spacex-lowered-costs-and-reduced-barriers-to-space-112586

Dutta, B., Babu, S., and Jared, B. (2019), Chapter 2 - Additive Manufacturing technology, in *Science Technology and Applications of Metals in Additive Manufacturing*, pp. 11-53. https://doi.org/10.1016/B978-0-12-816634-5.00002-9.

Ewert, M. K. (2020), Crew consumables Mass for 1 year on ISS and projected for a 1-year Exploration mission, EXCEL database, NASA-Johnson Space Center (Procured through Tracie Prater at MSFC-EM04, July 23, 2020).

Harris, L., Alba, R., Wignarajah,K., Fisher, J., Monje, O., Maryatt, B. Broyan, J. and Pace, G. (2014), Processing of Packing Foams Using Heat Melt Compaction, *Proceedings of the 44th International Conference on Environmental Systems*, Tucson, AZ; 13-17 July 2014.

Hossain, M.S.J. and Sarker, B.R. (2016) "Optimal locations of on-line and off-line rework stations in a serial production system," International Journal of Production Research, 54(12): 3603-3621.

Lockhart, L. (2018), Recycling in Space: Waste Handling in a Microgravity Environment Challenge, KSC, Oct. 2018; https://www.nasa.gov/feature/recycling-in-space-waste-handling-in-a-microgravity-environment-challenge.

Lopez, Jr., P., Mattfeld, B., Stromgrenm C. and Goodliff, K. (2015), Logistics need for potential deep space mission scenarios post asteroid redirect crewed mission, *Proceedings of 2015 IEEE Aerospace Conference*, 7-14 March 2015, IEEE *Xplore*: 08 June 2015; INSPEC AN: 15202101, DOI: 10.1109/AERO.2015.7119161.

Pai-Paranjape, V. (2018), How to pick the right plastic for Additive Manufacturing, *Design World,* Posted by Leslie Langnau (June 12, 2018). https://www.designworldonline.com/how-to-pick-the-right-plastic-for-additive-manufacturing/

Prater, T., Werkheiser, N. Ledbetter, F., and Morgan, K. (2020), In-Space Manufacturing at NASA Marshall Space Flight Center: A Portfolio of Fabrication and Recycling Technology Development for the International Space Center, *2018 AIAA SPACE and Astronautics Forum and Exposition,* Orlando, FL, 17-19 September 2018. https://doi.org/10.2514/6.2018-5364, or https://doi.org/10.2514/6.2018-5364.

Sarker, B. R., Prater, T. J., Roberts, C. E., Ledbetter, F. B., and Hall, P.B., (2020), Recycling In-Space Plastic Waste for Deep-Space Additive Manufacturing: Capability Assessment and Technology Development, *2020 Summer Faculty Fellow Report-Part I,* NASA Marshall Space Flight Center, Huntsville, Al 35812. August 10, 2020.

Snyder, R., Henslee, B., Vining, B., Shepherd, J., Davidson, J, Nieman, J., Fuller, I. and Pleiman, B. (2019), Reclaiming materials and processing for in-space additive manufacturing, NSMMS/CRASTE Confce, CRG, 25 June 2019.

USDOE (2015), 6A - Additive Manufacturing, in Chapter 6: Innovative Clean Energy Technologies in Advanced Manufacturing, *Quadrennial Technology Review 2015*, US Dept. of Energy, pp. 1-35. https://www.energy.gov/downloads/chapter-6-innovating-clean-energy-technologies-advanced-manufacturing.

Vilaplana, F., Karlsson, S. (2008), Quality concepts for the improved use of recycled polymetric materials: A review, *Macromolecular Materials and Engineering*, **293:** pp. 274-297.

Modeling Time Variations in the White Dwarf Confusion Background for LISA

Sarah J. Vigeland
Center for Gravitation, Cosmology and Astrophysics, Department of Physics, University of Wisconsin-Milwaukee, Milwaukee, WI 53211, USA

Tyson Littenberg
NASA Marshall Space Flight Center, Huntsville, Alabama 35811, USA

I. Nomenclature

A_0, A_1, A_2	=	amplitudes of periodic functions
f_1, f_2	=	frequencies of periodic functions
t	=	time
ϕ_1, ϕ_2	=	phases of periodic functions
σ	=	variance

II. Introduction

The Laser Interferometer Space Antenna (LISA) is a proposed space-based gravitational wave (GW) interferometer that will be sensitive to GWs in the millihertz band [1]. Among the many GW sources in this frequency range are Galactic white dwarf (WD) binaries. LISA will be able to resolve $\sim 10^4$ individual binaries; the remaining Galactic binaries will form a confusion background that can be thought of as a type of noise.

The WD confusion background is an example of cyclostationary noise, meaning that the noise is a periodically correlated random process rather than a stationary random process [2]. This periodicity comes from the orbit of the LISA spacecraft around the Sun. Since the noise is nonstationary, the frequency-domain representation of the noise covariance matrix is not diagonal, as is usually assumed in LISA data analysis. In this work, we explore a time-domain representation of the WD confusion background as a first step towards developing techniques for modeling this signal, and nonstationary noise in general.

III. Methods

We use the LISA Data Challenge (LDC) Radler data set[1]. This data set contains simulated GW data from Galactic compact binaries. We use the FisherGalaxy code [3] to simulate the LISA response to the galaxy, and identify and remove individually resolvable binaries. LISA uses time-domain interferometry (TDI) to combine the signals from the three spacecraft, the output of which is two orthogonal channels referred to as A and E [4]. We are then left with an estimate of the WD confusion background in the A and E channels. We apply a bandpass to focus on frequencies from 10^{-4} – 4×10^{-3} Hz and apply a Tukey window. Finally, we compute the whitened confusion background by normalizing by the variance.

Figure 1 shows frequency-domain and time-domain representations of the WD confusion background in the A and E channels. The modulation in the WD confusion background is clear when looking at the time-domain representation. In particular, the variance shows periodic changes, with periods of six months and a year.

[1] https://lisa-ldc.lal.in2p3.fr/ldc

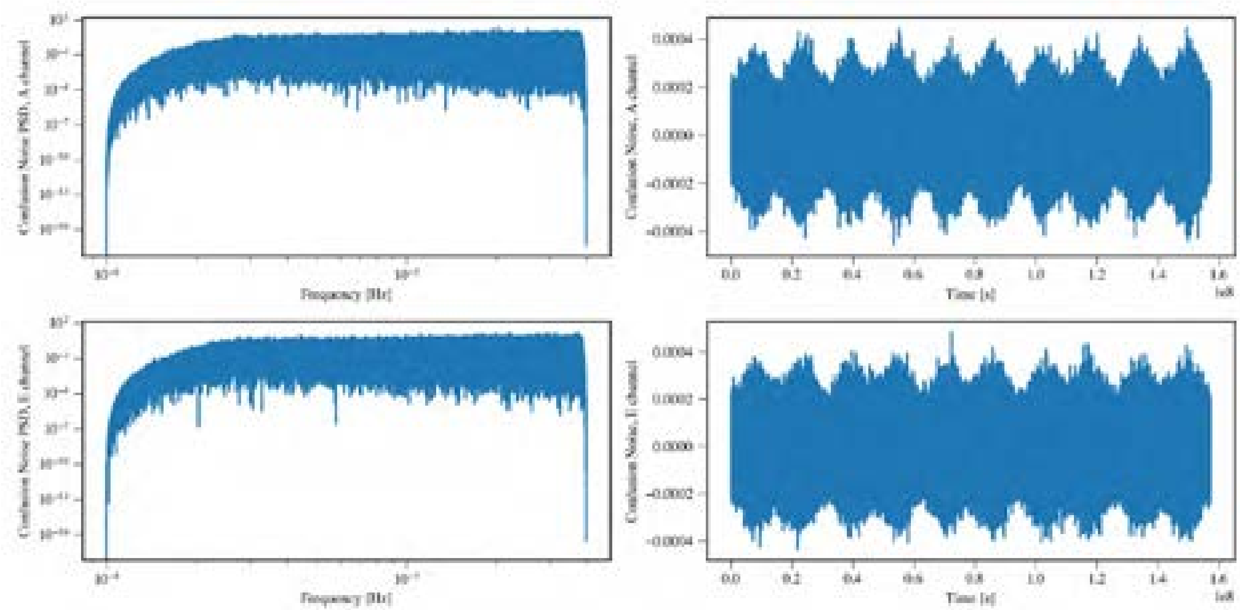

Figure 1: WD confusion noise in the A channel (top panels) and E channel (bottom panels). The figures on the left show the frequency-domain representation, while the figures on the right show the time-domain representation. The time-domain representations show that the variance in the noise has periodic modulations.

We model the variance as

$$\sigma(t) = A_0 + A_1 \cos(2\pi f_1 t + \phi_1) + A_2 \cos(2\pi f_2 t + \phi_2) \quad (1)$$

where $f_1 = \frac{1}{1\text{ year}} = 3.179 \times 10^{-8}$ Hz and $f_2 = \frac{1}{0.5\text{ year}} = 6.357 \times 10^{-8}$ Hz. We generate a reduced data set to fit to the model by averaging the variance into time bins with width of seven days, with uncertainty equal to the standard deviation of the samples within each time bin. We sample the posteriors using the Markov Chain Monte Carlo (MCMC) sampler PTMCMCSampler [5], which uses a combination of Adaptive Metropolis sampling and Differential Evolution.

IV. Results

The results of the MCMC are shown in Figures 2 and 3. Figure 2 shows the parameter, with the vertical dashed lines indicating the maximum-likelihood parameter values. Figure 3 compares the binned variance to the modeled variance using the maximum-likelihood parameter values from Figure 2. There is good agreement between the model and data. Figure 4 shows the modeled WD confusion background, with the data points pulled from a Gaussian distribution with mean of zero and variance given in Eq. (1). It looks very similar to the simulated WD confusion background shown in Figure 1, demonstrating that our simple model does a good job of reproducing the features of the simulated confusion background.

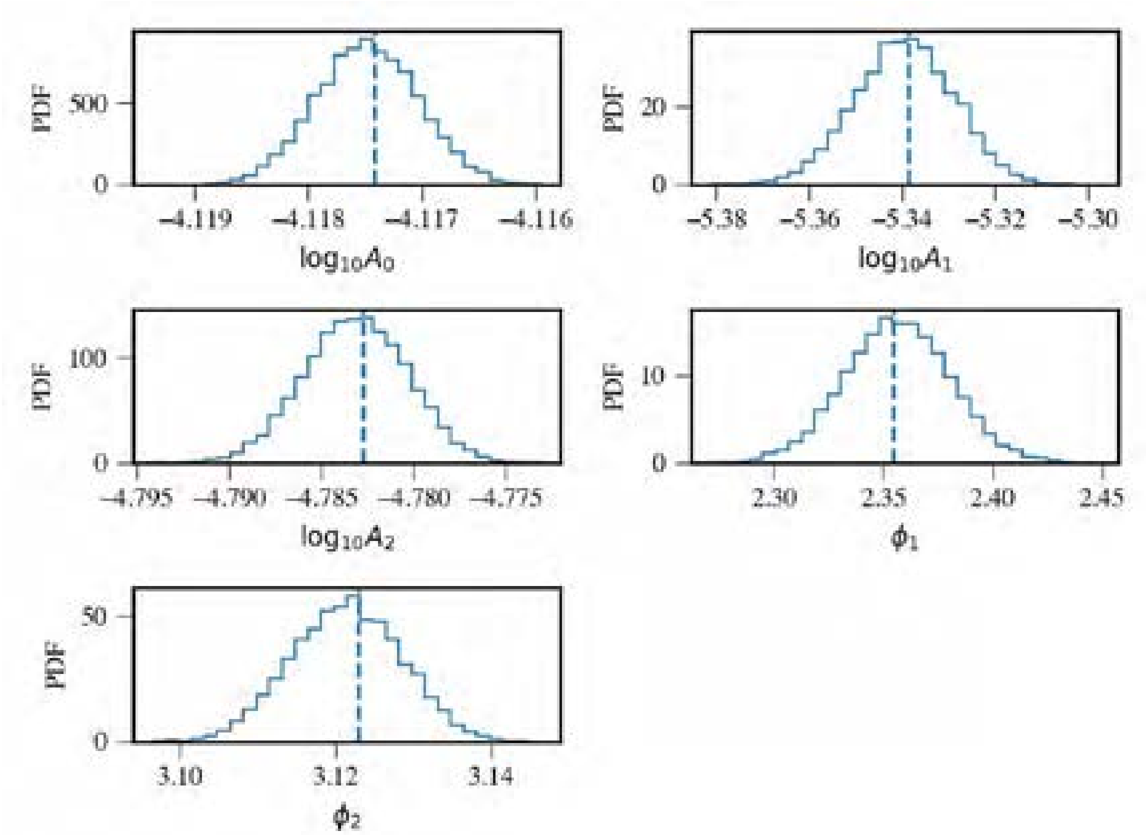

Figure 2: Posterior distributions for the variance amplitudes and phases. The variance is modeled by Eq. (1). The vertical dashed lines indicate the maximum-likelihood values.

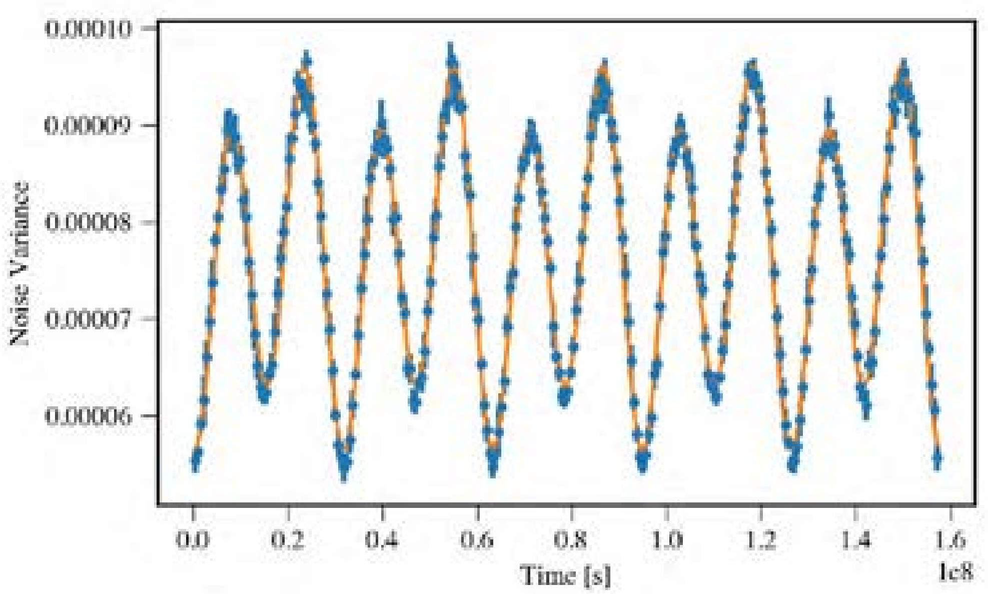

Figure 3: Comparison between the binned noise variance (blue points) and the modeled variance (orange line), where the parameters of Eq. (1) are set to the maximum-likelihood values shown in Figure 2.

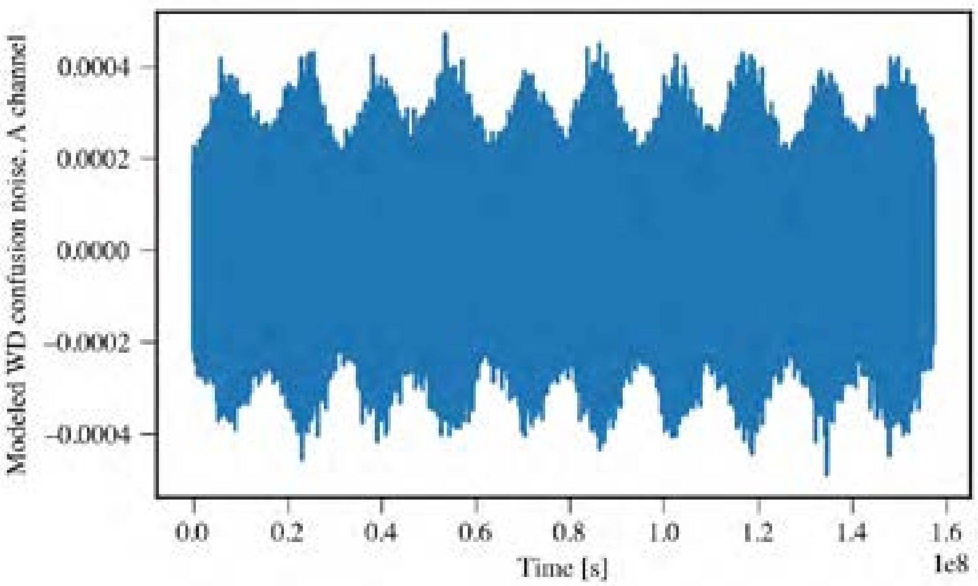

Figure 4: Modeled WD confusion noise, using the modeled variance from the results of the MCMC. The modeled WD confusion noise reproduces the features of the simulated WD confusion noise shown in Figure 1.

V. Conclusion

The annual variation in the WD confusion background can be modeled in the time-domain using a simple sum of periodic terms. We use the Radler galaxy to compute the confusion background for a simulated galaxy, and fit the background to our model using an MCMC. Interestingly, we find that the phases of the two periodic terms is related by almost exactly $\pi/4$, suggesting that the phases of the two terms are correlated. It is likely that this correlation between the two terms can be derived by considering the geometry of the detector and the Galactic bulge. Future work will study how the parameters of this model relate to the properties of the Galaxy. We will also investigate how to model this variation in the frequency domain, so that this model can be easily combined with models for other LISA astrophysical signals and noise.

Acknowledgments

S. J. Vigeland was supported by the NASA Marshall Faculty Fellowship Program.

References

[1] Thorpe, J. I., *et al.*, "The Laser Interferometer Space Antenna: Unveiling the Millihertz Gravitational Wave Sky," Bulletin of the American Astronomical Society, Vol. 51, Issue 7, id. 77 (2019).

[2] Edlund, J. A., Tinto, M., Krolak, A., and Jelemans, G., "Simulation of the White Dwarf – White Dwarf galactic background in the LISA data," *Classical and Quantum Gravity*, Volume 22 (2005).
doi: 10.1088/0264-9381/22/18/S05

[3] Littenberg, T. B., Cornish, N. J., Lackeos, K., and Robson, T., "Global analysis of the gravitational wave signal from Galactic binaries," *Physical Review D*, Vol. 101, 2020.
doi: 10.1103/PhysRevD.101.123021

[4] Prince, T. A., Tinto, M., Larson, S. L., and Armstrong, J. W., "The LISA Optimal Sensitivity," *Physical Review D*, Vol. 66, 2002.
doi: 10.1103/PhysRevD.66.122002

[5] Ellis, J., and van Haasteren, R., "jellis18/PTMCMCSampler: Official Release," doi:10.5281/zenodo.1037579, 2017.

APPENDIX A—NASA MARSHALL SPACE FLIGHT CENTER FACULTY FELLOWSHIP PROGRAM ANNOUNCEMENT

MARSHALL AEROSPACE FELLOWSHIP PROGRAM

JUNE 1, 2020 – AUGUST 7, 2020

Application Deadline February 7, 2020

- The Marshall Space Flight Center is offering Aerospace Fellowships for qualified researchers and graduate students at U.S. colleges and universities to conduct research with NASA colleagues during a ten-week residential program in Huntsville, Alabama.
- Aerospace Fellows will receive stipends of $15,000 (Assistant Professor, Research Faculty), $17,000 (Associate Professor), $19,000 (Professor), and/or $13,000 (Graduate Student).
- A relocation allowance of $1,500 will be provided to those fellows who live more than fifty miles from MSFC and a $500 travel supplement for one round-trip.
- Applicants must be U.S. citizens who hold full-time teaching, research appointments, or are graduate students at accredited U.S. universities or colleges.
- During the ten-week program, fellows are required to conduct their research on-site at the Marshall Space Flight Center.

Women and under-represented minorities, and persons with disabilities are encouraged to apply.

APPENDIX B—NASA MARSHALL SPACE FLIGHT CENTER FACULTY FELLOWSHIP PROGRAM DESCRIPTION

Program Description

- The Marshall Aerospace Fellowship program is a residential research experience. Fellows are required to conduct their research, during the ten-week program, on-site at the Marshall Space Flight Center.
- Participants cannot receive remuneration from other entities or other programs or other university or government sources during the Aerospace Fellowship 10-week period.
- An oral presentation by the Fellow to the Marshall group with which s/he has been affiliated is required, near the end of the fellowship period.
- A written final report is required at the end of the Fellowship.
- A written evaluation of the program by the Fellow is expected at the end of the Fellowship.

Eligibility

- US citizen
- Full time teaching or research appointment, or graduate student appointment at an accredited US university or college.
- Fellowship is awarded for one summer period, but Fellow may apply again for a second year.
- Women, under-represented minorities, and persons with disabilities are encouraged to apply.
- Graduate student applicants must be chosen by the Faculty Researcher who is applying, and both must be matriculated at the same university. Each must submit a completed application. If selected by Marshall, the faculty member and the graduate student would be a team engaged in the same research project at Marshall. To be selected, the graduate student must remain enrolled at the same university for a minimum period of two years following the summer research, teaming with the faculty researcher.

Selection

The applicants selected to be Aerospace Fellows will be chosen by the Marshall group which has been assigned the area of investigation (concentration) chosen by the applicant.

Marshall Collaborator

A Marshall Collaborator will be identified to serve as the co-investigator and day-to-day contact. At the end of the ten-week period, the Aerospace Fellow and the Marshall Collaborator will prepare a white paper summarizing the summer effort, including results and recommending follow-up work.

Compensation

Stipends for Aerospace Fellows are set as follows for the 10-week period:

Graduate Students	$13,000
Assistant Professors and Research Faculty	$15,000
Associate Professors	$17,000
Professors	$19,000

A relocation allowance of $1,500 will be provided to fellows who live more than fifty miles from the Marshall Center.

A travel supplement of $500 will be provided to those fellows receiving the relocation allowance.

REPORT DOCUMENTATION PAGE

Form Approved
OMB No. 0704-0188

1. REPORT DATE *(DD-MM-YYYY)*	2. REPORT TYPE	3. DATES COVERED *(From - To)*
01–05–2021	Technical Memorandum	

4. TITLE AND SUBTITLE
Marshall Space Flight Center Faculty Fellowship Program

5a. CONTRACT NUMBER

5b. GRANT NUMBER

5c. PROGRAM ELEMENT NUMBER

6. AUTHOR(S)
N.F. Six, Program Director and G. Karr, Compiler*

5d. PROJECT NUMBER

5e. TASK NUMBER

5f. WORK UNIT NUMBER

7. PERFORMING ORGANIZATION NAME(S) AND ADDRESS(ES)
George C. Marshall Space Flight Center
Huntsville, AL 35812

8. PERFORMING ORGANIZATION REPORT NUMBER
M–1525

9. SPONSORING/MONITORING AGENCY NAME(S) AND ADDRESS(ES)
National Aeronautics and Space Administration
Washington, DC 20546–0001

10. SPONSORING/MONITOR'S ACRONYM(S)
NASA

11. SPONSORING/MONITORING REPORT NUMBER
NASA/ TM–20210011456

12. DISTRIBUTION/AVAILABILITY STATEMENT
Unclassified-Unlimited
Subject Category 31
Availability: NASA STI Information Desk (757–864–9658)

13. SUPPLEMENTARY NOTES
Prepared by the Academic Affairs Office, Office of Human Capital
*The University of Alabama in Huntsville

14. ABSTRACT
The 2020 Marshall Aerospace Fellowship Program involved 11 faculty in the laboratories and departments at Marshall Space Flight Center and one faculty researcher working from Colorado. These faculty engineers and scientists worked with NASA collaborators on NASA projects, bringing new perspectives and solutions to bear. This Technical Memorandum is a compilation of nine research reports of the 2020 Marshall Aerospace Fellowship program, along with the Program Announcement and the Program Description. The research affected the following five areas: Materials, Spacecraft Systems, Human-Systems Interactions, Vehicle Systems, and Space Science.

15. SUBJECT TERMS
wireless sensors, propulsion, green propellant, materials, 3D printing, friction stir welds, instruments, solar neutrinos, gamma-ray polarimeter, lightning

16. SECURITY CLASSIFICATION OF: a. REPORT	b. ABSTRACT	c. THIS PAGE	17. LIMITATION OF ABSTRACT	18. NUMBER OF PAGES	19a. NAME OF RESPONSIBLE PERSON / 19b. TELEPHONE NUMBER *(Include area code)*
U	U	U	UU	126	STI Help Desk at email: help@sti.nasa.gov STI Help Desk at: 757–864–9658

Standard Form 298 (Rev. 8-98)
Prescribed by ANSI Std. Z39-18

National Aeronautics and
Space Administration
IS02
George C. Marshall Space Flight Center
Huntsville, Alabama 35812